THE UNIVERSITY OF ASTON IN BIRMINGHAM

DEPARTMENT OF PHYSICS

THE MEASUREMENT OF Ti(n,p)Sc AND Ni(n,p)Co REACTION CROSS-SECTIONS IN THE ENERGY RANGE 3.5 MeV TO 5.5 MeV

A thesis submitted for the degree

of

Doctor of Philosophy

by

CHARAN SINGH BUNGER B.Sc.,M.Sc.,M.Inst.P.

(March, 1983)

SUPERVISOR: Dr. A Bore B.Sc.,Ph.D.

TO

MY PARENTS AND TEACHERS

THE UNIVERSITY OF ASTON IN BIRMINGHAM

DEPARTMENT OF PHYSICS

The measurement of Ti(n,p)Sc and Ni(n,p)Co reaction cross-sections in the energy range 3.5 MeV to 5.5 MeV

by

Charan Singh Bunger B.Sc.,M.Sc.,M.Inst.P.

(Ph.D. March, 1983)

SUMMARY

The measurement of neutron cross-sections for $^{46,47}Ti(n,p)^{46,47}Sc$, $^{58}Ni(n,p)^{58}Co$ and $^{29}Si(n,\alpha)^{26}Mg$ reactions has been performed relative to the $^{238}U(n,f)$ cross-section in the neutron energy range of 3.5 MeV to 5.5 MeV.

The neutron source was a deuterium gas target,employing the $D(d,n)^{3}He$ reaction. The neutron flux measurements were made with a low mass parallel-plate ionisation chamber, to detect the fission fragments from the ^{238}U standard. The ^{238}U content of the fission foil was determined using an alpha particle assaying technique.

A surface barrier silicon detector was used for the on-line detection of charged particles from titanium and nickel foils. Initially, an inert gas scintillation detector was developed to avoid using a silicon detector, but the technique proved unsuccessful owing to the high gamma-radiation sensitivity of the scintillator.

A Monte Carlo program was applied to determine neutron beam profile from the gas target and to determine the irradiation geometry of sample and fission foil.

The measured cross-section data show good agreement with some previously reported measurements and meet the accuracy requirements of recent data requests.

Neutron Cross-sections.

Ti(n,p)Sc.

Ni(n,p)Co.

Si(n,α)Mg.

ACKNOWLEDGEMENTS

I am grateful to Professor S.E. Hunt, the Head of Department of Physics, for the provision of facilities used in this work.

I am very much indebted to Dr. A. Bore, for his continuous guidance and supervision throughout the project work.

I am also grateful to other members of the academic staff for many valuable discussions and to the workshop staff for their help to build the experimental components.

My thanks are due to the staff at Birmingham Radiation Centre for their co-operation in operating the Dynamitron accelerator and computer facilities.

I am also grateful to the Science Research Council and the University of Aston in Birmingham authorities for financial support, which enabled me to follow the research project.

Finally, I would like to thank my wife and children for their patience and understanding during this work.

CONTENTS

LIST OF TABLES.

LIST OF TABLES (contd.)

LIST OF FIGURES.

LIST OF FIGURES. (contd.)

LIST OF FIGURES.(contd.)

LIST OF FIGURES. (contd.)

CHAPTER 1

MEASUREMENT OF NEUTRON CROSS-SECTIONS

CHAPTER 1

1.0 Measurement of Neutron Cross-sections.

The neutron interactions with nuclear reactor materials used as fuel, for cladding and biological shields and in dosimetry, need to be investigated to provide accurate data for the design, operation and safety programmes of these reactors.

Several (n,p) reactions play important roles in, for example, neutron dosimetry.[1] Also, the (n,p) process contributes significantly to radiation damage in materials. The (n,p) and (n,α) reactions in structural materials such as steel produce hydrogen and helium, which may affect the strength of the material. Data on (n,p) and (n,α) cross-sections are needed for the understanding of neutron damage problems.

The need for (n,p) and (n,α) cross-section data in nuclear applications is evident from recent nuclear data request lists.[2] Groups such as the national nuclear data committees, serving all member states of the International Atomic Energy Agency (I.A.E.A.), produce request lists which serve as a guide to the experimentalist, evaluator and administrator when planning nuclear data measurements and evaluation programmes. The compilation of nuclear data requests is published every two years by the nuclear data section of the I.A.E.A. in a document

called the World Request List for Nuclear Data (WRENDA). In the current edition of WRENDA, there are 1667 requests for data related to the fission reactor technology, including nuclear materials safeguards, and 501 requests for nuclear fusion programmes. Each request details the accuracy and priority of the data assignments. The highest priority is given to requests for nuclear data for reactors to be built in the near future. The priority 2 requests are for nuclear data which will be required during the next few years in the applied nuclear energy programmes, e.g. the design of a reactor or fuel processing plant; data for construction materials such as neutron moderators, absorbers and radiation shields; space applications and biological studies. The priority 3 goes to requests for nuclear data of more general interest to form a body of information needed for nuclear technology.

1.1 Nuclear Data Requirements.

Calculations of the neutron physics behaviour of a reactor require accurate data which must be supplied by nuclear physics measurements supplemented by integral measurements on mock-up zero power reactors. The accuracy required increases as the reactor progresses from the design-concept stage through detailed design to construction and operation. The precise independent definition of the required accuracy for all cross-sections

cannot be obtained but that the published data request list (e.g. WRENDA) forms a good working guide for the experimentalist.

There are three fairly distinct requirements. Firstly, the designer needs to be able to calculate and optimise the behaviour of his projected design and, later, needs sufficient information to complete the detailed design of the reactor. Secondly, since he will be concerned in ensuring that his design is a safe one, he will also need physics information pertinent to those accident conditions which form that part of a safety programme. Thirdly, when the construction is complete, a detailed understanding is required to operate the reactor as efficiently as possible. The more detailed and accurate the data, the greater the safety margins, thus enabling the reactor to be run at higher powers, to higher burn-ups and with greater reliability. The accuracy with which the data are needed to satisfy these requirements tends to become steadily more exacting as the design proceeds from a conceptual study through engineering design and development to reactor operation.

For neutron shielding and dosimetry, data is required for a variety of materials. The most frequent shielding materials involve light elements such as: hydrogen, carbon, nitrogen, oxygen through to silicon and calcium and the structural elements such as nickel, titanium and

iron. When hydrogen is present in a shield in significant proportions, the most important cross-sections are the total and the elastic but in heavy element shields, the details of the inelastic scattering become highly significant.

The measurement of the neutron flux spectrum at specific positions in an assembly is of great importance as it is applied to correlate the material properties such as radiation damage, to the radiation environment. Fluence measurements (time-integrated flux over long periods) are also needed to study radiation damage to materials and reactor parameters such as the speed of control, reactivity and fuel utilisation. In material damage studies, the variations introduced by different reactor spectra contribute to the spread in experimental data and for this accurate spectra are required.

A number of methods exist for the measurement of neutron flux. Thermal and epithermal neutrons are detected through (n,γ) reactions. Fissionable materials such as ^{235}U and ^{239}Pu are used to detect thermal neutrons and ^{238}U, ^{232}Th are employed to measure fast neutron fluxes, through the detection of fission products produced by neutron bombardment. Neutron monitoring is undertaken with (n,p) and (n,α) reactions through the detection of charged particles produced in these reactions. For fast flux measurements over long irradiations, the

reaction products must have long half-lives e.g. $^{58}Ni(n,p)^{58}Co$, 71.3 days; $^{46}Ti(n,p)^{46}Sc$, 3.43 days; $^{54}Fe(n,p)^{54}Mn$, 314 days; and $^{63}Cu(n,\alpha)^{60}Co$, 5.26 years.

1.2 The Selection of Elements for Nuclear Cross-section Measurements.

A study of cross-section measurement requests in WRENDA, led to the selection of Ti(n,p)Sc and Ni(n,p)Co reactions for measurement in the neutron energy range 3 to 6 MeV.

The cross-section data requests for Ti(n,p)Sc require accuracies between 5% to 10%, with standing priorities 1 and 2 for neutron dosimetry applications.

The $^{46}Ti(n,p)^{46}Sc$ and $^{47}Ti(n,p)^{47}Sc$ reactions are particularly suitable as fluence monitors in radiation damage studies because of simple modes of decay of the ^{46}Sc and ^{47}Sc nuclei and their long half-lives, 84 days and 3.4 days respectively. Hogg et.al.[3] suggested that the $^{46}Ti(n,p)^{46}Sc$ reaction may provide a promising substitute to the $^{58}Ni(n,p)^{58}Co$ reaction due to its low burn-up cross-section to thermal neutrons (0.25 barns) and the ease of measurements of the burn-up of ^{46}Sc in comparison to ^{58}Co. Unfortunately, the use of this reaction has been limited by the lack of accurately known cross-section data.

Previous measurements of these reactions have mostly employed activation techniques. An initial aim of the present work was to develop an alternative technique

In this work, (n,p) and (n,α) reactions were monitored through on-line measurement of the emitted charged particles. The on-line method has been demonstrated by Konijn and Lauber[4], and is particularly suited to measurements where the reaction product is either stable or exhibits a very long or very short half-life. In the activation technique, the reaction rate is determined by detecting gamma rays from the decay modes of the reaction products. The decay modes of the nuclides with different half-lives emit gamma rays of different energies, which may overlap. The activity of these nuclides can be measured but, for a long-life nuclide, the activity is low and it requires a longer measurement time to obtain good counting statistics.

The cross-section measurements for Ti(n,p)Sc reactions were made for ^{46}Ti and ^{47}Ti isotopes only. The reaction threshold for ^{50}Ti(n,p)^{50}Sc is above the maximum neutron energy available for this work. ^{49}Ti(n,p)^{49}Sc reaction has a threshold, but no proton peak was observed and no data has been published for this reaction in the energy range below 6 MeV. For the ^{48}Ti(n,p)^{48}Sc reaction, the cross-section is known to be

low[5, 6] and the low proton energy makes the reaction difficult to detect.

Only a limited number of measurements have been reported for $^{46}Ti(n,p)^{46}Sc$ and $^{47}Ti(n,p)^{47}Sc$ reactions. A review of these measurements is given in Tables 1.1 and 1.2, but with the exception of the work performed by Jalil[6] and Smith et. al.[5], the measurements do not meet the "below 10% accuracy" requirements quoted in WRENDA. Further to this, there has been little agreement between the measurements. The measurements by Jalil and Smith et. al. are the most accurate and comprehensive to date.

One of the important factors, to be taken into account when comparing measured cross-sections, is the accuracy of the standard to which these measurements are normalised. The U(n,f) cross-section has become a commonly-used standard. Luckic and Carroll's[7] measurements were made relative to different standards at a given energy and the results show a marked fluctuation. The data of Ghorai et. al.[8], measured relative to the $^{27}Al(n,p)^{27}Mg$ cross-section values of Grundl[9], shows considerable difference to the data of Smith et. al. even though the corresponding data for $^{27}Al(n,p)^{27}Mg$ by Smith et. al. agreed with that of Grundl.Other standards used, have been $^{27}Al(n,\alpha)^{24}Na$[10] and $^{31}P(n,p)^{31}Si$[11] reactions and their cross-section data is less accurate.

There is an increasing demand for accurately known cross-section data for fast reactor design and other applications to fast neutron dosimetry. The data request in WRENDA, for $^{58}Ni(n,p)^{58}Co$, requires accuracies between 2 to 10% mostly with priority 1. There is a great deal of data presently available and Table 1.3 shows several recent evaluations. There are sizeable discrepancies between measurements. The careful and extensive measurements by Smith et.al. rule out the structure evident in earlier measurements by Konijn and Lauber. However, only Konijn and Lauber have produced data through a non-activation technique.

The on-line measurement of the emitted charged particles was made through the use of a surface barrier silicon detector. Initially, an inert gas scintillation detector was developed to monitor (n,p) and (n,α) reactions. This proved unsuccessful. Full details of these experimental techniques are given in Chapter 4.

A gas-flow fission counter was employed for neutron flux measurements, in which the fission fragments from ^{238}U deposit were detected. This technique is described in Chapter 3.

The details of the deuterium gas target, as a neutron source, are given in Chapter 2.

AUTHOR(S)	NEUTRON ENERGY (MeV)	RELATIVE STANDARD.*	CROSS-SECTION DATA	ACCURACY	REF.
Jalil (1980)	3.5 to 6.0	$^{235}U(n,f)$	15mb at 3.51 MeV to 122mb at 5.91 MeV.	6%	(6)
Lu-Han Lin (1979)	4.8	$^{27}Al(n,\alpha)^{24}Na$.	63mb	11%	(10)
Smith et.al. (1976)	Threshold to 10 MeV	$^{235}U(n,f)$ and $^{238}U(n,f)$	14mb at 3.7 MeV to 125mb at 5.9 MeV.	5 to 8%	(5)
Ghorai et.al. (1971)	4.1 to 6.1	$^{27}Al(n,p)^{27}Mg$ of Grundl.	46mb at 4.1 MeV to 149mb at 6.1 MeV.	17 to 18%	(8)
Luckic and Carroll. (1970)	4.91 to 7.0	(1) $^{56}Fe(n,p)^{56}Mn$ (2) $^{27}Al(n,\alpha)^{24}Na$ (3) $^{58}Ni(n,p)^{58}Co$	119mb at 5.48MeV rel. to (1) 139mb at 6.01MeV rel. to (2) 87mb at 4.91MeV rel. to (3) 81mb at 5.48MeV rel. to (3)	15%	(7)

* Relative standard used for neutron flux measurements.

Table 1.1 THE REPORTED DATA ON $^{46}Ti(n,p)^{46}Sc$ REACTION.

AUTHOR(S)	NEUTRON ENERGY(MeV)	RELATIVE STANDARD *	CROSS-SECTION DATA.	ACCURACY	REF.
Jalil (1980)	3.5 to 6.0	$^{235}U(n,f)$	60mb at 3.51MeV to 100mb at 5.91MeV.	5%	(6)
Smith et.al. (1976)	Threshold to 10 MeV	$^{235}U(n,f)$ and $^{238}U(n,f)$.	50mb at 3.70MeV to 96mb at 5.90MeV.	5 to 8%	(5)
Ghorai et.al. (1971)	4.1 to 6.1	$^{27}Al(n,p)^{27}Mg$ of Grundl.	68mb at 3.41MeV 86mb at 4.10MeV 93mb at 5.00MeV 135mb at 6.10MeV	17 to 18%	(8)
Armitage (1967)	3.5 to 6.0	$^{58}Ni(n,p)^{58}Co$. of Barry et.al.	97mb at 5.10MeV (absolute measurement)	-	(12)
Gonzalez (1961)	2.0 to 3.6	$^{31}P(n,p)^{31}Si$	40mb at 1.99MeV to 70mb at 3.41MeV.	13%	(11)

* Relative standard used for neutron flux measurements.

Table 1.2 THE REPORTED DATA ON $^{47}Ti(n,p)^{47}Sc$ REACTION.

AUTHOR(S)	NEUTRON ENERGY(MeV)	REL. STANDARD/ TECHNIQUE *	CROSS-SECTION DATA.	ACCURACY	REF.
Wu et.al. (1977)	3.0 to 4.8	H(n,n)p Proton recoil telescope.	214mb at 2.99MeV to 420mb at 4.80MeV.	4.5%	(13)+
Smith et.al. (1976)	Threshold to 10 MeV	$^{235}U(n,f)$ $^{238}U(n,f)$	163mb at 2.85MeV to 459mb at 5.00MeV.	5 to 8%	(5)+
Konijn and Lauber (1963)	2.2 to 3.8	H(n,p) proton recoil from polyethylene radiator.	76mb at 2.20MeV to 389mb at 3.80MeV.	6.5 to 40%	(4)@
Paulsen and Widera. (1971)	2.8 to 5.0	H(n,n)p proton recoil telescope.	202mb at 3.35MeV 367mb at 3.94MeV 338mb at 4.14MeV	4 to 6%	(14)+
Temperley (1968)	3.0 to 4.0	Associated Particle.	227mb at 3.12MeV 213mb at 3.35MeV 201mb at 3.48MeV	10%	(15)+
Nakai et.al. (1962)	2.98 to 4.8	Stilbene Scintillation Counter.	147mb at 2.98MeV 151mb at 3.30MeV 281mb at 3.67MeV 412mb at 4.34MeV	15 to 22%	(16)+

Table 1.3 THE REPORTED DATA ON $^{58}Ni(n,p)^{58}Co$ REACTION. (Continued)

AUTHOR(S)	NEUTRON ENERGY(MeV)	REL. STANDARD/ TECHNIQUE *	CROSS-SECTION DATA	ACCURACY	REF.
Barry et.al. (1962)	3.23 to 4.98	$^{235}U(n,f)$	235mb at 3.23MeV 305mb at 3.52MeV 474mb at 4.20MeV 509mb at 4.98MeV	11%	(17)+
Meadows and Whalen (1963)	1.0 to 2.67	$^{235}U(n,f)$	1.2mb at 1.04MeV to 139mb at 2.67MeV	8 to 9%	(18)+
Gonzalez et.al. (1960)	2.2 to 3.6	$^{31}P(n,p)^{31}Si$ Proportional Counter.	142mb at 2.23MeV to 195mb at 3.55MeV.	6 to 12%	(19)+

* Relative standard and technique used for neutron flux measurements.

\+ Activation technique used for reaction rate measurements.

@ Surface barrier silicon detector used for reaction rate measurements.

Table 1.3 THE REPORTED DATA ON $^{58}Ni(n,p)^{58}Co$ REACTION.

CHAPTER 2

THE NEUTRON SOURCE

CHAPTER 2.

2.0 THE NEUTRON SOURCE.

For this work, monoenergetic neutrons were required over the energy range from a few MeV, upwards, with a neutron energy spread of 150 keV or less and a flux of at least 10^6 neutrons cm^{-2} s^{-1}. The choice of neutron source was limited by the available particle accelerator beam, i.e.3 MeV deuterons, to the $D(d,n)^3He$ reaction. The practical energy range for the bombarding deuterons in the Dynamitron accelerator, Birmingham Radiation Centre, was 0.60 MeV to 3.0 MeV, producing neutrons in the energy range 3.5 to 6.3 MeV.Where required, lower energies can be obtained through the acceleration of doubly charged ions e.g. d_2^{++} instead of d^+.

The $D(d,n)^3He$ reaction cross-section is large for the production of primary monoenergetic neutrons in the range 3.5 to 6.0 MeV (Fig. 2.1) which enables the required neutron flux level to be achieved.

For bombarding particles of energy greater than 0.5 MeV it is feasible to use gas targets consisting of a small cell filled with the target gas in which the beam enters through a thin window. Further, for this work, the gas target meets the general requirements of an ideal target:

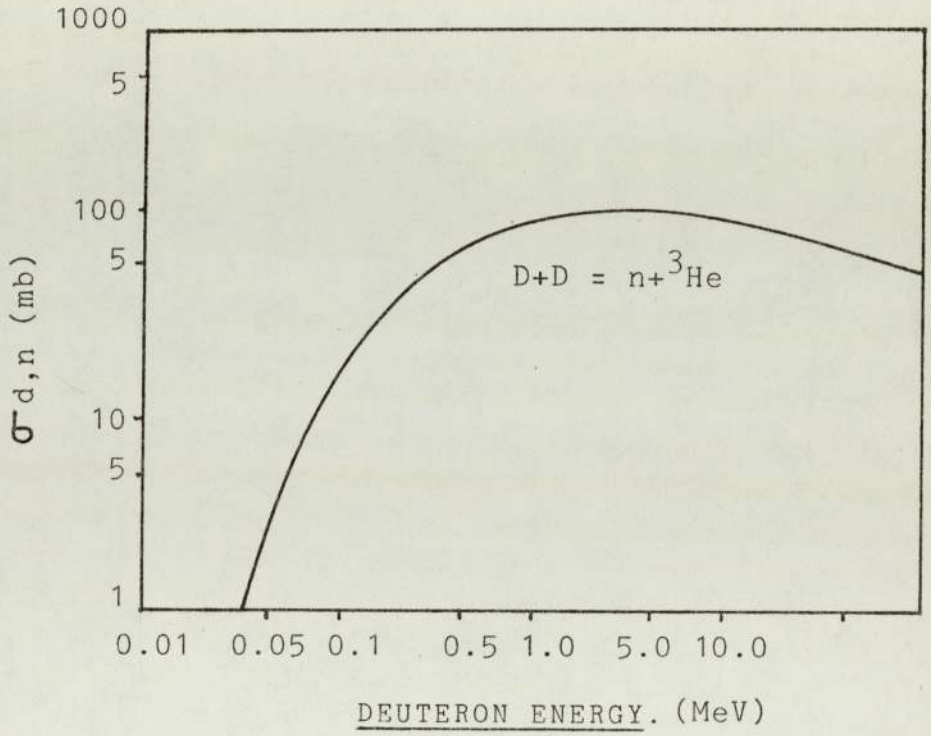

Fig. 2.1 ENERGY DEPENDENCE OF CROSS-SECTION FOR $D(d,n)^3He$ REACTION.

small neutron energy spread with angle of emission and minimum interference from competing neutron producing reactions. The gas target also allows greater flexibility as regards the gas pressure, which can be varied to allow changing in stopping power of the gas with deuteron energy,and the window thickness can be varied to suit the incident deuteron energy.

Other forms of deuterium targets are available and the most commonly used is the deuterated metal target.Deuterium, in the ratio of approximately 1:1 to titanium is absorbed in the metal. A layer of titanium or zirconium of thickness between 10 μgm cm^{-2} and 10 mg cm^{-2} is applied to a thicker plate of backing material, usually copper,which serves as a strong thermally conducting support. The thin layers are obtained through vacuum evaporation[20]. The impregnation of titanium with deuterium gas is carried out by heating the metal to very high temperature in the atmosphere of deuterium gas. When allowed to cool the metal absorbs the gas. Initially, good outgassing of the metal and vacuum of the order of 10^{-6} mmHg are obtained, in order to overcome contamination difficulties.

The deuterated metal targets, due to their high thermal conductivities, permit the use of higher beam currents than in gas targets but have poorer energy

resolution. Gas targets can provide neutron fluxes of 8-10 times those from deuterated metal targets at the same energy resolution. This is due to the fact that metal targets cause higher degradation in the energy of the bombarding particles than in the case of a gas target.

2.1 Design Considerations for a Gas Target.

A deuterium gas target was employed (constructed by Jalil[6]), and being available in the department. This target was designed to withstand up to three times the maximum beam power densities achieved in the conventional gas targets.

A schematic diagram of the gas target is given in Fig. 2.2. The nickel window, 3μm thick, was soft soldered onto a copper washer of external diameter 1 cm and internal diameter 0.6 cm. The gas cell walls are of stainless steel thickness 0.25 mm and the end face of the cell is made of 0.1 mm thick molybdenum to provide an adequate beam stop.

There were a number of reasons for the choice of the window and gas cell materials. A thin metal window allows the beam to pass into the target gas with minimum energy loss and at the same time retains the gas at a pressure against vacuum in the beam line of the

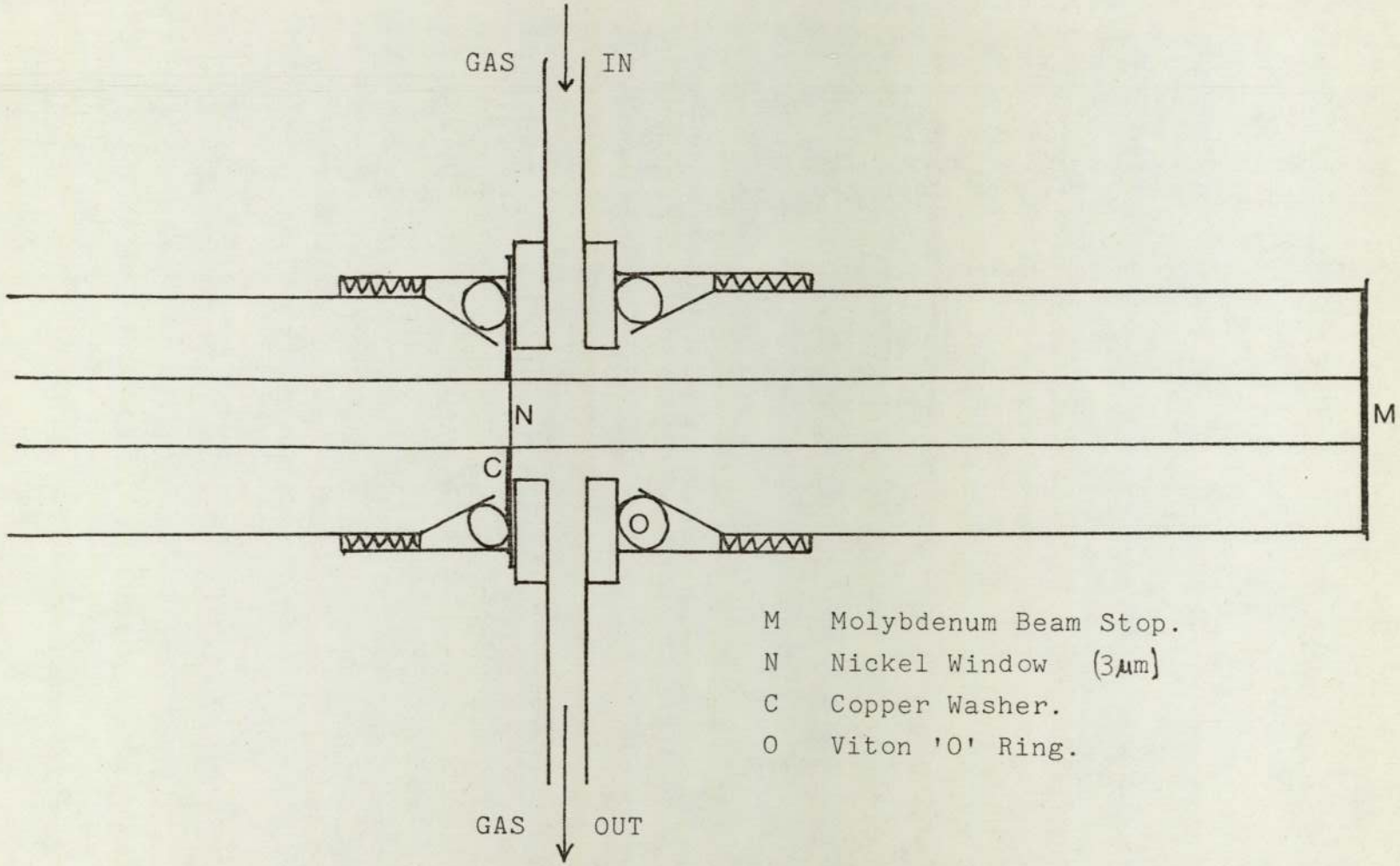

Fig. 2.2 SCHEMATIC DIAGRAM OF GAS TARGET.

accelerator. The thin window puts a limitation on the use of gas targets as it can easily be punctured by the high temperature resulting from high beam current densities. High beam densities are required to obtain better neutron fluxes and consequently cooling of the target windows becomes a necessity.

Some of the more important properties of a good window material are:

(a) Availability in various thicknesses, uniform and hole free.

(b) Low stopping cross-section for minimum beam energy loss.

(c) Good mechanical strength to withstand gas pressure over a reasonably large aperture.

(d) High thermal conductivity and melting point to withstand high beam currents.

(e) Low multiple coulomb scattering to minimise angular divergence of the beam.

(f) Small contribution of background neutrons.

The most commonly used window materials are aluminium, nickel, molybdenum and tantalum all of which may be obtained in fairly uniform sheets free from pin holes. Aluminium has low mechanical strength and a large neutron production cross-section. The stopping power of tantalum is high; it is not available in thin, pin-hole free foils, which restricts its use as a

window material. Molybdenum has high mechanical strength, even at higher temperature, and it has high thermal conductivity, but it is available only as relatively thick foil. Nickel was considered to be the most acceptable material for the gas cell window.

The stainless steel, used for the gas cell walls had the necessary requirements for design purposes. The material has low (d,n) reaction cross-section and a minimum wall thickness can easily be obtained, thus reducing scattering. The end face of the gas cell is of molybdenum which acts as the beam stop. This material has high thermal conductivity and high threshold for neutron production.

The limit on the length of gas cell (30 mm) was set by the divergence of the beam through multiple coulomb scattering by the nickel window. Sawyer[21] has calculated the mean square scattering angles for some materials using Fermi's formula[22]:

$$\langle \theta^2 \rangle = \frac{2\pi z^2 Z^2 e^4 N}{E^2} \ln \left(E a_o / e^2 Z^{4/3} z \right) \quad ..(2.1)$$

where, z and Z are atomic numbers of bombarding and the target nuclei; e is the electronic charge, N is the number of nuclei cm^{-2} in the window, E is the bombarding particle energy in eV and a_o is the radius of the hydrogen atom.

When applied to a nickel window $3\mu m$ thick the value of the root mean square scattering angle, as calculated from the above formula , is approximately 2.5^{o}, giving a 1.3 mm deviation of the beam at the beam-stop face of the 30 mm long target.

The maximum gas pressure which the nickel window can withstand was determined from the yield strength data supplied by Goodfellow Metals Co. For nickel the yield strength is 59 MPa. A foil with radius 0.3 cm and thickness 3 microns will withstand a maximum gas pressure of 1.2 atmospheres, as calculated from the relation:

$$P_{max.} = \frac{2\,Y\,t}{R} \quad \ldots\ldots\ldots\ldots (2.2)$$

where, Y is the yield strength, t the foil thickness and R, the foil radius. In this work, a gas pressure of one atmosphere was used for all the measurements. Fig. 2.3 shows the gas target assembly.

The energy loss in the nickel window can be estimated from the relation given by Whaling[23] , (adapted to deutrons):

$$E_{loss} = \left[0.48(Z/E_d) \left\{ \ln(E_d/2Z) + a \right\} 10^{-15} \right] T \quad \ldots (2.3)$$

where, Z = atomic number of the window material, of thickness T, in nuclei cm^{-2}.

a = an adjustable parameter varying with Z.

Fig. 2.3 The Gas Target Assembly.

E_d = the deuteron energy in MeV.

Whaling quoted a of the order of 5.1 for Z less than 45 and therefore, for the nickel window described above, the deuteron energy loss is given by:

$$E_{loss} = \left[(13.44/E_d) \left\{ \ln (E_d/56) + 5.1 \right\} 0.02739 \right] \quad ....(2.4)$$

The energy loss values for deutrons traversing the nickel window, perpendicular to the beam, are given in table 2.1.

E_d (MeV)	0.5	1.0	1.5	2.0	2.5	3.0
E_{loss}(MeV)	0.281	0.395	0.363	0.325	0.295	0.266

Table 2.1 Deutron energy loss through nickel window.

2.1.1 The Window Cooling and Gas Circulation System.

Higher beam currents are achieved by circulating the cooled deuterium gas past the window at high speeds. In the present design, liquid nitrogen was used to pre-cool the gas. Fig. 2.4 shows the schematic diagram of the cooling and gas filling system.

The gas circulating pump consisted of a rubber diaphragm oscillating at 11,200 revolutions per minute

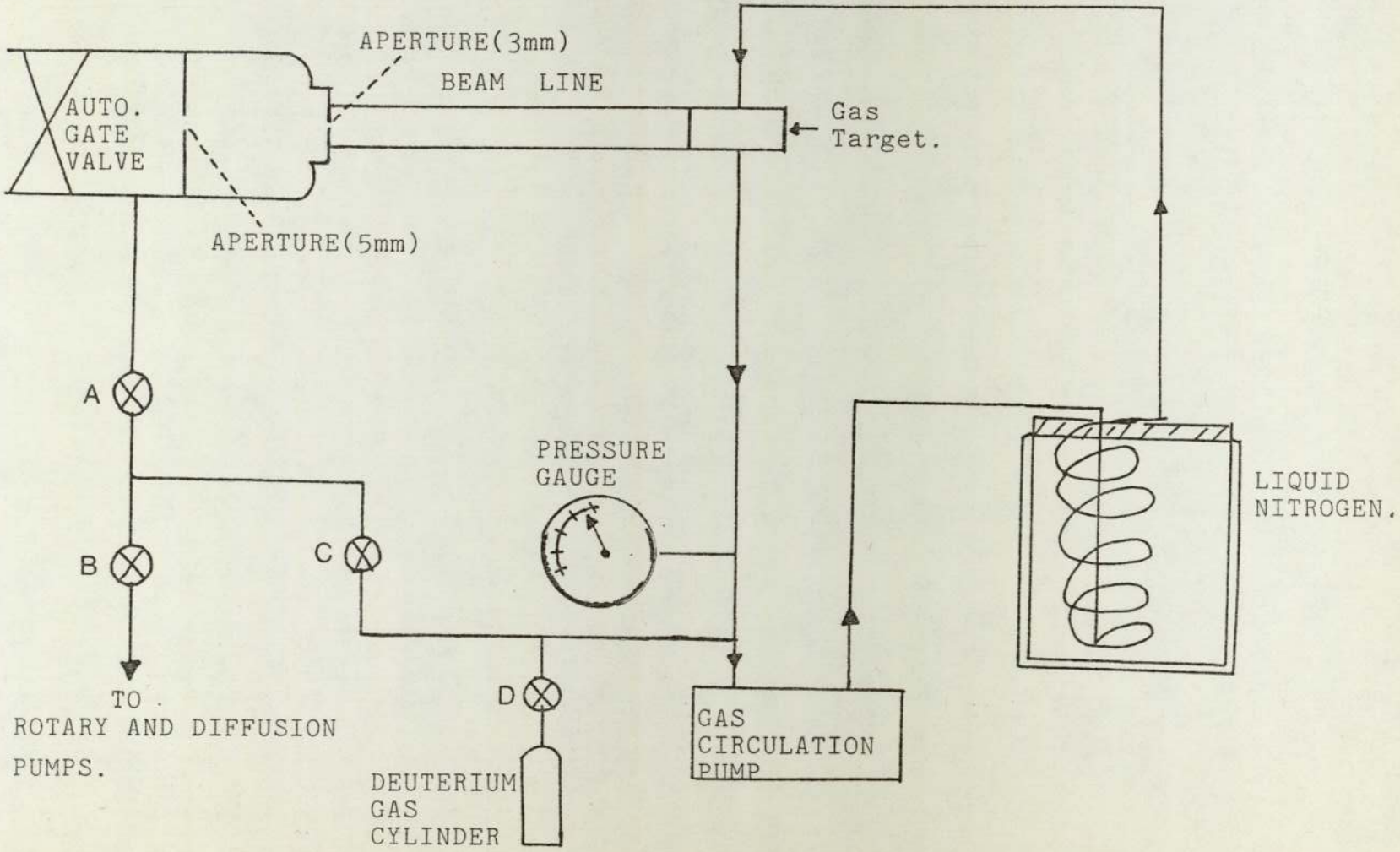

FIG. 2.4 SCHEMATIC DIAGRAM OF THE COOLING AND GAS FILLING SYSTEM.

driven by a 190 watt, 2800 revolutions per minute motor. The rotational motion of a pulley is converted into vertical oscillations of the diaphragm through a cam shaft pivoted 0.1 cm off-centre from the rotational axis of the drive shaft. Fig. 2.5 shows the sectional view of the circulating pump.

The effective pumping speed of the system, 1.12 litres per second, is less than that available from the pump due to the conductance of the pipe-work. The conductance (C) for round and smooth bore pipes can be determined as:

Conductance per unit pressure(torr) = Flow rate (Q) in litres per second.

The flow rate depends on internal diameter (D) and length (L) of the pipe and for air it is given as[106]:

$$Q(\text{air}) = (250\ D^4/\ L)\ \text{litres per second} \quad .....(2.5)$$

where D and L are in centimetres.

For deuterium, a correction factor of 2.07 is applied, giving:

$$Q(\text{deu.}) = (2.07 \times 250\ D^4/L)\ \text{litres per second.}$$

Therefore the conductance (C) of a pipe of D = 0.2 cm and L = 300 cm, for deuterium at a pressure of one atmosphere (760 torr), is calculated from:

$$C = (2.07 \times 250\ D^4/L) \times 760\ \text{litres per second} \quad .....(2.6)$$

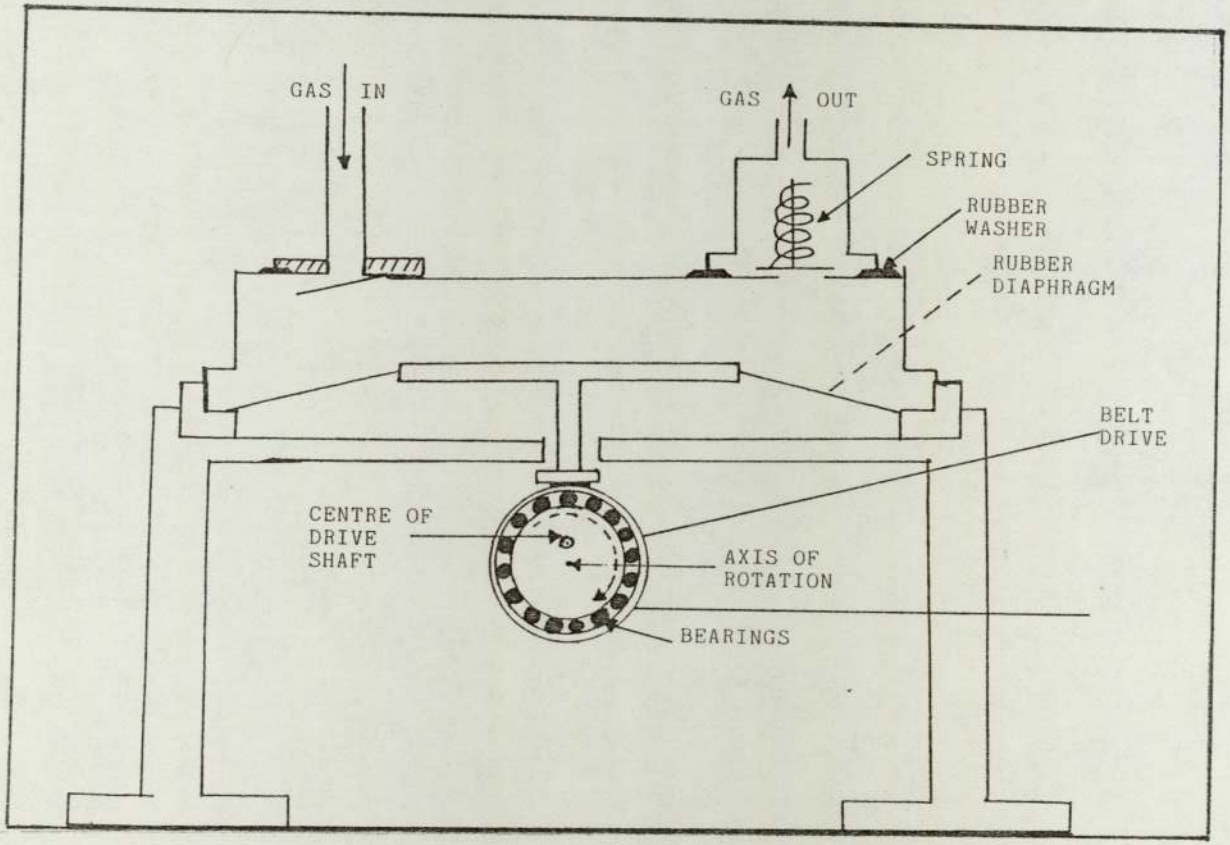

Fig. 2.5 Sectional View of the Gas Circulating Pump.

The effective pumping speed ($S_{eff.}$) is determined from the relation[106]:

$$S_{eff.} = (C.S_p) / (C+S_p) \quad .....(2.7)$$

where C is the conductance of the pipe,which is equal to 2.1 litres per second as calculated from equation 2.6, and S_p is the pump speed taken to be 2.37 litres per second.

The heat removal from the vertical surface of the window is increased through forced convection. Ennis and Walton[107] calculated that for a 3μm thick nickel window, the heat dissipation at near maximum beam current is 85% by conduction through the foil to the mounting case, 10% by conduction to the gas and the remaining 5% by radiation. It was estimated following from Langmuir[24], that with an effective pumping speed of 1.12 litres per second, the heat removal from the front surface of the window increased by a factor of about 16. Pre-cooling of the gas target increased the heat removal still further.

The performance of the pre-cooled gas circulating system was checked through destruction of a few window foils, with and without gas cooling. Beam currents were increased in steps of 0.1μA and at each current level, the performance of the accelerator vacuum was observed for periods lasting about 10 minutes. Without the gas cooling system, one foil failed at 1.1μA of beam, which

was indicated by a gradual increase in the beam line pressure. With the cooling system on, a beam current of 2.6μA on the target was reached. These tests were carried out with 2.8μA deuteron beam.

A single tantalum collimator (3mm aperture diameter), placed before the gas cell, restricts the beam current incident on the window to 13μA (equivalent of 40 watts). Two tantalum discs were employed with apertures of 5mm and 3mm, which reduced beam current stopped at any one collimator, so avoiding overheating of the collimator system. A careful procedure was adopted in operating the system in order to avoid accidental damage to the window. The whole system and the part of the accelerator beam line were first evacuated to approximately 10^{-3} mbar. The filling system was then isolated by closing valve C (Fig. 2.4), allowing deuterium gas into the system slowly through fine control valves D and H. The beam line was further evacuated to the level of operation of the accelerator. When the beam line vacuum pressure was low enough to operate the ion pump, the valve A was closed in order to isolate the beam line from the diffusion pump. This was necessary to avoid the introduction of carbon contamination from the vacuum system, onto the target window during beam bombardment. The liquid nitrogen trap further minimised the introduction of hydrocarbons.

2.2 The Neutron Energy Spectrum from the Deuterium Gas Target.

Fig. 2.6 illustrates the geometric configuration of gas target with fission detector and semiconductor detector used in the later measurements. The spatial and energy distribution of neutrons from the deuterium gas cell is dependent upon several factors:

(1) Deuteron energy loss in the nickel window.

(2) Deuteron energy loss and broadening in the gas.

(3) Neutron energy and intensity variation with the angle of emission.

The neutron profile for the gas target used in this work has been reconstructed through a Monte Carlo method [6], for an extended line source. The Monte Carlo program 'NPROFILE' is described in detail in Appendix 2 and , hence, only a brief discussion is given here.

The program determines the position at which a neutron is created in the target. The neutron emission at a given angle is weighted by using the differential cross-section data of Liskien et.al.[25]. From the position co-ordinates of the point of creation of a neutron, the polar co-ordinates of its emission and the distance between the neutron source and the sample, the program determines whether or where the neutron is

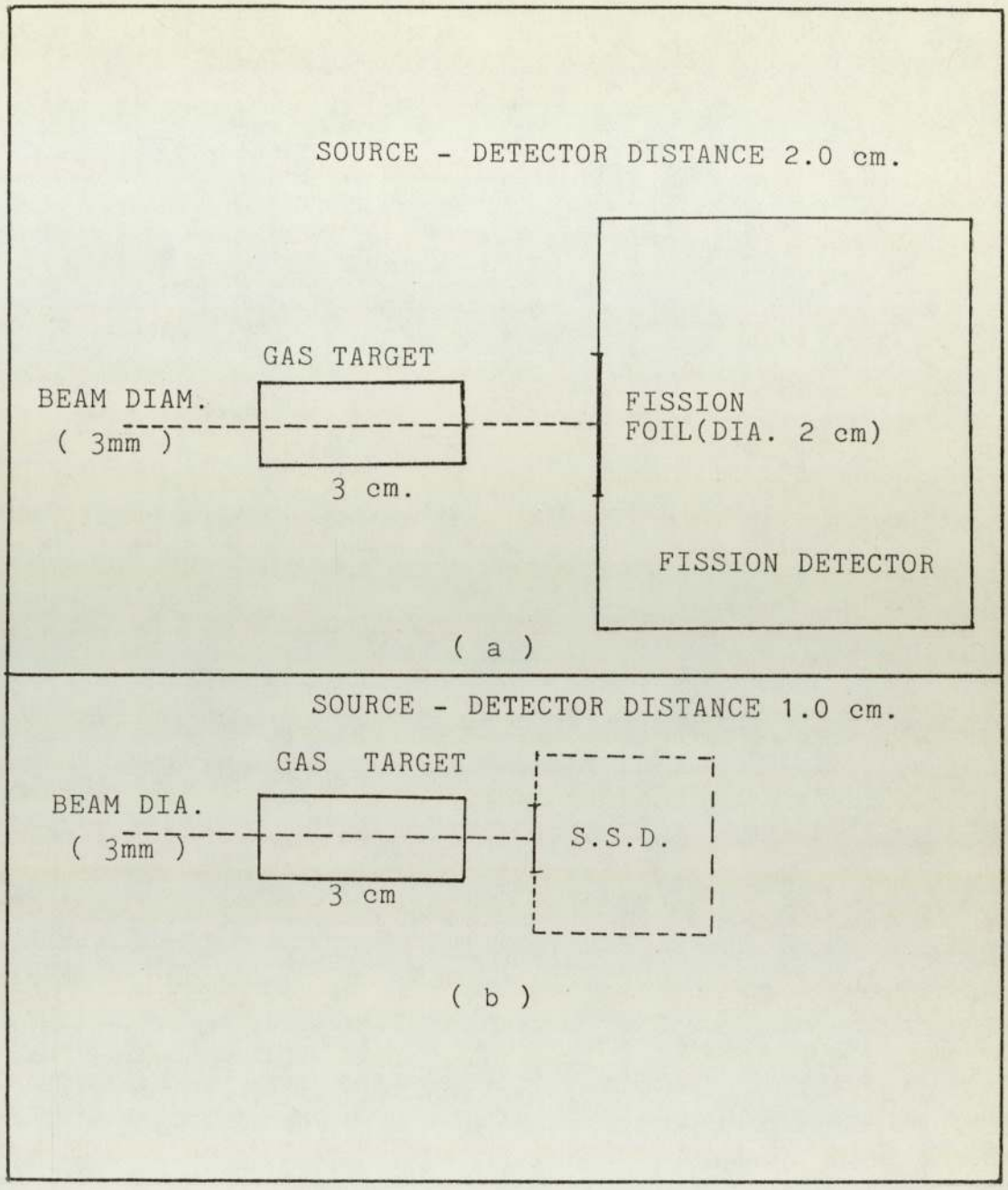

Fig. 2.6 GEOMETRIC CONFIGURATION OF GAS TARGET WITH (a) FISSION DETECTOR (b) SOLID STATE DETECTOR.

incident on the sample. An energy profile at the sample is obtained following a large number of neutron histories.

Neutron spectra were obtained for the geometric configurations depticted in Fig. 2.6, at deuteron beam energies of 1.0 MeV to 2.4 MeV in steps of 200 keV. These are shown in Figs. 2.7 and 2.8. The mean neutron energy and FWHM resolution for each spectrum, Tables 2.2 and 2.3, were obtained from computer programs (PEAKFIT, Appendix 1 and NPROFILE, Appendix 2).

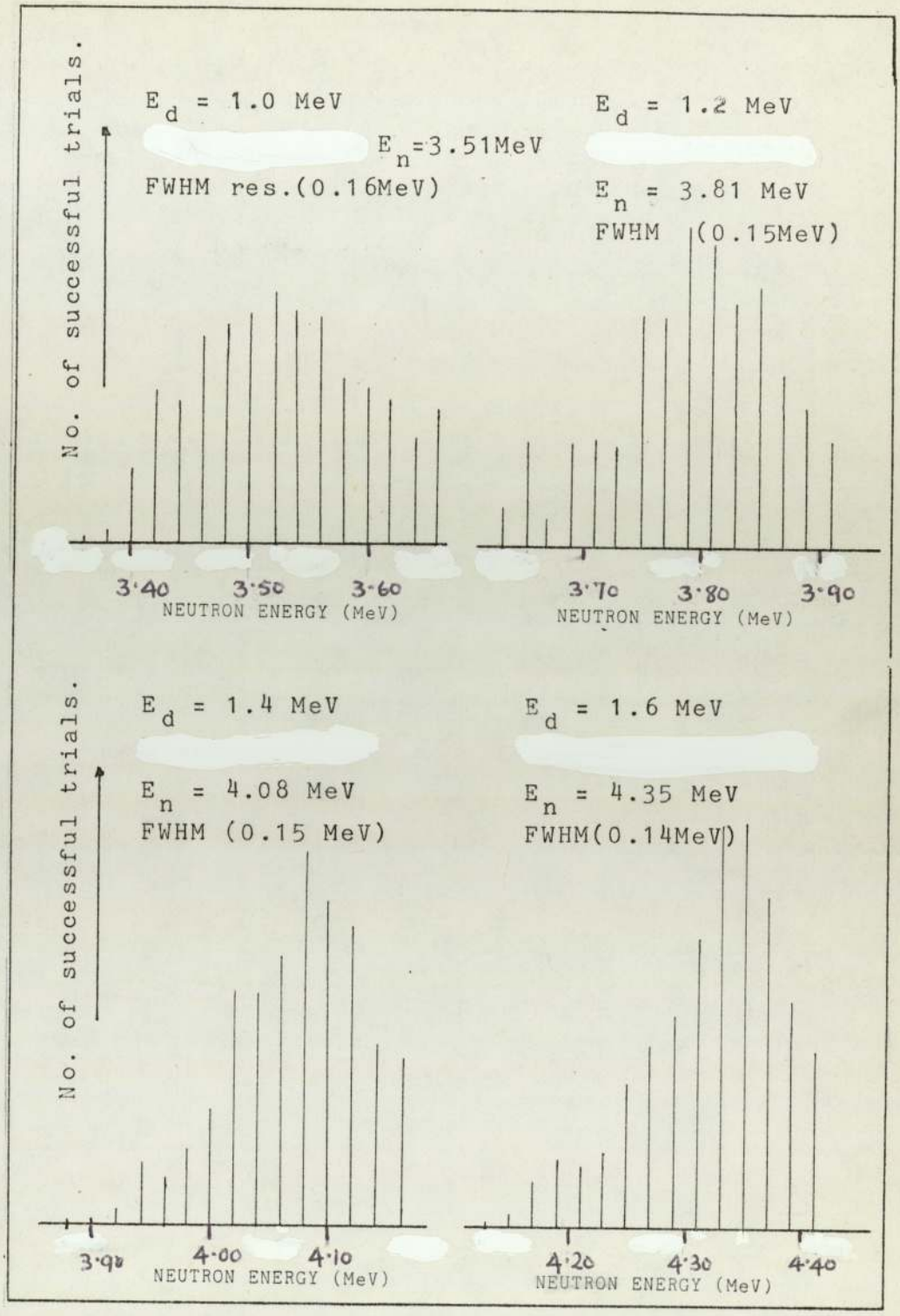

Fig. 2.7 (a) NEUTRON SPECTRUM AT FISSION FOIL.
(MONTE CARLO CALCULATIONS)

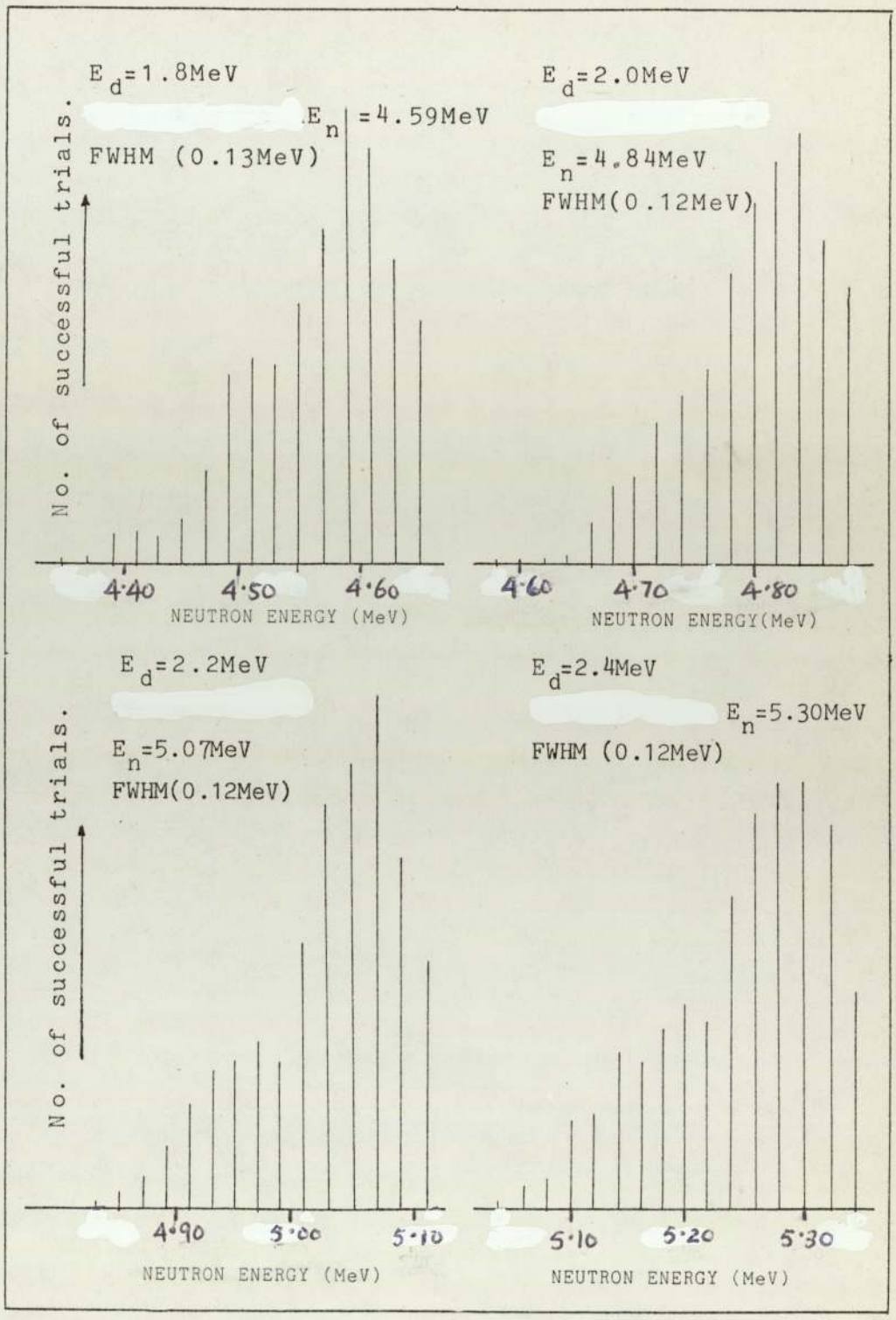

Fig. 2.7 (b) NEUTRON SPECTRUM AT FISSION FOIL.
(MONTE CARLO CALCULATIONS)

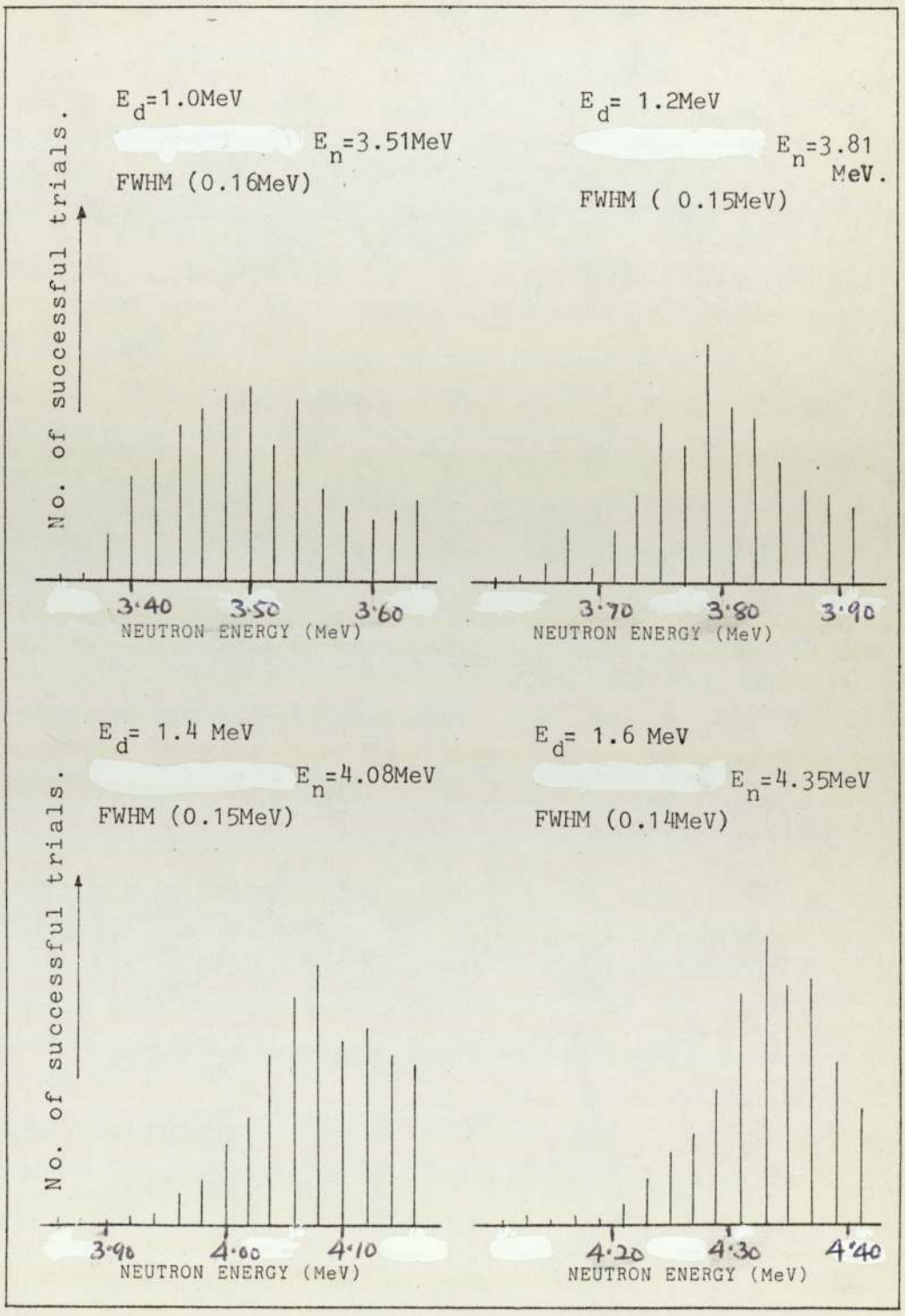

Fig. 2.8(a) NEUTRON SPECTRUM AT THE SAMPLE.
(MONTE CARLO CALCULATIONS)

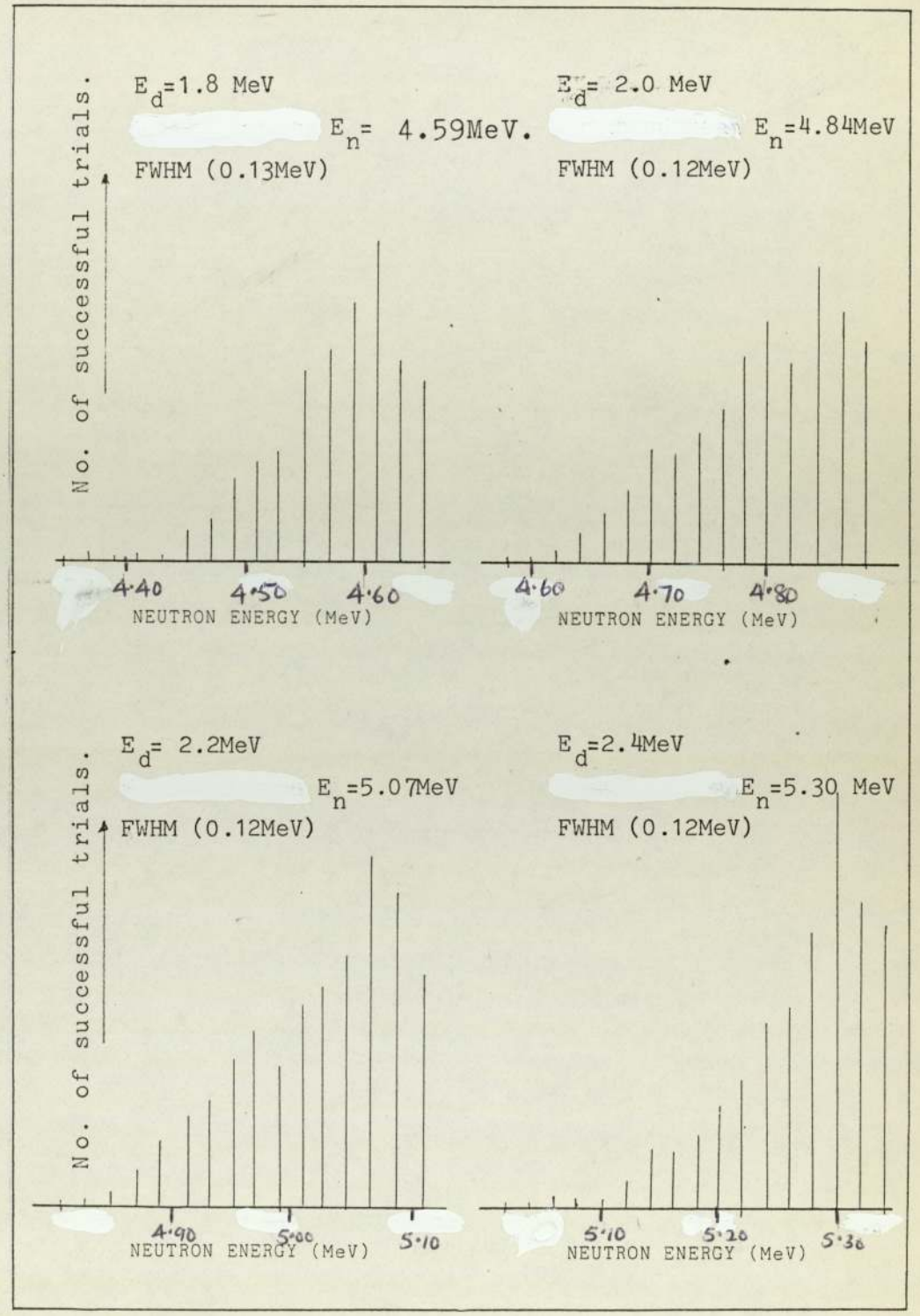

Fig. 2.8(b) NEUTRON SPECTRUM AT THE SAMPLE.

(MONTE CARLO CALCULATIONS)

DEUTERON ENERGY. (MeV)	MEAN NEUTRON ENERGY. (MeV)	FWHM RESOLUTION. (MeV)
1.0	3.51	0.16
1.2	3.81	0.15
1.4	4.08	0.15
1.6	4.35	0.14
1.8	4.59	0.13
2.0	4.84	0.12
2.2	5.07	0.12
2.4	5.30	0.12

Table 2.2 NEUTRON ENERGY AT THE FISSION COUNTER.

DEUTERON ENERGY. (MeV)	MEAN NEUTRON ENERGY. (MeV)	FWHM RESOLUTION. (MeV)
1.0	3.51	0.16
1.2	3.81	0.15
1.4	4.08	0.15
1.6	4.35	0.14
1.8	4.59	0.13
2.0	4.84	0.12
2.2	5.07	0.12
2.4	5.30	0.12

Table 2.3 NEUTRON ENERGY AT THE SOLID STATE DETECTOR.

CHAPTER 3

TECHNIQUES FOR THE MEASUREMENT OF NEUTRON FLUX

CHAPTER 3

3.0 Techniques for The Measurement of Neutron Flux.

The neutron cross-section determination requires the measurement of neutron flux, employing a suitable technique to obtain a good accuracy. Some techniques use a standard of accurately known cross-section and are called"relative methods". In the"relative methods" of neutron flux measurements, the cross-section of the standard must be known accurately and vary only slowly with incident neutron energy. The cross-section must be large to ensure good counting statistics. Other methods are absolute and do not require the use of a standard. Techniques which fall into this second category are associated particle, associated activity and total absorption.

$^{1}H(n,p)$ reaction provides a suitable standard for neutron energy range 100 keV to 20 MeV. The cross-section of this reaction is known to an accuracy of better than 1%. Most often, the recoil proton is detected using a proportional or scintillation counter.

In a gas proportional counter, the hydrogenous medium is usually hydrogen or a hydrogen-argon mixture. The detector configurations are chosen to achieve a sensitive volume, and the upper neutron energy limit is about 3 MeV, which is set by the proton range in the gas.

When the recoil proton range exceeds the counter dimensions, wall and edge effects are observed. Increases in counter diameter or gas pressure are limited by the increased sensitivity of the detector to gamma radiation and by electrical breakdown effects when using high voltages.

The scintillation counter provides good proton detection efficiency but which decreases with increasing neutron energy. The efficiency can be improved by increasing the detector size but with the risks of gamma pile-up. Organic scintillators produce non-linearity in light output with energy.

In many cross-section measurements, secondary standards have been used as alternatives. $^{235}U(n,f)$ and $^{238}U(n,f)$ cross-sections are most widely used as secondary standards. The cross-section values of these reactions are known to an accuracy between 2.5 to 3%. The major sources of systematic error lie in the assay of the fissile deposit. The technique of fission counting is generally simple and provides accurate reaction rate measurements, with good discrimination against background or other competing reactions.

The reactions used in the "associated particle" neutron flux measurements are:

(1) $D(d,n)^3He$; associated particle, ^3He.

(2) $T(d,n)^4He$; associated particle, alpha.

(3) $T(p,n)^3He$; associated particle, ^3He.

The emitting neutron is accompanied by the simultaneous production of a charged particle. The detection of the charged particle provides a measure of the neutron flux.

In the $D(d,n)^3He$ reaction at low energies, there exists an isotropic distribution of ^3He particles and neutrons. At higher energies, the distribution becomes anisotropic. At low energies, the $D(d,n)^3He$ reaction has a competing $D(d,p)^3H$ reaction and the detection of protons becomes an alternative to ^3He detection.

The $T(d,n)^4He$ reaction has been mostly used for 14 MeV neutron fluxes. The associated alpha particles have nearly isotropic distribution.

There are a number of limitations of the "associated particle" methods which are due to:

(a) the multiple Coulomb scattering of the residual nuclei before detection.

(b) the neutron scattering in the target-holder material.

(c) the variation of the angle and energy of the associated particle with the variation of incident particle energy at a fixed neutron angle (laboratory).

(d) problems of identification of the particle. In $D(d,n)^3He$ reaction ^3He must be counted in presence of protons from the D(d,p)T competing reaction.

In"total absorption methods", all the neutrons of any energy incident upon the detector are absorbed. The activity of the irradiated detector is determined to calculate neutron flux.

In this work the neutron flux measurements were carried out relative to ^{238}U, and with a 2π gas-flow fission counter already developed and successfully employed for neutron monitoring experiments in the department.[6] The fission cross-section of ^{238}U is well known and smoothly varying. The technique utilises the detection of fission fragments released from ^{238}U deposit when bombarded with neutrons through the process of ionization produced as the fission products are brought to rest within the detector gas. A large output pulse is produced since the light and heavy fission fragments have energies of approximately 93 MeV and 61 MeV respectively.

The geometry allows an accurate measurement of counting efficiencies and the approximate choice of chamber dimensions provides improved discrimination between alpha particles and fission fragments. The energy resolution is poor but this does not pose a problem in fission counting.

The"associated activity" reactions such as

$$^{7}Li(p,n)^{7}Be$$

$$^{57}Fe(p,n)^{57}Co$$

$$^{65}Cu(p,n)^{65}Zn$$

produce gamma active products, following irradiation. Measurement of induced activity provides a measure of the neutron flux.

3.1 Design Considerations for a 2π Gas-flow Fission Counter.

The energy loss of fission fragments in a material differs considerably from that of alpha particles or protons. An alpha particle or a proton maintains a constant charge for almost its entire range in the stopping material and the capture of electrons is important only near the very end of the range. For a fission fragment, however, the initially large positive charge obtained through the loss of several electrons decreases continually by the capture of electrons in the slowing down process. This has a marked effect on the energy loss mechanism of the fragment towards the latter part of its range where collisions between the fragment and the nuclei of the stopping material are more important than the electronic excitation processes.

Calculations of the range of fission products is complicated by having to consider the decrease of the net charge of the fragments and the incidence of nuclear collisions. Bohr[26] made two approximations in calculating the fragment range

(1) The fragment will shake off all those of its electrons whose orbital velocity in the atom is smaller than the velocity of the fragment itself.

(2) The velocity of the fragment will decrease linearly with distance as long as the energy loss is due

mostly to electronic collisions, thus relating to the case of energy loss of an alpha particle. He obtained a relationship between the range of a fission fragment and that of an alpha particle with the same velocity v :

$$\frac{R_F}{R_{alpha}} \simeq 7 . \frac{A_1}{(Z_1^{eff})^2} \quad \ldots\ldots\ldots\ldots\ldots (3.1)$$

A_1 is the mass number of the fragment and Z_1^{eff} is determined in approximation by

$$Z_1^{eff} = Z_1^{1/3} (hv/e^2) \ldots\ldots\ldots\ldots (3.2)$$

where Z_1 is the full value of the fragment charge free from electron shielding.

Katcoff, Miskel and Stanley[27] , measured the ranges of plutonium fission products in air and their results (Table 3.1) are in sufficient agreement with Bohr's theory. The ranges in argon are also included in the table following their calculation from the Bragg-Kleeman formula (equation 4.11). The mean range in air for the heaviest to the lightest fission fragment varies from 1.79 cm to 2.65 cm and in argon from 0.35 cm to 0.51 cm. The mean range in air at N.T.P. for alpha particles from ^{238}U (4.19MeV) is approximately 2.96 cm. Therefore, an appropriate choice of source to electrode spacing of 0.5 cm to 2.5 cm in argon at N.T.P., would effect discrimination between alpha particles and fission fragments from the ^{238}U deposit.

Mass Number	Fission Product	Half-life	Mean Range(cm) air	Mean Range(cm) argon
83	Br	2.4 hr.	2.65	0.511
91	Sr	9.7 hr.	2.55	0.490
92	Y	3.5 hr.	2.55	0.490
93	Y	10.0 hr..	2.53	0.488
94	Y	20.0 min.	2.52	0.486
97	Zr	17.0 hr.	2.50	0.482
99	Mo	67.0 hr.	2.48	0.478
105	Rh	36.5 hr.	2.42	0.467
109	Pd	13.4 hr.	2.35	0.453
112	Pd	21.0 hr. .	2.24	0.432
117	In	1.95 hr.	2.08	0.401
127	Sb	93.0 hr.	2.09	0.403
129.	Sb	4.2 hr.	2.09	0.403
132	Te	77.0 hr.	2.05	0.395
133	Te	60.0 min.	2.04	0.393
134	Te	43.0 min.	2.04	0.393
140	Ba	12.8 days.	1.92	0.370
143	Ce	33.0 hr.	1.89	0.364
157	Eu	15.4 hr	1.79	0.355

Table 3.1 Mean Range of Plutonium Fission Fragments in Air and Argon at N.T.P.

The maximum detector pulse output per unit energy deposition depends on the ionization properties of the filling gas. In an impurity-free gas, the mean energy required to form an ion-pair 'W' is of interest. This quantity is relatively sensitive to the nature of the gas but independent of the type and energy of the particle particularly if the gas is pure.'W' is not very different for different stopping gases and is smallest for the inert gases[28]. The choice of gas can be determined from consideration of 'W' values. Some gas mixtures with argon gas as the main constituent have been reported to have minimum values of 'W'[29] and in such case the effective value of 'W' is determined as:[30]

$$\frac{1}{W_{ij}} = (1/W_i - 1/W_j)\, Z_{ij} + 1/W_j \quad \ldots\ldots (3.3)$$

Where $Z_{ij} = \dfrac{P_i}{P_i + a_{ij}P_j}$

with P_i = partial pressure of gas with value W_i,

P_j = partial pressure of gas with value W_j,

a_{ij} = an empirical constant which in some cases is equal to the ratio of the stopping powers of the component gases.

The presence of electronegative impurities in the gas such as argon (the most common) results in the capture of electrons, thereby reducing their mobility. The electron agitation energy reduces following inelastic collisions with impurity molecules. This attachment of

electrons to the impurity molecules forming negative ions produces loss in the pulse. Bistline[31], derived a relation which accounts for this loss;

$$S_o - S = \frac{1}{2}(S.x/\lambda) \qquad (3.4)$$

S_o is the voltage pulse in absence of electron attachment and which can be defined in terms of detector configurations as;

$$S_o = (N.e/C.d) x \qquad (3.5)$$

N is the total number of electrons released through ionization. e, the electronic charge. C represents the capacitance of the parallel plate detector with d as source to electrode spacing. λ is electron attachment mean free path and x is the distance from point of origin of the electron to the collecting electrode.

The use of a mixture, such as of argon and a polyatomic gas, reduces the sensitivity of the detector response to the presence of electronegative impurities. High drift velocities for the electrons would contribute to achieve a fast electron pulse rise time. Small amounts of nitrogen in argon, though provide higher drift velocities yet nitrogen being an impurity causes electron attachment thereby reducing the agitation energy. Methane on the other hand provides the highest drift velocity[32] and does not act as an impurity. Fig.3.1 presents the electron drift velocity as a function of E/p (E is the electric field strength and p is the gas pressure) for pure argon, methane and methane-argon mixture. The

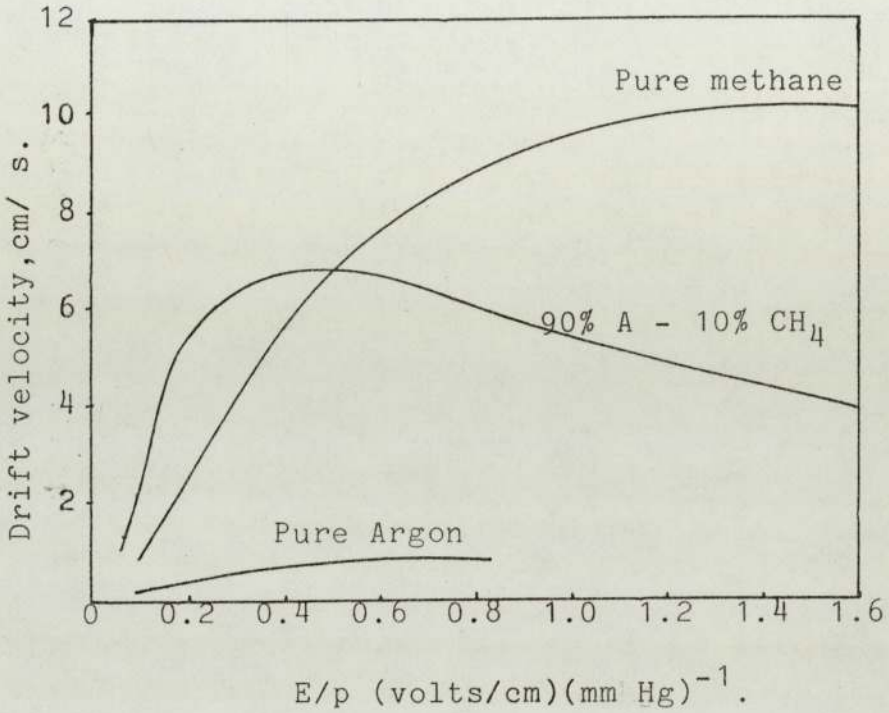

Fig. 3.1 Electron Drift velocity as a function of E/p for argon, methane and argon-methane mixture.

proportion of methane in argon needs to be considered as its increasing concentration would provide increasingly fast pulses but, the corresponding increase in effective 'W', would reduce ionization yield per unit energy deposited. ('W' for methane is much higher than for argon). A mixture of 90% argon and 10% methane was selected to be most suitable.

3.2 Performance of the 2π Gas-flow Fission Counter.

The schematic diagram of the fission counter, employed in this work, is given in Fig. 3.2. The thickness of the aluminium casing was kept at a minimum to reduce neutron scattering by the counter. Aluminium has an advantage over other possible counter shell materials in that its neutron cross-section is low in the energy range of the present measurements (3.5 to 5.5MeV).The collecting electrode has curved edge to avoid build-up of surface charge. The perspex rod attached to the collector slides across a millimetre scale allowing the source-collector distance to be varied. The counter chamber diameter (about 7 cm) was determined by the size of the platinum disc (diameter 6 cm) carrying the uranium deposit and by the range energy considerations for the particles depositing energy in the gas mixture. The gas flow through the counter was continuous, at a low flow rate and at a pressure just above atmospheric.
Fig. 3.3 shows the photograph of the fission counter.

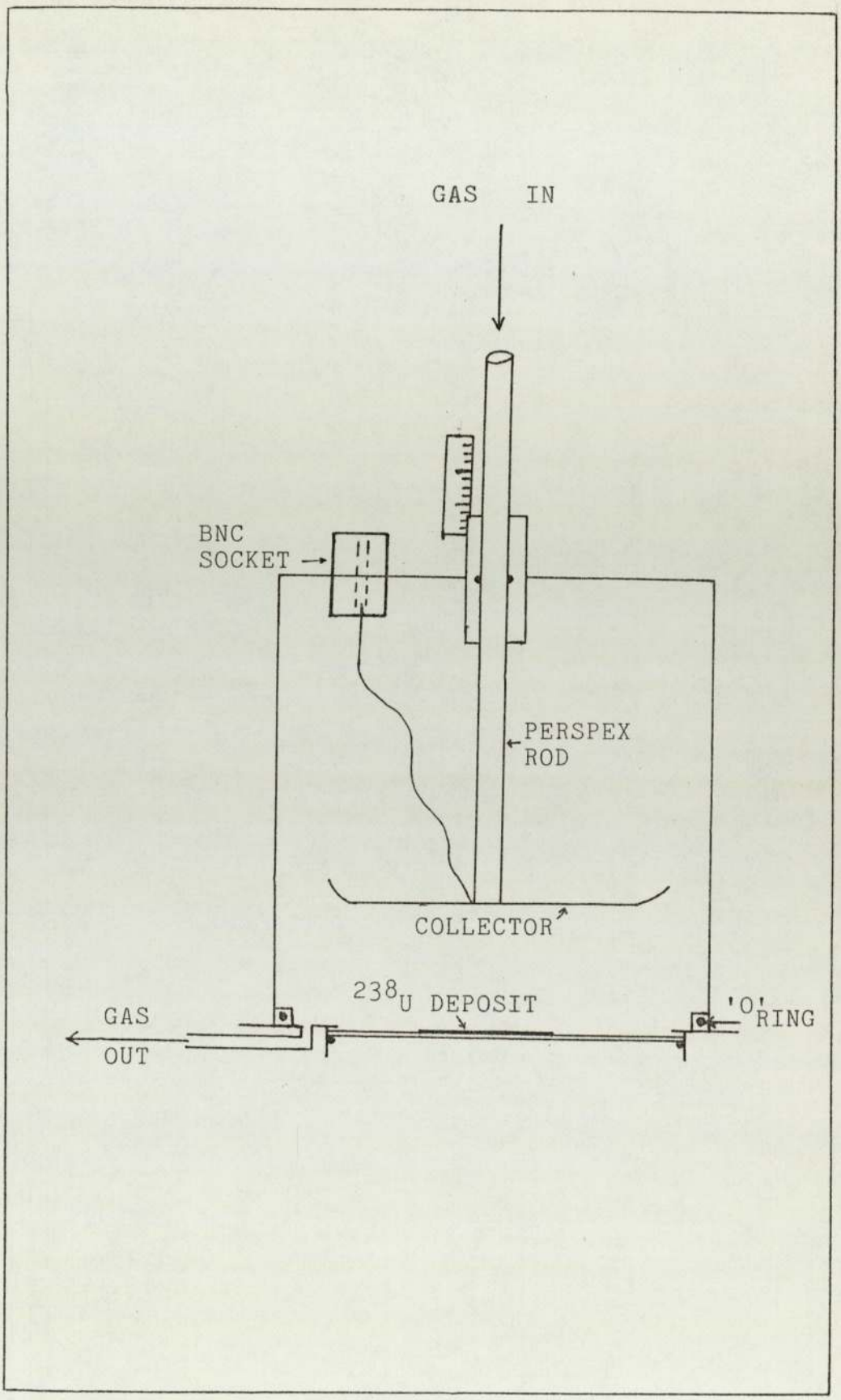

FIG. 3.2 SCHEMATIC DIAGRAM OF THE FISSION COUNTER.

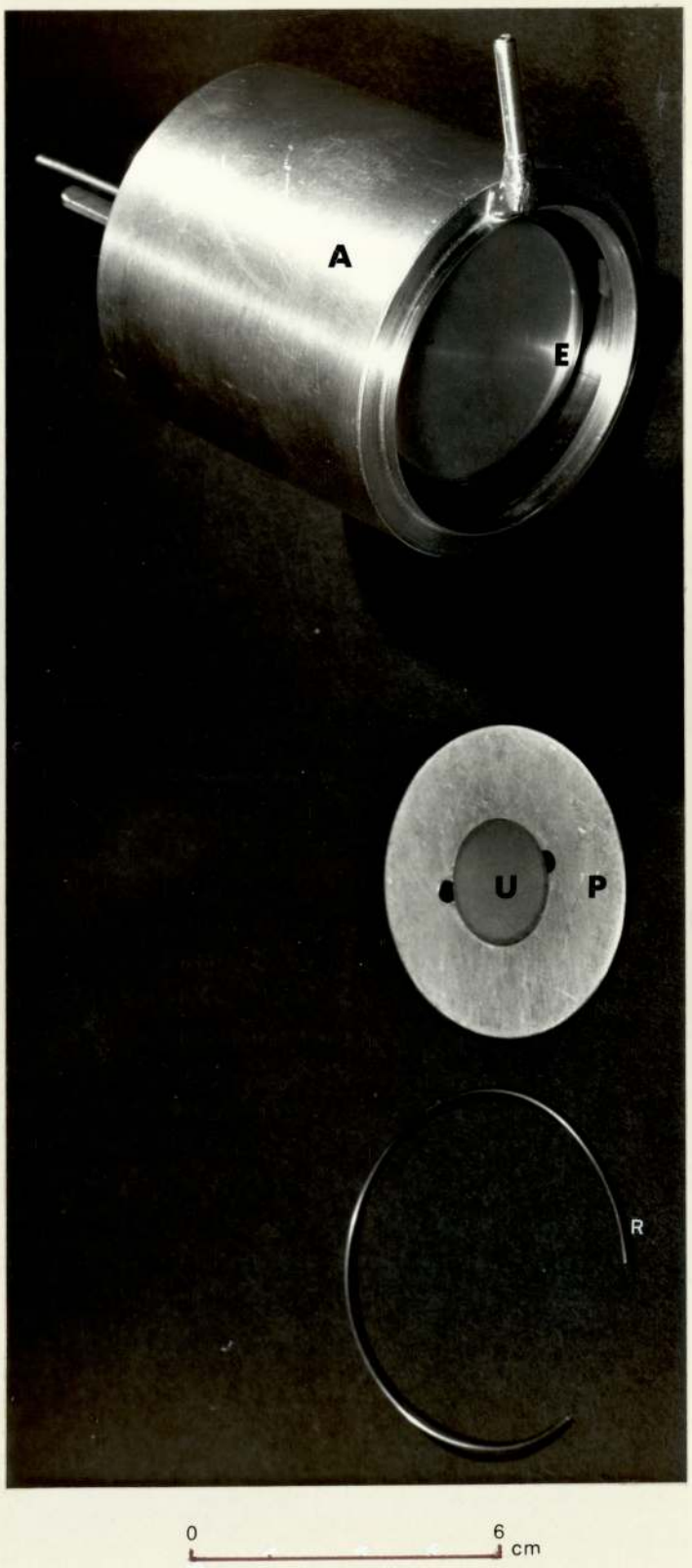

A Aluminium chamber

E Electrode

P Platinum disc

U Uranium deposit

R Supporting ring.

Fig. 3.3. The Fission Counter.

The detector was operated at about +300 volts supplied by a standard E.H.T. unit. The ancillary electronics, employed to process the output pulses, consisted of a pre-amplifier (Ortec 124), a main amplifier (Ortec 472 A), shaping constant 2μs.

In initial tests a ^{235}U alpha particle (4.8 MeV) spectra were obtained, with argon gas flow, at a source-to-electrode spacing of 2 cm and 4 cm (Figs. 3.4 and 3.5). The first spectrum (Fig. 3.4) is not that expected from an alpha particle source. The two peaks in the spectrum are due to the source-electrode configuration. The lower energy peak is that due to alpha particles with ionization tracks intercepting the electrode thus depositing part of their energy in the gas. The alpha particles traversing past the electrode deposit their full energy and contribute to the higher energy peak. The distortion in the lower energy peak is attributed to a fraction of alpha particles emitted at low grazing angles to the surface of the source which lose part of their energy in the chamber walls. This explanation is underlined by Fig.3.5 for which the source - electrode spacing is greater than the 3.6 cm range of 4.8 MeV alpha particles,and by measurements made at higher gas pressures. The distortion of the spectrum can easily be eliminated by increasing gas pressure. This was not done in this work as the detector was not to be used for the measurement of alpha particle spectra.

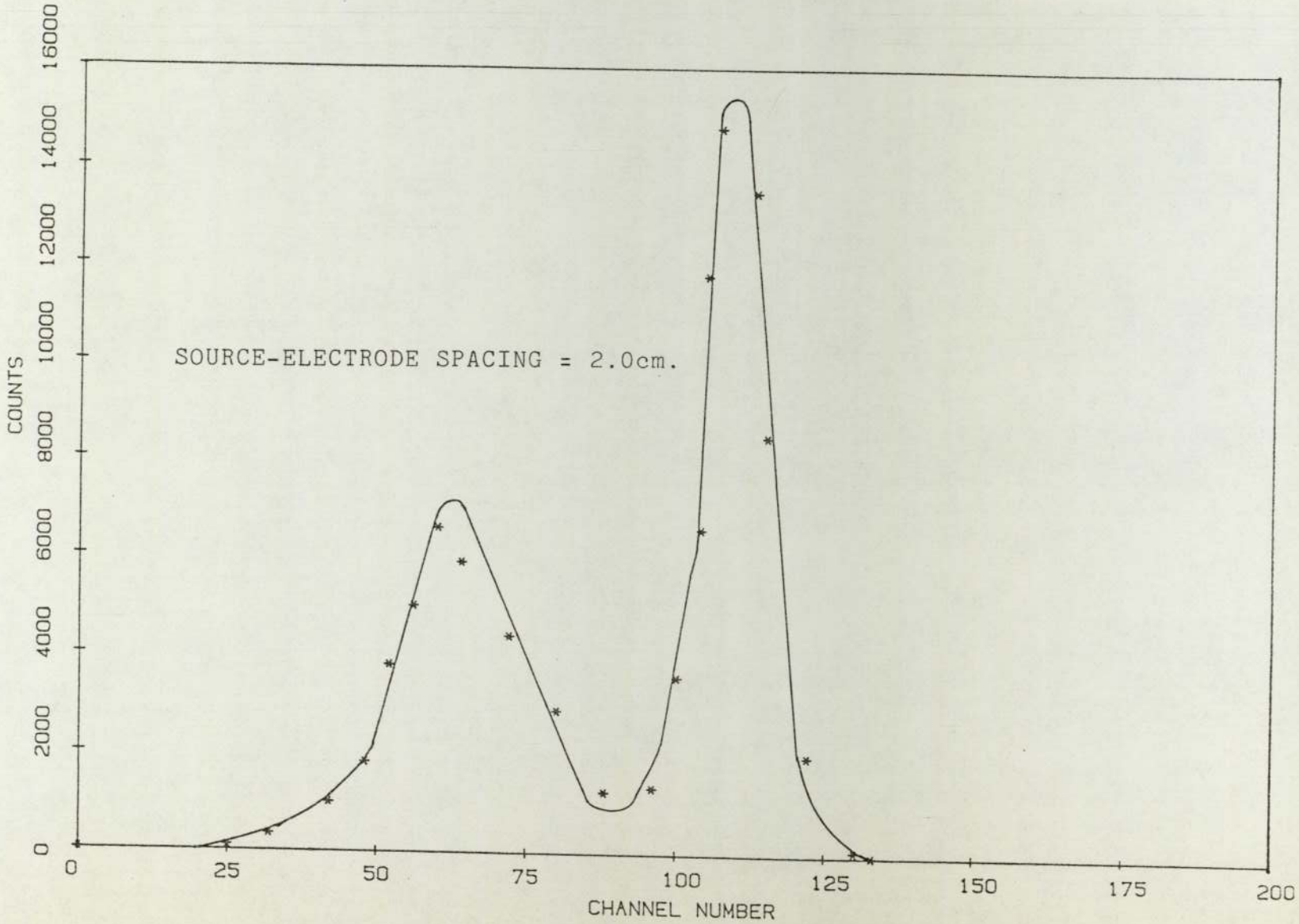

Fig. 3.4 Alpha Spectra from ^{241}Am, with Argon-filled Counter.

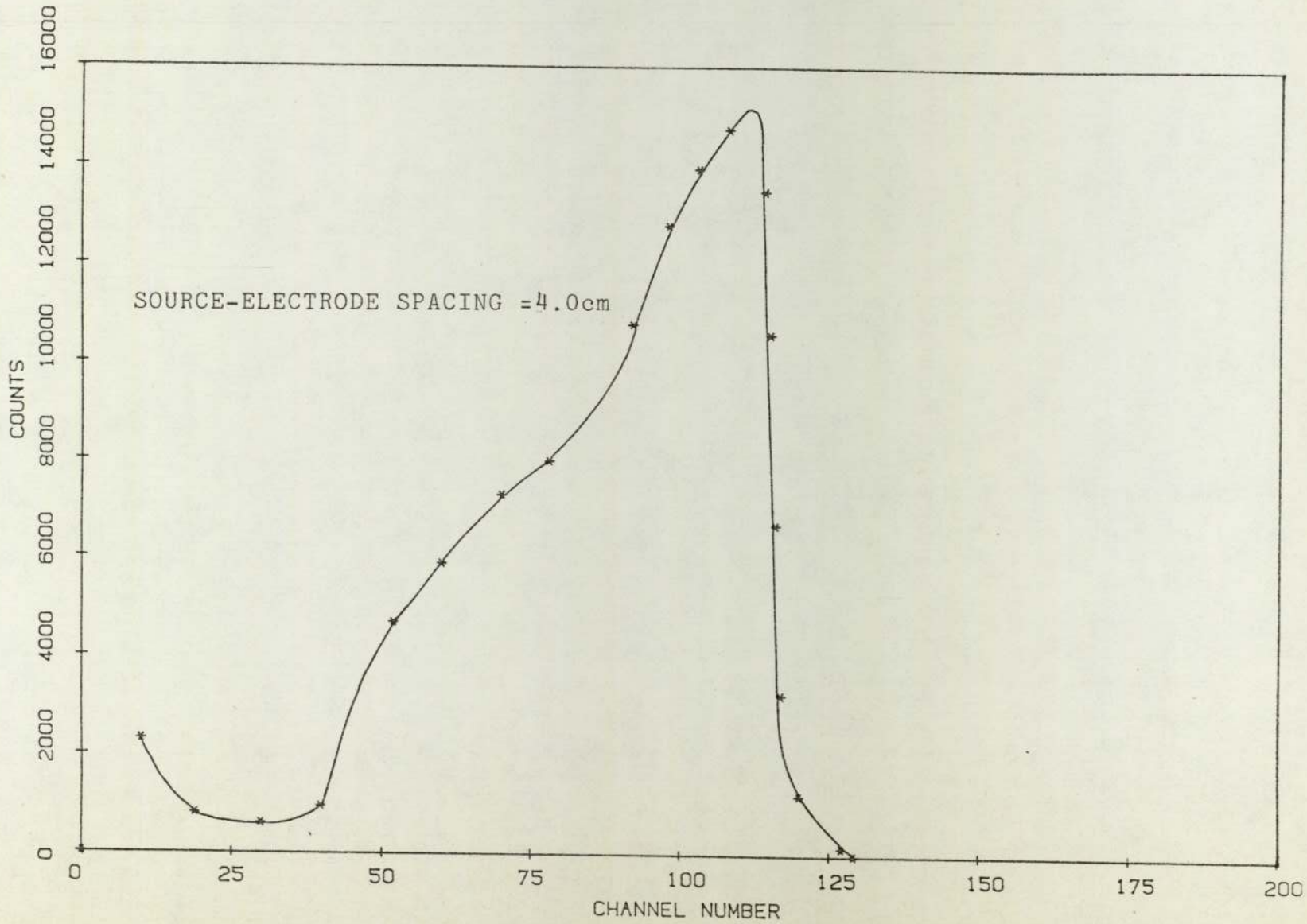

Fig. 3.5 Alpha Spectra from ^{241}Am, with Argon-filled Counter.

In further tests, fission spectra (e.g. Fig. 3.6) were obtained at various electrode spacings and at a source-electrode spacing of 2.0 cm, using moderated Am-Be source neutrons. No spectral distortion was observed. The mean range of fission fragments in argon of between 2.0 and 2.5 cm provides the most symmetric sensitive volume for the detector. Further, the specific ionization of fission fragments is greatest at the start of the ionization tracks. This electrode spacing also provides good alpha particle/ fission fragment discrimination.

In the neutron flux measurements associated with cross-section measurements, the fission counter was operated under the same experimental conditions described above. Details of such measurements are given in chapter 5.

3.3 Corrections to Observed Fission Counts.

Even from a thin source, fission fragments lose energy within the source and those emitted at grazing angles to the surface are totally absorbed. White[33] stated that for 2π-geometry, the fraction F of fragments lost due to absorption in a deposit of thickness t, was

$$F = t/2R$$

where R = mean range of the fission fragments. Furthermore, some fission fragments do not emerge with sufficient energy and are not recorded because of low level electronic

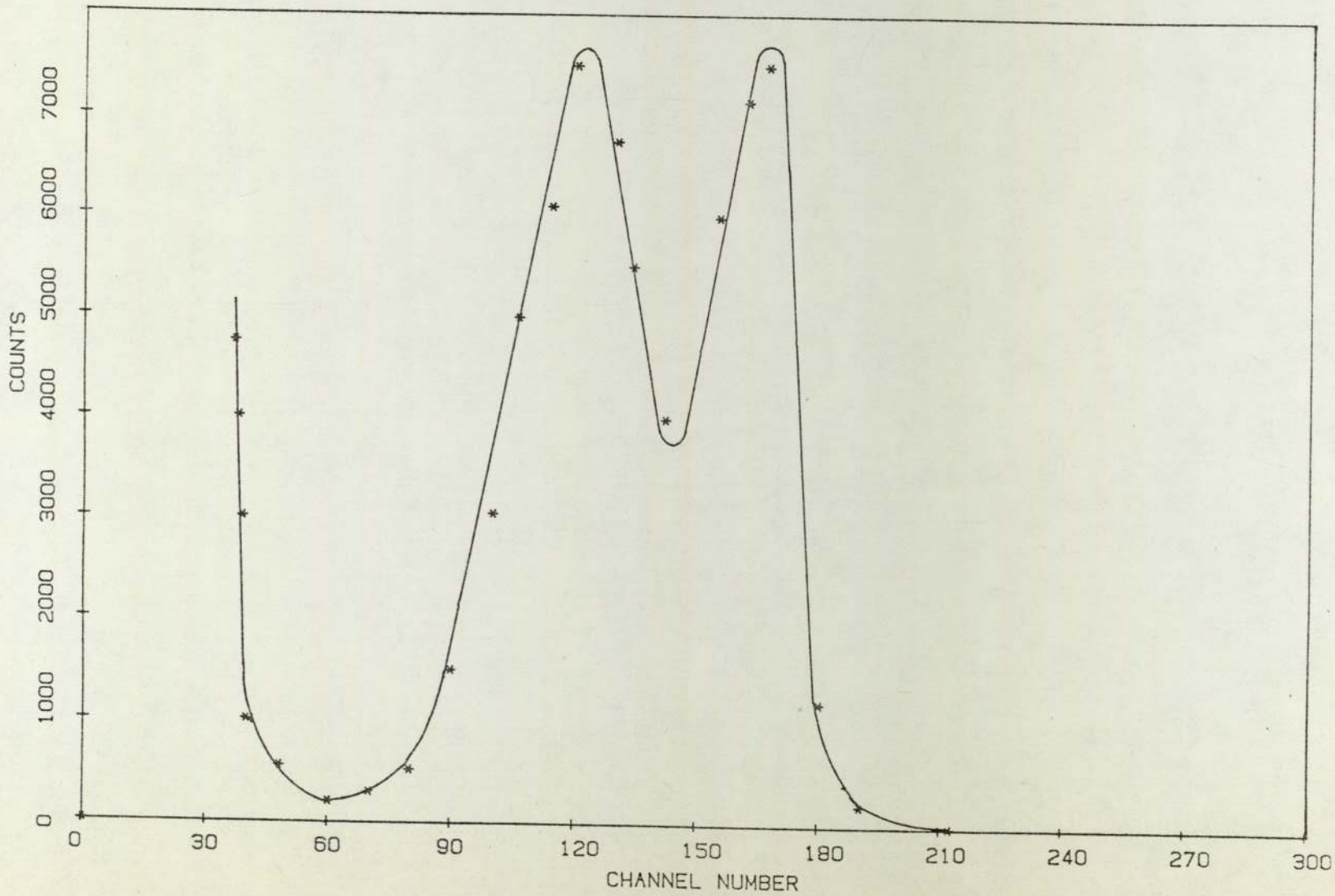

Fig. 3.6 The Fission Spectrum from ^{235}U, with Argon-filled Counter.

discrimination. The above formula was modified by Rossi et. al.[34], giving

$$F = t/2(R-R_o) \quad \ldots\ldots\ldots\ldots\ldots (3.6)$$

where R_0 is the range of fission fragments of energy equivalent to the discrimination level. The non-uniformity of the foil also contributes to the fragment absorption. The equation 3.6 may be further modified as

$$F = (t^2 + \sigma^2) / 2t(R - R_o) \quad \ldots (3.7)$$

where σ is the standard deviation on source thickness variation. For the ^{235}U foil used in this work, Jalil[6] calculated , taking into account the measurements of Akhtar[35] and White[33] , a foil non-uniformity (σ / t) of approximately 0.5.

A further correction, generally required, is for the momentum gained by the compound nucleus when bombarded by an energetic neutron. This affects the fragment velocity when it is driven out of the deposit. Lamphere[36] has suggested a momentum correction,

$$F_m = \pm 0.0026(E_n)^{\frac{1}{2}} \quad \ldots\ldots\ldots\ldots (3.8)$$

where E_n is the neutron energy. Positive and negative values of F_m correspond to the deposit facing away from or towards the neutron source.

The above correction does not take into account the effect of anisotropy of the fission fragment angular distribution. Another relation was suggested by

White[33] for the case in which anisotropy is not insignificant;

$$F_m = t/2R(1 - 2QR/t)^2 . (3/2+A) \quad \ldots\ldots\ldots\ldots (3.9)$$

where Q is the ratio of the neutron momentum to the mean fragment momentum, A is the ratio of the fragment flux at zero degree to the neutron direction, to that at 90°. When at least one fragment escapes from the foil the factor (2QR/t) becomes equal to 1 and $F_m = 0$.

CHAPTER 4

CHARGED PARTICLE DETECTION FROM A SAMPLE UNDER NEUTRON IRRADIATION

CHAPTER 4.

4.0 Charged Particle Detection from a Sample under Neutron Irradiation.

The (n,p) and (n,α) reactions at neutron energies below 6 MeV have been investigated only in a few elements and mainly by activation methods. In the range of neutron energies up to a few MeV, the study of these reactions is quite difficult due to the generally high reaction thresholds, very small cross-section values and in some cases very short or long half-lives of reaction products. For these reasons, the data on these reaction cross-sections is less complete in this neutron energy range.

In the detection of charged particles from neutron-induced reactions, techniques are required which would allow these particles to produce direct ionization in the stopping medium of the detector used and with a linear response to the particle energy deposited in the medium.

Gas filled detectors[37] have been used to detect heavy charged particles especially through gas multiplication in proportional counters. Such counters have large output pulses but suffer from space charge-induced nonlinearities. At high voltages, the strong electric fields produce inelastic collisions between electrons and neutral gas molecules. These molecules are elevated

to excited states and during de-excitation, photons are emitted which then interact with other parts of the counter to produce spurious unwanted pulses. This effect is also observed in the gas proportional scintillation counter which combines some of the properties of a proportional counter with those of the scintillation detector. The light output from a gas proportional scintillation detector consists of a prompt and delayed response. The prompt light output is weak but has a fast rise time of the order of 10^{-8} s. The delayed component is due to electrons accelerated by the applied electric field and has a rise time of 5 to 6 μs.

An inert gas scintillation counter is particularly suitable for the detection of heavy charged particles emitted by a fixed source or produced in neutron-induced reactions. It is equally useful in the detection of fission fragments. For these uses, the most useful features of the gas scintillation counter are:

(1) The scintillation response is linear with the particle energy, E, deposited in the gas over a wide range of dE/dr.

(2) Good 2π or 4π geometry can be obtained quite easily.

(3) A scintillation decay time of the order of or less than 10^{-8} s is obtainable.

(4) The shape and size of the scintillator volume

can be adjusted depending on counter design requirements.

(5) The stopping power of the gas can be controlled by varying its pressure, to allow particle-discrimination techniques to be employed. Where there is a group of charged particles of different energies, the sensitivity to the more penetrating particles can be minimised, whilst the lower energy particles deposit their full energy within the scintillator and produce a larger scintillation pulses.

The use of gas filled detectors, is limited by the high gas pressures required to stop charged particles in the gas and the application of intense electric fields at these higher gas pressures.

Solid or liquid scintillation detectors are more suitable for the detection of neutrons, X-rays or γ-rays.

The detection by surface barrier silicon detectors of the charged particles emitted during nuclear reactions is now a standard technique. Since their development in the early 1960s, semiconductor detectors have become the instrument of choice for the majority of applications in the measurements of charged particle spectra in neutron-induced reactions. Two main advantages are the improved stopping power of the solid state medium and the small value of the energy required to produce an electron-hole pair. In addition to superior energy resolution, solid

state detectors have a number of other advantages; good peak stability and freedom from drift; good timing characteristics, but require very thin entrance windows; insensitivity to ambient magnetic fields; ease of fabrication of special detector configurations and relatively low cost.

The main disadvantages are: the limitation to small detector sizes; inability to stop particles of relatively long range and the relatively high susceptibility of these devices to performance degradation from radiation induced damage. The radiation damage effects in a semiconductor detector can become quite significant under typical conditions of use for heavy charged particles. When radiation damage is extreme, multiple peaks appear in the pulse height spectrum for monoenergetic particles.(38)

On the basis of the relevant features of different detecting techniques available, the choice for this work was between the surface barrier semiconductor detector and the gas scintillation detector. Initially, it was decided to develop a gas scintillation detector.

An argon gas scintillation detector was designed, built and used to measure alpha particle spectra from ^{241}Am and ^{235}U radioactive sources. Modifications to the design were carried out to enable measurements of (n,p) and (n,α) reactions in the neutron energy range of

3 MeV to 6 Mev. Full details of the gas scintillation detector and associated gas purification system are given in section 4.1. However, the on-line detection of charged particles proved unsuccessful due to the high gamma sensitivity of the gas scintillation detector.

The surface barrier detector was then used successfully to monitor (n,p) and (n,α) reactions. Full details of this detector are given in section 4.2.

4.1 Development of a Gas Scintillation Detector.

The light which is emitted in gas scintillators is that coming from the gaseous molecules which are ionized and excited by the passage of charged particles. The excitation energy of the molecules is emitted as scintillations in the visible and ultraviolet regions of the spectrum. This luminescence emitted from gases is a well known phenomenon; the inert gases, helium, neon, argon, krypton and xenon are effective scintillators, particularly krypton and xenon.

Grün and Schopper[39] were the first to develop a gas scintillation counter. Muehlhause[40] introduced the use of an intermediate fluorescent material (later called a wavelength shifter) to improve the efficiency of the counter. He also suggested that the scintillation efficiency of gases should be nearly independent of dE/dr, the specific energy loss for the incident charged particle, thus giving a linear scintillation response to heavy ions

such as fission fragments. Further understanding of the properties of the detector were provided by Nobles et. al.[41], Boicourt and Brolley[42], Northrop and Gursky[43], Sayres and Wu[44] and Koch[45].

Koch observed the effect of a uniform electric field on the scintillation emission of xenon when excited by 4.7 MeV alpha particles. She found an increase in the scintillation pulse height with the increase in the applied field and the amplified light pulse consisted of two components. The prompt primary component which is due to ionization of the gas, produced by the incident charged particle, is fast (rise time less than 10^{-8}s). The magnitude of this component is unaffected by the applied electric field. The secondary component is due to the electrons (liberated by the charged particle) acquiring sufficient energy under the influence of the field to excite, but not ionize, the atoms of the inert gas. The secondary component is thus attributed to excitation of the gas by electrons accelerated by the field. The magnitude of this secondary component increases with the applied electric field but with a decrease in the pulse rise time. This important modification to the standard gas scintillation counter has been recently adopted by a few workers, notably Conde and Policarpo[46,47,48] and provides a much improved energy resolution.

4.1.1 Scintillation Phenomenon.

Ionization and Excitation

When heavy charged particles pass through a gaseous medium they lose energy by interaction with atomic electrons. These

particles impart energy to atoms by excitation and ionization. Atoms of the medium are either ionized or excited and, subsequently, there is emission of light of recombination or light of de-excitation. The recombination process occurs much too slowly to account for the fast light pulses which are characteristically observed. Moreover, these processes of ionization and excitation for an inert gas by the passage of a heavy charged particle are quite insensitive to the nature and energy of the particle.

The mean energy expended per ion pair produced, W, and W/I, where I is the ionization potential of the gas, for inert gases are given in Table 4.1 [49].

Gas	He	Ne	Ar	Kr	Xe
W (eV)	42.3	36.6	26.4	24.1	21.9
W/I	1.72	1.70	1.68	1.72	1.80

Table 4.1 Energy expenditure per ion pair W and Ionization Potential of inert gases.

The value of W/I = 1.7 represents the energy balance of the absorbed energy in terms of its partition between electrons, ions and atoms in the excited state.

If,

E = the absorbed energy.

N_i = the number of singly ionized charged atomic ions or electrons.

$\bar{E}_i$ = the average energy expended per ion pair produced.

$\bar{\mathcal{E}}$ = the average kinetic energy of the atom.

N_{ex} = number of excited atoms.

$\bar{E}_{ex}$ = average energy expenditure per excited atom,

then,

$$W = E/N_i = \bar{E}_i + \bar{E}_{ex}(N_{ex}/N_i) + \bar{\mathcal{E}} \quad \text{.....(4.1)}$$

Platzman[49] has obtained values for quantities on the right hand side of the equation for helium gas, viz $\bar{E}_i/I = 1.06$, $\bar{E}_{ex}/I = 0.85$, $N_{ex}/N_i = 0.40$ and $\bar{\mathcal{E}} = 0.31I$. Substitution of these values in the energy balance equation, gives $W/I = 1.71$ which is in good agreement with the experimental value given in table 4.1.

Emission Spectra.

The emission spectrum of light emitted during the de-excitation and ion recombination processes is complex. It is different for each inert gas and covers a wide range of wavelengths extending into the far ultraviolet region.

When an atom returns to the ground state by successive allowed transitions to lower excited states, with the emission of photons of corresponding energy, it yields an atomic line spectrum. The life time of the optical levels is of the order of 10^{-8}s. If an inert gas atom or ion is excited to a resonance level, it will usually return directly to the ground state with the emission of resonance radiation in the far ultraviolet region. The life time of the excited state is of the order

of or less than 10^{-9}s. In the presence of other atoms, the resonance radiation is reabsorbed and re-emitted many times with the consecutive formation of the same excited state.

When the transition to a lower excited state, particularly the ground state, is forbidden, the life time is limited by collisions with neutral or excited atoms, or ions. These metastable levels lead to the formation of excited dimers or molecular ions whose life time depends strongly on the temperature and pressure of the gas. The excited dimers and molecular ions are formed by double and triple collisional processes with metastable excited atoms,[50]

e.g.
$$He^{*} + He = He_2^{*}$$
$$He^{*} + He = He_2^{+*} + \bar{e}$$
$$Ar^{*} + Ar + Ar = Ar_2^{*} + Ar$$
$$Xe^{*} + 2Xe = Xe_2^{*} + Xe = 2Xe + h\nu + Xe.$$

As the excited dimer can not exist in the ground state, radiation emission accompanying its dissociation yields a spectral continuum. Colli[51] investigated the triple collisional process in argon as a function of pressure. The emission intensity I shows a rise and decay with time t as:

$$I = c \exp(-t/\tau_F) - \exp(t/\tau_D) \quad \text{.....(4.2)}$$

where, τ_F = time constant for formation of excited dimer.

τ_D = time constant for decay of excited dimer.

The peak of dimer emission for argon occurs at wavelengths of 125±10 mμ.

To summarize the above, the scintillation emission spectrum of an inert gas is a complex system of lines, bands and continua. It extends from the visible into the far ultraviolet. It shifts towards longer wavelengths with increase in the atomic number of the gas, and relative intensities and decay times of different parts of the spectrum are influenced by the gas pressure which determines the collisional frequency. The wavelength ranges for inert gases are given in Table 4.2.

Inert Gas(es).	λ(mμ)	Observer	Ref.
Ar, Ar + N_2 Xe + N_2	200-680	Grün	(52)
He + N_2, Ar Ar + N_2, Kr, Xe	210-600	Koch	(53)
He, Ne, Ar, Kr, Xe with N_2 as impurity.	240-550	Bennet	(54)

Table 4.2 Wavelength ranges for Inert Gases.

Emission Spectrum and Gas Pressure.

The relative intensities and decay times of different parts of the spectrum are strongly influenced by the pressure of the gas which determines the collisional frequency. The pressure also determines the rate at which

the excited dimer and molecular ion are formed and other similar processes.

The quantum efficiency of fluorescence Q is given in terms of gas pressure p as

$$Q = Q_0 / (1+p/p') \quad \text{.....(4.3)Ref.(55)}$$

where, Q_0 = fluorescence quantum efficiency if there is no collisional quenching, and p' corresponds to the conditions of gas at atmospheric pressure and number of molecules per unit volume at that pressure.

Similarly, the fluorescent decay time can be expressed in terms of gas pressure p as

$$\tau = \tau_0/(1+p/p') \quad \text{.....(4.4)}$$

τ_0 represents the decay time in the absence of collisional quenching. The energy expenditure per ion-pair produced is independent of gas pressure p , which means that the efficiency of primary excitation will be independent of p . But because the scintillation efficiency is proportional to primary excitation and quantum efficiency of fluorescence, it will vary with p as

$$S = S_0 (1+p/p') \quad \text{.....(4.5)}$$

where, S_0, again represents the scintillation efficiency in the absence of collisional quenching.

The scintillation efficiency S is also related to scintillation response L and particle energy

dissipated E as

$$(dL/dr) = S.(dE/dr) \quad .....(4.6)$$

where, r = particle range (dependent on gas pressure).

Scintillation Pulse Rise Time and Duration.

A gas scintillator has a very fast response time. This enables fission fragments to be detected in the presence of a high alpha particle background. Nobles et. al.[41] were able to detect fission fragments with no interference from multiple pile-up of alpha particle pulses. A scintillation rise time of the order of 10^{-8}s or less can be obtained. Koch[45] observed this rise time equal to 2.2ns when working with xenon gas at 10^5 N m^{-2} (760 mmHg). Boicourt and Brolley[42] used krypton gas in their counter and obtained an upper limit for the rise time of 10^{-8}s.

The contribution of all the observed emission components described above accounts for the scintillation decay time of a gas scintillator. The decay time is determined by the relative intensities and also the relative efficiency of detection of the various components Some components have a finite rise time which is dependent on pressure and temperature, and the decay time of the other components is also subject to different degrees of collisional quenching and thus dependent on pressure and temperature,(equation 4.4).

Schmidt[56] found the behaviour of xenon to be complex. At pressure less than 0.08×10^5 Pa (60 mmHg), xenon has a pure line spectrum but, at greater pressures, the continuum appears. The variation of observed decay time with pressure for xenon is shown in Fig. 4.1. The value of the decay time at 10^5 Pa (760 mmHg) extrapolates to about 9 ns which is a higher value than obtained by Koch. Schmidt's value appears to be mainly from light in the continuum whilst Koch's value refers to the line spectrum. This means that the continuum value is more realistic for practical gas scintillators, since much of the scintillation emission occurs in the continuum. Kugler[57] later confirmed that the xenon luminescence was mainly in the continuum and was due to the emission of excited dimers formed in the process.

Scintillation response to different particles.

The important feature of the inert gas scintillators is that the scintillation response is practically proportional to the particle energy lost in the scintillator over a wide range of dE/dr, the specific energy loss. The scintillation response versus particle energy is a linear relationship. This property makes gas scintillators superior to any other type of scintillator. Noble's[58] work with xenon gas proved the scintillation response of the counter to be independent of the nature of the particle. Boicourt and

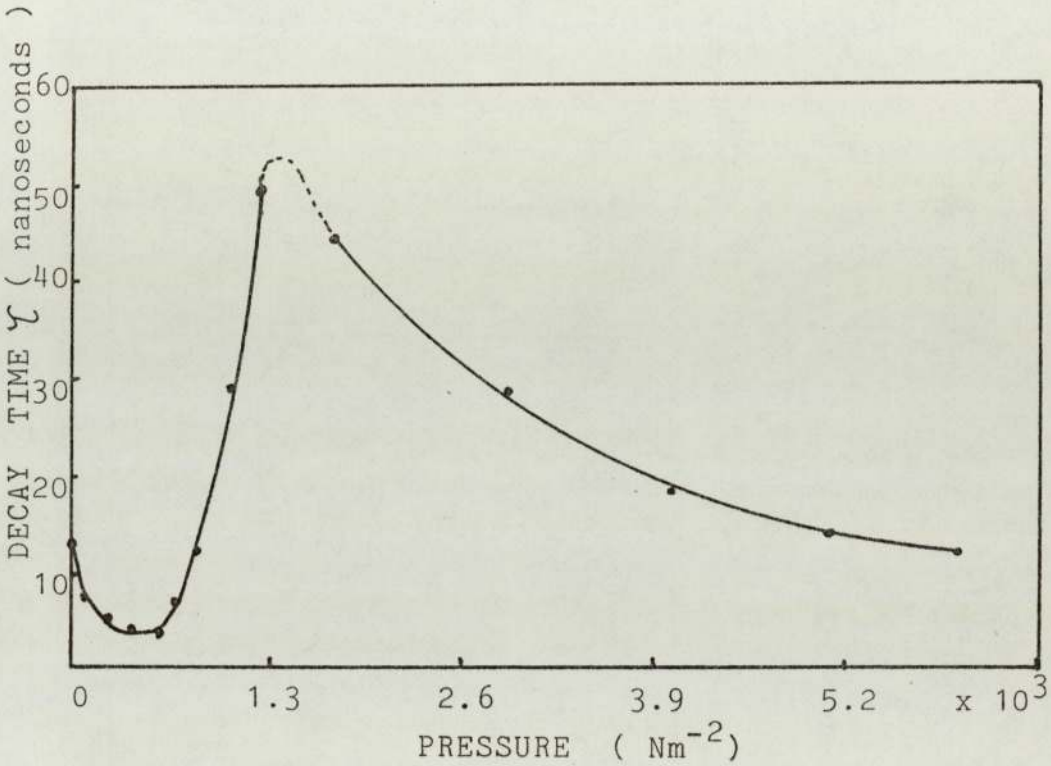

Fig. 4.1 SCINTILLATION DECAY TIME OF XENON AS A FUNCTION OF PRESSURE.

Brolley[42] measured the scintillation pulse spectra for fission fragments and alpha particles in krypton and found that the scintillation response to the light and heavy fission fragments were proportional to their energies. A similar measurement by Koch[53] confirmed these results for xenon gas at nearly atmospheric pressure. Sayers and Wu[44] used a xenon counter to detect Li^7 ions and alpha particles from the $B^{10}(n,\alpha)Li^7$ reaction and determined the 4:7 ratio of their energies.

Scintillation poisoning by impurities.

The presence of a small trace either of nitrogen or of some other molecular gases can quench the characteristic fluorescence spectrum of the inert gas and replace it by the band spectrum of the molecular gas. A small concentration of nitrogen as low as 0.001% can produce marked quenching. Koch[53] observed that mercury vapour, also commonly present as an impurity in all inert gases, quenches fluorescence and produces its own resonance line at 253.7 mμ. These impurities are either present in the inert gas itself or are occluded on the walls of the gas cell of the detector. A trace of nitrogen is generally present in even the highest purity inert gases. The various ways in which impurity excitation takes place are

(1) by electron impact.

(2) by collision with metastable atoms or

molecules.

(3) by charge exchange collisions and

(4) by ultraviolet photon absorption.

Although the addition of a small quantity of nitrogen to the lighter inert gases such as helium or argon results in an enhancement of light emission in the visible region, it is evident from the results of several observers[39, 53, 59] that nitrogen always acts as a quenching agent and decreases the absolute scintillation efficiency.

Various methods have been adopted by workers to overcome this difficulty.

(a) A gas cell cooled to 0 °C or below reduces the impurity outgassing.

(b) A clean system incorporating Viton 'O' rings when baked properly while maintaining vacuum, provides a simpler solution, and was the method adopted in this work. It proved successful in maintaining pulse height stability over a long time (section 4.1.5)

(c) A less expensive gas can be used in a continuous flow counter at a rate sufficient to remove contaminant occluded from the counter walls. Expensive gases such as xenon can be circulated in a closed system containing a gas purification unit. Sayers and Wu[44] were the first to design and use a closed circulating system. Their system had a gas circulating pump which incorporated a hot calcium purifying unit. Conde and

Policarpo and their collaborators[46, 60, 61] adopted this technique. A different technique was used in this work; a molecular sieve material was used to purify gases (section 4.1.4)

Use of a Wavelength Shifter.

As described earlier, the emission spectrum of light of an inert gas scintillator extends over a wide range of wavelengths, into the far ultraviolet region. The light is mostly in the range below 400 nm, i.e. the U.V. and vacuum (far) U.V. regions. This cannot be readily detected by an ordinary glass-windowed photomultiplier since glass is opaque to ultraviolet. A quartz-windowed photomultiplier must be used to allow maximum trasmission of light from the ultraviolet region. A further increase in photo-efficiency is obtained by employing an intermediate fluorescent material to convert the wavelengths from the far U.V. to that more nearly matching the photocathode response of the tube.

An organic compound can be used for this purpose. The organic molecules absorb, very strongly the fluorescent in the U.V. and far U.V. regions and then themselves fluoresce in the blue-green region of the visible spectrum. For this reason, such organic compounds are called 'wavelength shifters'. They are transparent to their own fluorescence.

A wavelength shifter is usually painted or vacuum deposited (evaporated) on top of the reflecting coatings on the walls of the gas cell of the detector. The reflective coatings on the walls are either paints such as MgO or Al_2O_3, or highly polished metal foils, and have a high co-efficient of reflectivity. Hence, a better photocollection efficiency is achieved. The wavelength shifter is also coated on the exit window from the glass cell to photomultiplier photocathode, with typical layer thickness of the order of 75-100 $\mu g\ cm^{-2}$. Some commonly used wavelength shifters for gas scintillators are given in Table 4.3.

Chemical Name.	Gas or Gas Mixture	Ref.
p-quaterphenyl (QP).	He, Ar, Kr, Xe, He + Xe.	44,46,62
Tetraphenylbutadiene (TPB)	Ar, Kr, Xe.	62,63
Diphenylstilbene(DPS)	He, Ar, Kr, Xe He + N_2	43,46,62
Sodium salicylate.	Ne, Ar, Kr, Xe, Ar + N_2, Ar + O_2	62,64,65

Table 4.3 Commonly Used Wavelength Shifters.

A major disadvantage of using a wavelength shifter is its tendency to quench the gas scintillation which then causes the deterioration in the scintillation pulse height with time. In this work, the use of a wavelength shifter was avoided. A photomultiplier was chosen with

its spectral response extending to far U.V. ($\sim$ 150 nm) region of the spectrum. Full details of the photomultiplier are given in section 4.1.3.

4.1.2 Design Principles of an Inert Gas Scintillation Detector.

The design of a gas scintillation detector requires the knowledge of the charged particles' range in the gas and the pressure, sufficient to stop the particles in the scintillator volume. The pulse height also depends on gas pressure. These features are described in this section.

Range of Heavy Charged Particles in Inert Gases.

Detector design considerations require the determination of the range of the ionizing particles in the gases used as scintillators. The path of the particle is nearly straight, apart from the rare case of a nuclear collision when a large-angle scattering may occur, and is of mean range r.

There is no accurate experimental "range-energy" data available for scintillators. Evans[66] plotted the range-energy relationships for protons and alpha-particles in dry air at 15°C and 760 mmHg pressure. Figs. 4.2 and 4.3 show these plots. These relationships which have been developed by a combination of experimental

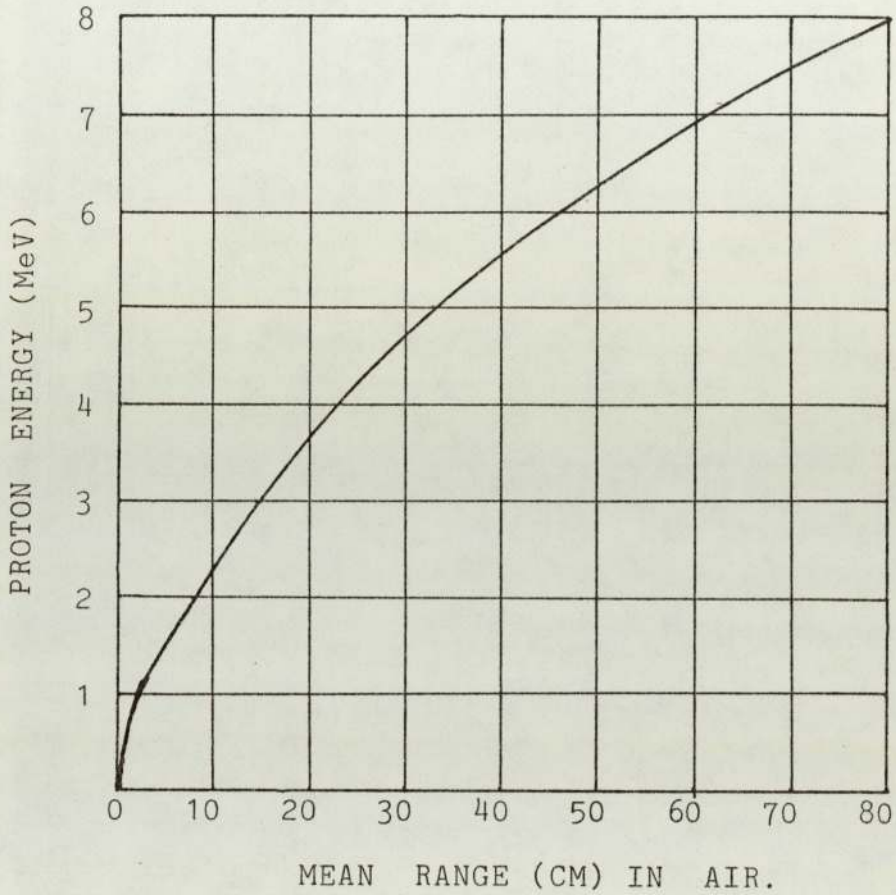

Fig. 4.2 RANGE-ENERGY RELATIONSHIP FOR PROTONS.

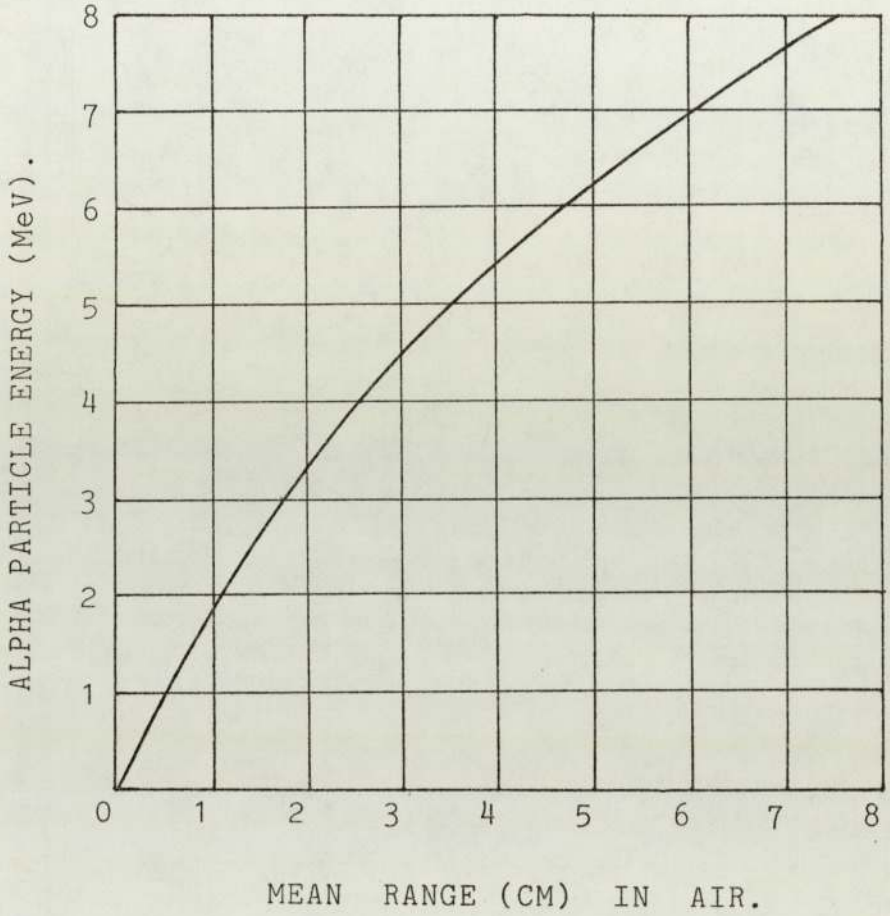

Fig. 4.3 RANGE-ENERGY RELATIONSHIP FOR ALPHA PARTICLES.

and theoretical data by Bethe[67] and Jesse & Sadauskis[68] provide a useful 'standard reference' for the behaviour of the other absorbing materials. The well known "Bethe-formula" in the relativistic case:

$$dE/dr = (4\pi e^4 Z^2/m_0 V^2)\ NZ \left[\ln\ (2m_0 V^2/I) - \ln(1-\beta^2) - \beta^2 \right] \qquad \text{.....(4.7)}$$

provides the value of dE/dr , the 'Stopping Power' of the slowing down medium.

This equation represents a particle of rest mass M ($\gg m_0$, the rest mass of an electron of charge e), charge Ze, velocity V ($= \beta c$) and energy E, transferring energy dE as excitation or ionization along an element of path dr in a homogeneous medium containing N atoms cm^{-3}, each of atomic number Z. I is a constant for the medium corresponding to the mean excitation and ionization potential.

Whilst dealing with a heavy charged particle below 10 MeV, the above equation can be modified to a non-relativistic case. Using $\beta \ll 1$ and $E = \frac{1}{2} M V^2$ or $dE = MV\ dV$,

$$dr = M/Z^2 \left\{ (m_0/4\pi e^4).1/NZ.(V^3\ dV)/\ln(2m_0 V^2/I) \right\} \qquad \text{.....(4.8)}$$

Therefore, for two particles of same initial velocity, V but different M/Z^2, from equation 4.8

$$dr_1/dr_2 = (M/Z^2)_1/(M/Z^2)_2$$

$$\text{OR,} \quad r_1/r_2 = \frac{(M/Z^2)_1}{(M/Z^2)_2} \quad \ldots\ldots\ldots\ldots (4.9)$$

A more simple but sufficiently accurate relationship known as the 'Bragg-Kleeman' rule is used for most purposes in the scintillator design to determine the thickness of the scintillator required to stop particles of a given energy. According to the rule, the effective stopping power is proportional to the square root of the atomic weight A of the medium, i.e. $dE/dr \propto A^{\frac{1}{2}}$

Therefore, the range is inversely proportional to the product of atomic stopping power and N, the atoms per cm^3 in the stopping medium.

$$\text{i.e.} \quad r \propto \frac{1}{N \text{ (atomic stopping power)}}$$

$$\text{or,} \quad r \propto 1 \,/\, (A^{\frac{1}{2}} . N_0 \rho / A)$$

(N_0 = Avogadro's number, ρ = density of the medium).

So, the range r_1 in medium 1 relative to range r_0 in a reference medium 0 is given by :

$$\frac{r_1}{r_0} = \frac{\rho_0 A_1^{\frac{1}{2}}}{\rho_1 A_0^{\frac{1}{2}}} \quad \ldots\ldots\ldots\ldots\ldots (4.10)$$

For air, $A_0^{\frac{1}{2}} = 3.82$, $\rho_0 = 1.226 \times 10^{-3}$ g cm^{-3} at N.T.P.

Equation 4.10 becomes,

$$r = 3.2 \times 10^{-4} \frac{A^{\frac{1}{2}}}{\rho} r_{air}. \quad \ldots\ldots\ldots (4.11)$$

The values for r_{air} for protons and alpha particles were obtained from Figs. 4.2 and 4.3. Table 4.4 below gives the approximate ranges, calculated using equation 4.11.

Particle	Energy (MeV)	RANGE (cm).				
		Air	He	Ar	Kr	Xe
Alpha Particles	1	0.5	1.93	0.61	0.42	0.33
	2	1.1	4.24	1.34	0.92	0.73
	3	1.7	6.56	2.07	1.43	1.33
	4	2.4	9.25	2.93	2.02	1.60
	5	3.5	13.49	4.27	2.94	2.33
	6	4.7	18.13	5.73	3.95	3.13
	7	5.9	22.75	7.19	4.95	3.93
	8	7.4	28.54	9.03	6.22	4.93
	9	8.8	33.94	10.74	7.39	5.86
	10	10.6	40.88	12.93	8.90	7.07
Protons	1	3.3	12.73	4.03	2.77	2.20
	2	7.5	28.93	9.15	6.30	5.00
	3	14.4	55.54	17.57	12.09	9.60
	4	23.6	91.03	28.79	19.82	15.74
	5	33.5	129.21	40.87	28.14	22.34
	6	46.5	179.35	56.60	39.06	31.01
	7	61.3	236.43	74.78	51.49	40.88
	8	77.6	299.30	94.67	65.18	51.75
	9	95.4	367.95	116.38	80.13	63.63
	10	115.0	443.55	140.30	96.60	76.70

Table 4.4 RANGE OF PROTONS AND ALPHA PARTICLES AT N.T.P.

Scintillator Volume and Gas Pressure.

The range of a charged particle of a given energy is determined by the gas pressure and increases considerably with particle energy at a given pressure (Table 4.4). The dimensions of the gas cell must allow full deposition of particle energy in the scintillator volume. Protons require higher gas pressures as compared to alpha particles of the same energy due to their mass difference. Argon gas pressure of approximately 1.9 atmospheres is sufficient to stop completely 6 MeV alpha particles in a gas cell of length 3 cm, whereas for protons of the same energy a pressure of 18.8 atmospheres is required. Moreover, 6 MeV protons would be stopped in about 10 atmospheres of xenon gas. The advantage of xenon is that the dimensions of the cell will be smaller. However, its higher cost puts some limitation on its use as a scintillator.

Pulse Height and Gas Pressure.

The pulse height increases with gas pressure and this increase becomes gradual once the distance from the source to the photocathode exceeds the range of the particle in that gas. The increase in gas pressure also improves energy resolution. This is due to the concentration of the charged particle tracks in the centre of the gas volume. Experimental verification of this fact would be

given in section 4.1.5.

Sayers and Wu[44] made measurements to show variation of pulse height and resolution with gas pressure. They used a Po^{210} alpha source(Energy 5.3 MeV), Figs. 4.4 and 4.5. Nobles'[58] used a Pu^{239} alpha source (Energy 5.15 MeV) and made a series of measurements with argon gas at different gas pressures. He varied the gas pressure to change the alpha particle range from 4 mm to 13.5 and observed that the shape of the pulse height distributions changed but the position of the peak maximum remained approximately the same, Fig. 4.6. This broadening of the pulse height distrbutions with the decreasing pressure is due to the shifting of the centroid of scintillation light outward from the source with increasing range of alpha particles. In the present work, the detector was employed to verify this broadening effect. Details are given in section 4.1.5 and Fig. 4.23.

4.1.3 THE GAS SCINTILLATION COUNTER: PHYSICAL DESIGN.

The gas scintillation detector was designed and built initially for preliminary measurements with argon gas and alpha particle sources. Its design is shown schematically in Fig. 4.7 and physical appearance in Fig. 4.8(a). The gas cell G is made of brass, wall thickness 2 mm, sufficient to withstand gas pressure up to 10 atmospheres; the internal dimensions of the cell are 30 mm x 50 mm diameter. Fig. 4.8(b).

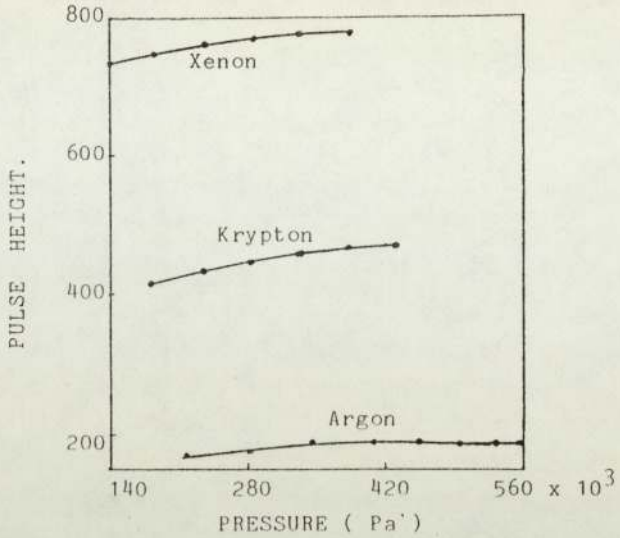

Fig. 4.4 PULSE HEIGHT AS A FUNCTION OF PRESSURE.

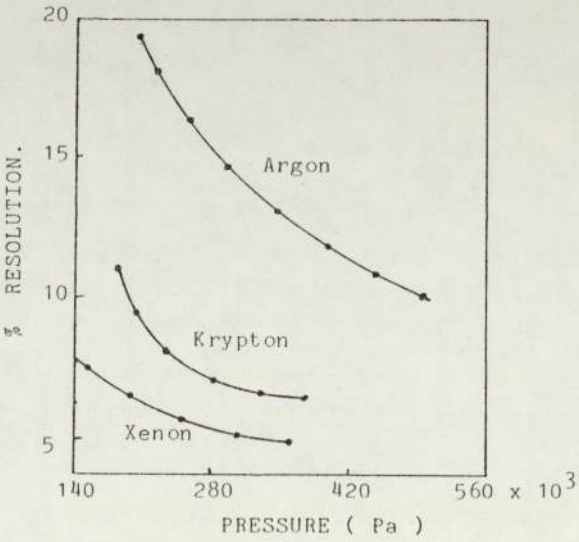

Fig. 4.5 PEAK RESOLUTION AS A FUNCTION OF PRESSURE.

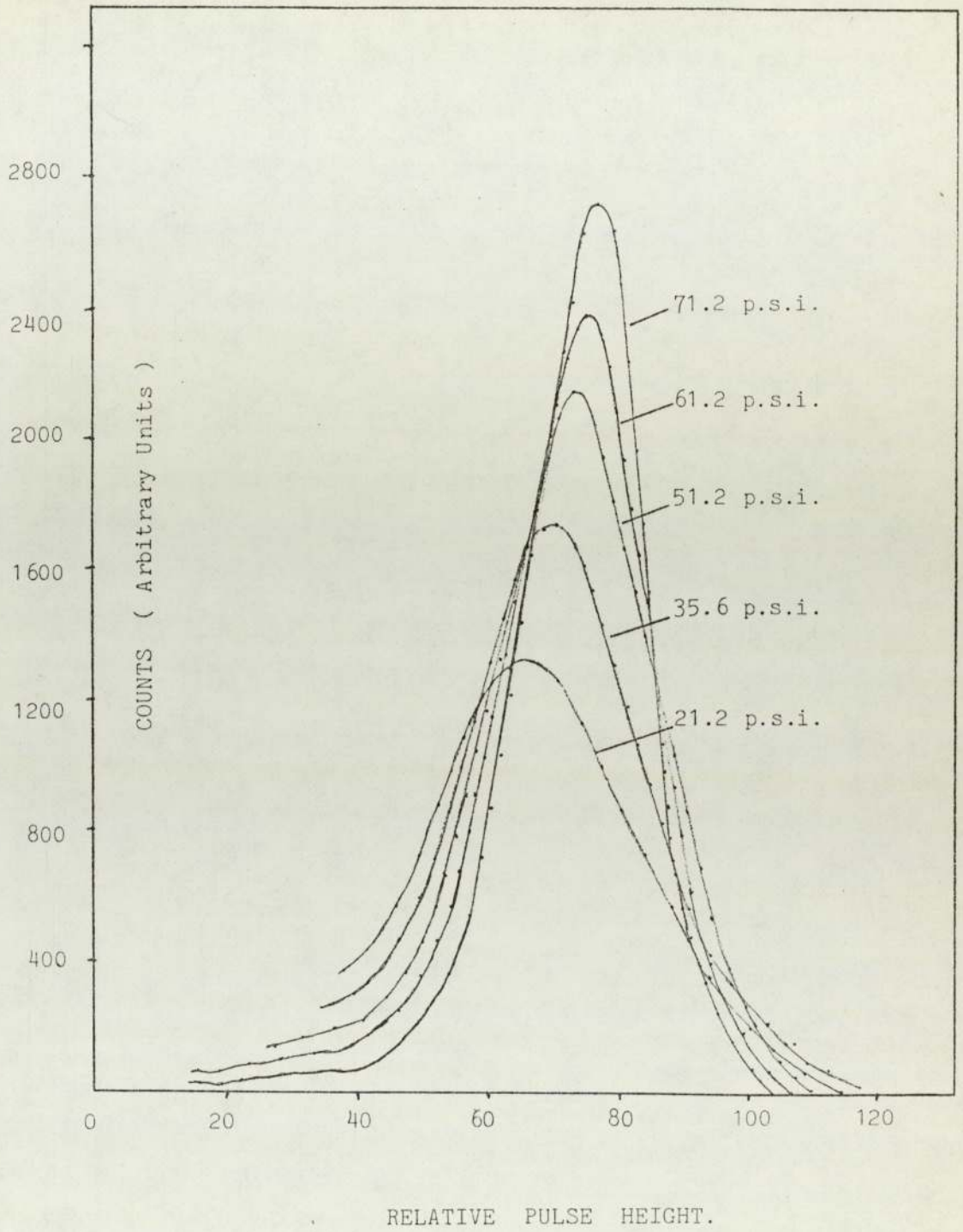

Fig. 4.6 PULSE HEIGHT DISTRIBUTION AT VARIOUS GAS PRESSURES.

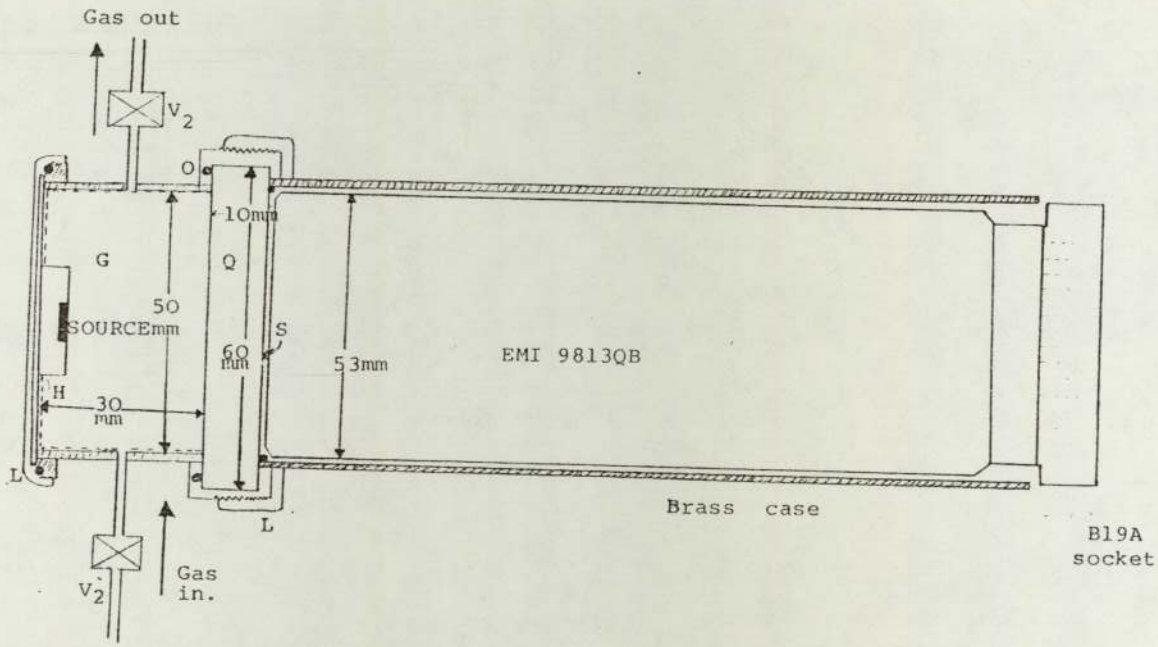

L are brass locking rings.

O are viton 'O' rings.

H is the source holder.

S is silica gel as an optical contact.

Fig. 4.7 SCHEMATIC OF GAS SCINTILLATION DETECTOR.

Fig. 4.8(a) The Gas Scintillation Counter.

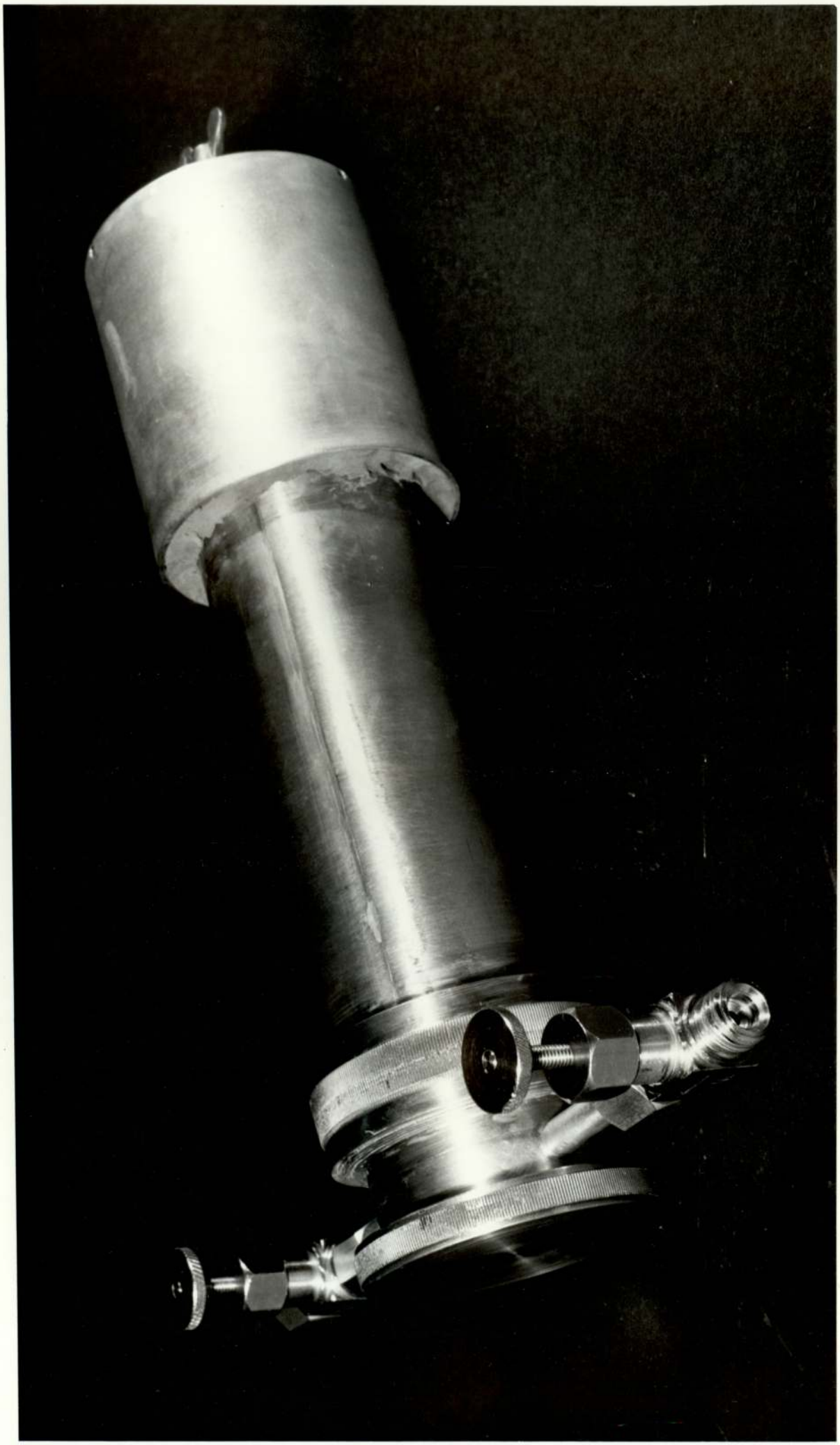

Fig. 4.8 (b) The Gas Cell.

The minimum wall thickness, to withstand high gas pressures was determined by applying the tensile stress relationships to the longitudinal and circumferential sections of the cell[69]. The tensile stress on the longitudinal section;

$$S_l = PD/2t$$

and the tensile stress on circumferential section;

$$S_c = PD/4t$$

where, P = gas pressure in Nm^{-2}.
D = diameter of the gas cell in cm.
t = wall thickness in cm.

The tensile stress for brass was taken to be 170 MNm^{-2}.

The inside surface of the cell walls were coated subsequently with an aluminium layer by vacuum evaporation, to improve the light collection efficiency of the detector. Two stainless steel valves V_1, V_2 were used to allow the detector to be evacuated, filled with gas and sealed. Viton 'O' rings were used to seal the gas cell. The Viton material has very low outgassing property and can be used at temperature up to 200 °C. The quartz disc Q which measures 10mm x 60mm diameter acts as an optical window and couples the cell to the photomultiplier. A silicone fluid was applied on the face of the photomultiplier tube to obtain a good contact between the photomultiplier tube and the quartz window.

Photomultiplier Tube.

The photomultiplier tube, type EMI 9813 QB was chosen and has the following characteristics:

(1) A quartz window (spectrosil) for transmission of ultraviolet light.(Fig. 4.9)

(2) A spectral response extending into the far (vacuum) ultraviolet ($\sim$150 nm) (Fig. 4.10)

(3) 14 dynodes with Cs-Be-O surfaces for maximum gain and good stability.

(4) A maximum envelope diameter of 55mm. The photocathode (46mm diameter) is a semi-transparent curved surface on the quartz end window which is flat externally.

(5) A non-linear dynode chain structure Figs.4.11 and 4.12. The voltage characteristics of photomultiplier dynode chain are given in Fig. 4.13

(6) Typical overall sensitivity up to 10,000 amperes per lumen.

(7) Low dark current with noise equivalent input of the order of 9.5×10^{-14} lumens.

(8) Anode pulse rise time, typically 2.4 ns and electron transit time of the order of 45 ns.

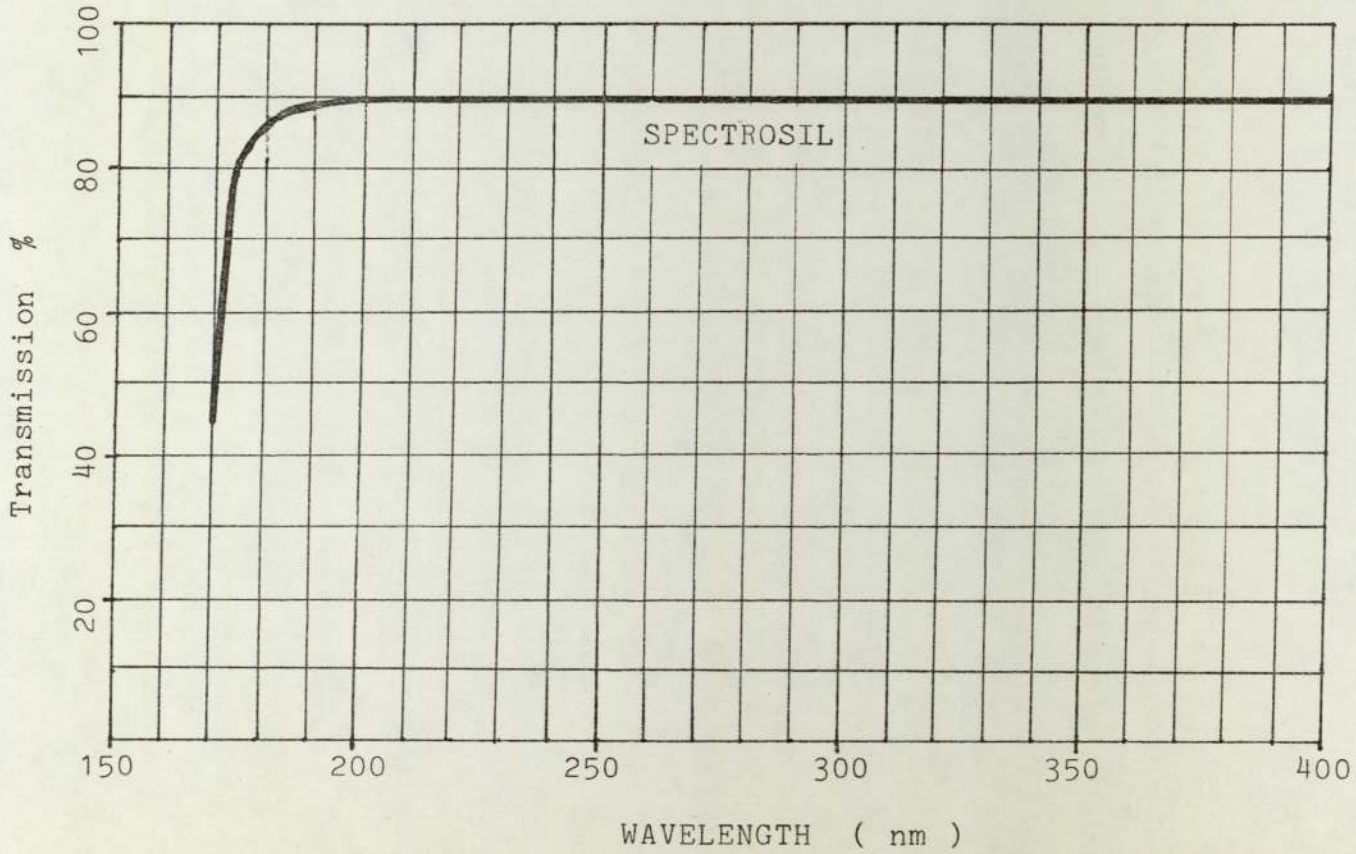

Fig. 4.9 Ultraviolet Transmission of a Spectrosil Quartz Window.

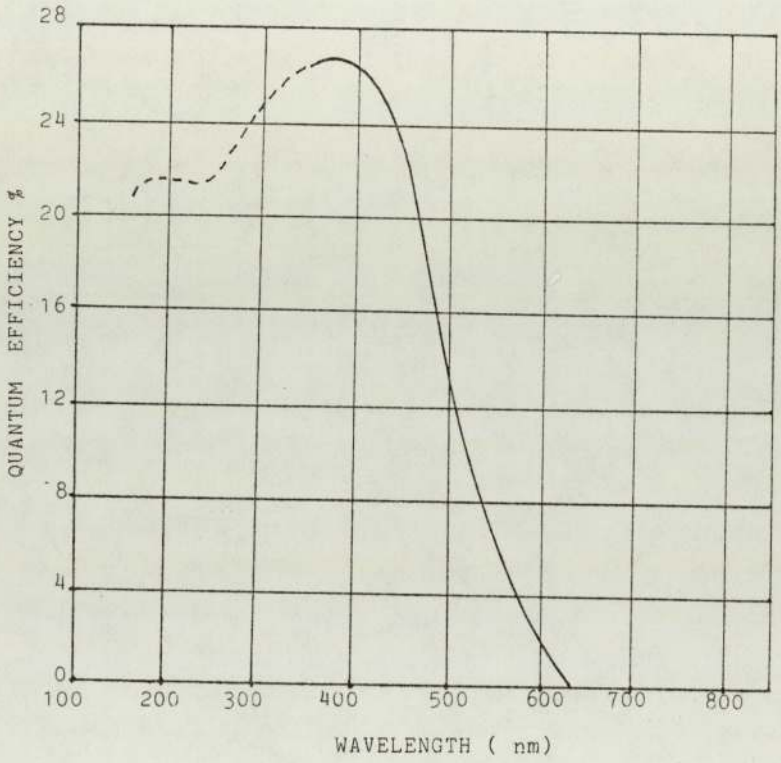

Fig. 4.10 Spectral Response of a Cs-Be-O Quartz Window in terms of Quantum Efficiency.

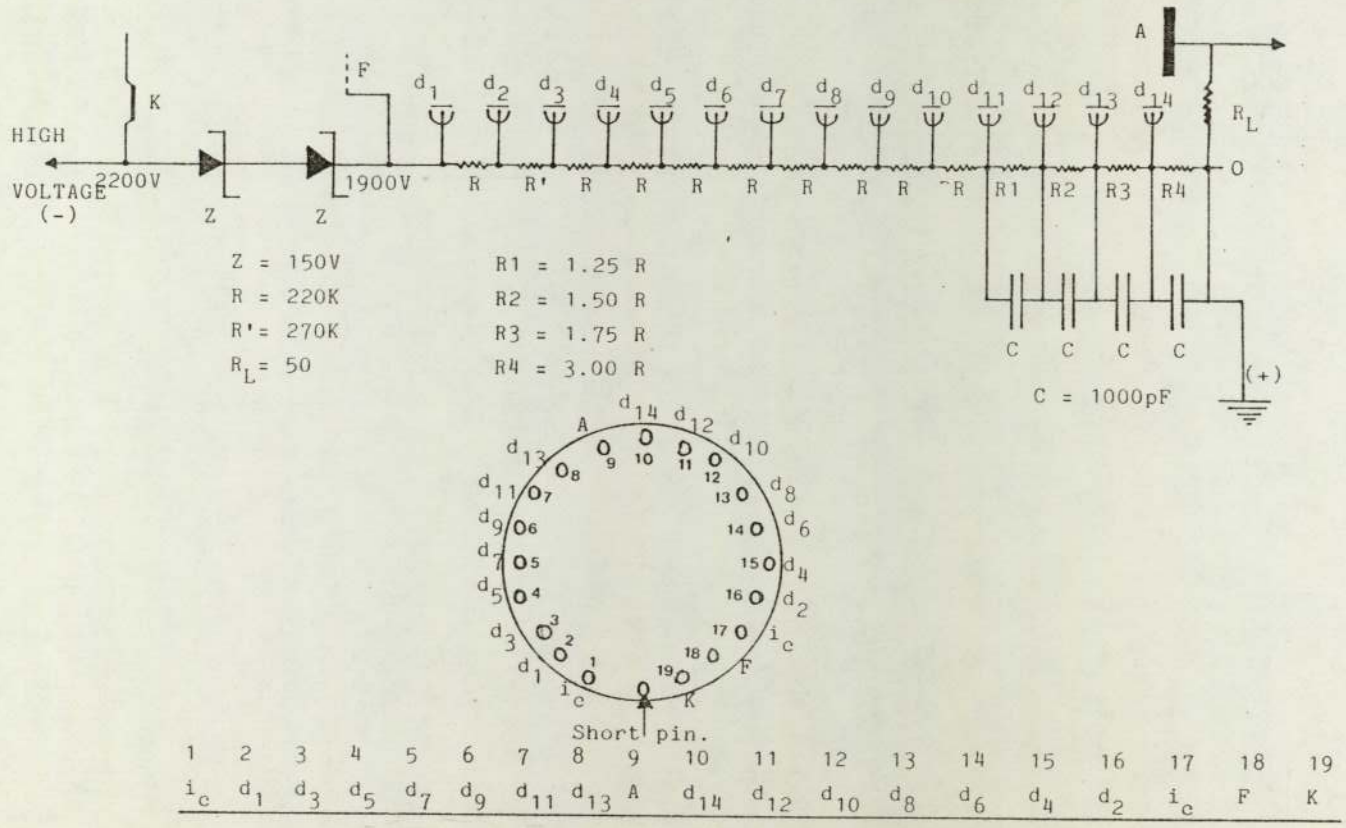

Fig. 4.11 PHOTOMULTIPLIER DYNODE CHAIN.

Fig. 4.12 The Photomultiplier Tube.

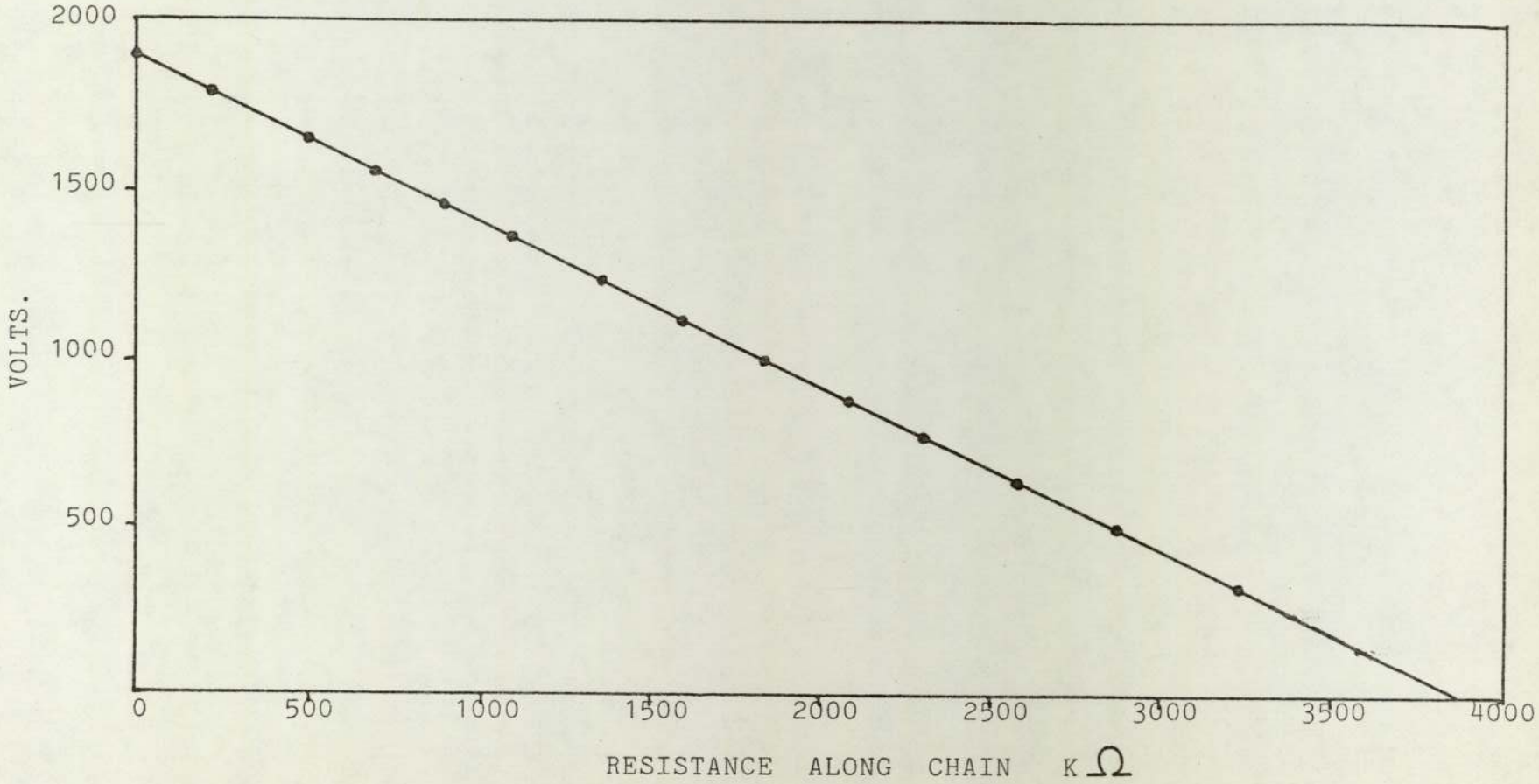

Fig.4.13 Voltage Characteristics of PHOTOMULTIPLIER DYNODE CHAIN.

The Detector Electronics and Data Acquisition System.

The system used with the gas scintillation counter follows the general requirements of any counter system with a low noise level to reduce broadening of the pulse height resolution and to limit pulse pile up of the counter pulses at higher counting rates. The pre-amplifier must have a fast rise time capability to compete with the scintillation rise time which is of the order of 10^{-8}s or less. The pre-amplifier type Ortec 113 was found to have matching characteristics for scintillation counting and it accepted pulses with rise time less than 60 ns. The main amplifier was a Canberra spectroscopic type 1417 model which accepts pulses with rise time from 0-500 ns. The operating characteristics of these electronics matched with those of the photomultiplier tube which produced anode pulses with rise time between 2-5 ns. A schematic diagram of the data acquisition system is shown in Fig. 4.14. The detector was operated with 2000 volts applied to the photomultiplier and with amplifier shaping constant of 0.25 micro-second. The multi-channel analyser with Analog to Digital converter, used to process pulses had input from 0-8 volts and accepted pulses with rise time in the range 0.1 μs to 5 μs and fall time 0.1 μs to 10 μs, over a range 0-8volts.

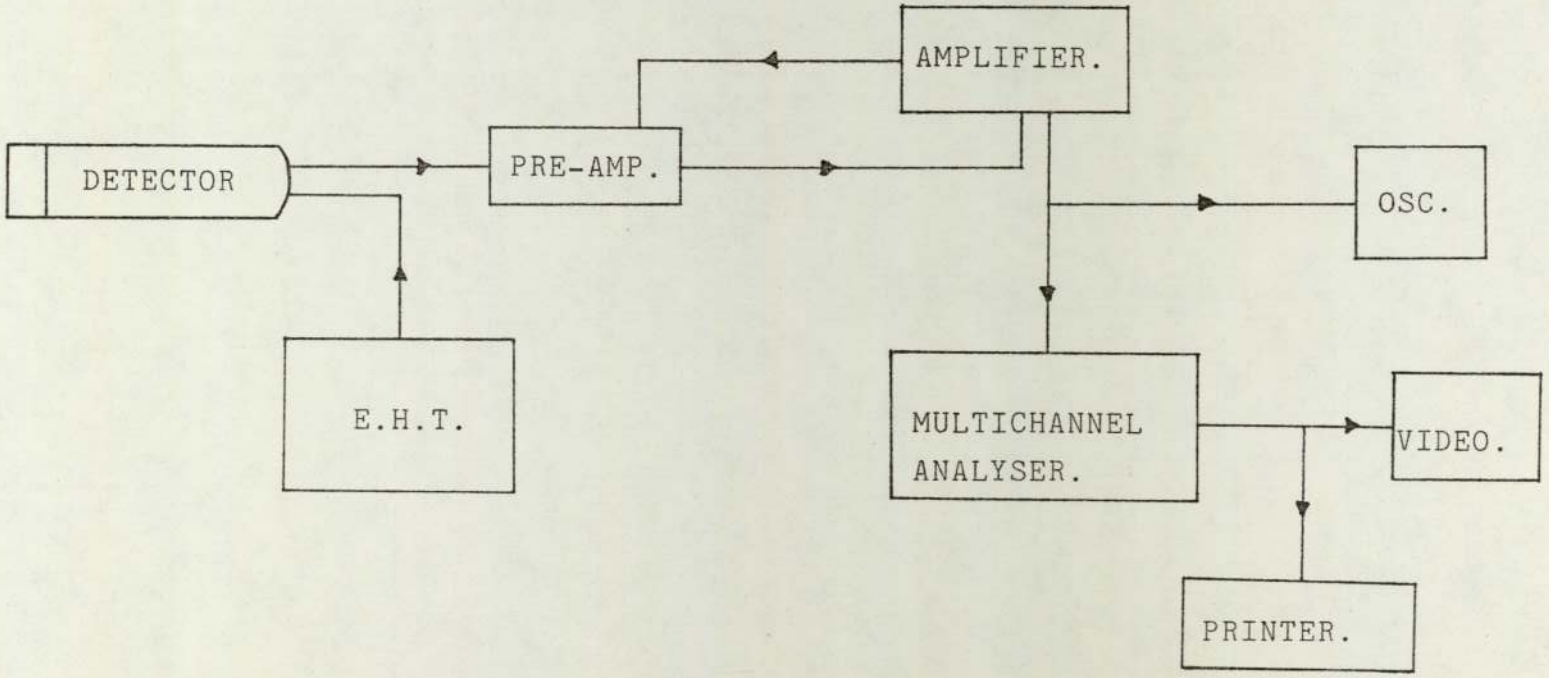

Fig. 4.14 Schematic of Detector Electronic and Data Aquisition System.

Factors determining the energy resolution of a Gas Scintillation Detector.

The factors which contribute most to the energy resolution of a scintillation counter are:

(1) The intrinsic effects in the scintillator; such as changes in light production efficiency, light collection efficiency, light transmission and reflection efficiencies. Light production efficiency depends upon the gas used as scintillator and the amount of impurity present. The gas cell design and reflectivity of its walls contribute towards light collection and reflection efficiencies.

(2) The changes in the function of the photomultiplier, affecting processes such as production of electrons at the photocathode, electron collection at the first dynode and electron multiplication along the dynode chain.

The full width at half maximum (FWHM) resolution of the full energy peak for an energy E deposited in the scintillator can be written in the form[70],

$$(\mathrm{FWHM})_E = \left[(\delta c)_E^2 + \frac{5.56\,\bar{R}}{\bar{n}\,\bar{p}(\bar{R} - 1)} \right]^{\frac{1}{2}}$$

where, $(\delta c)_E$ is the contribution to peak resolution due to the intrinsic effects. The other term in this equation is related to the 'transfer variance' characteristic of the photomultiplier which determines

the probability that a photon generated by a scintillation event in the scintillator produces a photoelectron collected by the first dynode.

$\bar{R}$ = average value of the multiplication factor R for dynode stages.

$\bar{n}$ = mean number of photons produced per scintillation and is directly proportional to E for gas scintillators.

$\bar{p}$ = mean probability for the 'transfer variance', and the mean value of this quantity is given by:

$$\bar{p} = \mathcal{E} \int_{\lambda_1}^{\lambda_2} G''(\lambda) \, . \, n(\lambda) \, . \, Q(\lambda) \, d\lambda.$$

where, $\mathcal{E}$ = photocathode to first dynode electron collection efficiency.

$G''(\lambda)$ = light collection efficiency at wavelength λ.

$n(\lambda)$ = number of photons of wavelength λ produced per scintillation.(7.4 for argon, and 21 for xenon at N.T.P.)

$Q(\lambda)$ = quantum efficiency of the Cs-Be-O photocathode and is equal to 0.27 electrons per photon.

λ_1 = the U.V. cut off wavelength for the window of the photocathode.

λ_2 = the long wavelength cut off for the cathode material.

From Fig. 4.10, λ_1 is 170nm and λ_2, 600nm for the bialkali material.

4.1.4 The Gas Filling System.

The sensitivity of the scintillation properties of an inert gas to impurities contained in the gas (section 4.1.1), illustrates the importance of the gas purification. This purity must be maintained during experimental measurements. Hence, the gas cell was out-gassed, after initial cleaning, by baking the evacuated cell to a high temperature.

A vacuum-gas filling system was designed and built, similar to that described by Bore[71]. The system shown in Figs. 4.15 to 4.17 allows the counter to be evacuated, gas impurities removed and the counter to be filled at a required pressure.

The vacuum section consisted of an air-cooled diffusion pump with liquid nitrogen cold trap, backed by a single stage rotary pump. Standard Pirani and Penning gauges were used to read vacuum. The gas cell was fitted with a demountable stainless steel miniature valve (supplied by Hone Instruments Ltd) with PTFE sealing glands. This valve can be used with gas pressures upto 5000 p.s.i. and for high vacuum applications. The Viton 'O' rings were used to seal the counter as well as to attach the valve to the counter. Initially, two such valves were fitted to the counter to maintain a continuous flow of the gas through the gas cell (Fig. 4.8)

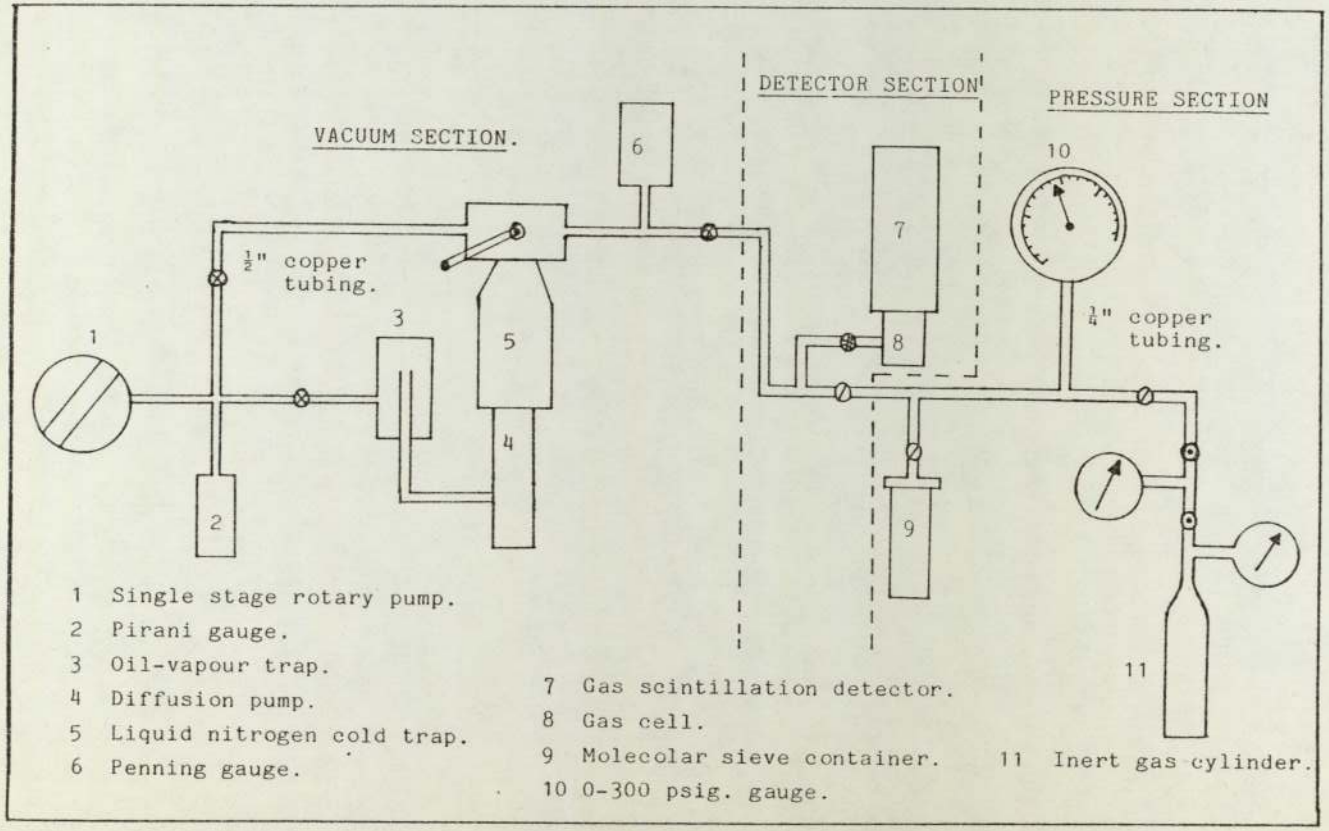

Fig. 4.15 THE VACUUM - GAS FILLING SYSTEM.

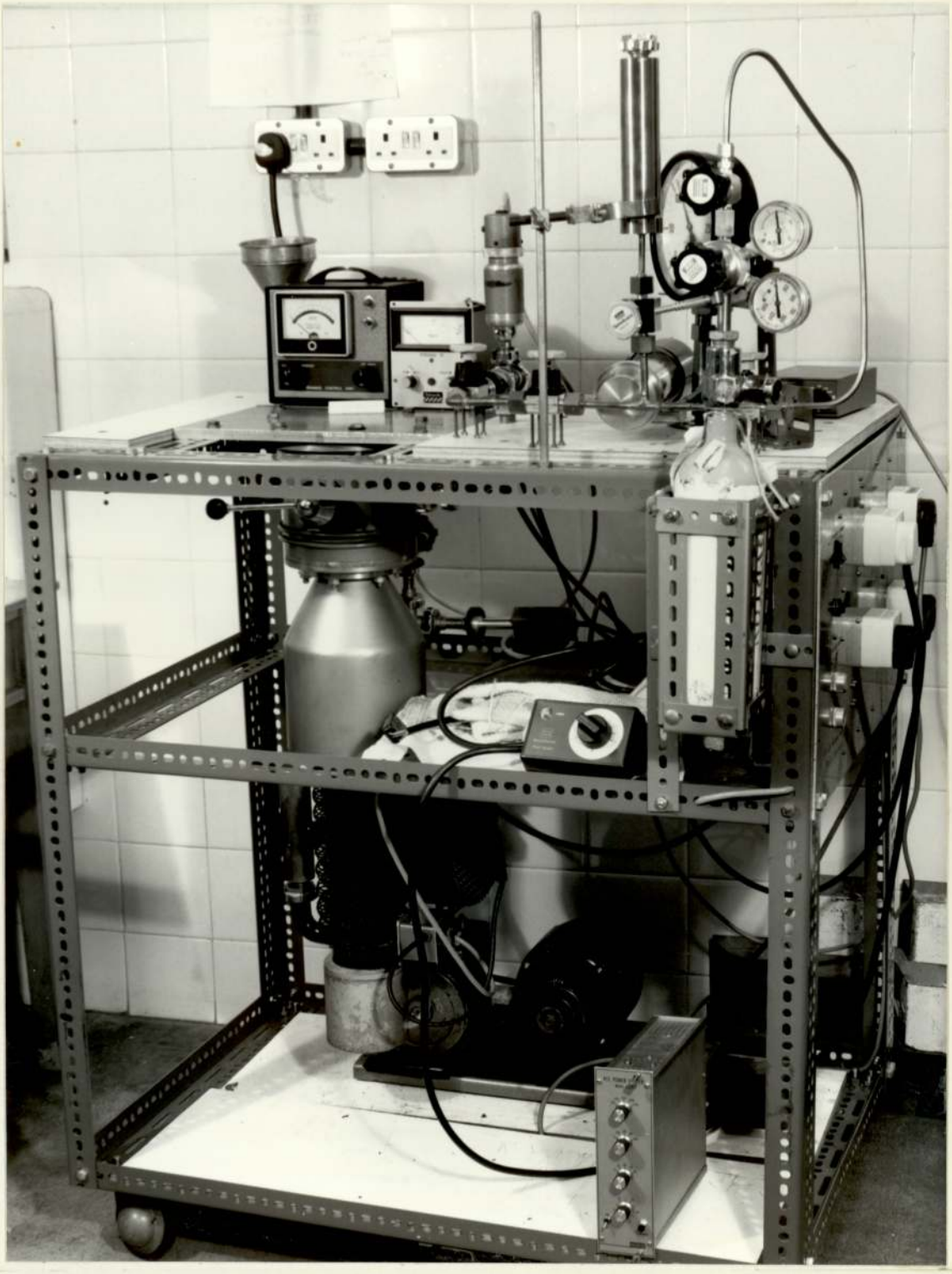

Fig. 4.16 The Vacuum and Gas Filling System.

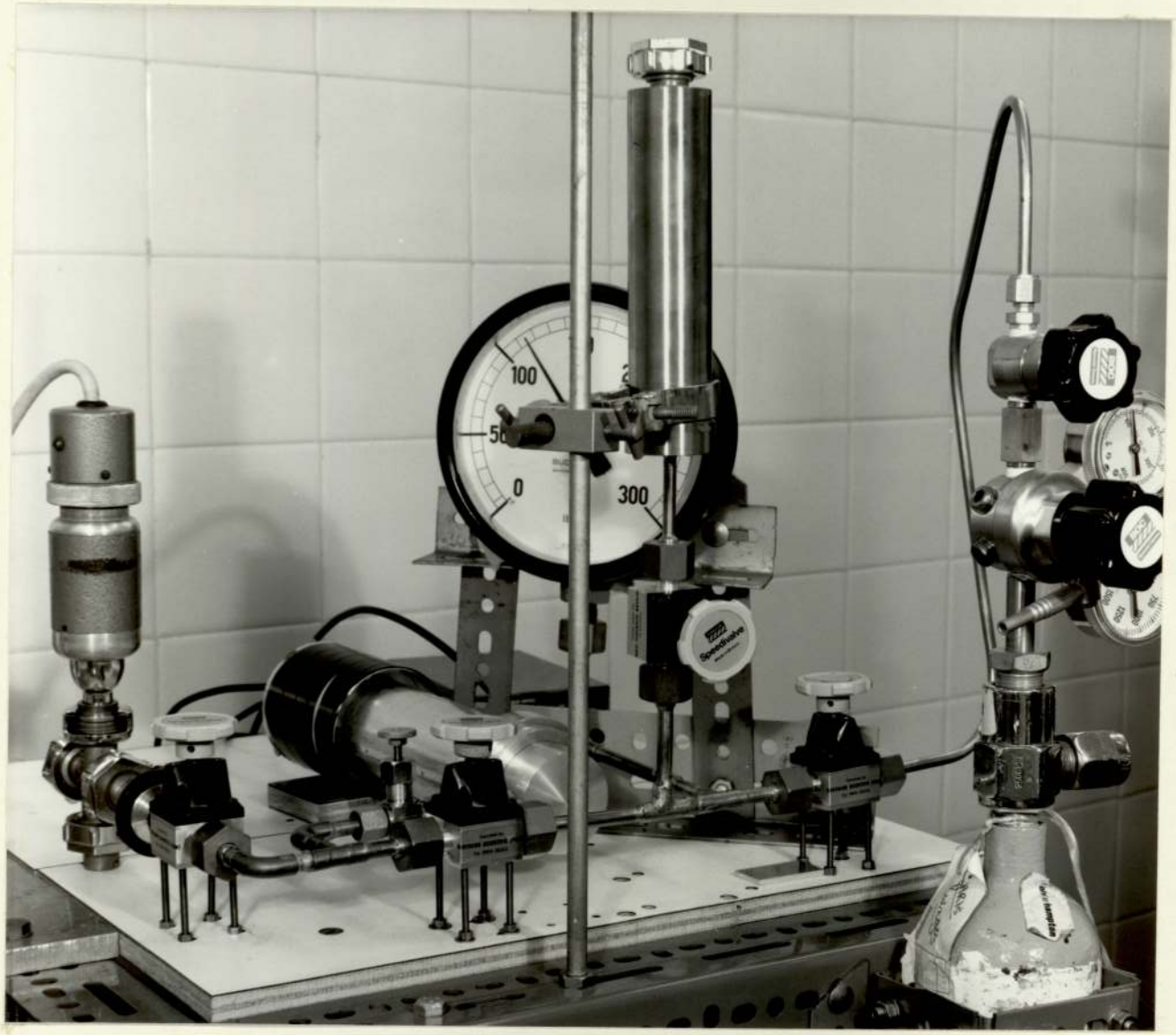

Fig. 4.17 The Gas Purification and Filling System.

Later, one of the valves was removed and gas outlet permanently sealed. This enabled the counter to be evacuated, filled with gas and removed from the system after closure of the remaining valve, (Fig. 4.18). In the gas filling and storage section, viton diaphragm and 'O' ring seals were used. This material could withstand temperature in the order of 200 °C and had a very low vapour pressure.

A vessel containing molecular sieve material (Fig. 4.19) was built into the gas filling system for use in purification of the counter gas. This technique, applied successfully by Bore[71], makes use of the property of the molecular sieve to absorb molecules of below a critical diameter. The material is highly porous with pores of molecular dimensions and absorbs only those molecules that are small enough to enter the pore system. Table 4.5 gives critical diameters of molecules of some inert gases and the impurities which may be present in them.

A crystalline Potassium alumino-silicate molecular sieve (Type 3A) was used in the form of 1/16" pellets. This material has a pore diameter of 3 Å. The molecular sieve vessel and remainder of the filling system were baked whilst under vacuum to remove occluded gases and gases trapped within the sieve material. Electrically heated tape was used for this purpose. This system was

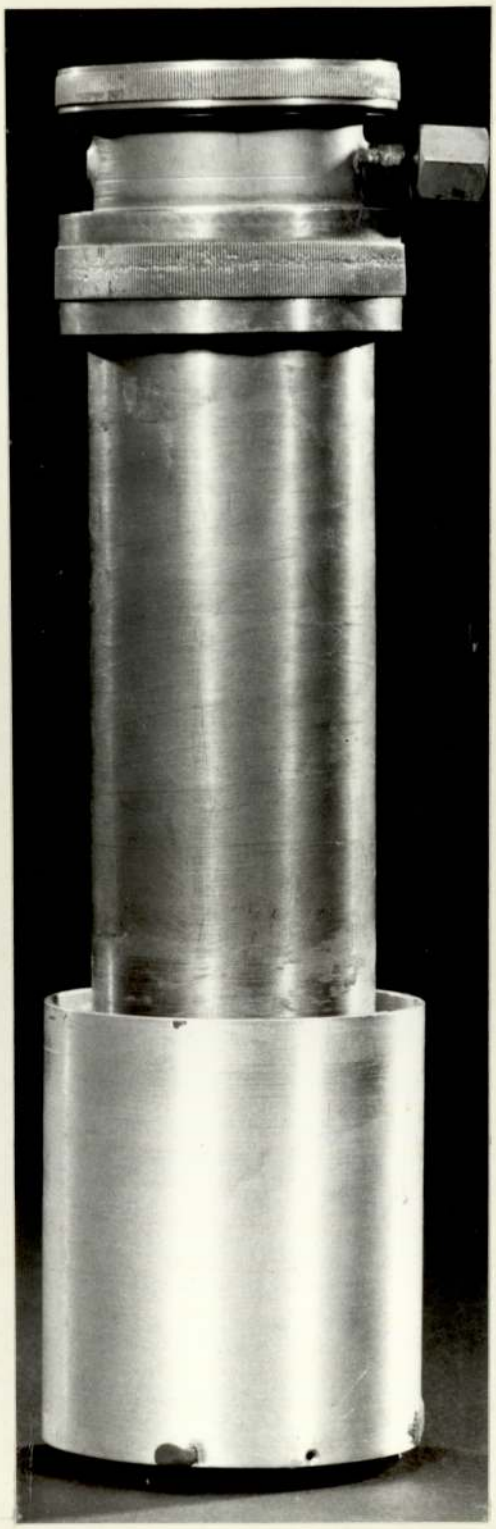

Fig. 4.18 The Gas Scintillation Counter.

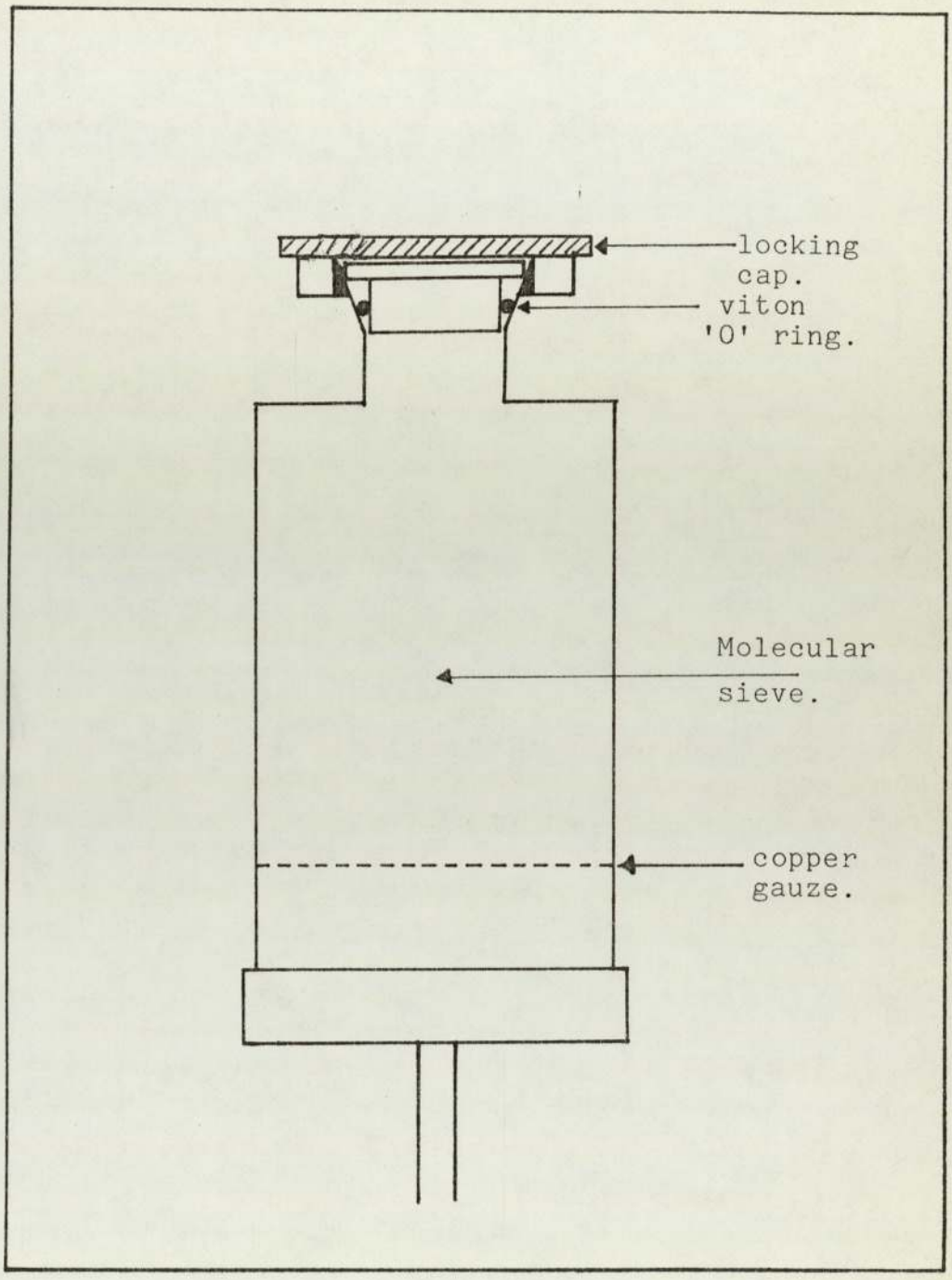

Fig. 4.19 Molecular Sieve Vessel.

then allowed to cool to ambient temperature. The vacuum achieved was better than 10^{-5} torr.

	MOLECULE	CRITICAL DIAMETER(°A).
Inert Gases	Helium	2.0
	Argon	3.8
	Krypton	4.18 at 0 °C,Ref(72)
	Xenon	4.90 at 0 °C,Ref(72)
Impurities.	Hydrogen	2.4
	Oxygen	2.8
	Carbon monoxide	2.8
	Carbon dioxide	2.8
	Nitrogen	3.1
	Water(vapour)	3.15
	Methane	4.0

Table 4.5 CRITICAL DIAMETERS OF SOME MOLECULES.

(Data supplied by BDH Chemicals Ltd).

The volume of the molecular sieve container and other components in the gas storage section were such that, when transferring gas into the counter, the counter could be filled to the required pressure.

The research grade argon and krypton gases were used as scintillators and manufacturer's typical analysis is given in Table 4.6.

A R G O N	
Argon	99.9997 %
Oxygen	less than 1 vpm.
Nitrogen	" " 2 vpm.
Hydrogen	" " 1 vpm.
Carbon dioxide	" " 1 vpm.
Hydrocarbons	" " 1 vpm.
Moisture	" " 1 vpm.

K R Y P T O N	
Krypton	99.997 %
Xenon	20 vpm.
Nitrogen	10 vpm.
Oxygen	less than 1 vpm.
Carbon dioxide	" " 1 vpm.
Hydrogen	" " 1 vpm.
Hydrocarbons	" " 1 vpm.
Moisture	" " 1 vpm.

Table 4.6 Typical Analysis of Research Gases.

4.1.5 Detector Performance.

The performance of the gas scintillation detector was tested initially with alpha particle sources and using research grade argon and krypton filled in the detector. The gas cell, first filled direct from the gas cylinder, a number of measurements were carried out and the resulting spectra are described in this section. During the course of these measurements, it was intended to improve and achieve a good resolution for the detector, to enable the detector to resolve protons of close energy grouping. Figs. 4.20 to 4.23, illustrate the spectra obtained at different experimental conditions and arrangements.

The alpha sources used for these measurements were,

(1) ^{241}Am source (5.48 MeV), in the form of an active disc 10mm diameter x 0.5mm thickness mounted in an aluminium holder and therefore having a wide energy spread.

(2) A ^{235}U foil, with the 1.2% ^{234}U content of the deposit, providing 97% of the alpha activity(4.4 MeV). The ^{235}U deposit (in the form of U_3O_8) was 2.0 cm in diameter and 0.1 mg cm^{-2} thick deposited on a 5.00 cm diameter and 0.15 mm thick platinum foil and therefore, providing a narrow energy spread.

Fig. 4.20, illustrates the ^{241}Am spectrum using argon gas

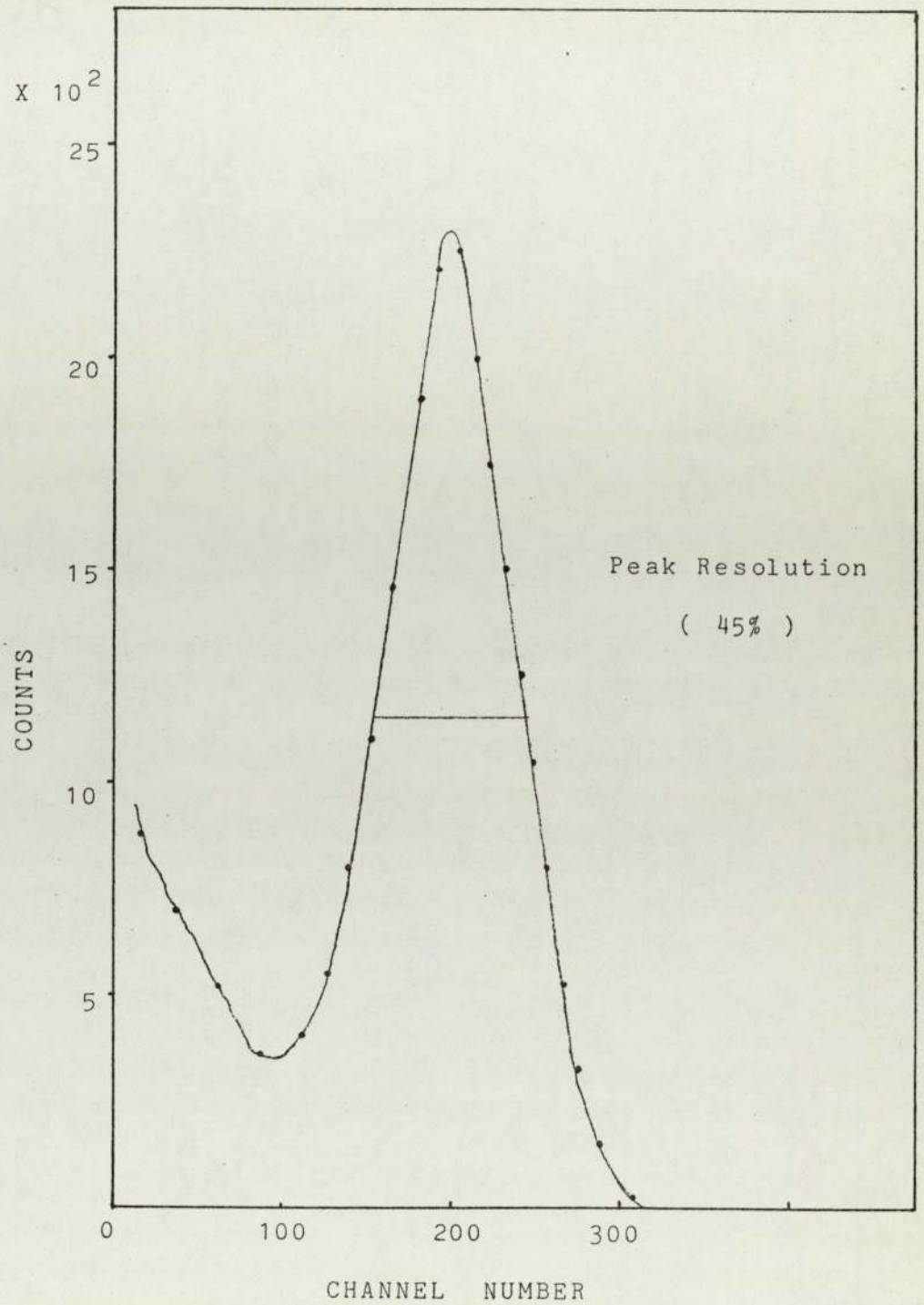

Fig. 4.20 ^{241}Am spectrum (5.48MeV), no reflector.

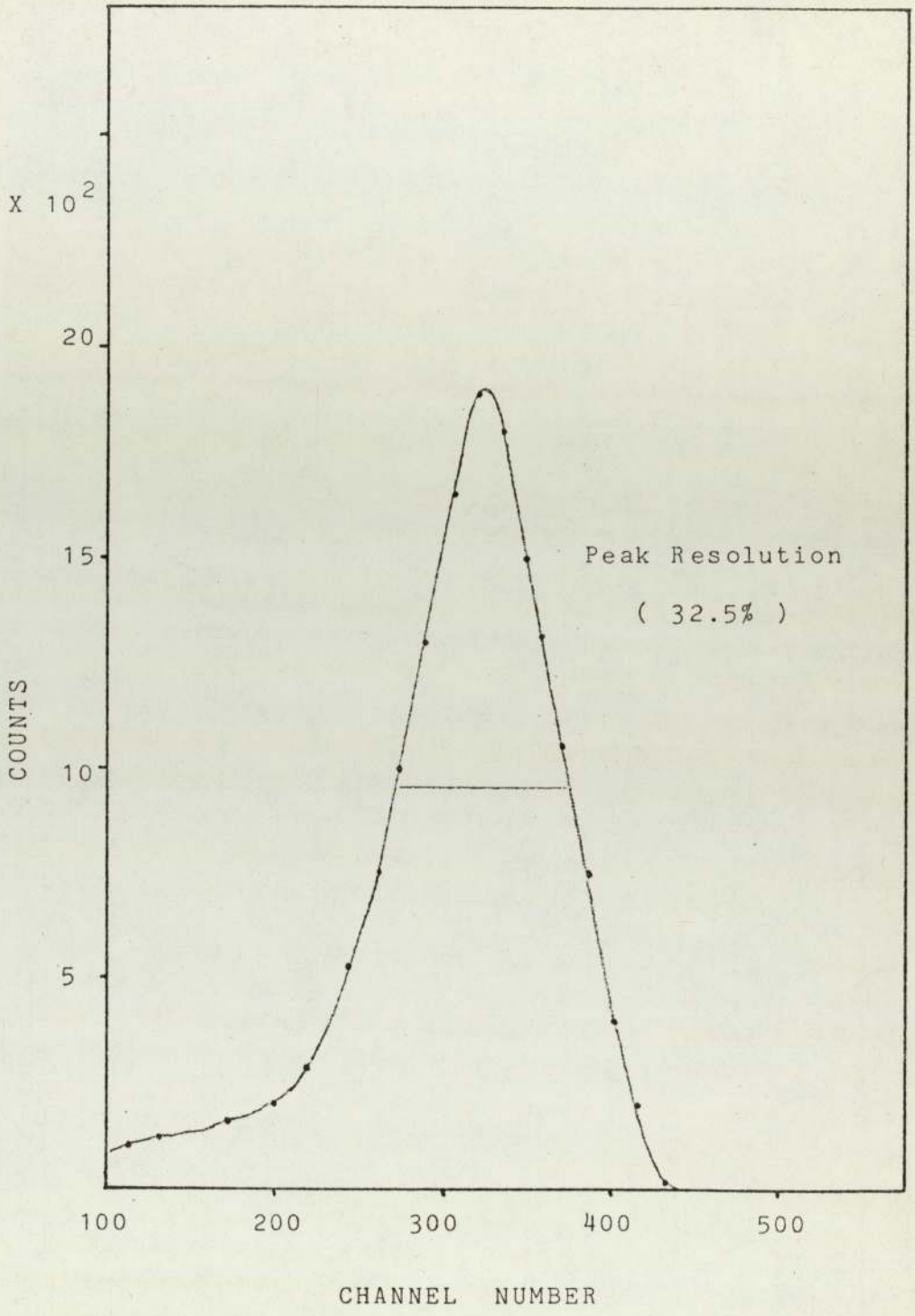

Fig. 4.21 ^{241}Am spectrum (5.48MeV), with reflector.

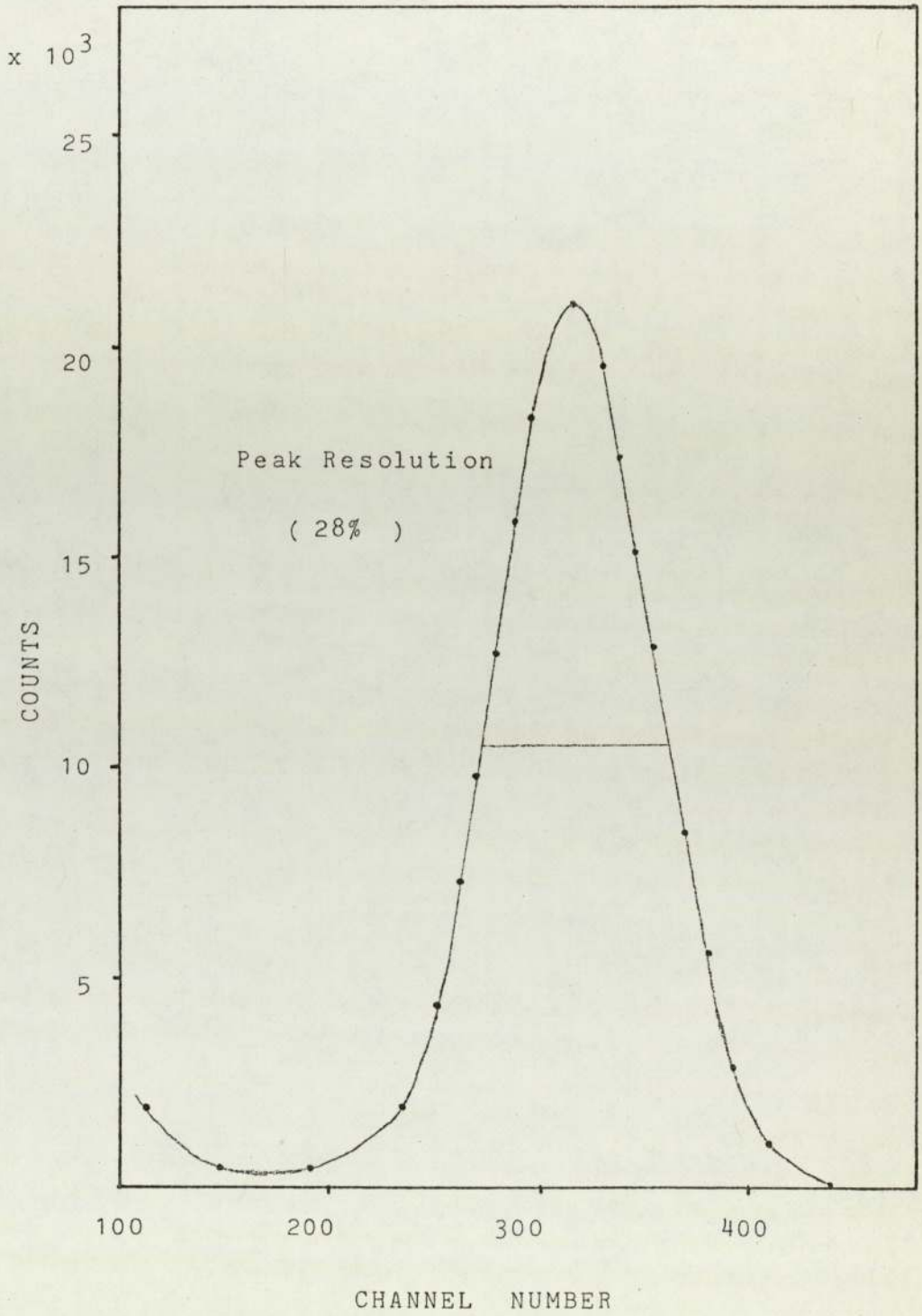

Fig. 4.22 ^{235}U spectrum (4.4MeV), with reflector.

at 40 p.s.i. In this measurement, the gas cell walls had no reflecting layer deposited on them. An energy resolution of 45% was obtained.

The gas cell walls were now coated with an aluminium layer deposited by vacuum evaporation. The alpha spectrum obtained is shown in Fig. 4.21. The pulse height has increased and the peak resolution improved to 32.5%. This is due to the contribution of the reflector to light collection efficiency and the light reflection efficiency of the detector. The surface reflectivity decreases with time as aluminium turns to aluminium oxide, requiring a renewal of the aluminium layer, prior to each measurement. Fig. 4.22 gives the spectrum obtained from the ^{235}U source and the alpha peak resolution is 28%.

To investigate the effect of increasing gas cell pressure, four ^{241}Am spectra were obtained at pressures of 29p.s.i., 40p.s.i., 50p.s.i. and 60p.s.i. Fig. 4.23 illustrates the variation of the pulse height with pressure. With the gas pressure above the value required to stop alpha particles within the cell, not only the pulse height increased but there was also a gradual improvement in the alpha peak resolution. This is accounted for by the increase in the light production efficiency with increase in pressure, and by a shift of the centroid of scintillation light production towards

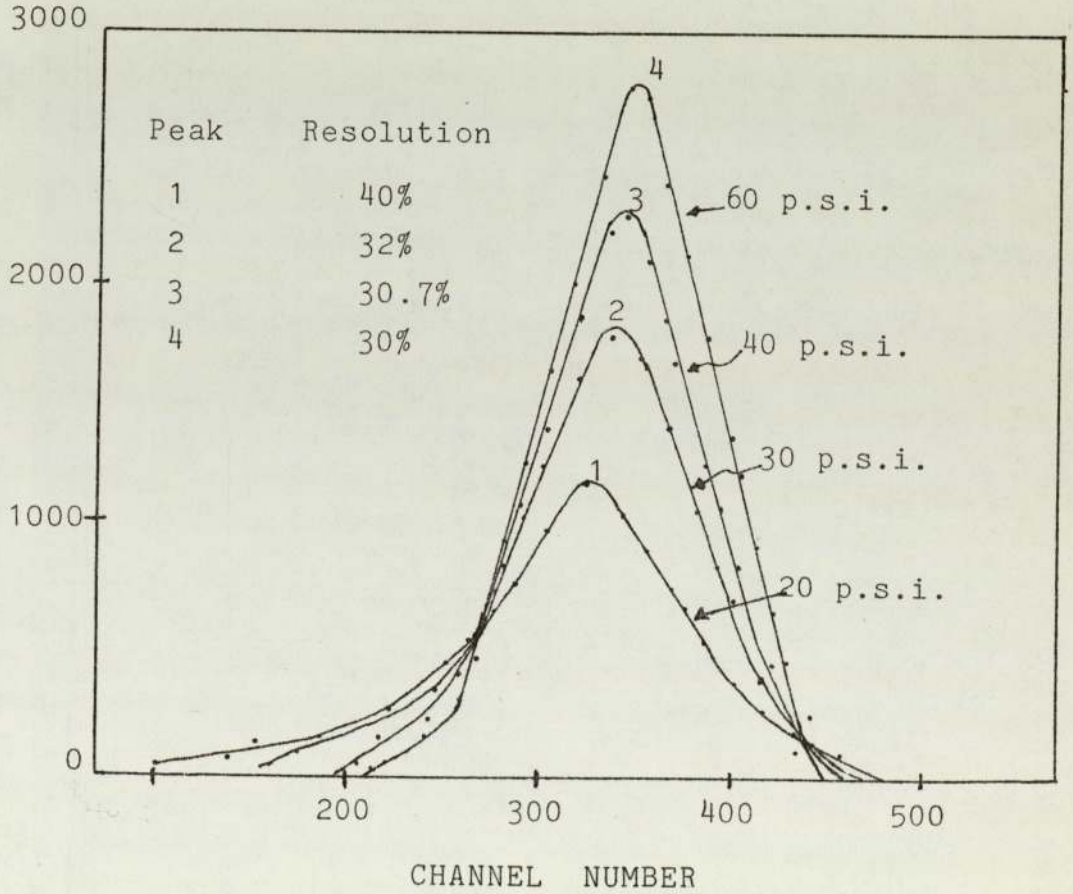

Fig. 4.23 ^{241}Am spectra at various gas pressures.

the alpha source, affecting the light collection efficiency of the detector.

Further spectra were obtained, detector with the gas cell filled from the molecular sieve vessel. Figs. 4.24 and 4.25 show the ^{241}Am alpha spectra obtained at argon pressure of 50 p.s.i., with and without storage of gas in the molecular sieve vessel. The alpha peak resolution of the two spectra is approximately the same. The contribution of gas purification to an improvement of peak resolution is difficult to observe as the poor resolution may have been due to (a) the wide spread in energy of alpha particles from the thick ^{241}Am source. (b) the low detection efficieny of argon gas.

Koch and Lesueur[73] and Sayers and Wu[44] have commented upon the low scintillation efficiency of argon gas which limits the peak resolution to a value close to the one obtained in this work.

Fig. 4.26 shows the ^{235}U alpha spectrum obtained with an 18 p.s.i. krypton gas cell filled direct from the gas cylinder; the alpha peak resolution is 12.8%. Koch & Lesueur suggest that relative scintillation efficiency of krypton is 2.25 times greater than argon. Nobles[58] has measured the pulse heights from krypton and argon gases and found that the pulse height from krypton was 3.6 times as great as that from argon. Fig. 4.27 shows the ^{235}U alpha spectrum obtained with the same gas cell, after an interval of 80 hours. There was a peak shift of

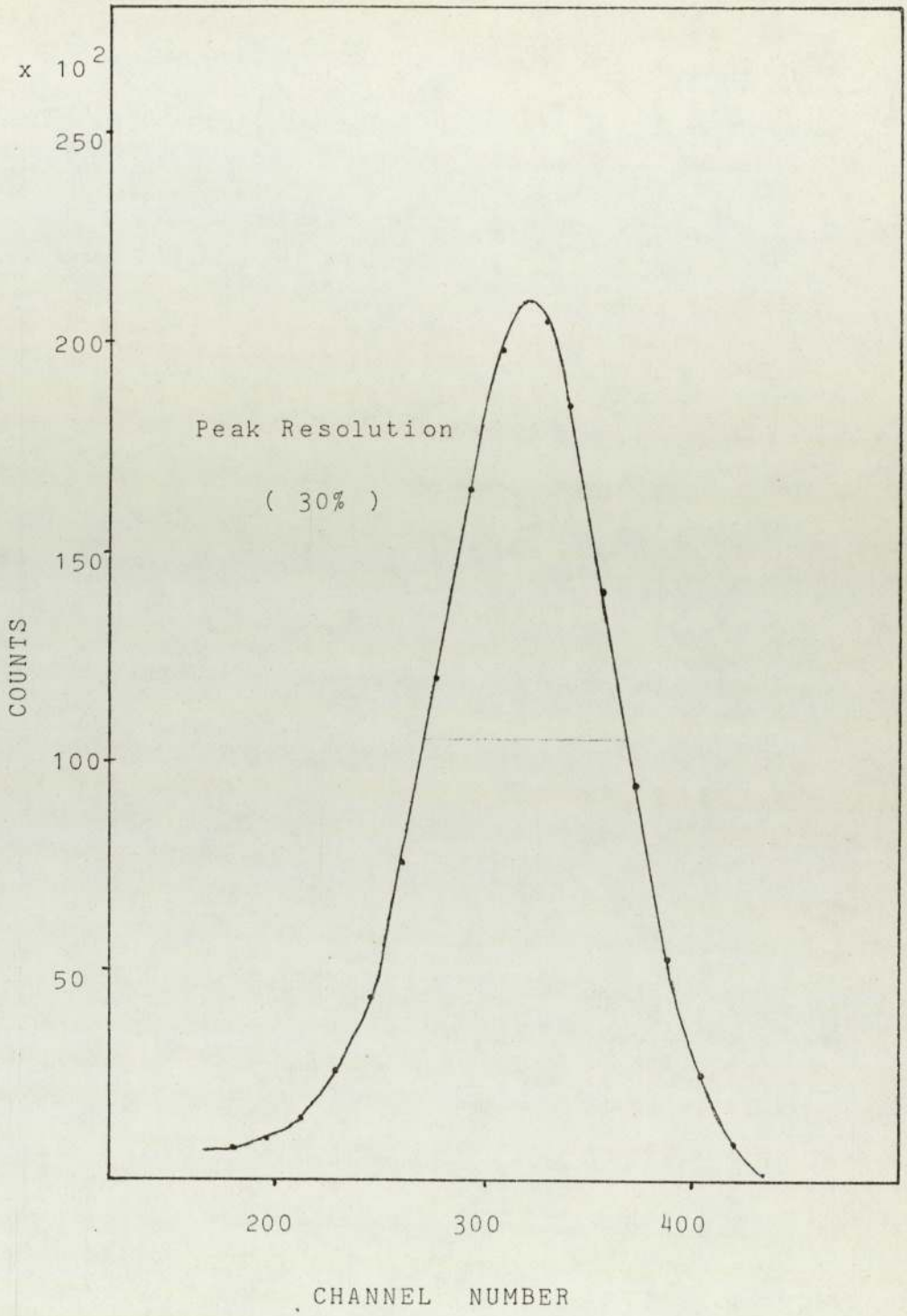

Fig.4.24 ^{241}Am spectrum, with argon from molecular sieve vessel.

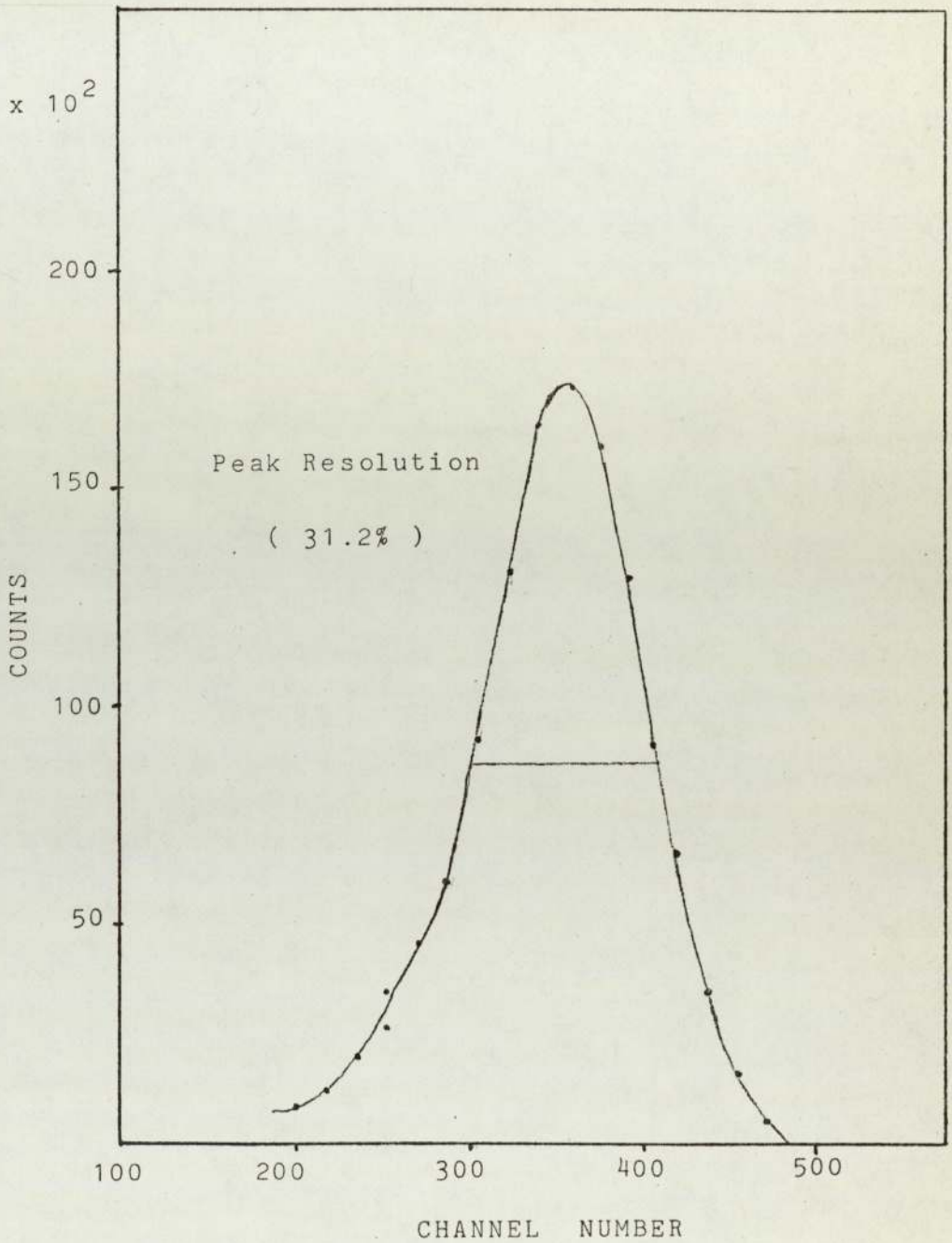

Fig. 4.25 ^{241}Am spectrum, with argon without storage in the molecular sieve vessel.

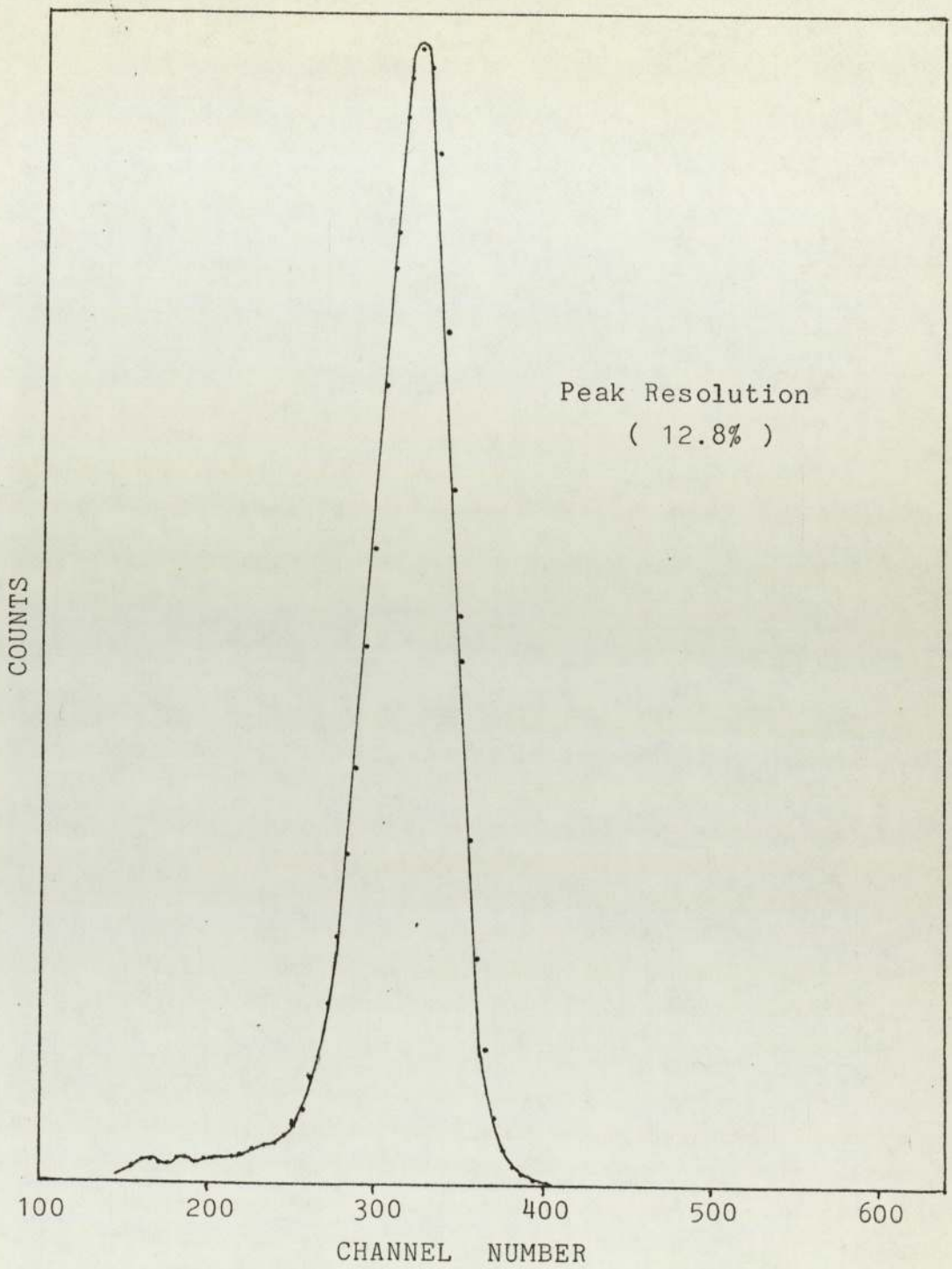

Fig. 4.26 ^{235}U spectrum, with krypton at 18 p.s.i.

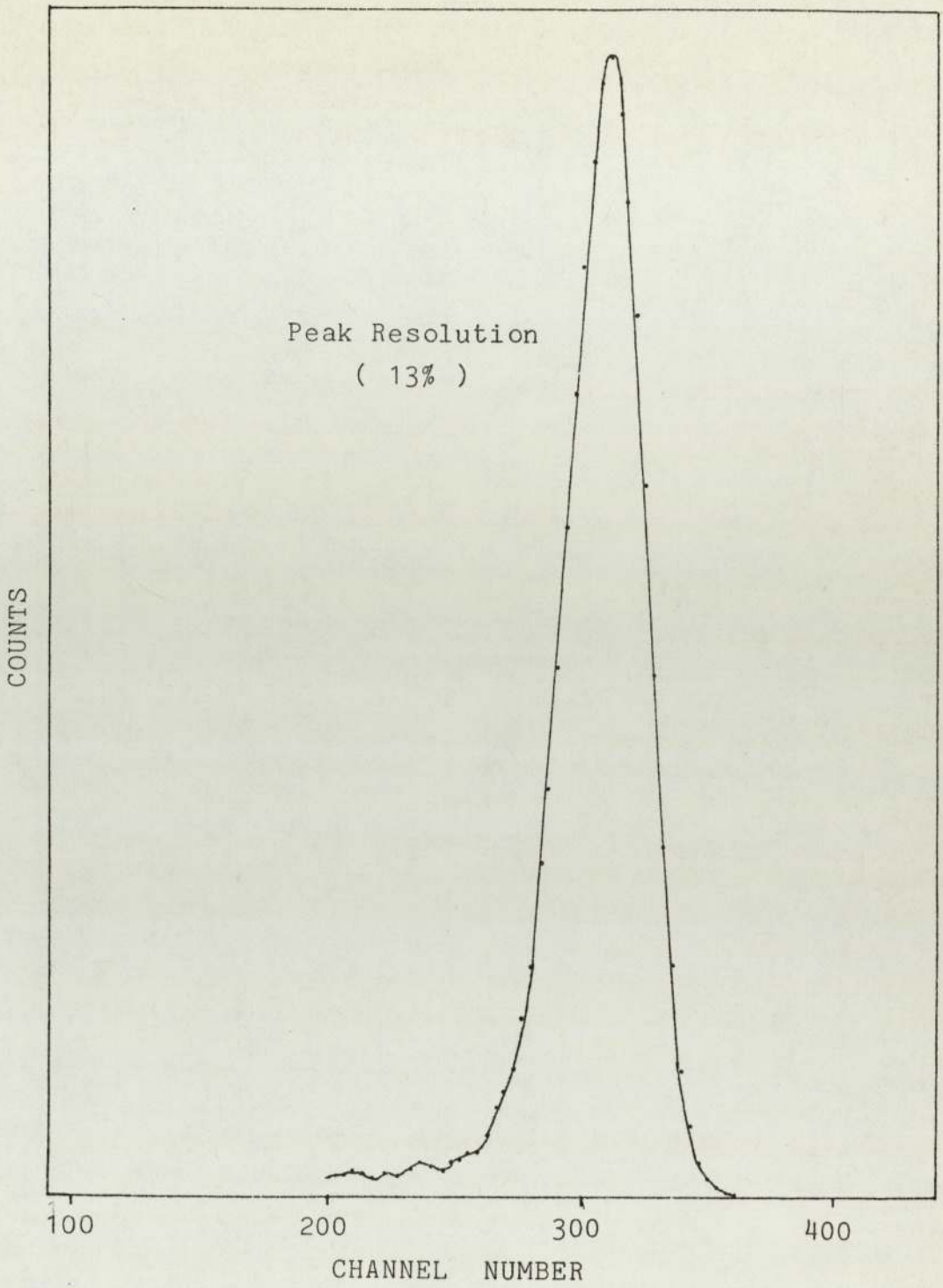

Fig. 4.27 ^{235}U spectrum, with krypton at 18 p.s.i., taken after 80 hours.

54 keV and resolution degradation of about 0.2%, indicating that the outgassing rate inside the gas cell was very low.

However, there was no significant improvement in resolution when the gas cell is filled from the molecular sieve storage vessel (Fig. 4.28).

This limitation to energy resolution is thought to be mainly due to the combination of factors contributing to the overall detection efficiency of the detector and not solely to inefficient gas purification. The energy resolution improved by a factor nearly equal to the relative scintillation efficiencies of the two gases. Although this improvement in resolution may have been affected by a higher gas purity in the case of krypton, a further improvement in detector resolution is probable by the use of xenon.

4.1.6 On-line Detection of Charged Particles.

The detector required a small modification to allow its use for the on-line detection of charged particles produced in (n,p) and (n,α) reactions. It is necessary for the walls of the gas cell to be lined with a polished metal foil which will act as a light reflector but will cut out charged particles produced by reactions in the cell walls. The choice of the metal foil was made by considering its reflectivity for light over the wavelength range 200-600 nm and from the requirement that the foil should have negligible (n,p) and (n,α) reaction

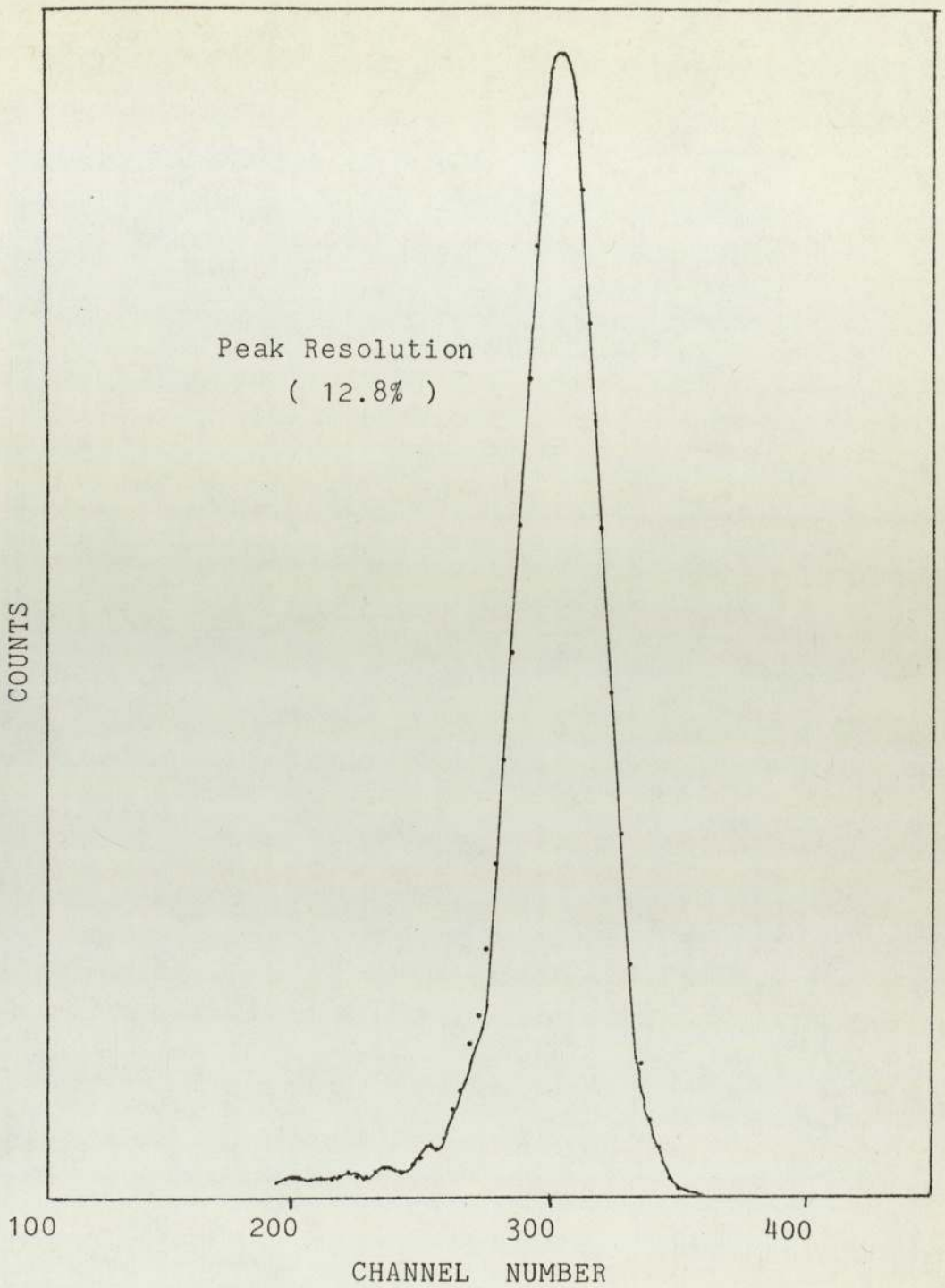

Fig. 4.28 ^{235}U spectrum, with krypton from molecular sieve vessel.

cross-sections over the neutron energy range 2-6 MeV. The choice was from silver, platinum, gold, steel, aluminium and tantalum. Table 4.7 shows the reflectivity of these metals over a range of wavelengths which extends to the U.V. part of the spectrum.[108]

WAVELENGTH(nm)	REFLECTIVITY (%)					
	Al	Ag	Pt	Ta	Steel	Au
180	-	75.0	34.6	53.0	21.8	-
200	-	77.0	38.0	56.0	27.0	-
250	80.0	34.1	33.8	58.7	38.0	38.8
300	-	10.0	39.7	69.1	43.7	31.8
350	84.1	75.0	43.2	62.3	49.8	27.5
400	85.0	85.0	47.5	68.7	-	28.7
450	87.0	91.0	54.7	71.0	53.2	33.1
500	88.0	92.7	58.4	73.0	55.0	47.0
550	-	92.7	61.1	79.6	56.1	74.0
600	89.0	92.6	64.2	83.0	58.3	84.4
650	91.0	94.7	66.5	88.0	59.0	88.9
700	87.0	95.6	69.0	-	59.2	92.3

Table 4.7 REFLECTION PROPERTIES OF SOME METALS.

Aluminium, silver, gold and steel (iron) all have significant (n,p) and (n,α) cross-sections over the 2-6 MeV energy range[74, 75, 76, 77]. Platinum could not be selected because of its high cost, leaving tantalum as the only suitable metal. The minimum thickness of tantalum foil required to stop 6 MeV protons is 0.122 mm. (determined applying Bragg-Kleeman rule described earlier) Consequently, the gas cell walls were lined with a tantalum foil 0.125 mm thick. The use of a polished tantalum foil, as a reflector, did not alter the detection efficiency of the detector. The ^{235}U alpha spectrum in

Fig. 4.29 is similar to that obtained with an evaporated aluminium reflector, Fig. 4.26.

An aluminium target was selected for a preliminary study of the on-line spectrum of protons produced in (n,p) reactions. Its advantage is that ^{27}Al has a natural abundance of 100%. Table 4.8, shows the reaction modes for aluminium and the maximum energy of the recoiling charged particle at various bombarding neutron energies (78).

An 80 p.s.i. krypton-filled gas cell was produced, incorporating a tantalum reflector and the ^{235}U foil. This gas pressure was sufficient to stop protons up to 4 MeV within the gas cell volume.

The neutrons were produced by the $D(d,n)^3He$ reaction using a deuterium gas target (already developed in the department) at Birmingham Radiation Centre 3MV Dynamitron Accelerator. Full details of the neutron source were given in Chapter 2.

The ^{235}U alpha spectrum for this detector is given in Fig. 4.30(a), and this was used to provide an energy calibration for the system. The alpha peak resolution was 23% compared to 12% at 18 p.s.i. pressure. Figs.4.30 (b) and (c) show the response of the detector to the $D(d,n)^3He$ source, for the neutron energies around 4 MeV,

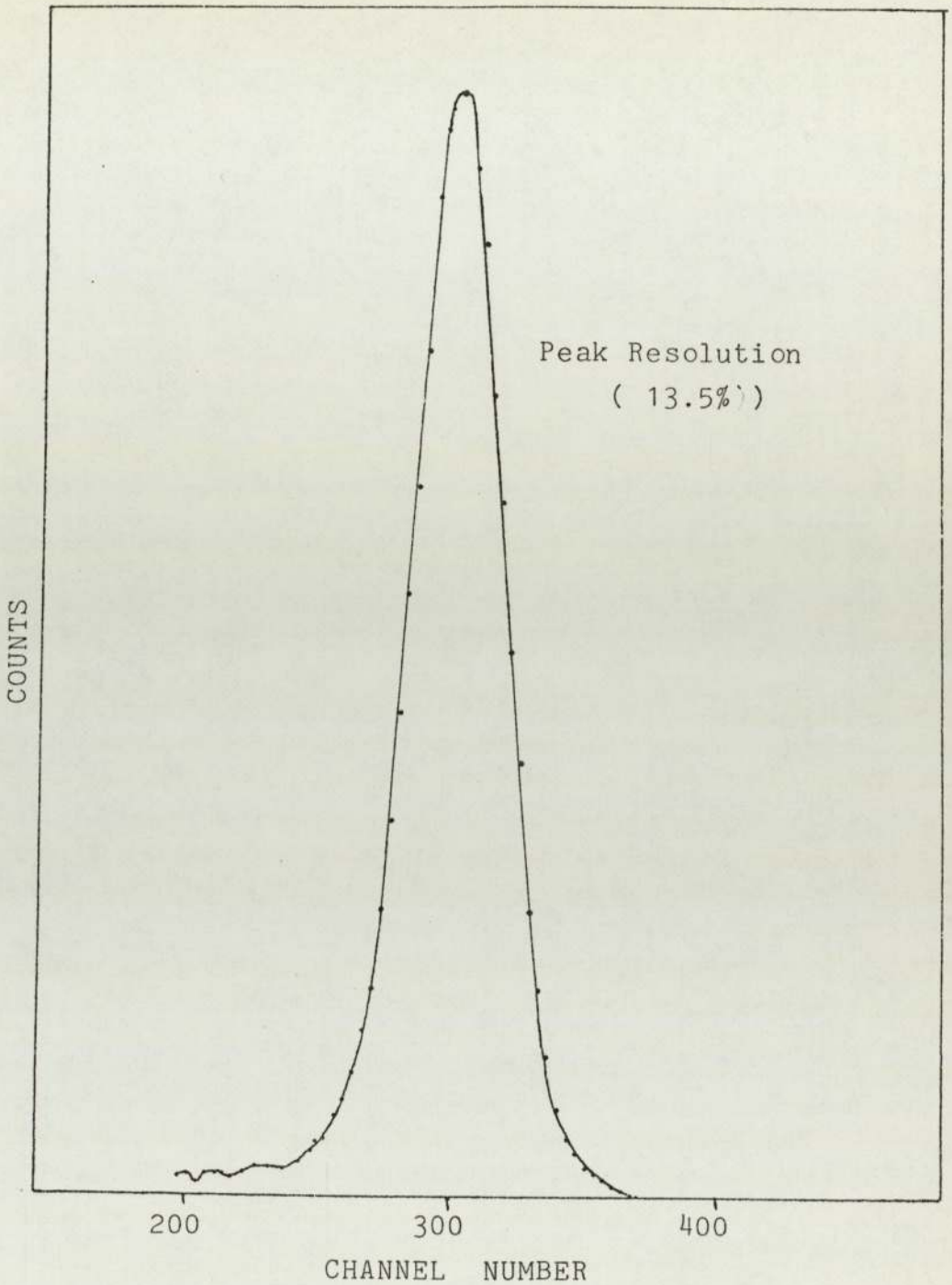

Fig. 4.29 ^{235}U spectrum, with krypton using tantalum foil reflector.

Reaction.	Q-value (MeV)	Charged particle energy (MeV) at Neutron Energy of				
		2.0 MeV	3.0 MeV	4.0 MeV	5.0 MeV	6.0 MeV
$^{27}Al(n,p)^{27}Mg$.	-1.827 MeV	0.132	1.157	2.163	3.165	4.166
$^{27}Al(n,\alpha)^{24}Na$.	-3.130 MeV	-	-	0.868	1.860	2.835

Table 4.8 Charged particle energies from $^{27}Al(n,p)$ and $^{27}Al(n,\alpha)$ reactions.

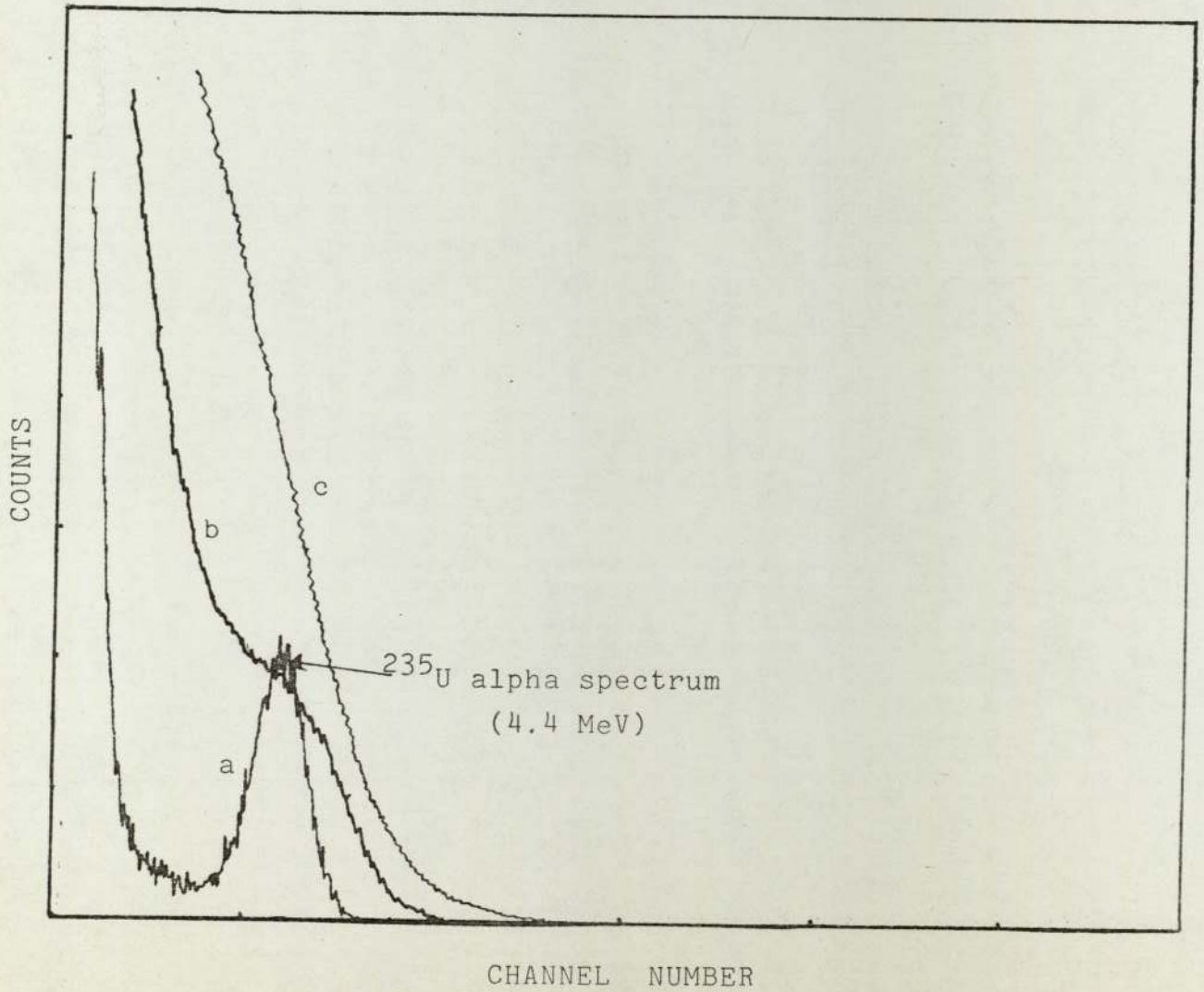

Fig. 4.30 (a) ^{235}U alpha spectrum, with krypton at 80 p.s.i.(b) & (c) the detector

and in the absence of aluminium target.

With the ^{235}U foil replaced by a 25μm aluminium foil, a similar spectrum was obtained Fig. 4.31 (a). There was no indication of the $^{27}Al(n,\alpha)$ or the $^{27}Al(n,p)$ peaks at 0.8 MeV and 2.0 MeV respectively. The same result was observed at higher neutron energies, viz. 5.0 MeV and 6.0 MeV(Figs.4.31 (b) and (c)).

The observed poor detector response proved to be due to a high gamma-sensitivity. Fig. 4.32 shows the spectrum obtained when a number of gamma sources were placed near to the gas cell and, from this result, the scintillation from Compton electrons mask the scintillation pulse arising from (n,α) and (n,p) events.

The use of the gas scintillation detector to monitor heavy charged particles from the neutron-induced reactions, proved unsuccessful. The conclusions and predictions made by earlier workers[39, 42], for the gas scintillation detector to be insensitive to gamma radiation, did not stand up in the case of on-line detection of heavy charged particles.

The use of surface barrier detector to monitor the charged particles from the (n,α) and (n,p) reactions is described in the following section.

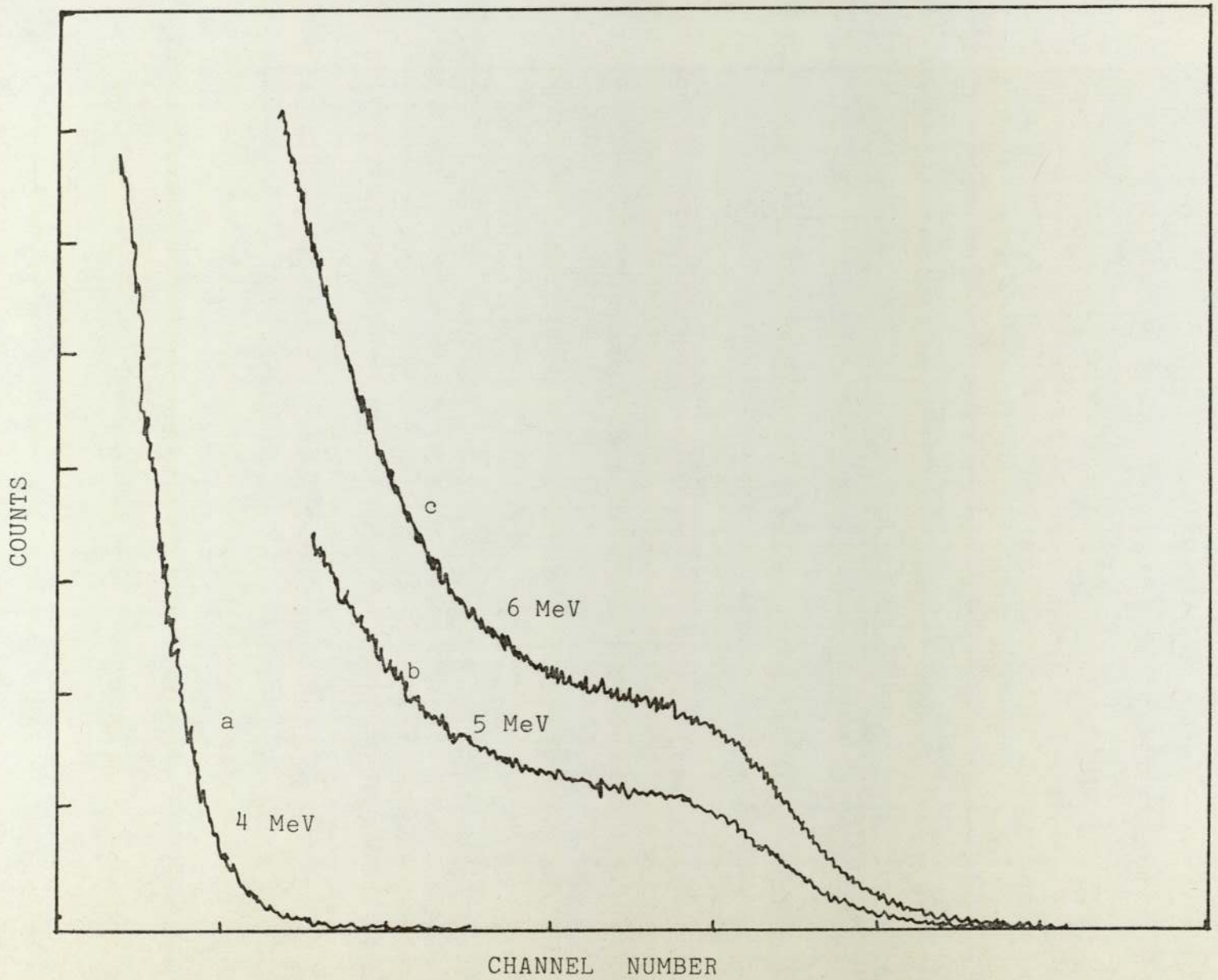

Fig. 4.31 An 80p.s.i. krypton-filled detector with aluminium sample, response to neutron beam at different energies.

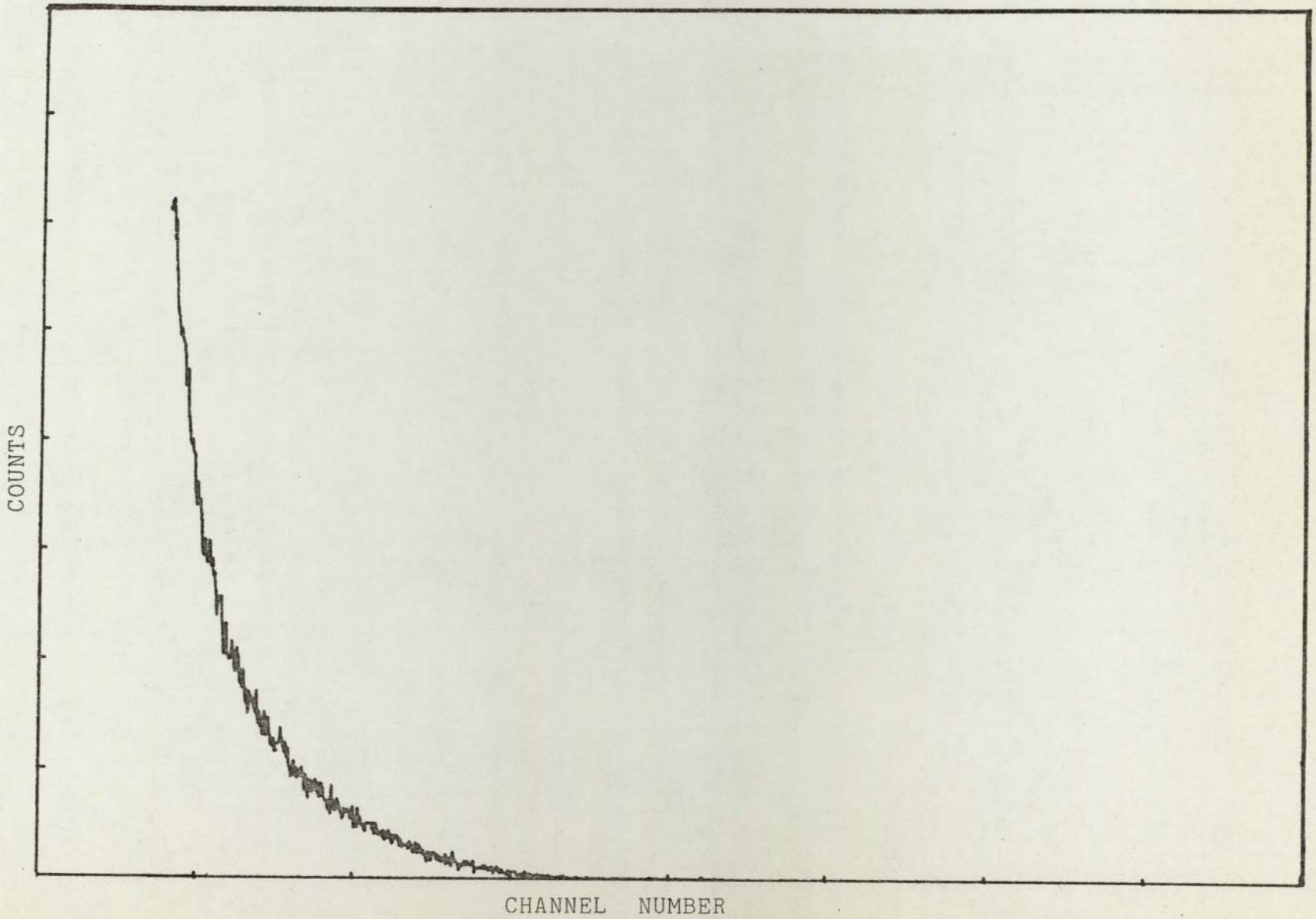

Fig. 4.32 An 80p.s.i. krypton-filled detector, response to gamma sources placed near to gas cell.

4.2 Measurements with a Surface Barrier Semiconductor Detector.

Some useful features of semiconductor detectors were described in the last section. The ionization energy i.e. the energy expended by the charged particle to create one electron-hole pair, is mostly independent of both the energy and type of the charged particle and has much smaller value ($\sim$ 3eV) as compared to the case of a typical gas-filled detector ($\sim$ 30eV). This provides greater number of charge carriers, thus leading to better energy resolution and signal to noise ratio.

A number of workers [79 - 82], have demonstrated the convenience of silicon semiconductor detectors for studying neutron-induced reactions in silicon. Konijn and Lauber [4] measured $^{29}Si(n,\alpha)^{26}Mg$ and $^{58}Ni(n,p)^{58}Co$ reaction cross-sections in the energy range 2.2 to 3.8 MeV, using a surface barrier detector to record the charged particles. Lauber and Malmskog[83] measured $^{54}Fe(n,p)^{54}Mn$ reaction cross-section. The half-lives of the reaction products from $^{58}Ni(n,p)^{58}Co$ and $^{54}Fe(n,p)^{54}Co$ reactions are 71 days and 300 days respectively and in the activation technique, although the measurement of the activity of the reaction products is not difficult, the statistical accuracy of the measurement will be poor. Potenza, Ricamo and Rubbino[84] obtained energy spectra of the charged particles produced in the (n,p) and (n,α)

reactions in silicon, using silicon detectors as targets and measured the excitation functions for $^{28}Si(n,p)^{28}Al$ and $^{29}Si(n,\alpha)^{26}Mg$ reactions in the energy range of 3.7 to 5.5 MeV.

4.2.1 Characteristics of the Surface Barrier Detector.

The operational characteristics and the design configurations of the detector, used in this work, are described here. The detector was n-type, partially depleted, type BA-024-150-300 supplied by Ortec. Fig. 4.33 shows the actual dimensions of the detector and its specifications are given in Table 4.9.

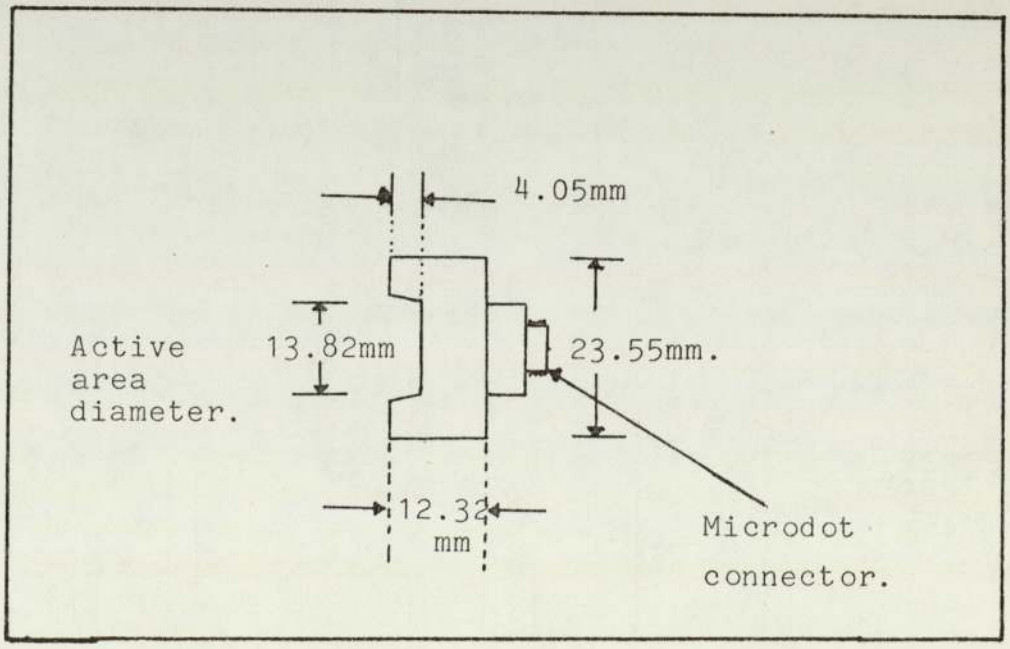

Fig. 4.33 Dimensions of Surface barrier detector.

Active area	150 mm^2.
Sensitive depth	300 μm.
Nominal resistivity	3600 Ωcm.
Electrode thickness	Gold: 40.0 μg. cm^{-2} Aluminium: 40.0 μg. cm^{-2}
Alpha FWHM resolution (^{241}Am source;5.48MeV)	14.2 keV.
Noise width	7.3 keV.

Table 4.9 Surface Barrier Detector Specifications.

A gold layer (40 μg cm^{-2}) acts as a window to the incident particles. A nuclear particle entering the detector must pass through this window and an insensitive region and, in doing so, a certain amount of energy degradation takes place. This energy loss is significant and the effective thickness of the dead layer needs to be known. The dead layer thickness of the detector concerned is 155nm of silicon equivalent and 100nm of which corresponds to energy loss of 4 keV for 1 MeV protons and 14 keV for 5 MeV alpha particles.

The detector depletion region thickness (x_0) is proportional to the square root of the applied voltage for a given material of resistivity (ρ)[85];

$$x_0 = \left[k \rho (V_a + V_0) \right]^{\frac{1}{2}} \quad \ldots\ldots\ldots\ldots (4.12)$$

where, x_0 is expressed in cm.

ρ is in Ωcm.

V_0, is the barrier height in absence of external voltage.

V_a, is the voltage applied externally to the junction.

k, is a constant equal to 3.2×10^{-9} for the surface barrier device utilizing n-type silicon.

The maximum detector bias of 125 volts would provide a depletion layer of 300 μm, sufficient to stop 22 MeV alpha particles and 6 MeV protons, Fig. 4.34[86]. The pulse height from radiations that are fully stopped within the depletion layer rises with applied bias voltage. This is due to the increasing charge collection as the electronic field is increased and once this field is sufficiently high, the charge collection becomes nearly complete and the pulse height no longer changes with further increase in the detector bias voltage.Fig. 4.35 shows the pulse height versus bias voltage characteristics for 5.48 MeV alpha particles from a thick ^{241}Am source. For subsequent measurements, the detector was operated at 80 volts bias, neglecting the voltage drop across the pre-amp. load resistor, to create the depletion layer sufficient to stop protons and alpha particles from the (n,p) and (n,α) reactions studied.

Data has been published (Ortec Ltd.) on the

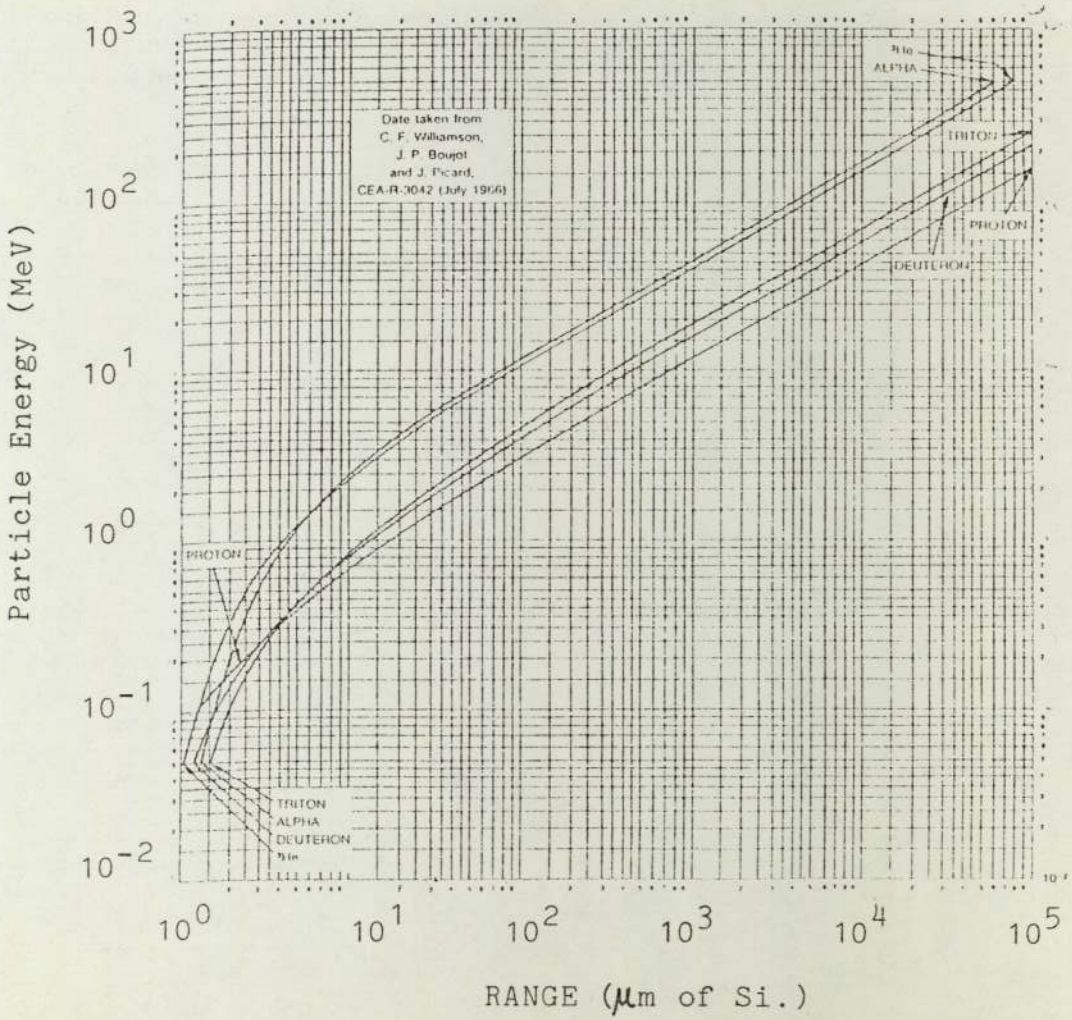

Fig. 4.34 Range-Energy Curves for Charged Particles in Silicon.

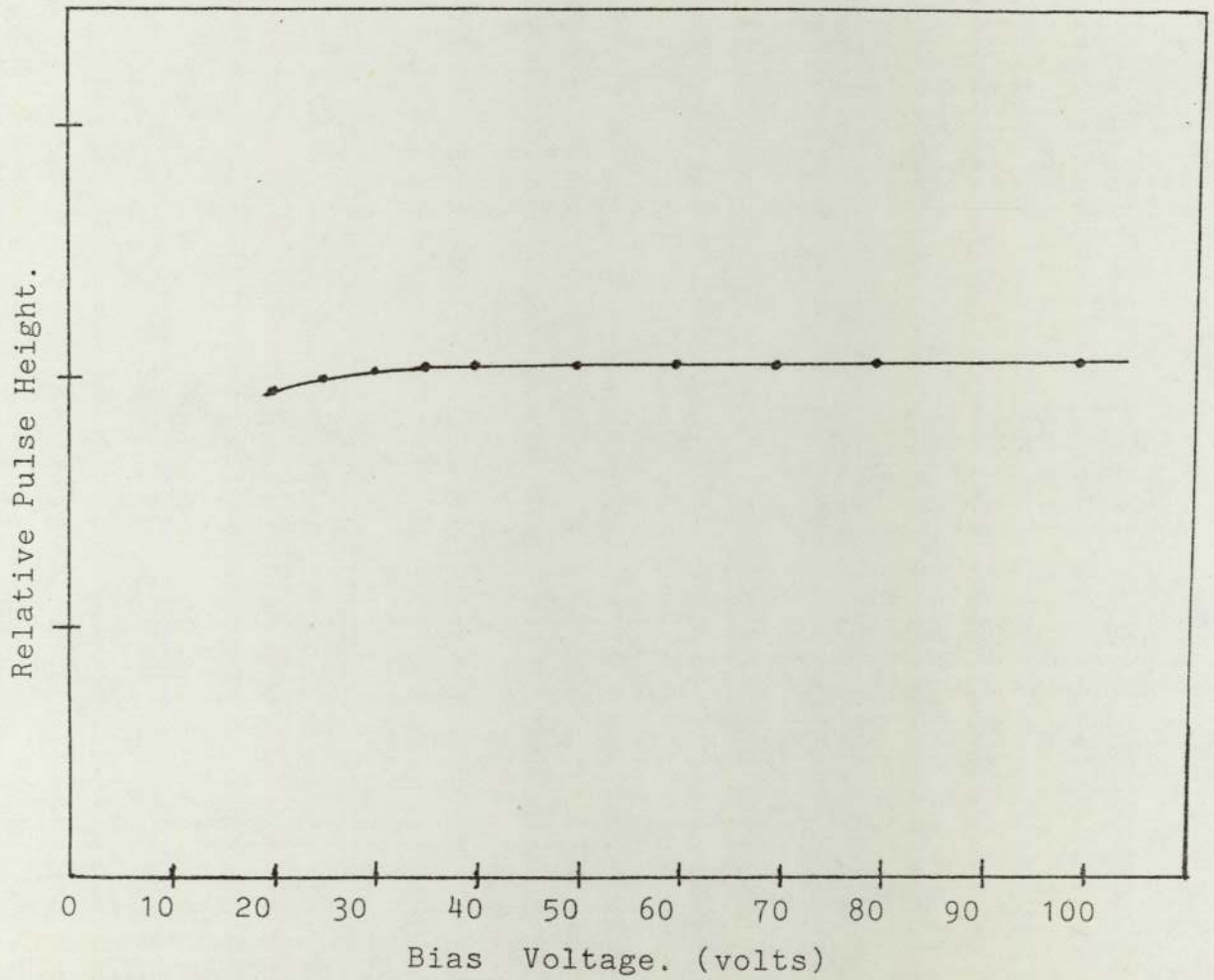

Fig.4.35 Bias voltage characteristics of surface barrier detector.

integrated flux of charged particles, neutrons and gamma radiation, required to produce a significant deterioration in silicon surface barrier detector performance. This is reproduced in Table 4.10 for a detector irradiated on the gold entrance window.

Radiation	Fluence /(Ref.)		Fluence.*
Fast electrons	$10^{14}cm^{-2}$	28	$10^{13}cm^{-2}$
Protons	10^{13} "	29	10^{10} "
Alpha particles	10^{11} "	30,31	10^{9} "
Fission fragments.	$3x10^{8}$"	32	10^{8} "
Neutrons	$3x10^{11}$"	31,33	10^{12} "
Gamma radiation	10^{6} R	33	-

Table 4.10 Radiation damage in silicon detectors.

In this work, the neutron flux incident on the detector was of the order of 10^{6} neutrons $cm^{-2}s^{-1}$, much below the damage limit, and no pulse deterioration over the period of use was observed.

*Fluence values supplied by Ortec Ltd., the manufacturer of the surface barrier detector used in this work.

4.2.2 Detection Efficiency.

The absolute efficiency ($\mathcal{E}_a$) of a counting system is defined as the number of recorded counts divided by the number of particles emitted by the source.

The intrinsic efficiency ($\mathcal{E}_i$) is equal to the number of useful recorded counts divided by the number of particles of interest actually striking the detector.

The geometric efficiency ($\mathcal{E}_g$) is determined by the fraction of emitted particles which actually strike the detector.

The above three are related as:

$$\mathcal{E}_a = \mathcal{E}_g \times \mathcal{E}_i \qquad \text{.....(4.13)}$$

In a surface barrier detector, for a particle to lose its energy completely, the sensitive depth must exceed the range of the particle and in such a case $\mathcal{E}_i$ is essentially 100%.

It was essential to calculate the detector efficiency from the "geometry" defined by the experimental configuration used in this work. The source and the detector were both circular, the latter of larger radius, and separated by a distance smaller than the radius of either. Their planes are perpendicular to the line through their centres.

The techniques of various workers[87, 88, 89], were studied; the method of calculation given by Jaffey[89] was most suitable. The "geometry" defined by the detector is the fraction of the total solid angle subtended by the detector as:

$$G(\mathcal{E}) = \Omega / 4\pi$$

For a point source on the axis, this "geometry" can be expressed as: (Fig. 4.36)

$$G(\mathcal{E}_1) = \frac{2\pi(1-\cos\alpha)}{4\pi}$$

From Fig.4.36, the above equation can be written as:

$$G(\mathcal{E}_1) = \tfrac{1}{2}(1-Z/D) = \tfrac{1}{2}(a^2/D(D+Z))$$

For a point source off the axis at distance ρ, $G(\mathcal{E})$ can be expanded in infinite series and each term of the series integrated separately. The simplest way is to utilize the fact that $G(\mathcal{E})$ satisfies Laplace's equation.

Therefore, it is possible to write for a point source off the axis:

$$G(\mathcal{E}_2) = G(\mathcal{E}_1) - \tfrac{3}{8}\rho^2 a^2 Z/D^5 + 15/32\,\rho^4 a^2 Z/D^9 (Z^2 - \tfrac{3}{4}a^2) + \ldots\ldots \quad (4.14)$$

When the area of the source is too large to approximate it as a point, an average value $G_s(\mathcal{E})$ of the geometry may be written as:

$$G_s(\mathcal{E}) = \int_0^b \frac{2\pi G(\mathcal{E}_2)}{\pi b^2}\,\rho\, d\rho \ldots\ldots \text{Ref}(88)$$

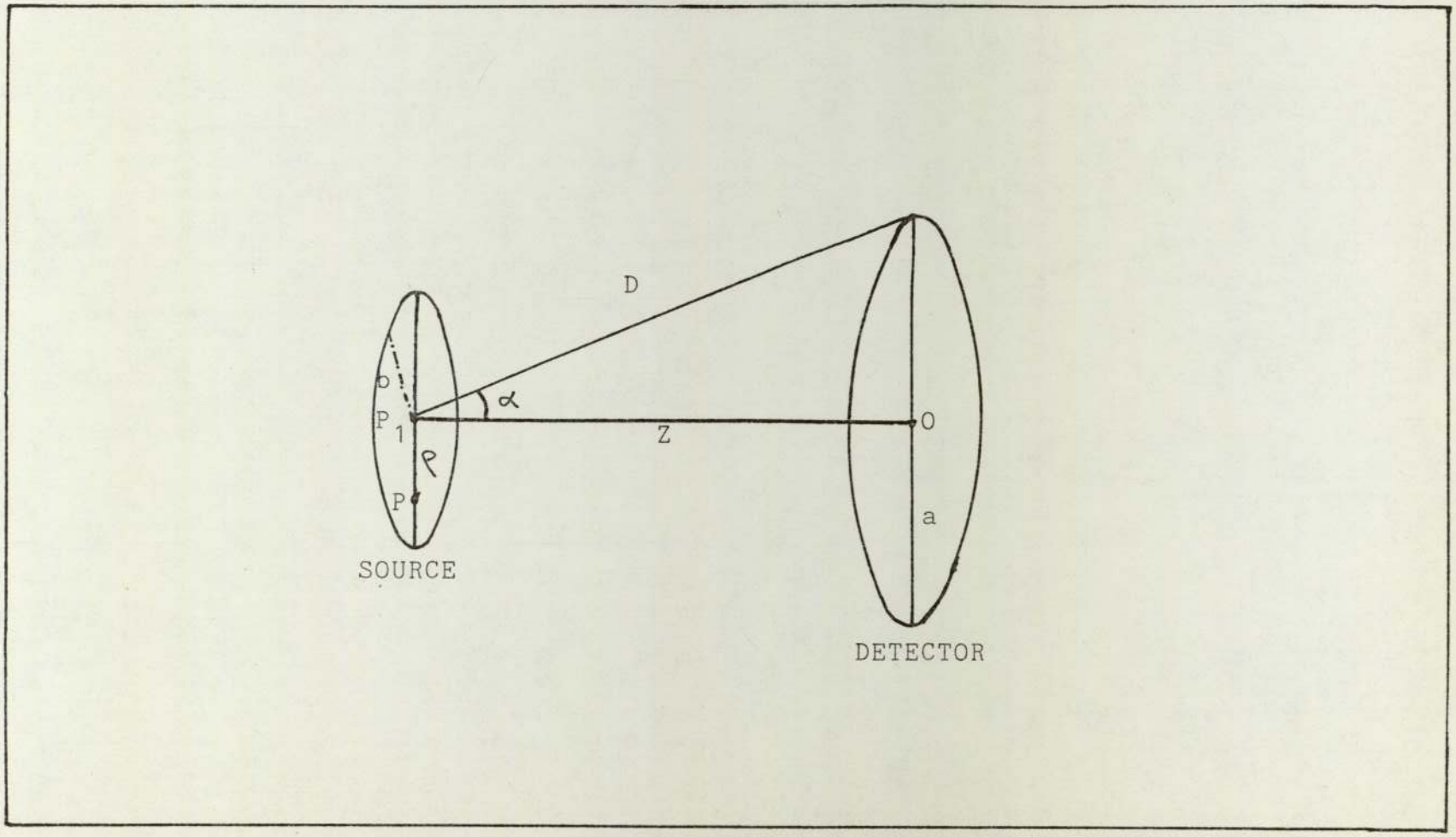

Fig. 4.36 SOURCE TO DETECTOR CONFIGURATIONS.

or $$G_s(\mathcal{E}) = \frac{2}{b^2}\int_0^b G(\mathcal{E}_2)\,\rho\,d\rho.$$

For the source to be circular, parallel and coaxial with the circular detector (sensitive area), equation 4.14 can be integrated explicitly;

$$G_s(\mathcal{E}) = \frac{2}{b^2}\left[\int_0^b \left\{\tfrac{1}{2}a^2/D(D+Z) - \tfrac{3}{8}\rho^2 a^2 Z/D^5 + 15/32\,\rho^4 a^2 Z/D^9 + 15/32\,{}^4 a^2 Z/D^9(Z^2-\tfrac{3}{4}a^2) + \ldots\ldots\right\}\rho\,d\rho\right]$$

Therefore,

$$G_s(\mathcal{E}) = \tfrac{1}{2}a^2/D(D+Z) - 3/16\,a^2 Z/D^5(b^2) + 5/32\,a^2 Z/D^9(Z^2-\tfrac{3}{4}a^2)(b^4) \ldots\ldots\ldots (4.15)$$

From the experimental configurations:

$a = 0.69$ cm, detector radius.
$b = 0.50$ cm, source radius.
$Z = 0.43$ cm, detector to source distance.
$D = (a^2+Z^2)^{\frac{1}{2}} = 0.813$ cm.

Substituting these values in equation 4.15

$$G_s(\mathcal{E}) = 0.206$$

For a detector count rate C from low geometry measurements, the 4π activity, A, can be determined from the relation:

$$A = C / G_s(\mathcal{E}) \qquad \ldots\ldots\ldots\ldots (4.16)$$

CHAPTER 5

THE MEASUREMENT OF (n,p) AND (n,α) CROSS-SECTIONS

CHAPTER 5.

5.0 The Measurement of (n,p) and (n,α) Cross-ections.

The neutron flux was measured as described in Chapter 3, whilst the methods employed to detect the charged particles from the neutron-induced reactions were described in Chapter 4. This Chapter describes the experimental method for the measurement of (n,p) and (n,α) cross-sections, and the treatment of the experimental data.

5.1 Experimental Arrangements.

In the experimental area of the accelerator there was little material within several metres of the neutron source and the radiation detectors. Figs.5.1 (a) and (b) show the accelerator beam line, neutron source and the detectors. Three measurements were made for each neutron energy. The first run was used to give an accurate value for the neutron flux, with the fission counter placed 2 cm from the neutron source at 0 degree to the beam line. In the second and third runs, the surface barrier detector was placed 1 cm from the neutron source at 0 degree to the beam direction.

In the second run, the surface barrier detector was exposed to the neutrons with the sample placed between the detector and the neutron source. The detector and

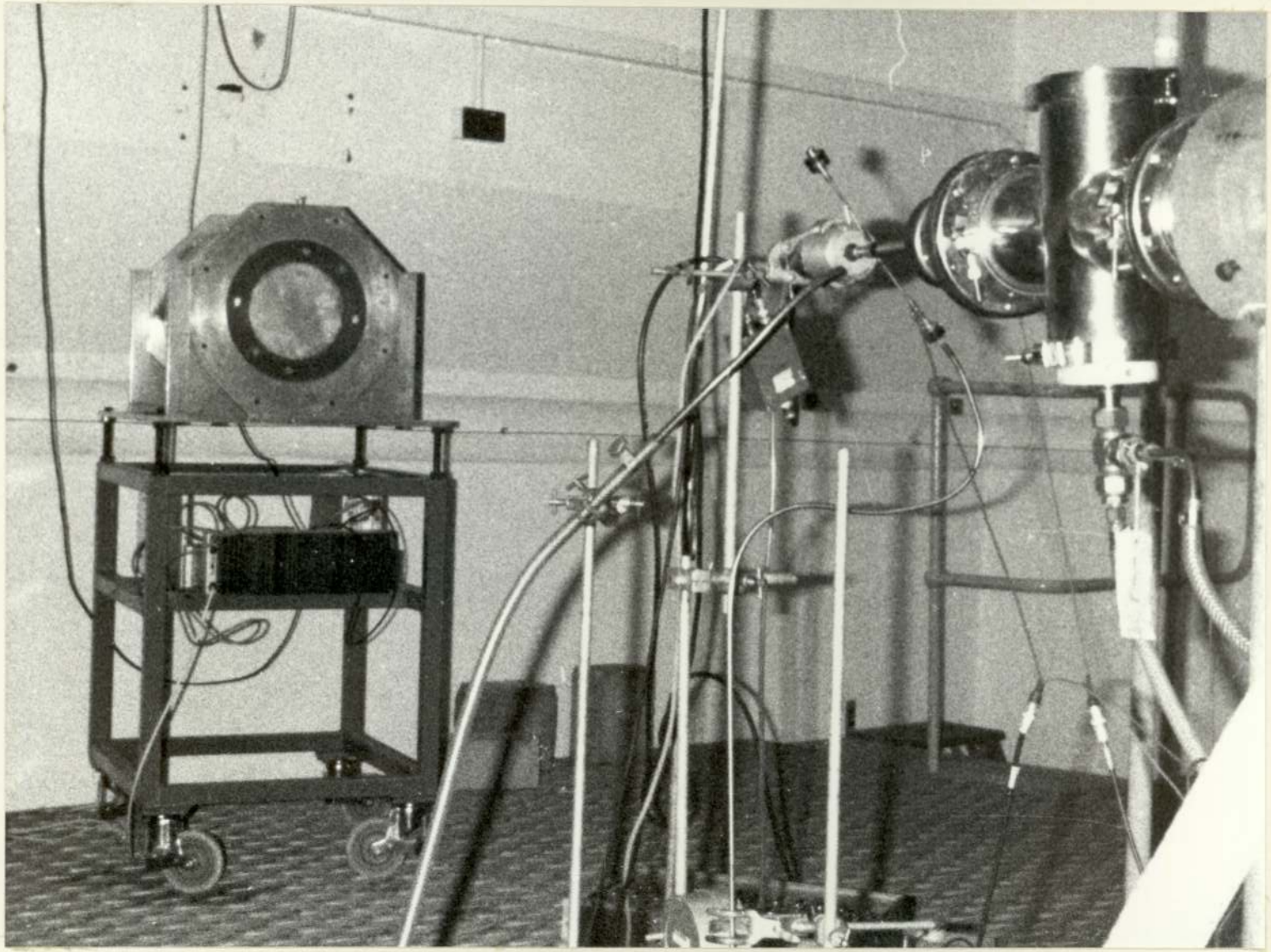

Fig. 5.1 (a) The Accelerator Beam Line, Neutron Source and Fission Counter.

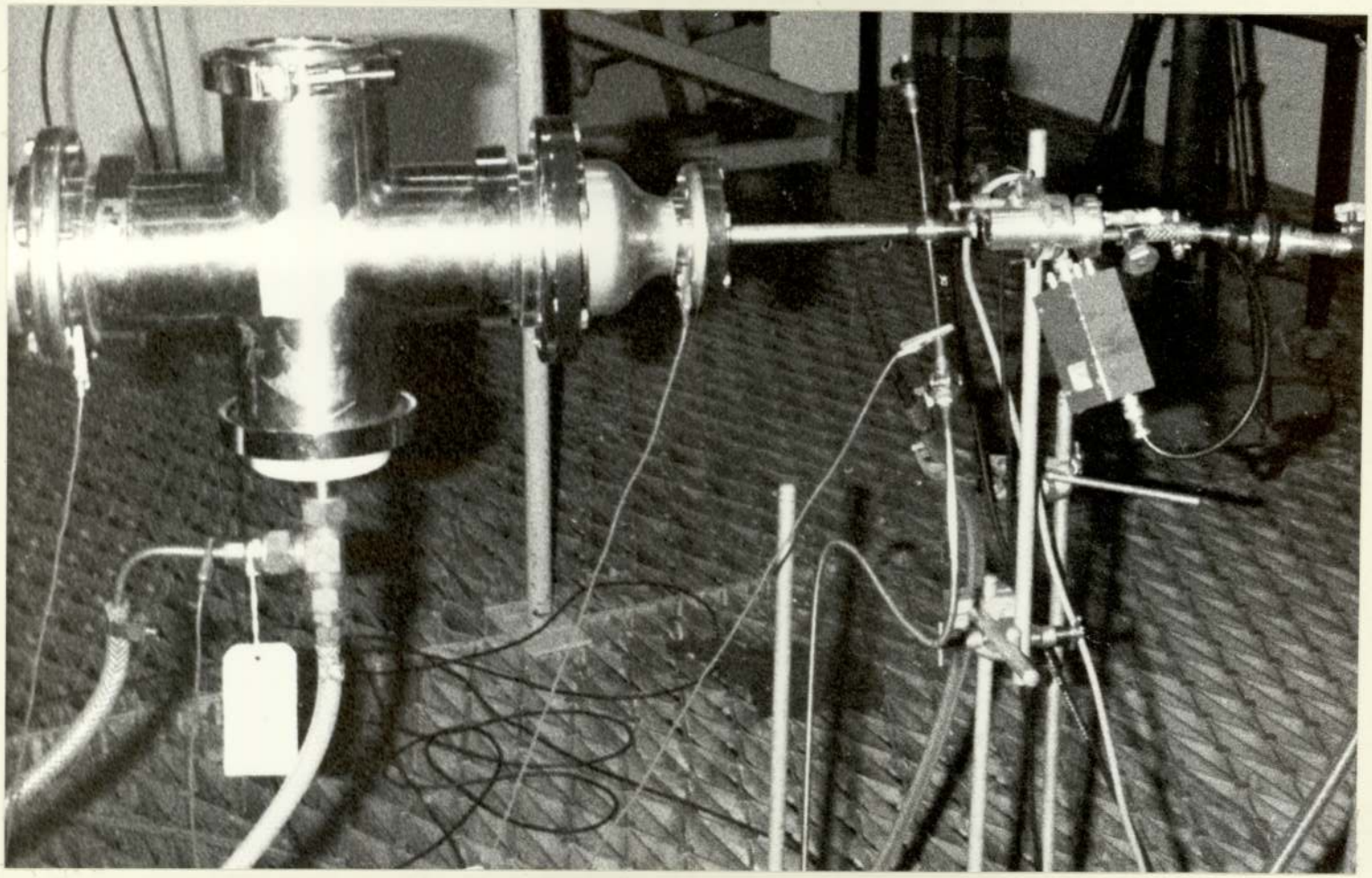

Fig. 5.1 (b) The Accelerator Beam Line, Neutron Source and Solid State Detector.

the sample were enclosed in a thin walled (thickness less than 1 mm) cylindrical aluminium chamber, which had a pure gold window of thickness 0.1 mm (Fig.5.2). Gold does not produce any interfering charged particles as its (n,p) and (n,α) reactions have thresholds[90] greater than 6 MeV. The sample under investigation was placed immediately behind the window, with a thin tantalum foil collimator (10 mm diameter) between the sample and the detector. The chamber was continuously evacuated during the run, to a pressure of approximately 10^{-3}mmHg.

During the third run, the target sample was removed to enable a measurement of the reactions within the surface barrier detector.

Although the three runs were performed for the same time duration and with similar experimental configurations, it was possible for the neutron flux to differ due to variations in the deuteron beam energy and flux. Consequently, a BF_3 long counter was used as a sub-standard to account for the neutron flux variation between the three runs. A DePangher long counter[91] was placed 4 m away from the neutron source and also at 0 degree to the beam direction. This counter has a uniform response with neutron energy over the range selected for this work and is stable over long periods of time. The operating conditions were described in Chapter 3 for the fission counter and in Chapter 4, for the surface barrier detector.

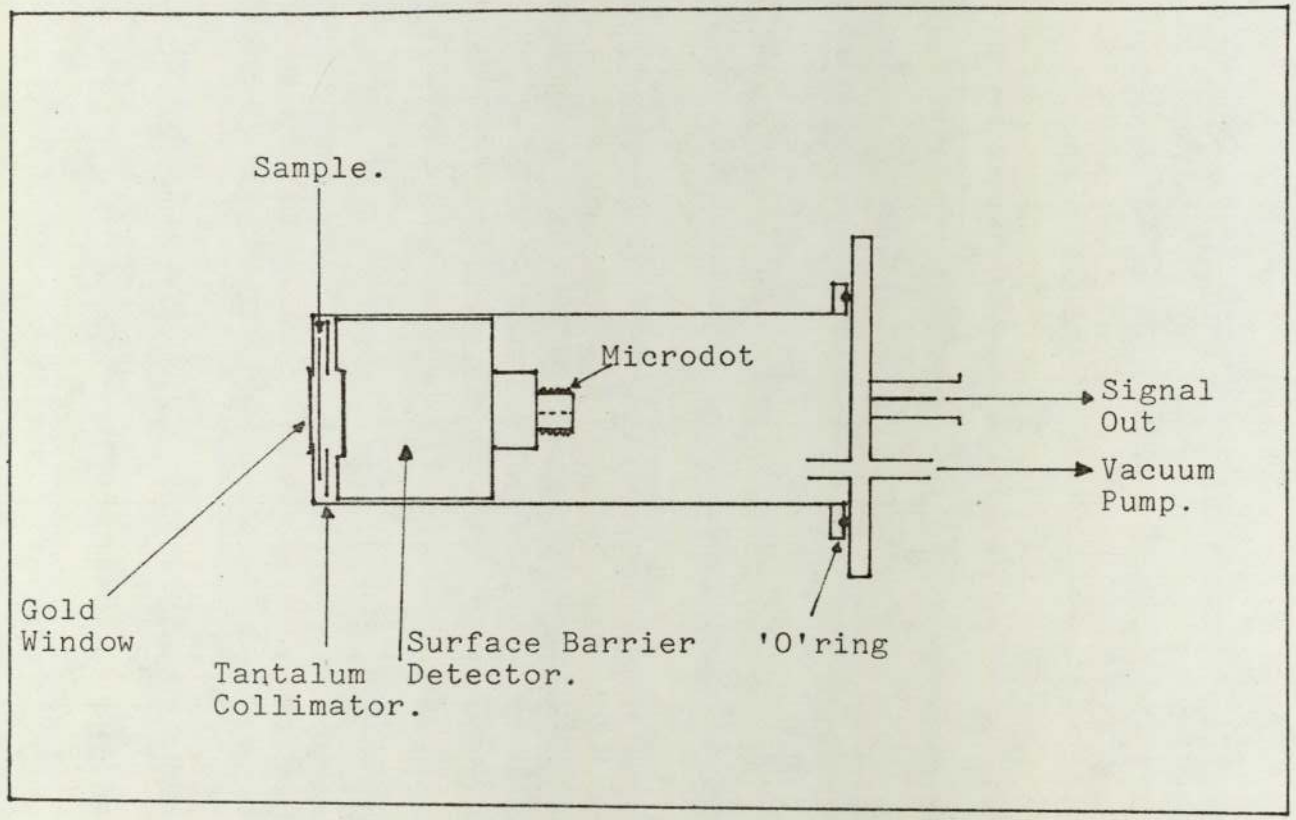

Fig. 5.2 The Surface Barrier Detector Chamber.

5.2 Estimation of the Neutron Flux.

The neutron flux ϕ_n , was determined from the equation:

$$\phi_n = \frac{R_f}{\varepsilon_f} \quad \ldots\ldots\ldots\ldots\ldots\ldots (5.1)$$

where, R_f is the ^{238}U fission count rate and ε_f is the neutron detection efficiency of the fission counter. The observed fission count rate for each neutron energy was obtained as described in Chapter 3, and corrected for fragment absorption and momentum effects. The absorption correction factor as determined by White[92] was 1.0171 for the ^{238}U foil with a mean fragment range of 7.5 $mgcm^{-2}$. Table 5.1 shows the combined absorption correction and momentum correction factor applied to the observed fission counts for the ^{238}U foil. Other corrections, for dead time and alpha particle pile up, were negligible.

NEUTRON ENERGY (MeV)	CORRECTION FACTOR
3.513	1.0120
3.810	1.0118
4.080	1.0117
4.351	1.0115
4.590	1.0114
4.841	1.0112
5.071	1.0111
5.300	1.0110

Table 5.1 Correction factors as applied to the observed fission counts in ^{238}U.

The neutron detection efficiency of the foil is given by:

$$(\mathcal{E}_f)_{238} = N_u \left[\sigma_{238} \times (\%)_{238} + \sigma_{235} \times (\%)_{235} \right] \qquad \text{.....(5.2)}$$

where, $(\%)_{238}$ and $(\%)_{235}$ are the isotopic abundances of ^{238}U and ^{235}U respectively in the foil and their values, as supplied by the manufacturer are;

$$(\%)_{238} = 99.995\%, \quad (\%)_{235} = 0.005\%.$$

σ_{238} and σ_{235} are the microscopic fission cross-sections at the relevant neutron energies.

The data for σ_{238} and σ_{235} was obtained from ENDF/B-IV (most recent) and is listed in Table 5.2. The interpolated data corresponding to measurements at specific energies is presented in Table 5.3.

The uranium content N_u in equation 5.2 is the number of uranium nuclei in the layer of uranium deposited on the platinum backing of the foil. This number was determined experimentally by an alpha-assaying technique described by White.[92] The technique involved the measurement of alpha-activity (dN/dt) from the uranium content, using a solid state detector in a 2π geometry configuration. The alpha-activity is related to N_u through effective decay constant $\lambda_{eff.}$, as

$$dN/dt = N_u \lambda_{eff.} \qquad \text{.....(5.3)}$$

The effective decay constant ($\lambda_{eff.}$) is represented as

NEUTRON ENERGY (MeV).	$(\sigma_{n,f})_{238}$ (barns)	$(\sigma_{n,f})_{235}$ (barns)
3.1	0.541	1.222
3.5	0.554	1.183
4.0	0.565	1.150
4.5	0.563	1.120
5.0	0.554	1.094
5.2	0.559	1.084
5.4	0.562	1.069
5.5	0.565	1.059
5.8	0.603	1.087
6.0	0.661	1.160

Table 5.2 ENDF/B Data for ^{238}U and ^{235}U Fission Cross-sections.

NEUTRON ENERGY(MeV)	$(\sigma_{n,f})_{238}$ (barns)	$(\sigma_{n,f})_{235}$ (barns)
3.513	0.554	1.184
3.810	0.559	1.163
4.080	0.565	1.155
4.351	0.565	1.131
4.590	0.563	1.125
4.841	0.560	1.103
5.071	0.556	1.111
5.300	0.562	1.084

Table 5.3 ENDF/B Data, Interpolated Cross-sections(Fission)

$$\lambda_{eff} = \left[\lambda_{235} \times (\%)_{235} + \lambda_{238} \times (\%)_{238} \right] \qquad \ldots\ldots\ldots\ldots(5.4)$$

where, $\lambda_{235} = \dfrac{0.6931}{(T_{\frac{1}{2}})^{235}U}$

and $\lambda_{238} = \dfrac{0.6931}{(T_{\frac{1}{2}})^{238}U}$

The half-lives $(T_{\frac{1}{2}})^{235}U$ and $(T_{\frac{1}{2}})^{238}U$ are given in Table 5.4[93] with the uncertainties associated with them.

ISOTOPE	$(T_{\frac{1}{2}})$	UNCERTAINTY.
^{235}U	7.1×10^{8} years	$\pm$ 2.8 %
^{238}U	4.5×10^{9} years	$\pm$ 1.5 %

Table 5.4 Half-lives of Uranium Isotopes.

The alpha count rate in 2π-geometry was measured as 4.25 ± 0.007 counts s^{-1}, giving an alpha-activity for the ^{238}U foil of 8.5 ± 0.015 disintegrations per second. The uncertainty is to account for the statistical errors in counting, and absorption scattering of the alpha particles.

The value for N_u, determined as above was $(1.7399 \pm 0.0257) \times 10^{18}$ nuclei. When subsituted in equation 5.2, with values of σ_{235} and σ_{238} the $\mathcal{E}_f$,

neutron detection efficiencies were determined. These are shown in Table 5.5

The observed fission count rate was corrected for background neutrons and for neutrons scattered in the platinum backing of the uranium foil.

The accelerator deutrons produce background neutrons from reactions in the gas target material, and from carbon deposits accumulated during deutron beam bombardment and loading of deuterium in the gas target beam stop. To determine this background contribution, the measurement was made of the neutron flux from the gas cell without its deuterium gas filling. The contribution at each neutron energy point was estimated from a single measurement at 4.59 MeV (deutron energy 1.6MeV). There was no correction for room-scattered (thermal) neutrons since these neutron energies are below the $^{238}U(n,f)$ threshold. The contribution due to thermal neutrons from 0.005% ^{235}U content was negligible.

The correction for neutrons scattered within the platinum foil was determined through calculations suggested by Smith et. al.[5] and later applied by Jalil[6]. A scattering correction (R_{scatt}) is written as:

NEUTRON ENERGY(MeV)	NEUTRON DETECTION EFFICIENCY, $\mathcal{E}_f$ (per unit fluence)
3.513	$(9.639 \pm 0.0142) \times 10^{-7}$
3.810	$(9.736 \pm 0.0144) \times 10^{-7}$
4.080	$(9.831 \pm 0.0145) \times 10^{-7}$
4.351	$(9.830 \pm 0.0145) \times 10^{-7}$
4.590	$(9.796 \pm 0.0144) \times 10^{-7}$
4.841	$(9.743 \pm 0.0143) \times 10^{-7}$
5.071	$(9.674 \pm 0.0142) \times 10^{-7}$
5.300	$(9.778 \pm 0.0144) \times 10^{-7}$

Table 5.5 Neutron Detection Efficiency.

$$R_{scatt} = \frac{\Sigma_{SP}}{\Sigma_{TP}} \exp(\Sigma_{TP}\, t_p) \frac{\left[1 - \exp(-\Sigma_{TP}\, t_p)\right]}{\left[1 - \exp(-\Sigma_{Tf}\, t_f)\right]} \cdot \left\langle \left[1 - \exp(-\Sigma_{TP}\, \Delta_f)\right] \right\rangle \qquad \ldots\ldots (5.5)$$

where,

Σ_{SP} = macroscopic elastic scattering cross-section in platinum.

Σ_{TP} = total macroscopic cross-section in platinum.

Σ_{Tf} = total macroscopic cross-section in ^{238}U.

t_p = thickness of platinum foil (0.0125cm)

t_f = uranium deposit thickness

$$= \frac{\text{deposit mass per unit area}}{\text{density of uranium}}$$

$$= 1.05 \times 10^{-5} \text{ cm}$$

(deposit mass = 0.2 mg cm^{-2})

Δ_f = ' neutron path ' of the scattered neutrons in the uranium foil.

The neutron path length was considered to be the same for all scattered neutrons as uranium deposit thickness was very small. The calculation also assumes an incident parallel neutron beam and isotropic neutron scattering. Values for Σ_{SP}, Σ_{TP} and Σ_{Tf} are listed in Table 5.6.

The correction factor was determined from R_{scatt} as:

$$\text{Correction Factor} = \frac{1}{1 + R_{scatt}}$$

and the values are given in Table 5.7.

NEUTRON ENERGY(MeV)	Σ_{TP}	Σ_{SP}	Σ_{Tf}
3.513	0.476	0.743	0.538
3.810	0.456	0.748	0.524
4.080	0.450	0.776	0.511
4.351	0.437	0.801	0.507
4.590	0.424	0.790	0.492
4.841	0.410	0.817	0.477
5.071	0.391	0.867	0.463
5.300	0.371	0.859	0.451

Table 5.6 Macroscopic Cross-section Data for Neutron Scattering Correction.

NEUTRON ENERGY(MeV)	$R_{scatt.}$	SCATTERING CORRECTION FACTOR.
3.513	0.001031	0.99897
3.810	0.001033	0.99896
4.080	0.001070	0.99893
4.351	0.001104	0.99889
4.590	0.001090	0.99891
4.841	0.001128	0.99887
5.071	0.001196	0.99880
5.300	0.001184	0.99881

Table 5.7 Neutron Scattering Correction Factor.

5.3 On-Line Measurement of Sample Reaction Rates.

The effect of neutron-induced reactions in the silicon of the surface barrier detector must be eliminated from the spectrum obtained from the sample under investigation. The most abundant isotope in natural silicon is ^{28}Si (Table 5.8), producing a background spectrum from $^{28}Si(n,\alpha)^{25}Mg$ and $^{28}Si(n,p)^{28}Al$ reactions.

Isotope	Abundance(%)	Q-value (MeV)	
		(n,p) reaction.	(n,α) reaction.
^{28}Si	92.17	-3.856	-2.655
^{29}Si	4.71	-2.980	-0.036
^{30}Si	3.12	-8.070	-4.213

Table 5.8 Isotopic Abundance and Reaction Q-values of Natural Silicon.

Accurate values of the charged particle energies were calculated from the relativistic kinematic equations for the appropriate reaction (Appendix 3). The $^{29}Si(n,p)^{29}Al$ reaction produces a spectrum in the same energy range but the $^{29}Si(n,\alpha)^{26}Mg$ reaction produces a higher energy spectrum due to its low reaction Q-value. ^{30}Si reactions do not produce an interference spectrum in the neutron energy range 3 to 6 MeV.

In the neutron energy range below 6 MeV, the study of silicon (n,p) and (n,α) reactions is quite difficult

due to the very small cross-section values[4, 84] and the statistical fluctuations in the decay of the excited states of the compound nucleus. A pulse height spectrum from the surface barrier silicon detector is reproduced in Fig. 5.3 and shows charged particle peaks corresponding to the ground and other excited states of ^{26}Mg, ^{25}Mg, ^{29}Al and ^{28}Al nuclei. The level schemes of these product nuclei are also shown. The emitted particle energies are given in Table 5.9.

Reaction	Peak	Particle Energy (MeV)
$^{29}Si(n,\alpha_0)^{26}Mg$	1	5.16
$^{29}Si(n,\alpha_1)^{26}Mg$	2	4.42
$^{28}Si(n,\alpha_0)^{25}Mg$	3	3.75
$^{29}Si(n,p)^{29}Al$	4	3.26
$^{28}Si(n,\alpha_1)^{25}Mg$	5	2.65
$^{28}Si(n,p)^{28}Al$	6	1.21

Table 5. 9 Charged Particle Energy for Silicon Reactions.

The alpha particle energy from $^{29}Si(n,\alpha)^{26}Mg$ reaction (ground state), Fig.5.4, is of particular interest as it is comparable to proton energy from the $^{47}Ti(n,p)^{47}Sc$ and $^{58}Ni(n,p)^{58}Co$ reactions described later. The alpha peak interferes with the proton peaks from ^{47}Ti and ^{58}Ni reactions.

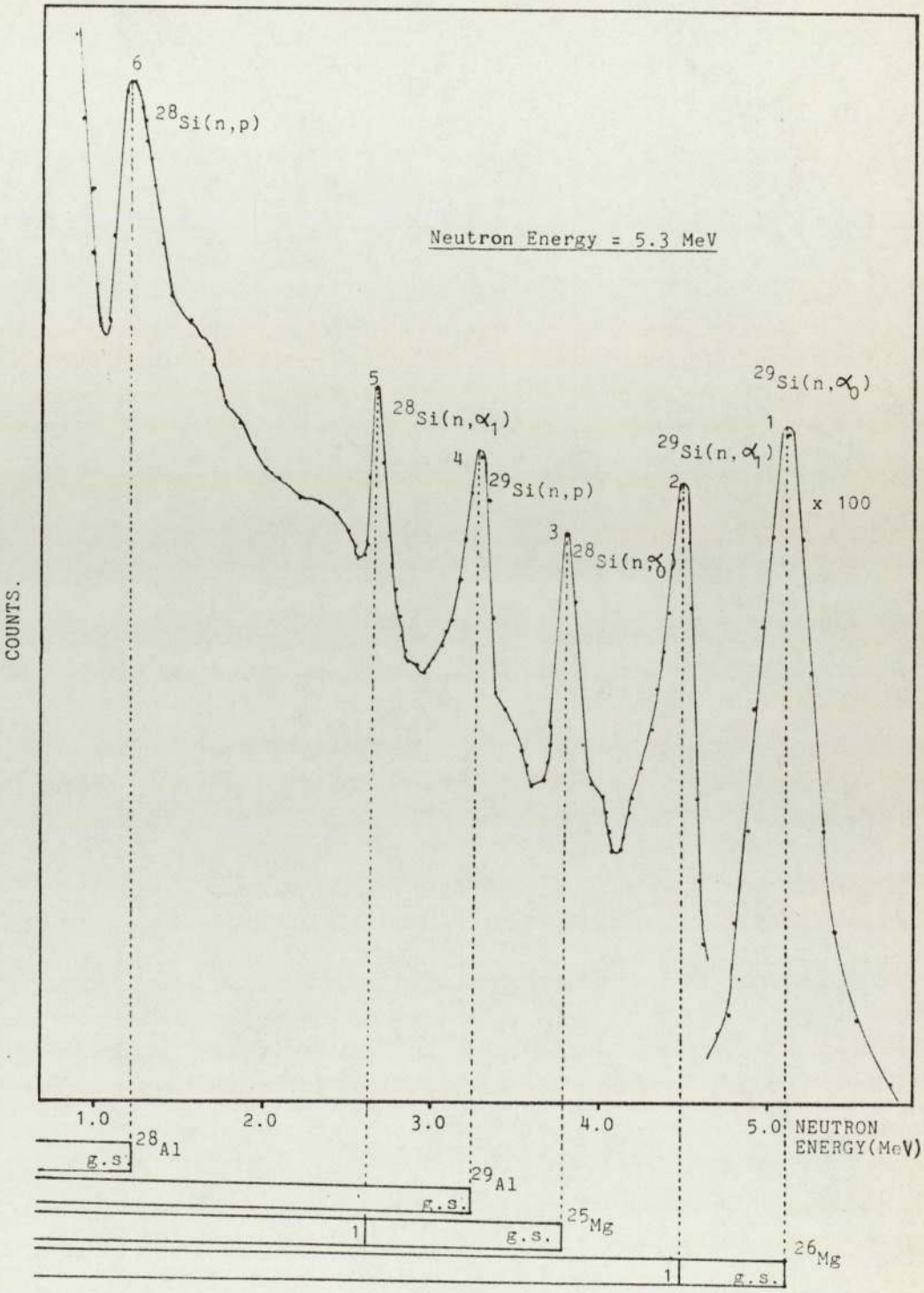

Fig. 5.3 PULSE HEIGHT SPECTRA FROM n+Si REACTIONS.

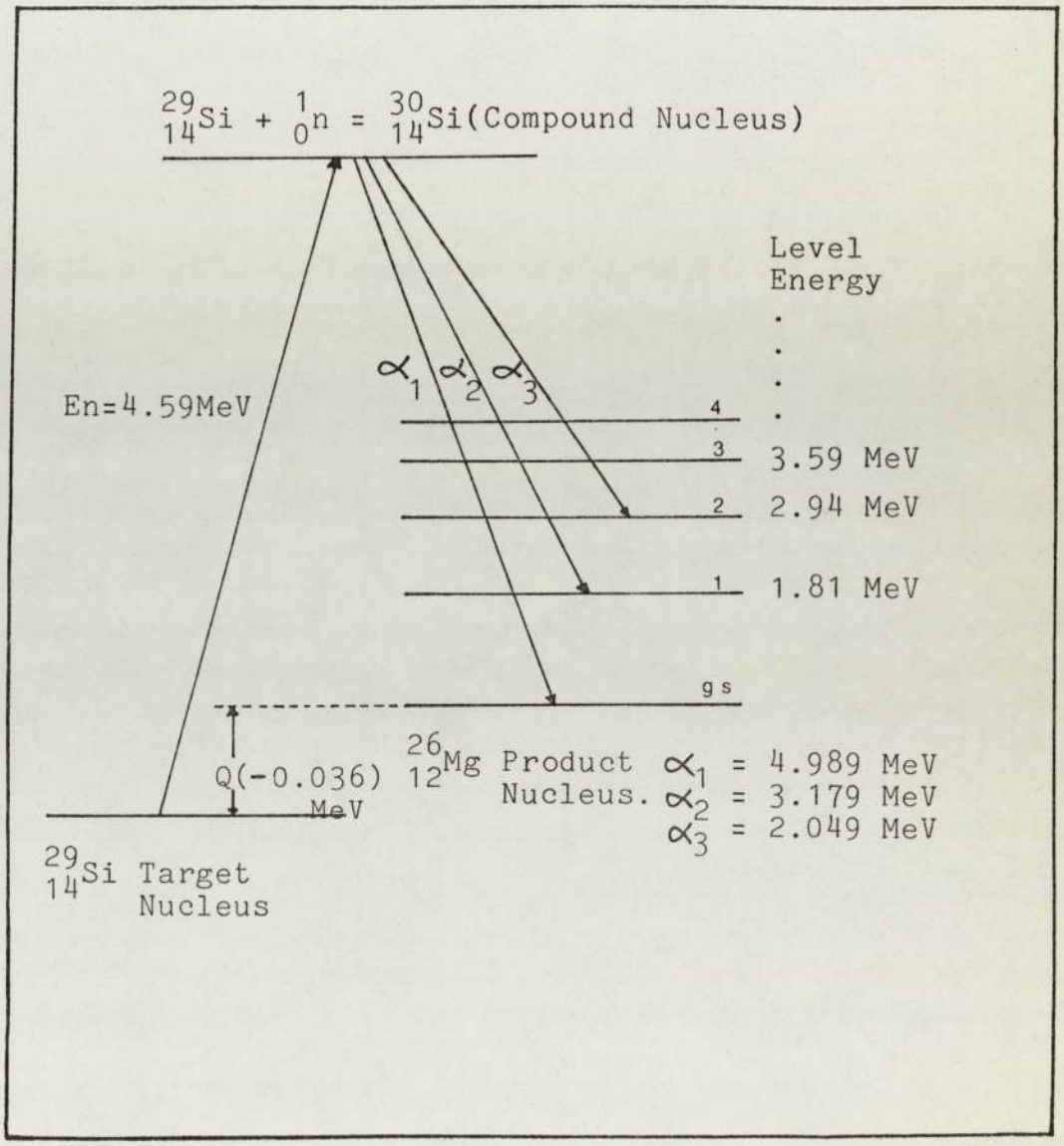

Fig. 5.4 Schematic $^{29}Si(n,\alpha)^{26}Mg$ reaction mode.

5.3.1 Titanium and Nickel Measurements.

The titanium target was a natural titanium foil, 20 μm thick. The elemental analysis of the sample, as supplied by Goodfellow Metals Ltd., is given in Table 5.10.

Element	Content (%)
Titanium	99.9600
Aluminium	0.0030
Iron	0.0015
Nickel	0.0005
Manganese	0.0010
Copper)	
Chromium)	
Carbon)	Traces.
Hydrogen)	
Nitrogen)	

Table 5.10 Elemental Analysis of Natural Titanium.

The impurity elements contribute to the measured spectrum as most of them have (n,p) and (n,α) reaction thresholds between 3 and 6 MeV. An examination of these reactions, due to impurities, revealed that there were no interfering charged particle peaks with those from the titanium (n,p) and (n,α) reactions.

Natural titanium consists of five stable isotopes; Table 5.11, lists their isotopic abundances and the Q-values[94,95] of the (n,p) and (n,α) reactions.

Isotope	Abundance (%)	Q-value (MeV)	
		(n,p)reaction	(n,α)reaction
^{46}Ti	7.930	-1.586	-0.080
^{47}Ti	7.28	+0.183	+2.181
^{48}Ti	73.94	-3.208	-2.032
^{49}Ti	5.51	-1.223	+0.228
^{50}Ti	5.34	-6.100	-3.444

Table 5.11 Isotopic Abundances and Reaction Q-values of Natural Titanium.

The (n,α) reaction Q-values and thresholds give an indication of the possibility of alpha particle emission. No work has been reported for (n,α) reaction cross-sections for the titanium isotopes in the range 3 to 6 MeV[5,6,7,8]. Data is available at 14 MeV for ^{48}Ti and ^{50}Ti isotopes; the cross-section values are 23 mb for ^{48}Ti ^{48}Ti(n,α)^{45}Ca and 10 mb for ^{50}Ti(n,α)^{47}Ca. Hoste[96] has calculated the energies required by an alpha particle to overcome the coulomb barrier and the values are such that no alpha particle emission is possible for titanium at energies below 8 MeV.

$^{50}Ti(n,p)^{50}Sc$ threshold of 6.22 MeV is greater than the neutron energies available in this work. No data is available for the $^{49}Ti(n,p)^{49}Sc$ reaction cross-section between 3 to 6 MeV and no proton peak was observed for this reaction. The reported cross-section for the $^{48}Ti(n,p)^{48}Sc$ reaction is very small[5, 6, 8] in the energy range of these measurements(1.5 mb at 6 MeV). However, despite an isotopic abundance of 73.94%, the low proton energy made the reaction difficult to detect. The remaining two reactions, $^{46}Ti(n,p)^{46}Sc$ and $^{47}(n,p)^{47}Sc$, were studied and their cross-sections measured.

The nickel sample was a 25μm thick foil, with the elemental analysis given in Table 5.12, and supplied by Goodfelllow Metals Ltd.

Element	Content (%)
Nickel	99.960
Manganese	0.0025
Iron	0.0010
Cobalt	0.0020
Copper)	
Chromium)	Traces.
Carbon)	

Table 5.12 Elemental Analysis of Natural Nickel.

The isotopic abundances and the reaction Q-values for Ni(n,p) and Ni(n,α) reactions are given in Table 5.13

Isotope	Abundance(%)	Q-value(MeV)	
		(n,p)reaction	(n,α)reaction
^{58}Ni	67.88	+0.399	+2.888
^{60}Ni	26.23	-2.030	+1.351
^{61}Ni	1.19	-0.507	+3.575
^{62}Ni	3.66	-4.437	-0.429
^{64}Ni	1.08	-7.001	-

Table 5.13 Isotopic Abundances and Reaction Q-values for Natural Nickel.

Due to the high coulomb barrier for alpha particles, the only possible reactions over the neutron energy range 3 to 6 MeV were ^{58}Ni(n,p)^{58}Co, ^{60}Ni(n,p)^{60}Co and ^{61}Ni(n,p)^{61}Co. The reported cross-sections for the ^{60}Ni(n,p) and ^{61}Ni(n,p) reactions have very low values. The ^{61}Ni(n,p)^{61}Co reaction has a cross-section of 3 mb at 4 MeV and the ratio of the (n,p) cross-sections of ^{58}Ni and ^{61}Ni is reported as 60 to 1 by van Loef[97]. However, in this work, only the ^{58}Ni(n,p)^{58}Co cross-section was measured, since the protons from the ^{60}Ni(n,p) and ^{61}Ni(n,p) reactions could not be resolved and their was no peak observed as interfering with the proton peak from the ^{58}Ni(n,p)^{58}Co reaction.

Typical charged particle spectra are presented in Figs. 5.5 to 5.7. The Fig. 5.5 shows the proton peak (curve a) from the $^{46}Ti(n,p)^{46}Sc$ reaction at 4.59 MeV neutron energy. The contribution from silicon reactions is shown in curve b, with no indication of a charged particle peak. The direct subtraction of curve b from curve a produced the resultant spectrum (curve c) for the $^{46}Ti(n,p)^{46}Sc$ reaction. Fig. 5.6 is a similar presentation for the $^{47}Ti(n,p)^{47}Sc$ reaction, but with background peak due to the $^{29}Si(n,\alpha)^{26}Mg$ reaction. The spectrum for the $^{58}Ni(n,p)^{58}Co$ reaction is shown in Fig. 5.7. The proton peak from $^{58}Ni(n,p)^{58}Co$ reaction has a broad appearance. The compound nucleus is highly excited and the peak contains protons from transitions to the ground state and low lying excited states of ^{58}Co. These states are very closely spaced(Fig. 5.8) and the emitted protons form a close energy grouping.

The $^{46}Ti(n,p)^{46}Sc$ reaction peak (Fig.5.5) also contains protons emitted from transitions to the ground state and first two excited states of ^{46}Sc. Due to very small difference in level energies, the emitted protons have energies differing only slightly.(Fig.5.9)

The proton peak from $^{47}Ti(n,p)^{47}Sc$ reaction is a single peak resulting only from the transition to the ground state of ^{47}Sc. Protons, from transitions to the excited states form separate peaks due to significant

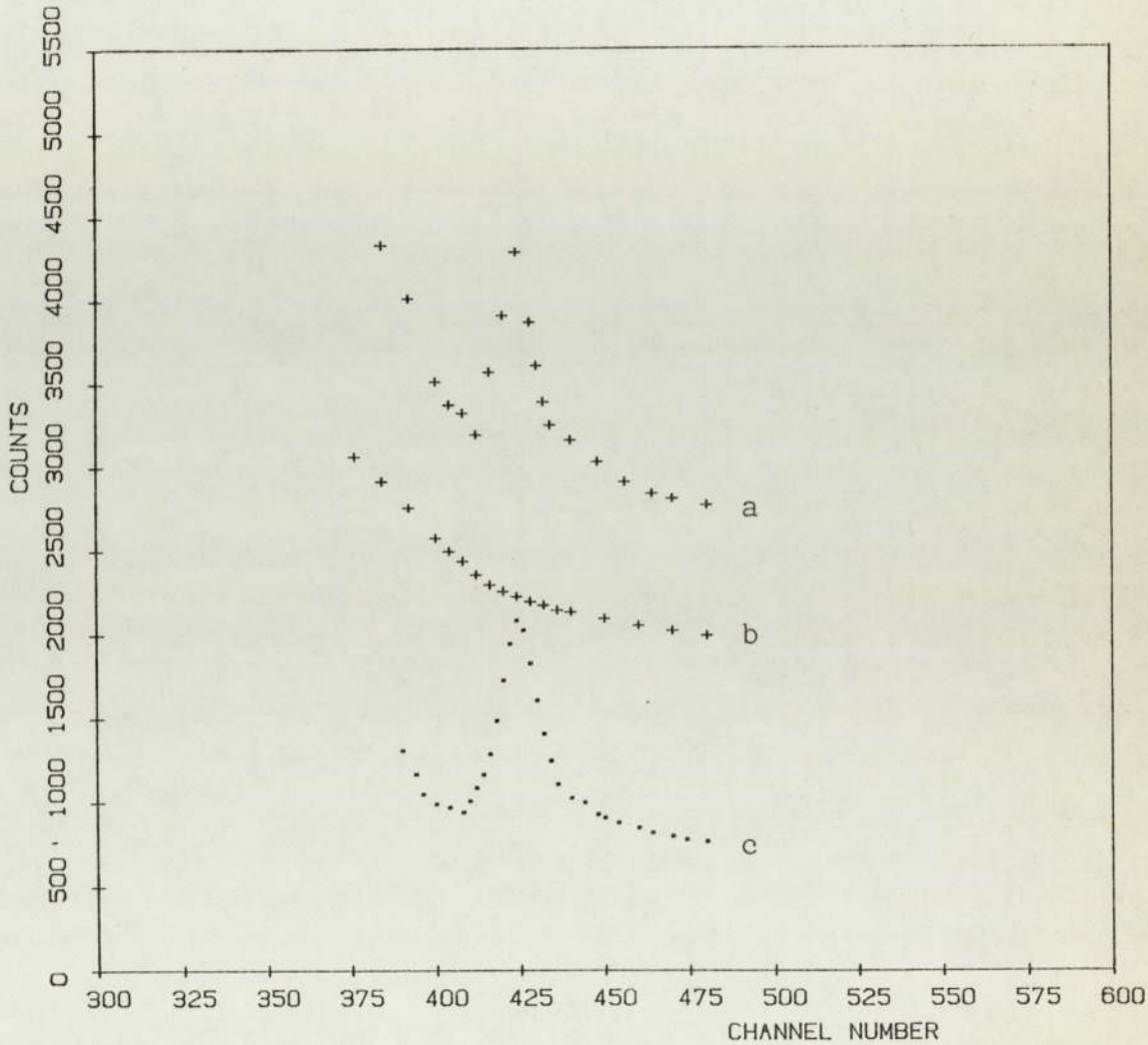

Fig. 5.5 Proton spectrum from $^{46}Ti(n,p)^{46}Sc$ reaction. (a) with sample (b) without sample and (c) the resultant.

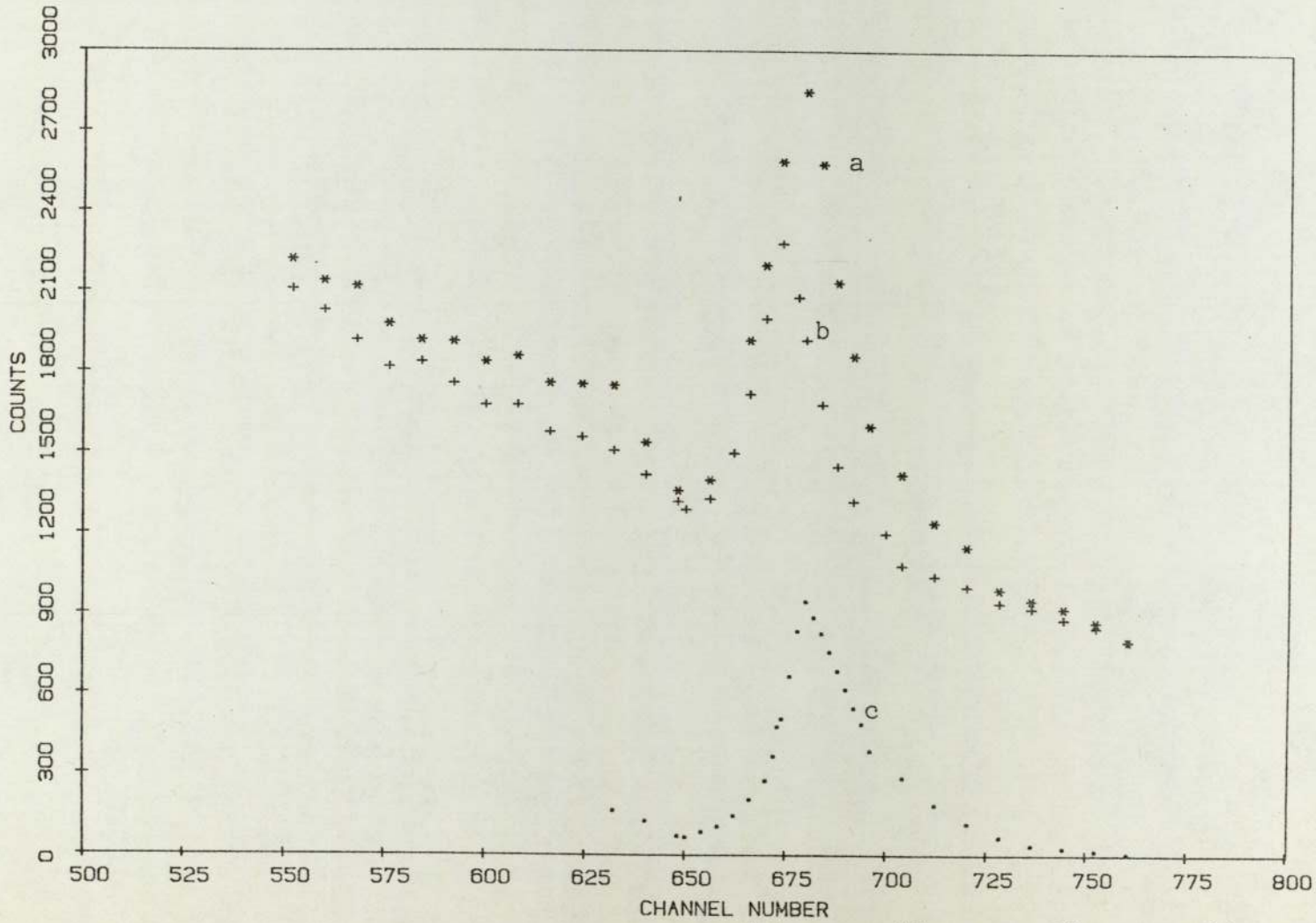

Fig. 5.6 Charged particle spectra from $^{47}Ti(n,p)^{47}Sc$ and $^{29}Si(n,\alpha)^{26}Mg$ reactions.

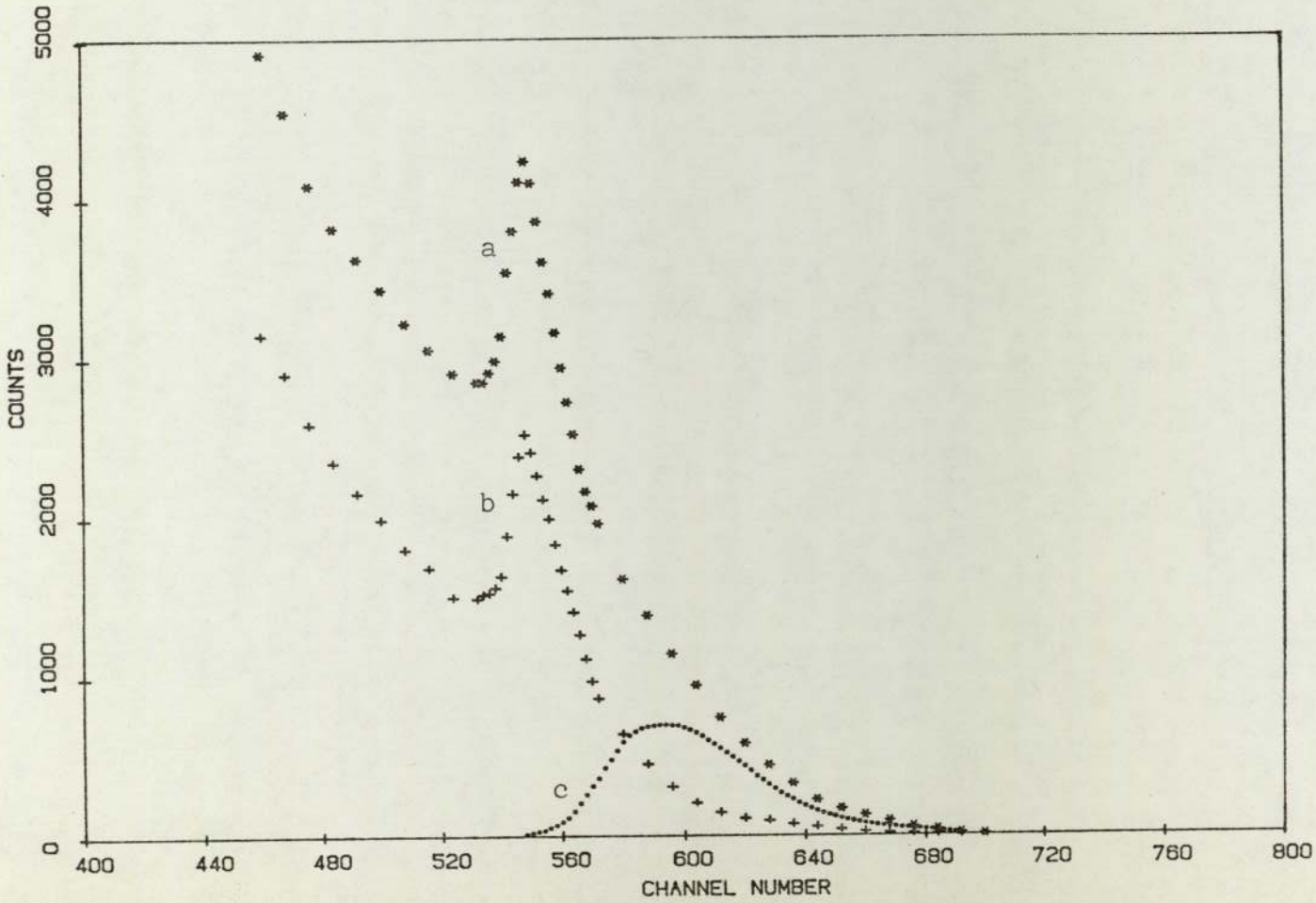

Fig. 5.7 Proton spectrum (curve c) from $^{58}Ni(n,p)^{58}Co$ reaction.

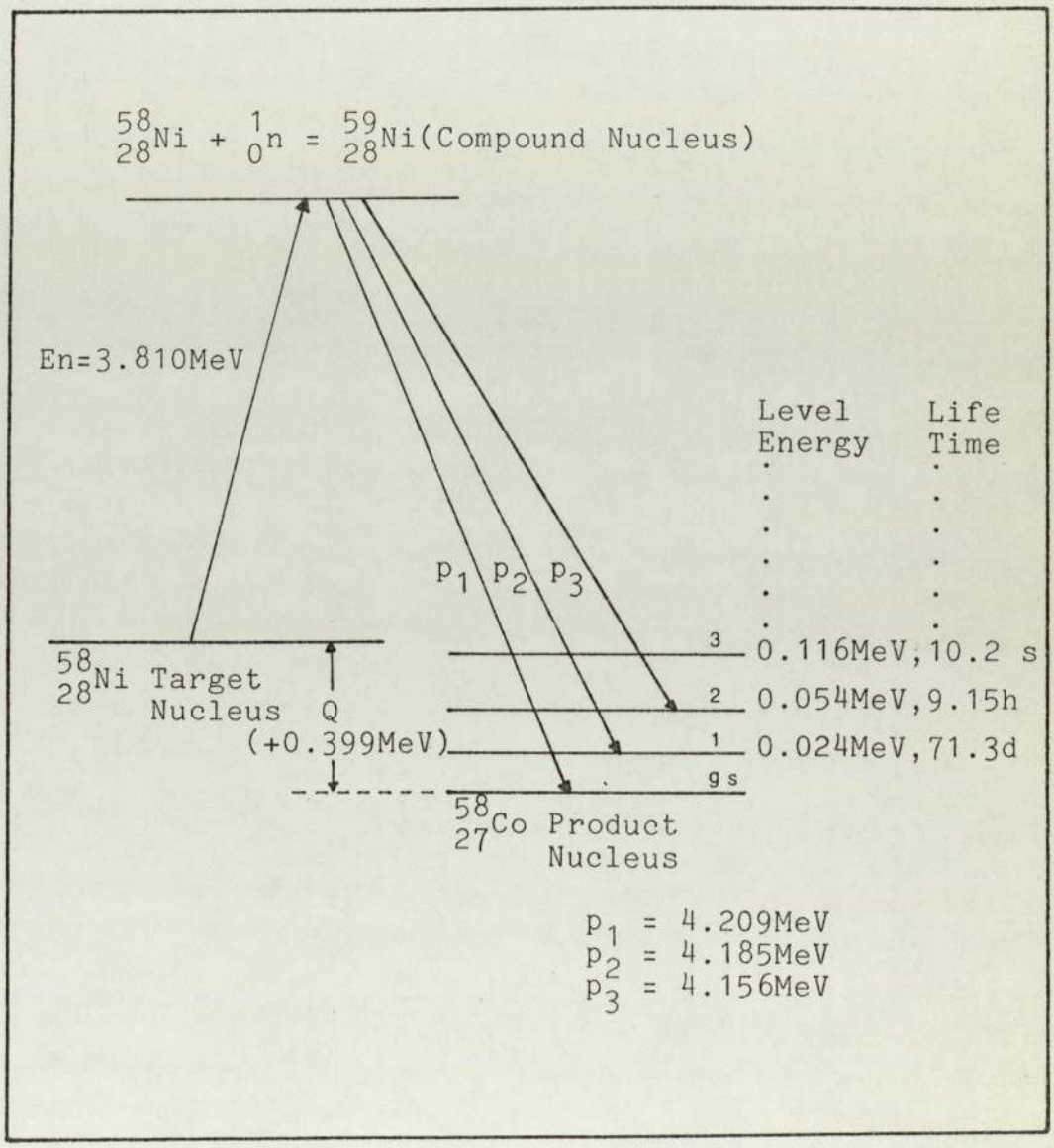

Fig. 5.8 Schematic $^{58}Ni(n,p)^{58}Co$ reaction mode.

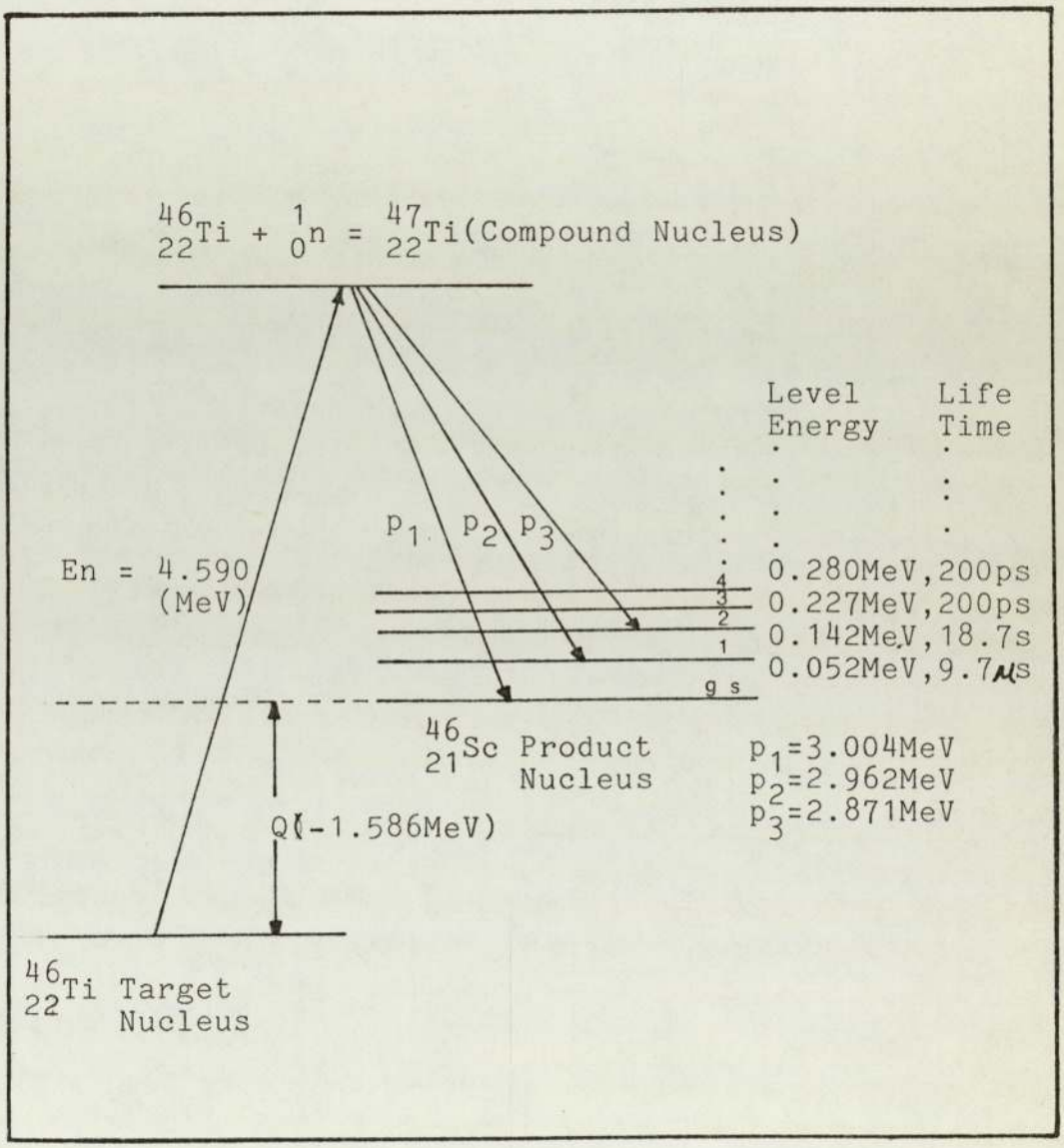

Fig. 5.9 Schematic $^{47}Ti(n,p)^{46}Sc$ reaction mode.

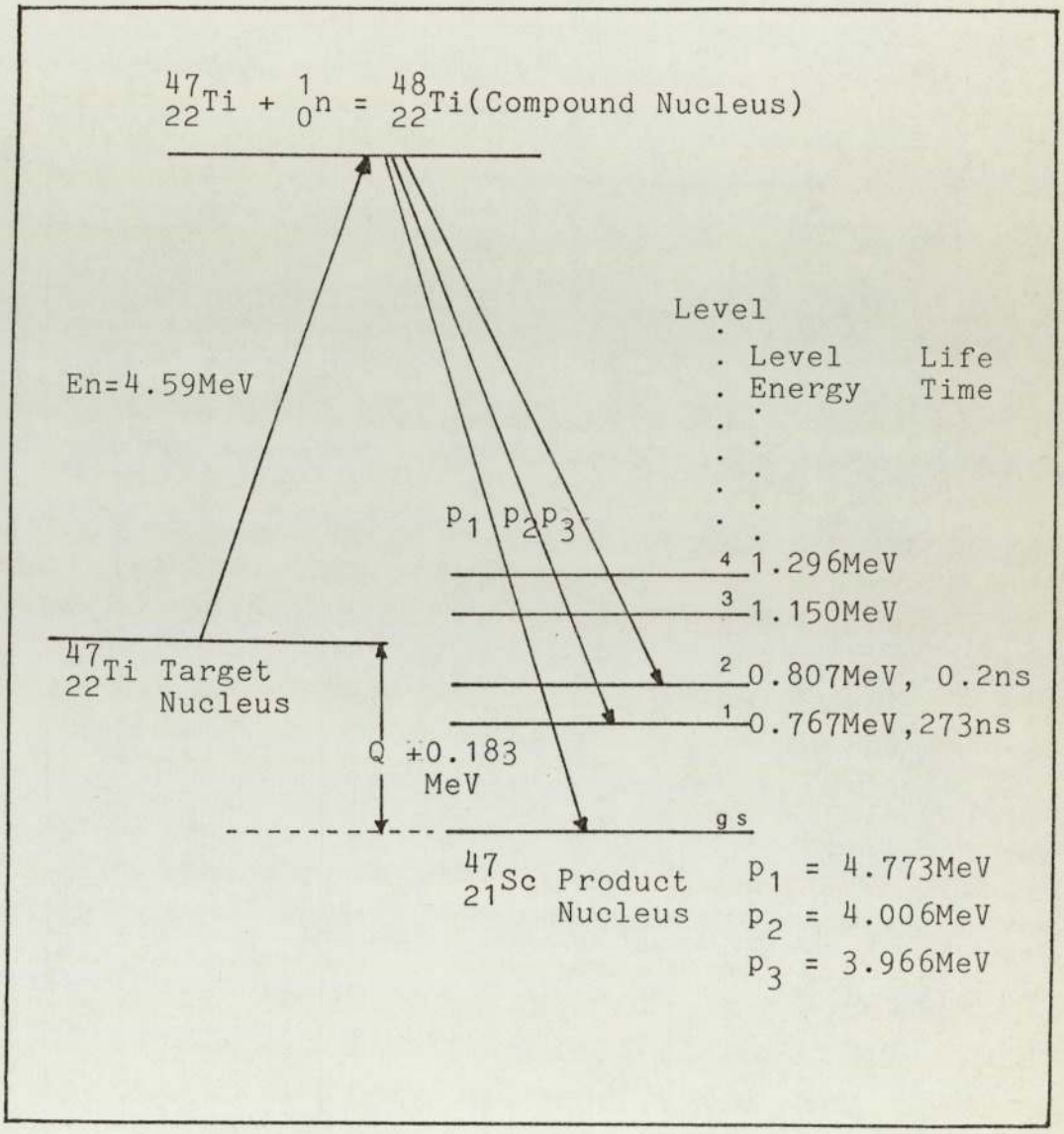

Fig. 5.10 Schematic $^{47}Ti(n,p)^{47}Sc$ reaction mode.

energy differences (Fig. 5.10). From the schematic reaction modes given in Figs. 5.8 to 5.10, it is evident that in the cases of $^{58}Ni(n,p)^{58}Co$ and $^{46}Ti(n,p)^{46}Sc$ reactions the proton emission from transitions to low lying states of ^{58}Co and ^{46}Sc is more favoured, compared to transitions to their ground states. For the $^{47}Ti(n,p)^{47}Sc$ reaction it is the opposite, in which the proton emission from transition to ground state has a priority.

5.3.2 Peak Area Analysis.

An analysis of the total-absorption peak determines the energy deposited by the radiation and the number of neutron interactions in the sample. Where there are no complications such as closely spaced or overlapping peaks, the peak area can be calculated from summation of digital data with linear interpolation between the continuum values on either or one side of the peak. The peak area is given;[98]

$$\text{Peak area} = \sum_{i=A}^{B} C_i - (B-A)\frac{C_A + C_B}{2} \quad .....(5.6)$$

where A,B are limit points and C_A, C_B are counts at these points. However, this approach is unlikely to provide sufficient accuracy.

A calculation of Gaussian parameters of the peak can be performed by an iterative non-linear least-squares

method. The least-square fitting is made by minimising the weighted sum of the squares:-

$$\chi^2 = \sum_{i=1}^{N} W_i \left[Y_i - y(x_i) \right]^2 \quad \ldots\ldots\ldots\ldots\ldots(5.7)$$

where Y_i are the measured values at channel x_i; W_i are the weights associated with Y_i ; $y(x_i)$ are the predicted values from the function used to fit and N is the number of channels.

In a non-iterative procedure[99], the pulse height distribution around the peak channel is represented by a Gaussian function:-

$$Y(x) = Y_0 \exp\left[-\frac{1}{2\sigma^2} (x - x_0)^2 \right] \quad \ldots\ldots\ldots(5.8)$$

where, Y_0 is the peak height.

x_0 is the peak position.

and σ , the standard deviation.

Simple non-iterative methods have been suggested[99, 100] in which application of equation 5.8. is made. The area under the peak is calculated from:-

$$A = (2\pi)^{\frac{1}{2}} \sigma y_0 \quad \ldots\ldots\ldots\ldots\ldots(5.9)$$

In the full-energy peak area analysis for the $^{46}Ti(n,p)^{46}Sc$ and $^{29}Si(n,\alpha)^{26}Mg$ reactions, a computer program was employed (Appendix 4), coded 'PROGRAM NEIB' [101]

The program fits a Gaussian function to a specified number of channels. Figs. 5.11 and 5.12 demonstrate the Gaussian fit to the experimental data for $^{46}Ti(n,p)^{46}Sc$ and $^{29}Si(n,\alpha)^{26}Mg$ reactions.

The peak analysis for $^{47}Ti(n,p)^{47}Sc$ reaction required a different fitting program as the peak showed a marked deviation from a Gaussian curve on the high energy side. A non-linear least squares fitting program, 'PROGRAM CBJJ4 FIT'[101] (Appendix 5), was employed. This program will fit more than one Gaussian to a curve, if required, up to the necessary number of parameters in any functional form to the required number of data points. The proton peak for the $^{47}Ti(n,p)^{47}Sc$ reaction required two Gaussians with 6 parameters to produce the best fit to the experimental data points. (Fig. 5.13). The proton peak from the $^{58}Ni(n,p)^{58}Co$ reaction required three Gaussians with 9 parameters to fit about 150 data points. Fig. 5.14 shows the adequacy of this method, in which the peak fit for the $^{58}Ni(n,p)^{58}Co$ reaction is depicted.

5.3.3 Calculation of Reaction Rates.

The reaction rate, R , was determined from the relationship;

$$R = \frac{\text{Charged particle peak area}}{G(\mathcal{E})}$$

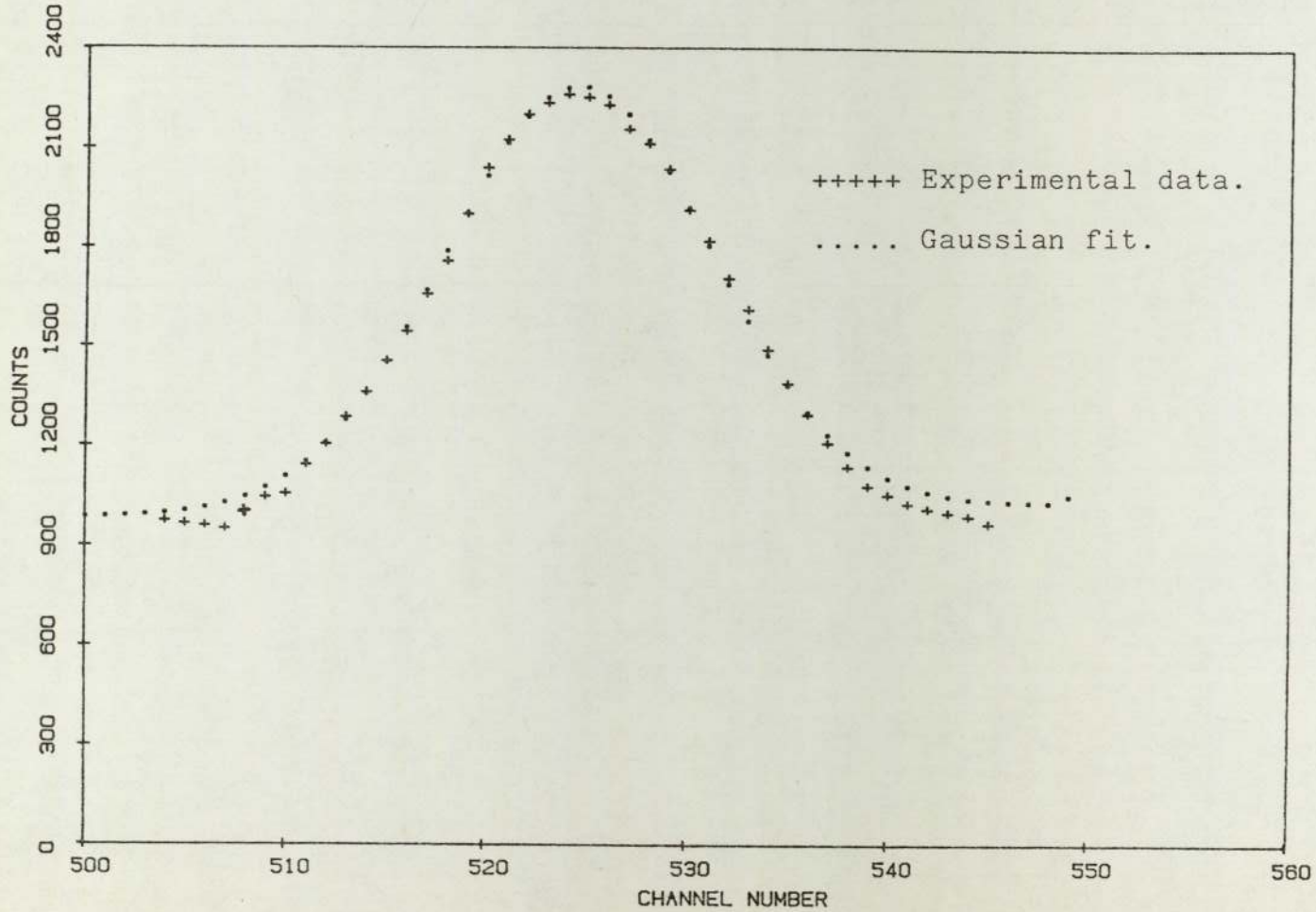

Fig. 5.11 The Gaussian fit to the proton peak from $^{46}Ti(n,p)^{46}Sc$ reaction.

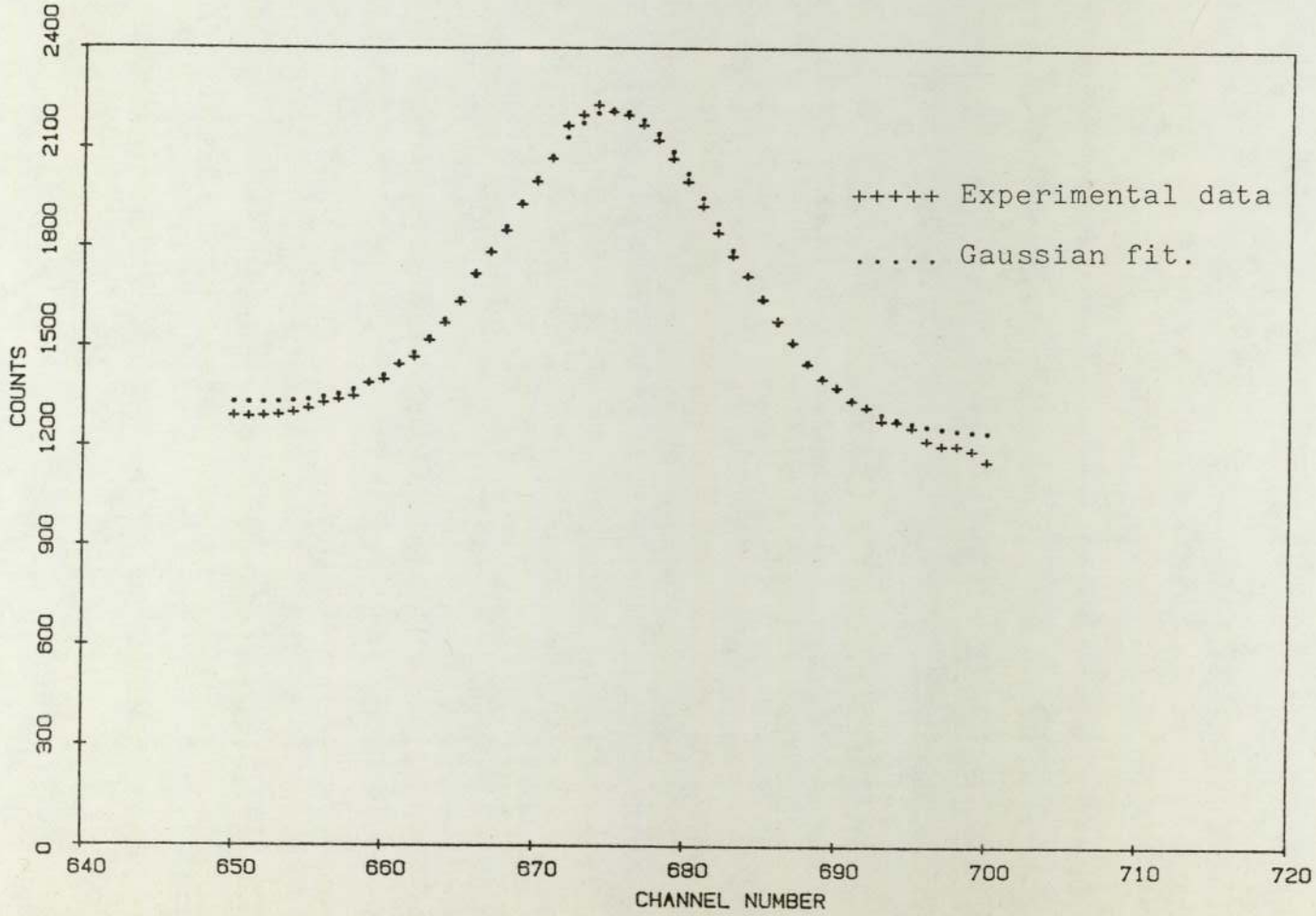

Fig. 5.12 The Gaussian fit to the alpha peak from $^{29}Si(n,\alpha)^{26}Mg$ reaction.

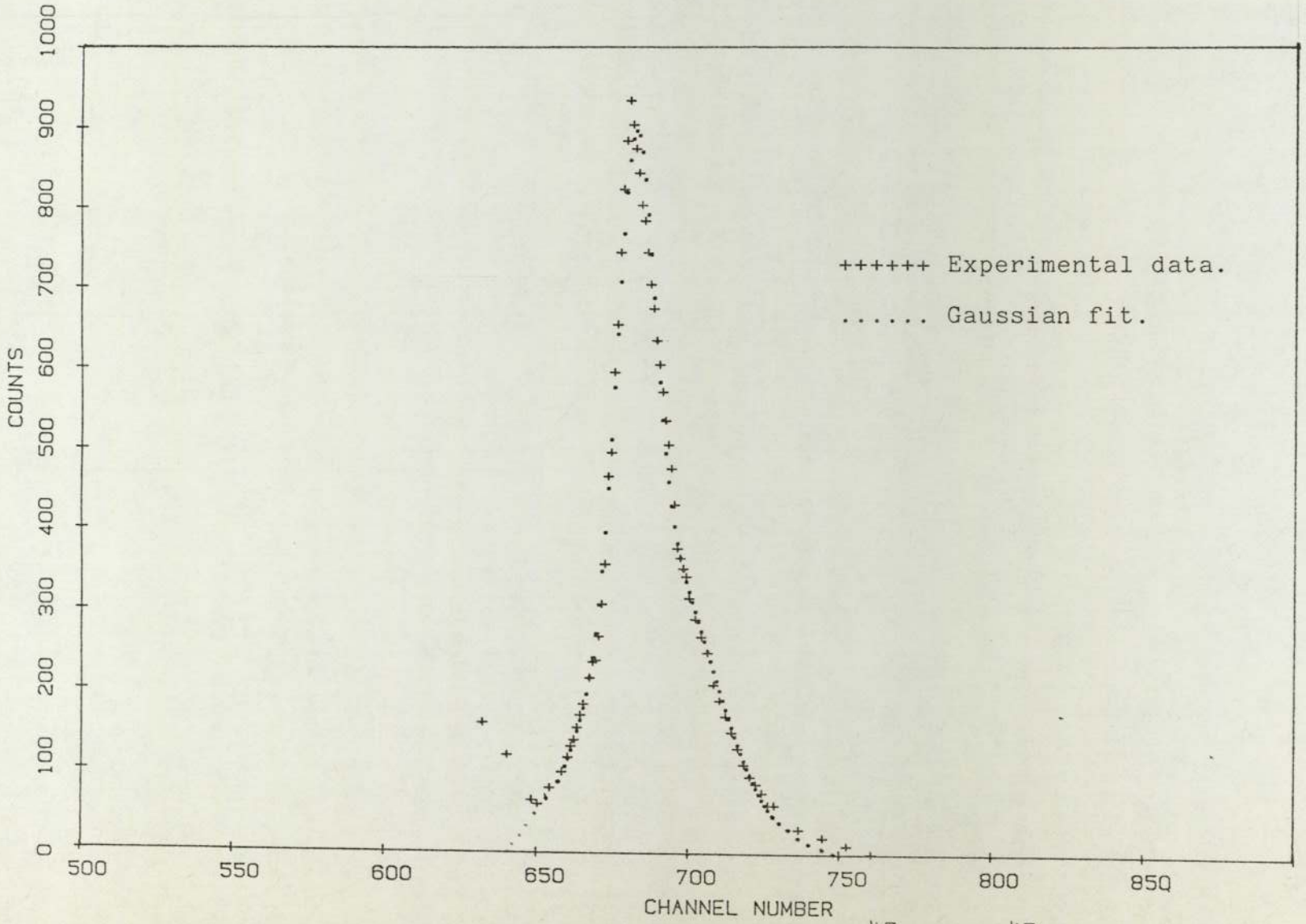

Fig. 5.13 The Gaussian fit to the proton peak from $^{47}Ti(n,p)^{47}Sc$ reaction.

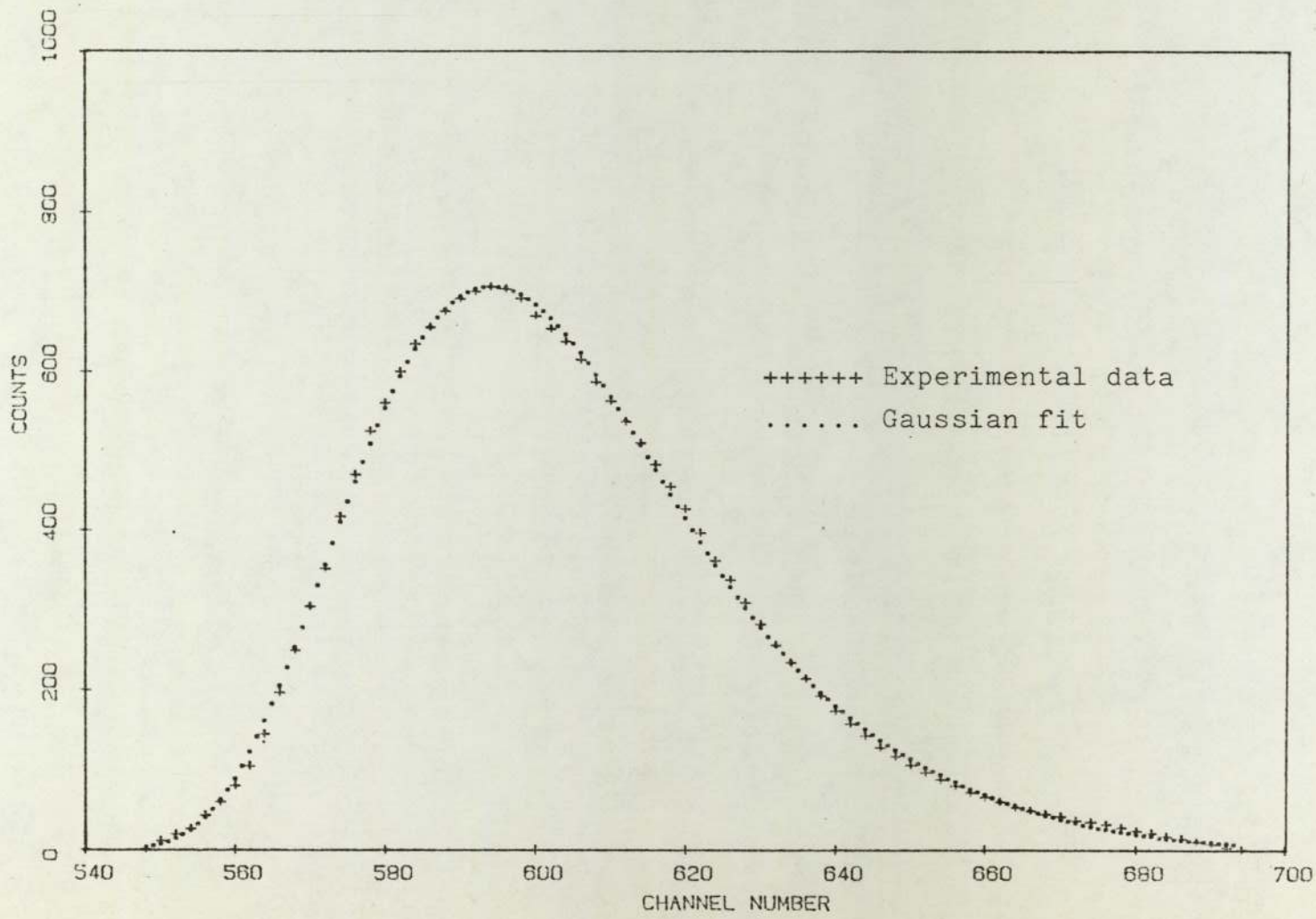

Fig. 5.14 The Gaussian fit to the proton peak from $^{58}Ni(n,p)^{58}Co$ reaction.

where, $G(\mathcal{E})$ is the 'geometric' detection efficiency of the surface barrier detector given in equation 4.16. For the experimental detector to source configuration (described in chapter 4), $G(\mathcal{E})$ had a value 0.206.

Corrections were applied for:-

(a) the neutron flux attenuation and neutron scattering in the chamber gold window (between sample and neutron source).

(b) the proton absorption in the titanium and nickel samples.

(c) charged particle energy loss in the dead layer of the surface barrier detector.

The neutron flux attenuation in gold window was calculated from the equation:

$$\phi = \phi_o \, e^{-\Sigma_T \cdot t_g}$$

where, ϕ is the neutron flux after attenuation.

ϕ_0, the incident neutron flux on the window.

Σ_T, the total macroscopic cross-section for gold.

t_g, the thickness of gold window (100 μm)

The neutron attenuation correction factors for different energies are listed in Table 5.14

The correction for reaction rate counts in the sample produced by neutrons scattered from the gold window was determined by calculations similar to those made for the fission counts. Equation 5.5 was modified to

NEUTRON ENERGY (MeV)	CORRECTION FACTOR
3.513	0.99985
3.810	0.99983
4.080	0.99973
4.351	0.99969
4.590	0.99961
4.841	0.99958
5.071	0.99964
5.300	0.99967

Table 5.14 Neutron Flux Attenuation in Gold Window.

$$R_{scatt.} = \frac{\Sigma_{SG}}{\Sigma_{TG}} \exp(\Sigma_{TG} t_g) \left[1 - \exp(-\Sigma_{TG} t_g)\right] . \langle 1-\exp(-\Sigma_{TG} \cdot \Delta_S) \rangle$$

where, Σ_{SG}, Σ_{TG} are macroscopic elastic scattering and total macroscopic cross-sections for gold foil of thickness t_g. Δ_S is the neutron path of scattered neutrons in the sample foil. The scattering correction factor was obtained from:

$$\text{Correction Factor} = \frac{1}{1 + R_{scatt.}}$$

Over the energy range 3 to 6 MeV this correction factor had a value of 0.99996.

The possibility of a correction factor for proton absorption in the titanium and nickel samples was also considered.

The geometric detection efficiency , G ($\mathcal{E}$), of the surface barrier detector was determined in section 4.2.2 and following from equation 4.16 (p.139) the reaction rate, R, for the protons emitted into the 4π-geometry was measured.

The geometric configuration for sample to detector is, once again, depicted in Fig. 5.15. The geometric detection efficiency accounts only for the solid angle subtended by the detector on sample. Some protons may be absorbed in the

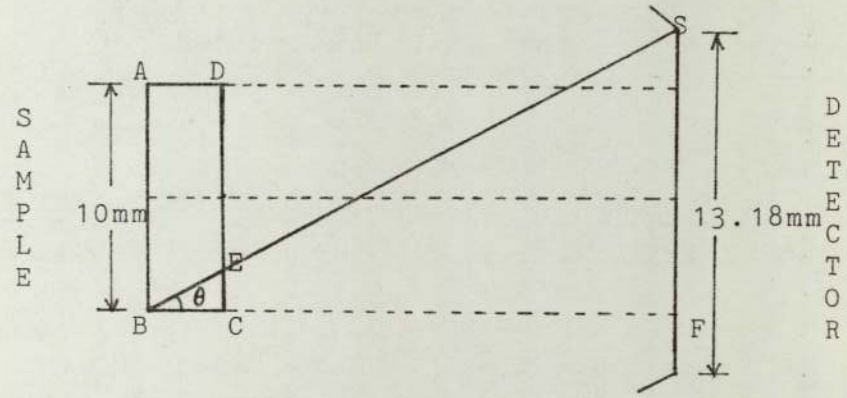

C F = 8.13 mm

B C = 20 μm (titanium)

= 25 μm (nickel)

B E = 35.4 μm (titanium)

= 44.25 μm(nickel)

Fig. 5.15 SAMPLE TO DETECTOR CONFIGURATION.

sample. The path length of protons travelling towards the detector, varies from zero to a maximum of length BE, as shown in Fig. 5.15. This length is equal to 35.4 μm for the titanium sample and 44.25 μm for the nickel sample.

In this work, protons of energy 2 MeV to 6 MeV are emitted from the $^{46,47}Ti(n,p)^{46,47}Sc$ reactions and from the $^{58}Ni(n,p)^{58}Co$ reaction, the proton energy range is from 3.9 MeV to 4.75 MeV. The proton range in titanium varies from 36.6 μm for 2 MeV to 227 μm for 6 MeV protons. For nickel, the proton range varies from 60.6 μm for 3.9 MeV to 81.65 μm for 4.75 MeV. This suggests that all the protons emitted into the solid angle subtended by the detector have a range greater than the sample thicknesses and that there is no correction required for the the absorption of protons in the samples. However, the proton energy loss in the sample will contribute to a broadening of the proton energy peak measured by the detector.

When heavy charged particles are detected with a surface barrier detector, some energy is lost in the window of the detector. The dead layer thickness of the detector used was 40 μg cm^{-2} of gold, which is equivalent to 155nm of silicon thickness. A thickness of 100nm of silicon equivalent corresponds to an energy loss of 4keV for 1MeV protons and 14keV for 5MeV alpha particles.[102] These data were applied to determine an energy loss correction factor for all charged particles. The value varied from 0.6% for 1MeV protons to 0.1% for 6MeV protons. For alpha particles the correction factor varied from 0.28% at 1MeV to 0.16% at 6 MeV.

CHAPTER 6

EVALUATION OF (n, p) AND (n, α) CROSS-SECTIONS

6.0 Evaluation of (n,p) and (n,α) Cross-sections.

The (n,p) and (n,α) reaction rate, R $[s^{-1}]$, can be related to the reaction cross-section and the neutron flux as:

$$R = \sigma . \phi_n . A . t_S n. \qquad \text{.....(6.1)}$$

where, σ is the microscopic (n,p) or (n,α) reaction cross-section,(cm^2).

ϕ_n is the neutron flux in neutrons $cm^{-2}s^{-1}$.

A is the area of the target sample, exposed to the incident flux, in cm^2.

t_S is the sample thickness in cm.

and n is the number of nuclei per unit volume.

The equation (6.1) is for a parallel neutron beam, free from attenuation by the target nuclei and the self-shielding of these nuclei is assumed to be negligible. This equation can also be written as;

$$R = \sigma . \phi_n . N \qquad \text{.....(6.2)}$$

where, N = $(A.t_S.n)$and becomes the number of nuclei in the exposed sample. The values for N for the samples studied, are listed in Table 6.1.

The reaction rate can also be written in terms of the macroscopic cross-section Σ ,

$$R = \Sigma \phi_n \qquad \text{.....(6.3)}$$

since, $\Sigma = N \sigma$

SAMPLE	NUMBER OF NUCLEI
^{46}Ti	7.11×10^{18}
^{47}Ti	6.53×10^{18}
^{58}Ti	1.22×10^{20}
^{29}Si	1.04×10^{20}

Table 6.1 Number of nuclei in samples.

The attenuation of the neutron flux across the sample, thickness t_S , is expressed as :

$$\phi = \phi_o \exp (- \Sigma_T . t_S) \quad .....(6.4)$$

in which Σ_T, the total macroscopic cross-section.

and ϕ_o, the neutron flux incident upon sample.

The reaction rate, for a parallel neutron beam, is written as:

$$R = \frac{\Sigma}{\Sigma_T} \phi_o \left[1 - \exp (-\Sigma_T . t_S) \right] .....(6.5)$$

To simulate the sample irradiation conditions through the program 'NPROFILE' (Appendix 2), the reaction rate can be expressed by the equation;

$$R = \frac{\Sigma}{\Sigma_T} \phi_o \left[1 - \langle \exp (- \Sigma_T . \delta) \rangle \right] \quad ....(6.6)$$

where the weighting factor ,

$$\langle \exp(-\Sigma_T . \delta) \rangle = \frac{1}{N_{hist.}} \sum_{i=1}^{N_{hist.}} \exp(-\Sigma_T \delta_i)$$

where, δ_i represents the neutron path length in the sample which is determined by;

$$\left[\frac{\text{Sample thickness}}{\cos \phi} \right]$$

ϕ is the angle between the neutron path and the direction of the incident deuteron beam. $N_{hist.}$ gives the number of neutron paths in the sample.

Similarly, the neutron flux attenuation can be simulated through the equation;

$$\phi_n = \phi_o N_F . \langle \exp(-\Sigma_{TP} . \delta_P) \rangle \quad .....(6.7)$$

and in this case, the weighting factor is for the attenuation of the neutron flux by the platinum backing of the uranium deposit.

N_F is the number of successful trials in the uranium deposit.

Σ_{TP} is the total macroscopic cross-section of the platinum backing.

and δ_P, the neutron path lengths in the platinum backing.

From equations (6.6) and (6.7),

$$\frac{R}{\phi_n} = \frac{\Sigma}{\Sigma_T N_F} . \frac{\left[1 - \langle \exp(-\Sigma_T \delta) \rangle \right]}{\langle \exp(-\Sigma_{TP} . \delta_P) \rangle}$$

From which,

$$\sigma = \frac{R}{N\,\phi_n}\,(\Sigma_T . N_F)\left[\frac{\langle \exp(-\Sigma_{TP}.\delta_P)\rangle}{\{1-\langle \exp(-\Sigma_T\,\delta)\rangle\}}\right] \qquad \ldots\ldots\ldots\ldots(6.8)$$

The'weighting'terms were determined using the program 'NPROFILE'.

ϕ_n was calculated from equation(5.1) using the fission counter, as described in Chapter 3. The reaction rate , R , was calculated as described in the previous Chapter.

6.1 The Measured Cross-sections.

The measured cross-sections for the $^{46}Ti(n,p)^{46}Sc$, $^{47}Ti(n,p)^{47}Sc$, $^{58}Ni(n,p)^{58}Co$ and $^{29}Si(n,\alpha)^{26}Mg$ reactions are given in Tables 6.2 to 6.5. The reported data of other workers, measured in the same neutron energy range of 3.5 MeV to 5.5 MeV, is compared for each reaction in Figs. 6.1 to 6.4.

$^{46}Ti(n,p)^{46}Sc$ reaction.

The measured $^{46}Ti(n,p)^{46}Sc$ cross-sections show general agreement with the recent data of Jalil[6] and Smith et.al.[5] (Fig. 6.2). Another recent measurement by Lu-Han Lin[10], at 4.8 MeV is also in

NEUTRON ENERGY (MeV)	NEUTRON ENERGY RESOLUTION. (keV)	CROSS-SECTION (mb)
3.513	161	12.11 ± 0.78
3.810	155	22.87 ± 1.49
4.080	148	39.34 ± 2.56
4.351	136	38.41 ± 2.49
4.590	126	48.63 ± 3.16
4.840	120	63.79 ± 4.15
5.071	120	67.47 ± 4.38
5.300	120	81.21 ± 5.28

Table 6.2 Measured $^{46}Ti(n,p)^{46}Sc$ Cross-sections.

NEUTRON ENERGY (MeV)	NEUTRON ENERGY RESOLUTION (keV)	CROSS-SECTION (mb)
3.513	161	54.30 ± 3.26
3.810	155	61.70 ± 3.70
4.080	148	69.40 ± 4.16
4.351	136	73.50 ± 4.41
4.590	126	76.60 ± 4.59
4.841	120	86.30 ± 5.18
5.071	120	81.70 ± 4.90
5.300	120	79.80 ± 4.73

Table 6.3 Measured $^{47}Ti(n,p)^{47}Sc$ Cross-sections.

NEUTRON ENERGY (MeV)	NEUTRON ENERGY RESOLUTION (keV)	CROSS-SECTION (mb)
3.513	161	266 ± 15.96
3.810	155	323 ± 19.38
4.080	148	391 ± 23.46
4.351	136	417 ± 25.02

Table 6.4 Measured $^{58}Ni(n,p)^{58}Co$ Cross-sections.

NEUTRON ENERGY (MeV)	NEUTRON ENERGY RESOLUTION (keV)	CROSS-SECTION (mb)
3.513	161	3.61 ± 0.32
3.810	155	2.59 ± 0.23
4.080	148	1.75 ± 0.15
4.351	136	2.52 ± 0.23
4.590	126	4.39 ± 0.39
4.841	120	3.40 ± 0.31
5.071	120	2.42 ± 0.22
5.300	120	4.83 ± 0.43

Table 6.5 Measured $^{29}Si(n,\alpha)^{26}Mg$ Cross-sections.

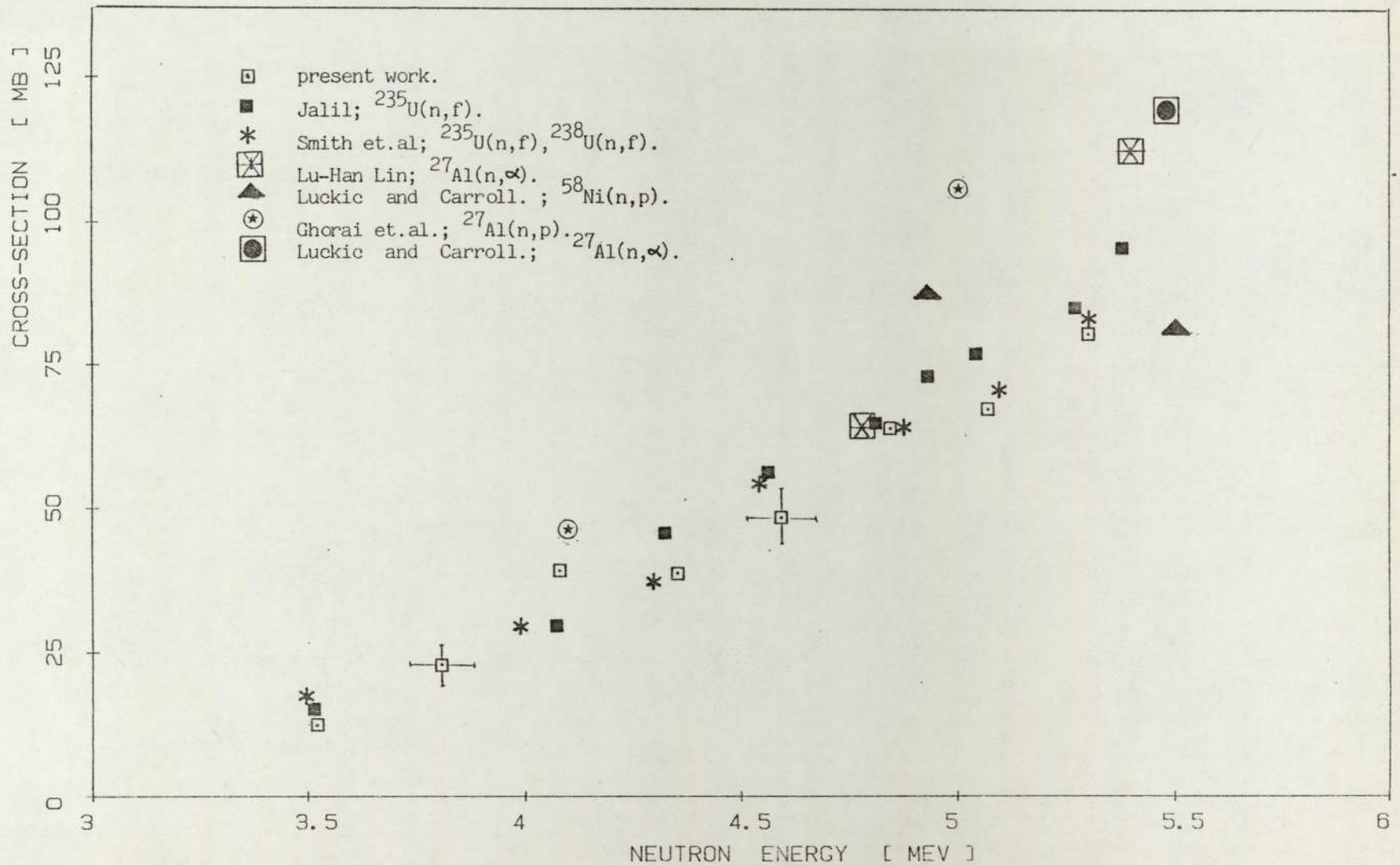

Fig. 6.1 The $^{46}Ti(n,p)^{46}Sc$ Cross-sections.

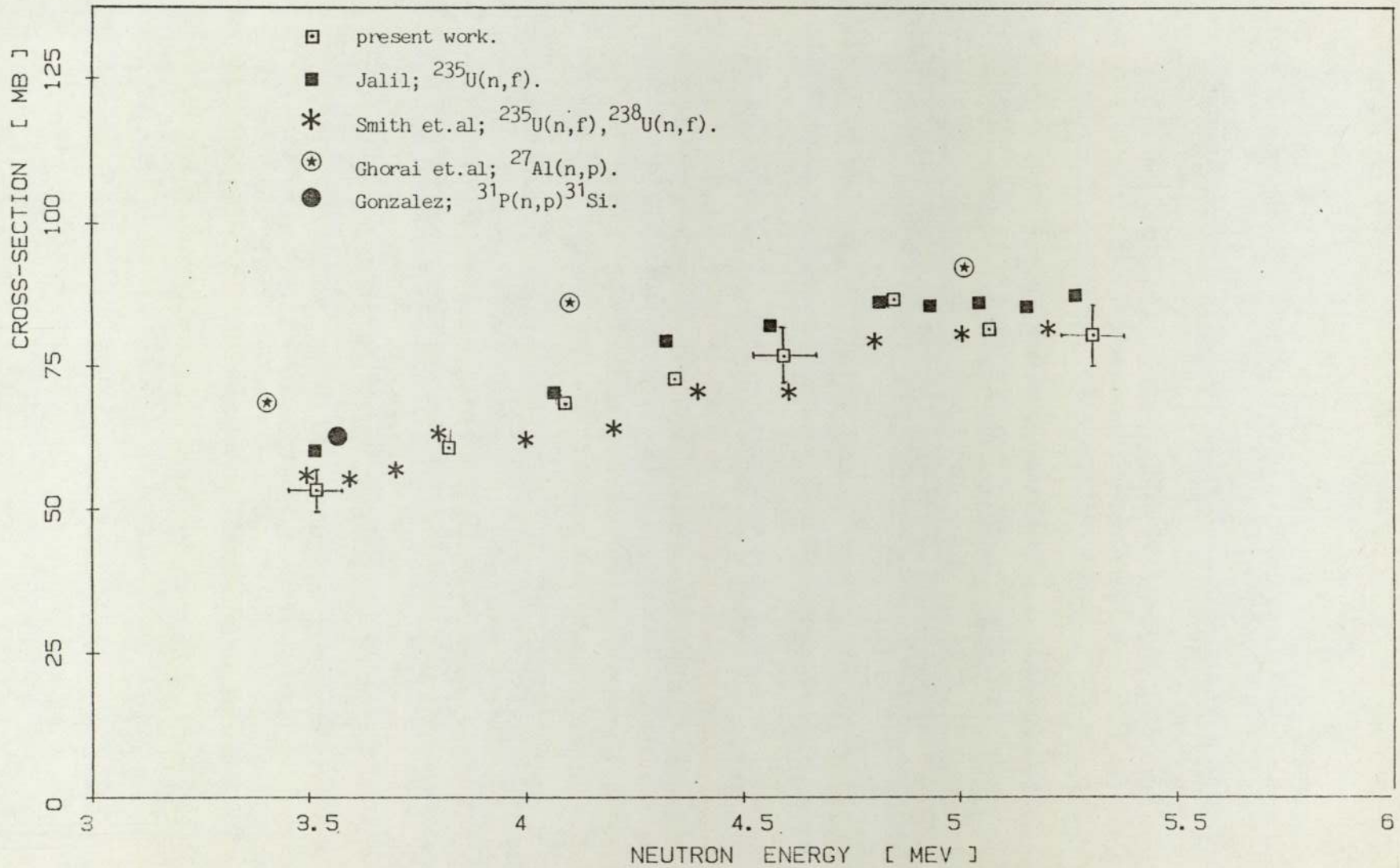

Fig. 6.2 The $^{47}Ti(n,p)^{47}Sc$ Cross-sections.

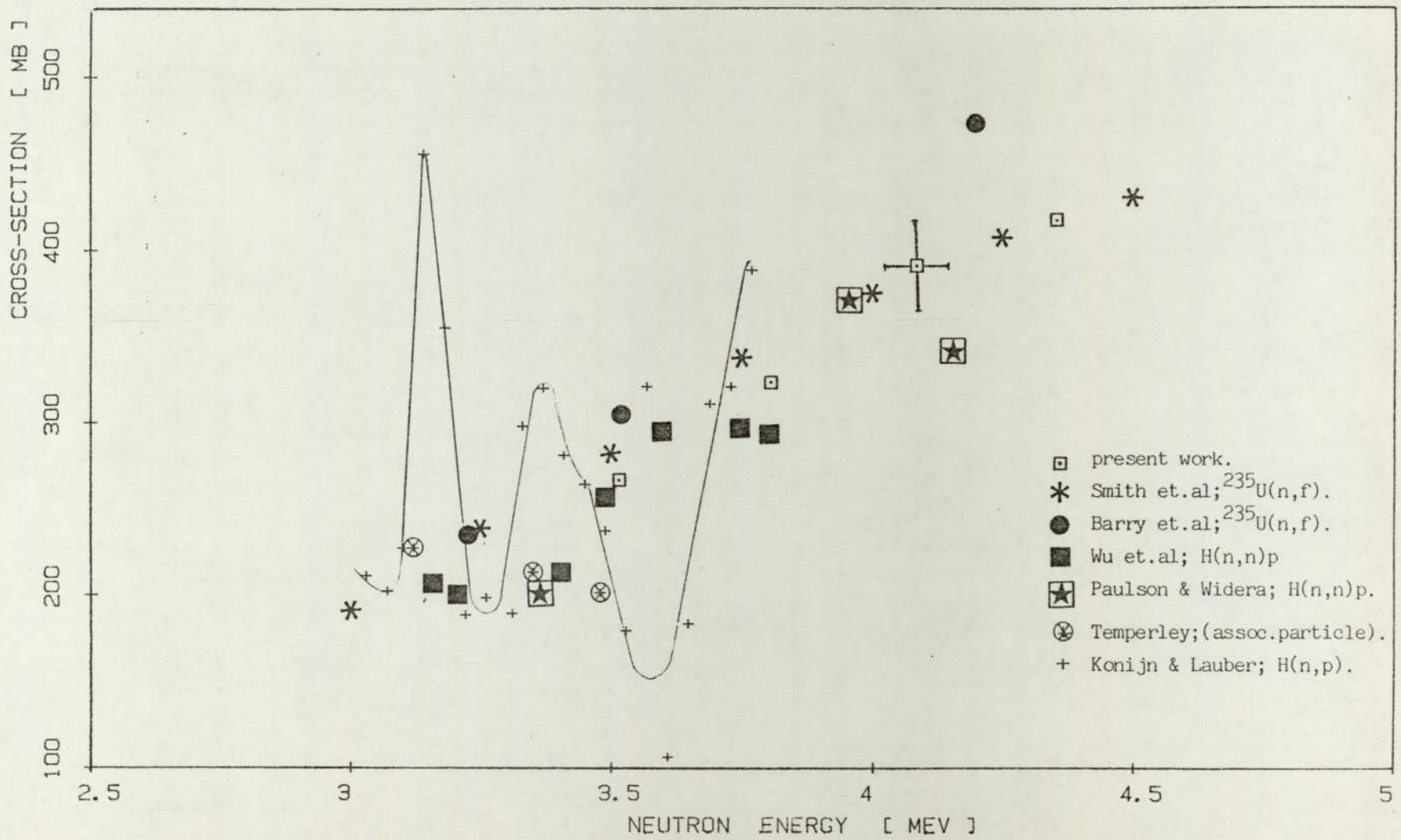

Fig. 6.3 The $^{58}Ni(n,p)^{58}Co$ Cross-sections.

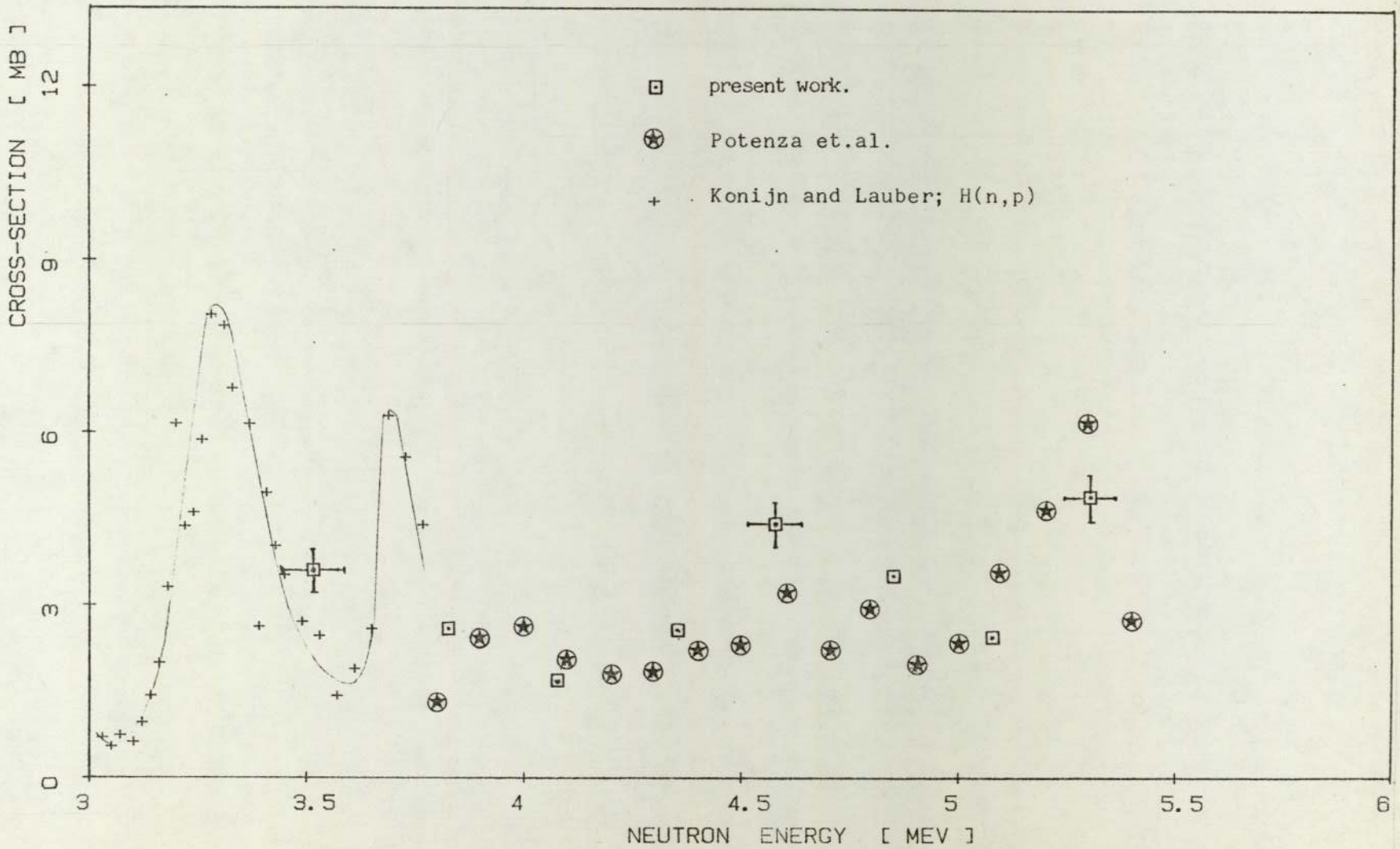

Fig. 6.4 The $^{29}Si(n,\alpha)^{26}Mg$ Cross-sections.

agreement with the present work. The measurements of Lu-Han Lin et.al. are relative to $^{27}Al(n,\alpha)^{24}Na$ cross-sections, which are not accurately known.[9] Moreover, their measurement at 5.40 MeV differs significantly from most other values reported around this energy and the closest agreement is with a measurement by Luckic and Carroll[7] which is also relative to $^{27}Al(n,\alpha)^{24}Na$.

Measurements by Luckic and Carroll[7] provide some data for comparasion in the region 4.5 to 6.0 MeV. Their results show fluctuations due to the use of different standards for neutron flux measurements and are systematically higher than present values.

Also there are two measurements by Ghorai et.al.[8] in the neutron energy range of 3.5 to 5.5 MeV. Their data was obtained relative to $^{27}Al(n,p)^{27}Mg$ cross-sections from the work of Grundl.[9] There is some agreement with their data at 4.1 MeV, but their measurement at 5.0 MeV differs considerably from this work and that of Smith et. al., despite good agreement between the $^{27}Al(n,p)$ cross-section values of Grundl and Smith et.al.

<u>$^{47}Ti(n,p)^{47}Sc$ reaction</u>.

The agreement between the present $^{47}Ti(n,p)^{47}Sc$ measurements and those of Jalil and Smith et.al. is good, considering the statistical fluctuations in the data.

Generally, the data of Jalil is slightly higher whilst of Smith et.al. slightly lower than the present values. The earlier measurements of Ghorai et.al.[8] relative to $^{27}Al(n,p)^{27}Mg$, are systematically higher than the present work and that of Jalil and Smith et.al. The one measurement of Gonzalez et.al.[11], at a neutron energy of 3.56 MeV, is also higher than the present nearest measurement at 3.513 MeV. Gonzalez et.al., measured the cross-section data relative to $^{31}P(n,p)^{31}Si$ reaction for which very little data was available.

$^{58}Ni(n,p)^{58}Co$ reaction.

The measurements for the $^{58}Ni(n,p)^{58}Co$ reaction cross-sections were made at four neutron energies between 3.5 MeV and 4.5 MeV. Earlier evaluations made by Bresesti et.al.[103] showed the presence of a pronounced structure in this energy range (preferably below 3.5 MeV). This was supported by the measured data of Konijn and Lauber[4] which showed a pronounced resonance structure (Fig. 6.3).

Smith et. al.[5] made an extensive study of $^{58}Ni(n,p)^{58}Co$ reaction between 2.85 MeV and 4.02 MeV, with a neutron energy resolution of the order of 40 keV. Their results are the most accurate to date and the excitation function varies smoothly showing no evidence

for the pronounced resonance structure observed by Konijn and Lauber. Smith et.al. have commented that the data by Konijn and Lauber was obtained by means of proton detection using a silicon solid state detector, suggesting that the observed structure may be due to the measurement technique.

The most recent data of Wu et.al.[13] show some indication of structure between 3.4 and 3.8 MeV. These workers have claimed that these discrepancies are attributable to the standard cross-section data used and not to the presence of a pronounced structure in the $^{58}Ni(n,p)^{58}Co$ cross-section. There is a good agreement between data of Wu et.al. and Paulson & Widera [14]. The measurements of Paulson and Widera were made at much poorer energy resolutions and they concluded that neutron energy resolution had no appreciable effects on the excitation function of the $^{58}Ni(n,p)^{58}Co$ reaction, in the energy range of 3 to 5 MeV.

The data obtained in the present work show a close agreement with the data of Smith et.al. and Barry et.al.[17]. However, further $^{58}Ni(n,p)^{58}Co$ measurements are possibly required, especially, in the 3.0 to 4.0 MeV region, using activation and non-activation techniques and in much smaller steps of neutron energy. The extensive disagreement between different measurements and the suggestion of structure have not been adequately resolved.

$^{29}Si(n,\alpha)^{26}Mg$ reaction.

The background spectrum due to neutron-induced reactions in the silicon of the surface barrier detector contains an alpha particle peak from $^{29}Si(n,\alpha)^{26}Mg$ reaction (ground state) with alpha particle energy comparable to proton energy from the $^{47}Ti(n,p)^{47}Sc$ and $^{58}Ni(n,p)^{58}Co$ reactions (section 5.3).Measurement of this spectrum at each neutron energy made it convenient to study $^{29}Si(n,\alpha)^{26}Mg$ reaction and determine the cross-section values for the reaction in the energy range 3.5 to 5.5 MeV.

There is limited reported data for comparasion with the present work. Potenza et.al.[84] studied the energy spectra of the charged particles produced in the (n,p) and (n,α)reactions in silicon, in the energy range 3.7 to 5.5 MeV, using silicon detector as a target. The excitation function for $^{29}Si(n,\alpha)^{26}Mg$ reaction for transitions to the ground state of the product nucleus shows extensive fluctuations (Fig. 6.4). This data is confirmed by the present work. The excitation function for the $^{29}Si(n,\alpha)^{26}Mg$ reaction, obtained by Konijn and Lauber[4] for energies below 3.77 MeV, is also presented in Fig. 6.4.

6.2 Uncertainties.

A summary of some contributing sources of uncertainty in the present measurements is presented in Table 6.6.

For neutron flux measurements the major source of uncertainty is in the $^{238}U(n,f)$ cross-section values, whilst for the sample reaction rate measurements the detection efficiency produces the largest uncertainty contribution.

For semiconductor detectors, the background rate is negligible for all charged particle measurements. The inherent radioactivity of the high-purity semiconductor material itself is negligible for silicon detectors. As the detector area is small (a few square cm) and the contact electrodes are extremely thin, there is little other material that can contribute background. The depletion layer of a silicon surface barrier detector is too small to develop significant pulses from low 'energy-range' radiations.

The accuracies obtained for $^{46}Ti(n,p)^{46}Sc$ and $^{47}Ti(n,p)^{47}Sc$ reaction cross-sections are close to the measurements by Jalil[6] and Smith et.al.[5] and meet the 5 to 10% accuracy requirements of cross-section data requests.

NEUTRON FLUX MEASUREMENTS.	$^{46}Ti(n,p)$	$^{47}Ti(n,p)$	$^{58}Ni(n,p)$	$^{29}Si(n,\alpha)$
Fission cross-sections.				
$^{238}U(n,f)$ / $^{235}U(n,f)$	2.5 - 3%	2.5 - 3%	2.5 - 3%	2.5 - 3%
Uranium content.				
Half-lives	1.7%	1.7%	1.7%	1.7%
Alpha-assay.	0.6%	0.6%	0.6%	0.6%
Fission counting.	0.5%	0.5%	0.5%	0.5%
Background neutrons.	0.5 - 1%	0.5 - 1%	0.5 - 1%	0.5 - 1%
Exposure geometry.	1.5%	1.5%	1.5%	1.5%
SAMPLE REACTION RATE.				
Sample mass.	0.7%	0.7%	0.9%	-
Detection efficiency.				
Soild angle estimation. / Distance measurements.	4%	4%	4%	-
Counting statistics.	2.5%	1.5%	1.5%	7.5%
Background neutrons.	0.5 - 1%	0.5 - 1%	0.5 - 1%	0.5 - 1%
Exposure geometry.	1.5%	1.5%	1.5%	2.5%
TOTAL	6.5%	6%	6%	9%

Table 6.6 Sources of Uncertainty and their Contributions.

The 6% accuracy obtained for the $^{58}Ni(n,p)^{58}Co$ cross-section is in agreement with the work of Smith et. al.[5] and Paulson and Widera[14]. The measurements of Wu et. al.[13] and Paulson and Widera are relative to H(n,n)p reaction, known to have greater accuracy than $^{238}U(n,f)$ cross-sections.[13, 105]

A P P E N D I C E S.

APPENDIX 1

PROGRAM PEAKFIT 1

LISTING OF PROGRAM PEAKFIT 1

The program is written in BASIC.

```
10 REMARK PROGRAM PEAK FIT
40 PRINT "HOW MANY DATA POINTS"
50 READ N
60 DIM X(N),Y(N),H(N),W(N),O(N)
70 A=0
80 B=0
90 C=0
95 R=0
100 D=0
110 FOR I=1 TO N STEP 1
130 READ  X(I),Y(I)
160 NEXT I
162 OPEN 1,4
163 CMD1
170 FOR I=2 TO N-1 STEP 1
180 L=I-1
190 M=I+1
200 K=N-2
210 H(I)=LOG(Y(L)/Y(M))
220 O(I)=(1/Y(L)+1/Y(M))
230 O(I)=1/O(I)
240 A=A+X(I)*O(I)
250 B=B+H(I)*O(I)
260 C=C+X(I)*H(I)*O(I)
270 D=D+X(I)*X(I)*O(I)
280 R=R+O(I)
290 NEXT I
300 E=(R*C-A*B)/(R*D-A*A)
310 F=(B*D-A*C)/(R*D-A*A)
315 PRINT E
320 S=SQR(2.0/E)
330 P=-F/E
340 PRINT "PEAK POSITION = ";P
350 PRINT "SIGMA = ";S
360 REMARK RESIDUALS
370 T=0
371 A=0
372 D=0
380 FOR I=2 TO N-1 STEP 1
390 Z=2*(X(I)-P)/S↑2
392 A=A+X(I)
393 D=D+X(I)*X(I)
400 R=(H(I)-Z)↑2
```

```
410 T=T+R
420 NEXT I
430 R=T/(K-2)
440 GOSUB 600
450 PRINT "PEAK HIGHT = ";U
460 A=2.507*S*U
470 PRINT "PEAK AREA = ";A
471 PRINT "CHANNEL LIMITS (XL,XL) ?"
472 READ L,M
480 FOR X=L TO M STEP 1
490 Z=((X-P)↑2)/(2*S↑2)
500 Z=-Z
510 A=U*EXP(Z)
520 PRINT X,A
525 NEXT X
540 END
600 REMARK SUBROUTINE PEAK HIGHT
610 V=K*D-A↑2
620 REMARK T IS ERROR IN SIGMA
630 G=SQR(K*R/V)
640 T=(0.7071*G)/(E↑1.5)
650 REMARK Q IS ERROR IN P
660 U=SQR(R/(V*D))
670 Q=SQR((U/E)↑2+(F*G/E↑2)↑2)
680 REMARK DETERMINE WEIGHTING
685 Z=0
686 B=0
690 FOR I=1 TO N STEP 1
700 V=Q↑2+((X(I)-P)↑2)*(T↑2)/(S↑2)
710 W(I)=1/Y(I)+(((X(I)-P)↑2)*V)/S↑4
720 W(I)=1/W(I)
730 A=W(I)*(LOG(Y(I))+((X(I)-P)↑2)/(2*S↑2))
740 B=B+A
750 Z=Z+W(I)
760 NEXT I
770 C=B/Z
780 REMARK PEAK HIGHT U
790 U=EXP(C)
800 RETURN
```

APPENDIX 2

PROGRAM NPROFILE

PROGRAM NPROFILE.

The Monte Carlo Program NPROFILE determines;

1. The deutron energy losses in the gas target neutron source, and in the nickel window.
2. Point of neutron creation in the source.
3. Direction of neutron emission and the angle of emission to the deutron beam line.
4. Conditions for the production of a neutron in the source.
5. The neutron energy profile.
6. The sample irradiation geometry.

Deutron Energy Losses.

The deutron energy (ED) losses in the gas target window (ELW) and the gas itself (ELG) are determined using equation 2.3.

(ELW) is constant with incident deutron energy whilst (ELG) depends upon the distance traversed in the gas prior to neutron creation.

Point Of Neutron Creation.

The neutron source is a cylinder 3 cm long and 0.3 cm in diameter. A two dimensional representation of

the point of creation is adequate with position co-ordinates (PL, R). (Fig. A1).

Direction Of Neutron Emission.

The angle of neutron emission (θ) lies in the range $0 \leq \theta \leq \pi$. This interval is divided into (N_θ) parts corresponding to angles of emission θ_i as;

$$\theta_i = \pi / N_\theta \, (i - \tfrac{1}{2}).$$

where, $i = 1$ to N_θ and each value of θ_i is weighted by:

$$\sin \theta_i (d\sigma/d\Omega). \, (E_d \, , \theta_i)$$

$\sin \theta_i$ accounts for the solid angle and $d\sigma / d\Omega(E_d,\theta_i)$ is the differential cross-section for neutron emission. E_d, the deutron energy after losses. The probability for neutron emission at angle θ_i is:

$$P(\theta_i) = \frac{\sin \theta_i \; d\sigma/d\Omega(E_d,\theta_i)}{\sum_{i=1}^{N_\theta} \sin \theta_i \; d\sigma/d\Omega(E_d,\theta_i).}$$

Production Of a Neutron.

The maximum possible value of the angle of emission (α) for a neutron to intercept the sample is given by

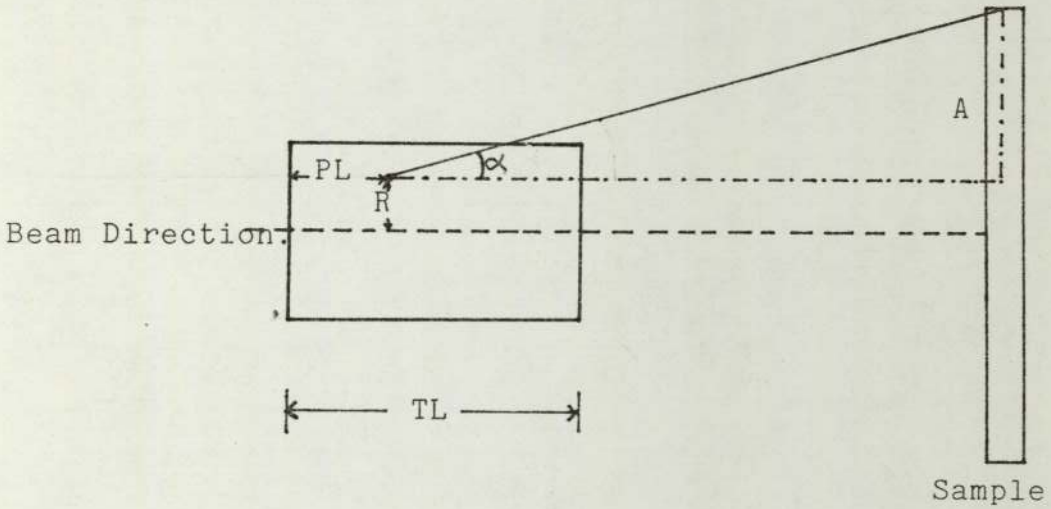

Fig. A 1 Schematic of Irradiation Geometry.

$$\tan(\alpha) = \frac{A}{(TL - PL + ST)}$$

ST, being the distance between neutron source and the sample.

A is given by :

$$A = R\cos\theta + (R^2\cos^2\theta + R_s^2 - R^2)^{\frac{1}{2}}.$$

R_s, is the sample radius.

If $\theta \leqslant \alpha$, the neutron hits the sample and the program proceeds to determine the neutron energy.

Neutron Energy Profile.

The neutron energy, E, is determined from the relativistic equation:

$$E = E_d m_G m_n \left[2\cos^2\theta + \frac{m_r(m_r + m_n)}{m_G m_n} \left\{ Q/E_d + (1 - m_G/m_r) \right\} \right]$$
$$+ 2\cos\theta \left[\cos^2\theta + \frac{m_r(m_r + m_n)}{m_G m_n} \left\{ Q/E_d + (1 - m_G/m_r) \right\} \right]$$

where, m_G is the mass of the target nucleus (${}^2_1H$).

m_n is the mass of a neutron.

m_r is the mass of the residual nucleus (${}^3_2He$)

Q, the Q-value for ${}^2_1H(d,n){}^3_2He$ reaction.

The mean neutron energy is determined using:

$$\langle E \rangle = \frac{1}{\sum_{j=1}^{N_{hist.}} \delta_j} \sum_{j=1}^{N_{hist.}} E\,\delta_i$$

Sample Irradiation

The neutron path length, , is given by

$$\delta = \frac{\text{Sample thickness } (t_s)}{\cos \phi}$$

where, ϕ is the angle between the neutron path and the direction of the incident deutron beam. This equation is applicable both to sample and the fission foil.

RELEVANT SYMBOLS USED IN LISTING THE PROGRAM.

ED = incident deutron energy (MeV).

ELW = energy loss in the gas target window.

ELG = energy loss in the gas.

BEAMD = beam diameter.

TL = neutron source length.

SAMPR = sample radius.

ST = source to sample distance.

DIFX = differential cross-section.

Listing of NPROFILE.

The program is written in FORTRAN.

```
      MASTER NPROFILE
      DIMENSION DIFX(36),W(30)
   10 FORMAT(36F0.0)
      READ(1,10)BEAMD,TL,SAMPR,ST
   70 READ(1,10)ED
      IF(ED.LT.0.0)GO TO 80
      READ(1,10)(DIFX(I),I=1,36)
      ELW=(13.44/ED)*(ALOG(ED/56.0)+5.1)*0.02739
      EDG=ED-ELW
      ELG=(0.48/EDG)*(ALOG(EDG*0.5)+4.7)*0.01613
      PO=2.0+5.97286*(3.26893/EDG+0.33214)
      RO=2.0*(1.0+5.97286*(3.26893/EDG+0.33214))**0.5
      ENMX=EDG*0.12545*(PO+RO)
      SSTTI=0.0
      DO 20 I=1,36
      F=I
      TTI=0.0872665*(F-0.5)
      STTI=(SIN(TTI))*DIFX(I)
   20 SSTTI=SSTTI+STTI
      ENMX=IFIX(ENMX*100.0+0.5)
      ENMX=ENMX/100.0
      WLOST=0.0
      RB=BEAMD*0.5
      DO 30 I=1,30
   30 W(I)=0.0
      DO 100 N=1,20000
C     DETERMINE POSITION AT WHICH NEUTRON IS PRODUCED
C     ALONG LENGTH OF TARGET
      RN=G05CAF(Y)
      PL=TL*RN
C     DETERMINE POSITION R, ALONG BEAM RADIUS.
      RN=G05CAF(Y)
      R=RB*RN
      WT=2.0*RN
C     DETERMINE DIRECTION OF EMISSION,PHI
C     ALONG BEAM CONE
      RN=G05CAF(Y)
      PHI=(1.0+RN)*3.1415927
C     DETERMINE MAXIMUM ANGLE,ALPHA,AT WHICH
C     NEUTRONS INTERCEPT THE SAMPLE
      A=R*COS(PHI)+(R**2*(COS(PHI))**2+SAMPR**2-R**2)**0.5
      ALFA=ATAN(A/(TL-PL+ST))
C     DETERMINE ANGLE OF EMISSIONTT,WEIGHTED
C     BY THE DIFFERENTIAL CROSS-SECTION AND SOLID ANGLE
      RN=G05CAF(Y)
```

```
      YTTI=0.0
      I=0
   40 I=I+1
      F=I
      TTI=0.0872665*(F-0.5)
      IF(TTI.GT.ALFA)GO TO 50
      PTTI=((SIN(TTI))*DIFX(I))/SSTTI
      YTTI=YTTI+PTTI


      WT=WT/COS(TTI)
      IF(RN.GTYTTI)GO TO 40
      RN=GO5CAF(Y)
      TT=(F-RN)*(0.0872665)
C     COMPUTE NEUTRON ENERGY
      EDL=EDG-ELG*PL
      V1=2.0*(COS(TT))**2+5.97286*(3.26983/EDL+0.33214)
      V2=2.0*COS(TT)*((COS(TT))**2+5.97286*(3.26893/EDL+0.33214))*
      EN=EDL*0.12545*(V1+V2)
      H=(ENMX-EN)/0.02
      I=IFIX(H+0.5)
      IF(I.LT.1)I=1
      W(I)=W(I)+WT
      GO TO 100
   50 WLOST=WLOST+WT
      K=(N/100)*100
      IF(K-N)100,99,100
   99 WRITE(2,400)N
  400 FORMAT(1H ,I5)
  100 CONTINUE
      WRITE(2,200)
  200 FORMAT(1H ,15HNEUTRON PROFILE)
      DO 60 I=1,30
      F=I
      ENP=ENMX+0.01-F*0.02
   60 WRITE(2,300)ENP,W(I)
  300 FORMAT(1H ,2F10.2)
      GO TO 70
```

```
C       THIS SECTION OF THE PROGRAM CORRECTS FOR THE
C       IRRADIATION GEOMETRY.

C       DETERMINE THE NUMBER OF SUCCESSFUL TRIALS IN
C       EACH SAMPLE AND THE CORRESPONDING MONTE CARLO
C       AVERAGED ATTENUATION FACTORS
        D=A/TAN(TT)-(ST+TL-PL)
        IF(D.LT.WB)GO TO 70
        ETA=SAMPT/COS(TT)
        ETAF=TF/COS(TT)
        ETAB=TB/COS(TT)
        WEN=ETA*EN
        SWEN=SWEN+ETA
        SETA=SETA+ETA
        N1=N1+1
        N2=N2+1
        NB=NB+1
        NF=NF+1
        Y=(SIGTS*ETA)/4.0
        F1=EXP(-Y)
        F2=F1
        F3=F1
        FF=EXP(-SIGTF*ETAF)
        FB=EXP(-ETAB*SIGTB)
        SF1=SF1+F1
        SF2=SF2+F2
        SFB=SFB+FB
        SFF=SFF+FF
        GO TO 160
   80   IF(D.LT.W4)GO TO 71
        ETA=SAMPT/COS(TT)
        GO TO 71
   81   ETA=D/COS(TT)
   82   WEN=ETA*EN
        SWEN=SWEN+WEN
        SETA=SETA+ETA
        B=W1/COS(TT)
        IF(D.GT.W4)GO TO 75
        IF=(D.GT.W3)GO TO 90
        IF=(D.GTW2)GO TO 91
        GO TO 110
   75   NB=NB+1
        ETAB=(D-W4)/COS(TT)
        FB=EXP(-SIGTB*ETAB)
        SFB=SFB+FB
        GO TO 115
   90   N4=N4+1
        ETA=(D-W3)/COS(TT)
        F4=EXP(-SIGTS*ETA)
        SF4=SF4+F4
        GO TO 120
  105   LOST=LOST+1
```

```
 160  CONTINUE
      XN1=N1
      XN2=N2
      XNB=NB
      XNF=NF
      AF1=SF1/XN1
      AF2=SF2/XN2
      AFB=SFB/XNB
      AVEN=SWEN/SETA
      WRITE(2,170)
170   FORMAT(1H,2X,1HN,4X,4HLOST,5X,2HN1,5X,2HN2,5X
      2HN,5X,2HNF)
      WRITE(2,180)N,LOST,N1,N2,NB,NF
190   FORMAT(1H,15,717//)
      WRITE(2,190)AVEN
210   FORMAT(1H,4HMEAN ENERGY=F4.3,1X,1HMEV/)
      WRITE(2,200)
220   FORMAT(6F8.4///)
      WRITE(2,200)
230   FORMAT(1H,15HNEUTRON PROFILE//)
      DO 250 I=1,30
      F=I
      ENP(I)=(ENMX+0.010)-(F*0.02)
      WRITE(2,230)ENP(I),L(I)
240   FORMAT(1H,F7.3,16)
250   CONTINUE
      STOP
      END
```

APPENDIX 3

CHARGED PARTICLE EMISSION

Charged Particle Emission.

A nuclear reaction can be described as a two stage process in terms of a compound nucleus;

$$X + a = C^* = Y + b$$

in which the compound nucleus C^* is formed by the amalgamation of an incident particle a with target nucleus X. In the capture process, the break up of C^* may result in the release of a photon; in other cases particle emission may occur.

The single-stage representation of this process is the'direct interaction', which may be envisaged by the potential well model leading to the same reaction products;

$$X + a = Y + b$$

Bohr's compound nucleus model suggests that for incident particles below 10 MeV, charged particle release from the compound nucleus is more favoured. Above this energy, the characteristics of reaction are better described by the direct interaction in which the first event is a collision between the incident particle and a nucleus. The struck nucleon may emerge from the nucleus without the formation of a compound nucleus. The momentum of

particle a tends to be transfered directly to b, in contrast to two-stage process where the momentum is conveyed in the first instance to the compound nucleus.

March and Morton[104] studied the proton emission in reactions of fast neutrons with medium weight nuclei. The probability of the emission of a particle b with energy between $\mathcal{E}$ and $\mathcal{E}+d\mathcal{E}$ is determined jointly by

(a) the energy $\mathcal{E}$

and (b) the level density $\omega_y(E)$ in the product nucleus Y to which it corresponds. This can be represented as:-

$$I(\mathcal{E})\, d\mathcal{E} \propto \mathcal{E}\, \omega_y(E)\, d\mathcal{E}$$

The emitted particle spectrum falls off at both high and low energies. For nuclei with atomic mass number around 50 and for a proton energy range 2 to 10 MeV, the spectrum shows a continous appearance, suggesting that the outgoing particles (protons) are products of a highly excited nucleus. This can also be expressed in terms of the level density of the product nucleus Y, at its maximum excitation.

The resulting spectrum may contain charged particles corresponding to the transitions from the excited compound nucleus to the ground and first a few low-lying excited states of the product nucleus. Consequently, the information about the low-lying states of the product

nucleus is essential as the energies of these states determine the energy of the emitted particle.

The energy of the emitted charged particle (Ee) can be estimated from,

$$Ee = (En \pm Q) - E_{ex.}$$

where, En is the neutron energy (incident particle) in MeV.

Q, the reaction Q-value in MeV.

and $E_{ex.}$ the excited state energy of the residual nucleus in MeV.

The above equation does not provide an accurate value for the emitted particle energy; this can be obtained from relativistic kinematics equation:-

$$(Ee)^{\frac{1}{2}} = (M_i M_e)^{\frac{1}{2}}/(M_R+M_e) \cdot (E_i)^{\frac{1}{2}} \cos\theta_e$$

$$\pm \sqrt{\frac{M_i M_e}{(M_R + M_e)^2} E_i \cos^2\theta_e + \frac{M_R - M_i}{M_R+M_e} E_i \frac{M_R}{M_R+M_e} Q}$$

The atomic values of Wapstra and Bos[78] were used.

The other symbols used have their usual meanings.

APPENDIX 4

PROGRAM PEAKFIT 2 (NEIB)

Listing of program NEIB.

The program is in FORTRAN

```
FTN,L
      PROGRAM NEIB
C
C
C     NEIB FITS A GAUSSIAN TO A SPECIFIED NUMBER OF
C     CHANNELS.   IP CHANNELS ON EACH SIDE OF THE PEAK
C     ARE USED IN COMPUTING THE STRAIGHT LINE APPROXIMATION
C     TO BACKGROUND.   IP CHANNELS AT THE HIGH ENERGY
C     END ARE USED TO DETERMINE THE ALTERNATIVE (IP -VE)
C     CONSTANT BACKGROUND.    IF IP EQUALS ZERO NO BACKGROUND
C     SUBTRACTION IS PERFORMED.   CALLED FROM 5406B STATION B
C
C                 RTE,NEIB,WWCYY,IP,XXX
C
C     WHERE WWCYY IS THE REGION TO WHICH THE PEAK IS
C     FITTED AND XXX IS TOTAL NUMBER OF CHANNELS IN
C     SPECTRUM (E.G.1024)
C
      REAL MU
      INTEGER DAT
      DIMENSION DAT(1024),X(1024),Y(256),IPR(5),A(3,3),
     1AINV(9),Z(256),BETA(3),DY(256),DZ(256),AGEMO(256)
     2,MSG1(7),MSG2(9),MSG3(8),MSG4(10),MSG5(3),MSG6(4)
      DIMENSION MSG7(19),MSG8(23)
      COMMON JJJ
      DATA MSG2/2HSI,2HGM,2HA=,2H  ,2H  ,2H  ,2H  ,2H  ,2H
     1,MSG1/2HA=,2H  ,2H  ,2H  ,2H  ,2H  ,2H  /
      DATA MSG3/2HMU,2H= ,2H  ,2H  ,2H  ,2H  ,2H  ,2H  /
      DATA MSG4/2HCH,2HI ,2HSQ,2H.=,2H  ,2H  ,2H  ,2H  ,2H
      DATA MSG5/2HER,2HRO,2HR /
      DATA MSG6/2HPR,2HOG,2H E,2HND/
      DATA MSG7/2HIN,2HPU,2HT ,2HER,2HRO,2HR=,2HCA,2HN ,2HO
     12HLY,2H F,2HIT,2H T,2HO ,2H25,2H6 ,2HPO,2HIN,2HTS/
      DATA MSG8/2HIN,2HPU,2HT ,2HER,2HRO,2HR ,2HLA,2HST,2H
     22HAR,2HAM,2HET,2HER,2H C,2HAN,2HNO,2HT ,2HEX,2HCE,2HD
     32H 1,2H02,2H4 /
      CALL RMPAR(IPR)
      CALL RDINT(IPR,DAT)
      JAJ=IPR(2)
      IF(JAJ.GT.256) GO TO 2
      GO TO 4
    2 CALL WRERR(MSG7,38,IPR(1))
      GO TO 76
    4 JJ=IPR(3)
      JJJ=1
      IF(IPR(5).GT.1024) GO TO 10
      GO TO 11
   10 CALL WRERR(MSG8,46,IPR(1))
      GO TO 76
   11 IF(IPR(4).LT.0) GO TO 60
      IF(IPR(4).EQ.0) GO TO 90
C
C     ASSUME LINEAR BACKGROUND
C
C     OBTAIN FRONT END BACKGROUND
```

```
C
      IP=IPR(4)
      SUM1=0.0
      DO 5 I=1,IP
    5 SUM1=SUM1+DAT(I)
      Y1=SUM1/IP
      X1=IP/2
C
C   OBTAIN BACK END BACKGROUND
C
      SUM2=0.0
      DO 6 I=1,IP
    6 SUM2=SUM2+DAT(JAJ-I+1)
      Y2=SUM2/IP
      X2=JAJ-IP/2
C
C   OBTAIN STRAIGHT LINE COEFFICIENTS
C
C         Y=CX+K
C
      C=(Y1-Y2)/(X1-X2)
      K=(Y1*X2-Y2*X1)/(X2-X1)
C
C   SUBTRACT BACKGROUND
C
      DO 7 I=IP,JAJ-IP
      Y=C*I+K
      DAT(I)=DAT(I)-Y
    7 IF(DAT(I).LT.0) DAT(I)=1
C
C   FIT GAUSSIAN
C
      DO 1 I=1,JAJ-2*IP
      X(I)=FLOAT(I)*5.0
      Y(I)=FLOAT(DAT(IP+I))
      DY(I)=SQRT(Y(I))
    1 CONTINUE
      JAJ=JAJ-2*IP
      JJ=JJ+IP
      GO TO 70
C
C   ASSUME CONSTANT BACKGROUND
C
   60 IPI=-IPR(4)
      SMS=0.0
      DO 62 I=JAJ,JAJ-IPI+1,-1
   62 SMS=SMS+DAT(I)
      ISMS=IFIX(SMS/IPI)
C
C   SUBTRACT BACKGROUND
C
      DO 63 I=1,JAJ-IPI
      DAT(I)=DAT(I)-ISMS
   63 IF(DAT(I).LT.0) DAT(I)=1
      DO 64 I=1,JAJ-IPI
```

```
0111          X(I)=FLOAT(I)*5.0
0112          Y(I)=FLOAT(DAT(I))
0113       64 DY(I)=SQRT(Y(I))
0114          JAJ=JAJ-IPI
0115          GO TO 70
0116   C
0117   C   NO BACKGROUND SUBTRACTION
0118   C
0119       90 DO 91 I=1,JAJ
0120          X(I)=FLOAT(I)*5.0
0121          Y(I)=FLOAT(DAT(I))
0122       91 DY(I)=SQRT(Y(I))
0123   C
0124       70   CALL GAUSS(JJ,X,Y,DY,A1,SIG,MU,JAJ,SUM)
0125   C
0126          IF(JJJ.NE.1) GO TO 77
0127          GO TO 78
0128       77 CALL WRERR(MSG5,6,IPR(1))
0129          GO TO 76
0130   C
0131       78 MU=MU-1+0.5
0132   C
0133   C  ADD 0.5 TO ABOVE TO GIVE POSITION RELATIVE TO CHANNEL 0
0134   C   -1 GIVES POSITION OF MU RELATIVE TO BASE CHANNEL 0 & N
0135   C       AS A RESULT OF ADC SHIFT
0136   C
0137          CALL FTOA(A1,MSG1(7),12,5)
0138          CALL WRERR(MSG1,14,IPR)
0139          CALL FTOA(SIG,MSG2(9),12,5)
0140          CALL WRERR(MSG2,18,IPR)
0141          CALL FTOA(MU,MSG3(8),12,5)
0142          CALL WRERR(MSG3,16,IPR)
0143          CALL FTOA(SUM,MSG4(10),12,5)
0144          CALL WRERR(MSG4,20,IPR)
0145          MU=MU+1
0146          IX1=INT(MU-4.0*SIG)
0147          IX2=INT(MU+4.0*SIG)
0148          B1=A1/(SIG*SQRT(2.0*3.141593))
0149          SI2=2*SIG**2
0150          DO 3 I=1,IPR(5)
0151          X(I)=FLOAT(I)
0152          DAT(I)=0
0153          IF(I.LE.IX2.AND.I.GE.IX1) GO TO 66
0154          GO TO 3
0155       66 IF(IPR(4).LT.0) IS=ISMS
0156          IF(IPR(4).GT.0) IS=IFIX(C*(X(I)-IPR(3))+K)
0157          IF(IPR(4).EQ.0) IS=0
0158          DAT(I)=IFIX(B1*EXP(-(X(I)-MU)**2/SI2))+IS
0159          IF(DAT(I).LT.0) DAT(I)=0
0160        3 CONTINUE
0161       80 IPR(4)=IPR(5)
0162          IPR(5)=IPR(5)
0163          CALL WRINT(IPR,DAT)
0164       76   CALL WRERR(MSG6,8,IPR(1))
0165          END
```

```
      SUBROUTINE GAUSS (JJ,X,Y,DY,A1,SIG,MU,JAJ,SUM)
      REAL MU
      DIMENSION X(256),Y(256),A(3,3),AINV(9),Z(256),
     1BETA(3),DY(256),DZ(256),AGEMO(256)
      COMMON JJJ
C
C     PROGRAM TO FIT A GAUSSIAN TO A GIVEN
C     SET OF POINTS USING A MATRIX INVERSION
C     TECHNIQUE.   N0 IS THE NUMBER OF POINTS
C
      N0=JAJ
        DO 201 J=1,N0
  201   DZ(J)=(DY(J)/Y(J))**2
        DO 16 J=1,N0
   16   AGEMO(J)=1.0/DZ(J)
      S1=0.0
      S2=0.0
      S3=0.0
      S4=0.0
      S8=0.0
         DO 15 J=1,N0
         S1=S1+X(J)*AGEMO(J)
         S2=S2+AGEMO(J)*X(J)**2
         S3=S3+AGEMO(J)*X(J)**3
         S4=S4+AGEMO(J)*X(J)**4
         S8=S8+AGEMO(J)
   15 CONTINUE
      A(1,1)=S8
      A(1,2)=S2
      A(1,3)=S1
      A(2,1)=S2
      A(2,2)=S4
      A(2,3)=S3
      A(3,1)=S1
      A(3,2)=S3
      A(3,3)=S2
C
      CALL INVRT(A,AINV)
C
      IF(JJJ.NE.1) RETURN
         DO 18 J=1,N0
         IF(Y(J).LE.0) Y(J)=1.0
   18    Z(J)=ALOG(Y(J))
      S5=0.0
      S6=0.0
      S7=0.0
         DO 19 J=1,N0
         S5=S5+Z(J)*AGEMO(J)
         S6=S5+Z(J)*AGEMO(J)*X(J)**2
         S7=S7+Z(J)*AGEMO(J)*X(J)
   19 CONTINUE
         DO 23 J=1,3
         BETA(J)=AINV(J)*S5+AINV(J+3)*S6+AINV(J+6)*S7
   23 CONTINUE
      IF(BETA(2).GT.0.0) GO TO 21
```

```
      ZZ=BETA(1)-BETA(3)**2/(4.0*BETA(2))
      IF(ZZ.GT.85.0.OR.ZZ.LT.-64.0) GO TO 21
      A1=EXP(ZZ)*SQRT(-3.141593/BETA(2))
      SIG=SQRT(-1.0/(2.0*BETA(2)))
      MU=BETA(3)*SIG**2
      A1=A1/5.0
      SIG=SIG/5.0
      MU=MU/5.0+JJ
      DO 3 I=1,N0
    3 X(I)=X(I)/5+JJ
C
C     FIT A CURVE USING THE PARAMETERS A1,SIG AND MU
C
      SIG2=SIG**2
      SQ=SQRT(2.0*3.141593)
      R=A1/(SIG*SQ)
      T=2.0*SIG2
      SUM=0.0
      DO 5 J=1,N0
      IF(DY(J).LT.1.0) GO TO 5
      CHI=R*EXP(-((X(J)-MU)**2)/T)
      SUM=SUM+(Y(J)-CHI)**2/DY(J)**2
    5 CONTINUE
      RETURN
   21 JJJ=3
      RETURN
      END
```

```
      SUBROUTINE INVRT(A,AINV)
      DIMENSION A(3,3),AINV(9),B(3),IPIVT(3)
      COMMON JJJ
C
C      PROGRAM TO INVERT A MATRIX OF ORDER N
C
      N=3
      NSQ=N*N
C
      CALL FACTR(A,A,IPIVT,B,N,IFLAG)
      GO TO (20,11),IFLAG
   11 JJJ=3
      RETURN
C
   20 DO 21 I=1,N
   21 B(I)=0.0
      IBEG=1
      DO 30 J=1,N
      B(J)=1.0
      CALL SUBST(A,B,AINV(IBEG),IPIVT,N)
      B(J)=0.0
   30 IBEG=IBEG+N
      RETURN
      END
```

```
      SUBROUTINE FACTR(A,W,IPIVT,D,N,IFLAG)
      DIMENSION A(3,3),W(3,3),IPIVT(3),D(3)
      IFLAG=1
C
C     INITIALIZE W,IPIVT,D
C
      DO 10 I=1,N
      IPIVT(I)=I
      ROWMX=0.0
      DO 7 J=1,N
    7 ROWMX=AMAX1(ROWMX,ABS(W(I,J)))
      IF(ROWMX.EQ.0.0)      GO TO 999
   10 D(I)=ROWMX
C     GAUSS ELIMINATION WITH SCALED PARTIAL PIVOTING
C
      NM1=N-1
      IF(NM1.EQ.0)          RETURN
      DO 20 K=1,NM1
      J=K
      KP1=K+1
      IP=IPIVT(K)
      COLMX=ABS(W(IP,K))/D(IP)
      DO 11 I=KP1,N
      IP=IPIVT(I)
      AWKOV=ABS(W(IP,K))/D(IP)
      IF(AWKOV.LE.COLMX)    GO TO 11
      COLMX=AWKOV
      J=I
   11 CONTINUE
      IF(COLMX.EQ.0.0)      GO TO 999
C
      IPK=IPIVT(J)
      IPIVT(J)=IPIVT(K)
      IPIVT(K)=IPK
      DO 20 I=KP1,N
      IP=IPIVT(I)
      W(IP,K)=W(IP,K)/W(IPK,K)
      RATIO=-W(IP,K)
      DO 20 J=KP1,N
   20 W(IP,J)=RATIO*W(IPK,J)+W(IP,J)
      IF(W(IP,N).EQ.0.0)    GO TO 999
                            RETURN
  999 IFLAG=2
                            RETURN
      END
```

```
      SUBROUTINE SUBST(W,B,X,IPIVT,N)
      DIMENSION W(3,3),B(3),X(3),IPIVT(3)
      IF(N.GT.1)        GO TO 10
      X(1)=B(1)/W(1,1)
                        RETURN
   10 IP=IPIVT(1)
      X(1)=B(IP)
      DO 15 K=2,N
      IP=IPIVT(K)
      KM1=K-1
      SUM=0.0
      DO 14 J=1,KM1
   14 SUM=W(IP,J)*X(J)+SUM
   15 X(K)=B(IP)-SUM
C
      X(N)=X(N)/W(IP,N)
      K=N
      DO 20 NP1MK=2,N
      KP1=K
      K=K-1
      IP=IPIVT(K)
      SUM=0.0
      DO 19 J=KP1,N
   19 SUM=W(IP,J)*X(J)+SUM
   20 X(K)=(X(K)-SUM)/W(IP,K)
                        RETURN
      END
```

APPENDIX 5

PROGRAM PEAKFIT 3 (CBJJ4)

PROGRAM CBJJ4

This is a non-linear least squares fitting program and will fit the required number of data points with upto 10 parameters in any functional form. The program needs to supply a function subroutine which evaluates the function being fitted and a subroutine which calculates the derivatives of the function with respect to each parameter. The best fit to the data is obtained by searching parameter space for the point which minimises χ^2 As well as providing the values of the parameters for the best fit, the program estimates the errors on the parameters and gives the value of χnumber for the fit;

$$\text{number} = \frac{\chi^2}{\text{No. of degrees of freedom.}}$$

For input data X(I) and Y(I); YFIT(I) and σ Y(I) are supplied by the program. The peak height Y_0 and peak position X_0 are also determined. The area of the peak is through integration of the fitted data poits. The program will perform more than one GAUSSIAN FUNCTION where required.

Listing of PROGRAM CBJJ4.

The program is written in FORTRAN.

```
FTN,L
      PROGRAM CBJJ4(3,99),   820818 JGO
      DOUBLE PRECISION ARRAY
      DIMENSION X(150),Y(150),SIGMAY(150),YFIT(150),WEIGHT(1
     1,A(10),SIGMAA(10),DELTAA(10),BETA(10),DERIV(10)
     2,ALPHA(10,10),ARRAY(10,10),B(10),IH(5),IY(150)
      DATA A/10*0.0/
      CALL RMPAR(IH)
C
C  TWO TYPES OF INPUT CASE ARE AVAILABLE:
C
C  1.  INPUT FROM RTE TELETYPE, FORM IS,
C        RU,JOJJ4,IH(1),IH(2),IH(3),IH(4),IH(5)
C      WHERE
C         IH(1)=99 FOR THIS CLASS OF INPUT
C         IH(2)=NO. OF DATA POINTS
C         IH(3)=LU FOR DATA INPUT OF X,Y,(SIGMAY)
C         IH(4)=LU FOR ALL OTHER DATA INPUT
C         IH(5)=0 IF SIGMAY(I)=SQRT(Y(I))
C         IH(5)=1 IF SIGMAY(I) IS TO BE SUPPLIED SEPARATELY
C
C
C  2.   MODDED TO READ DATA FROM SATELLITE
C      CALL BY:
C         RTE,JOJJ4,XXXCYYYRZ, 0,LEN
C      WHERE
C          LEN=REGION LENGTH OF DATA
C
C      MODIFICATION RECORD:
C           ORIGINAL PROGRAM (JJFIT):      JJ
C           GENERALISATION TO
C                 DISTRIBUTED SYSTEM:      JGO
C           CALC. OF COVARIANCE MATRIX:    DRW
C
C
      L=IH(4)
      IF(IH(1).EQ.99) GO TO 222
      CALL SPOOL(100,21,IH(1),1)
      L=21
  222 WRITE(L,333)
  333 FORMAT("WHEN INVITED TO TYPE 0,1, OR 2 THE MEANING IS:-
     1"0 TO EXIT"/"1 FOR A NEW FIT"/
     2"2 TO FIT OLD DATA FROM NEW START POINT")
      WRITE(21,223)
  223 FORMAT("        NON-LINEAR LEAST-SQUARES FIT USING MARQU
     1 ," METHOD"///)
    1 WRITE(L,5)
    5 FORMAT("MODE ←")
C                       GIVES WEIGHTED/UNWEIGHTED FIT
      READ(L,*)MODE
      IF(IH(1).NE.99)CALL RDINT(IH,IY)
      NPTS=IH(2)
      WRITE(L,668)
  668 FORMAT(2X,"NTERMS ?")
      READ(L,*)NTERMS
```

```
0056          LL=L
0057          IF(IH(1).EQ.99)LL=IH(3)
0058          IF(IH(1).EQ.99.AND.IH(5).EQ.0)GOTO 669
0059          IF(IH(1).EQ.99.AND.IH(5).EQ.1)GOTO 680
0060   C      RTE COMPUTER RUNS
0061   C
0062   C
0063   C      5406 COMPUTER RUNS
0064          JO=IH(3)
0065          DO 801 I=1,100
0066          IF(IH(3).LE.IH(5))GOTO 802
0067          IH(3)=IH(3)-IH(5)
0068      801 CONTINUE
0069      802 DO 666 I=1,NPTS
0070          X(I)=IH(3)+I-1
0071   C
0072   C    THE -1 ALLOWS FOR CALC. RELATIVE TO BASE 0, NOT 1
0073   C      (RESULTS FROM ADC CHANNEL SHIFT )
0074   C
0075          Y(I)=IY(I)
0076          SIGMAY(I)=SQRT(Y(I))
0077          IF(SIGMAY(I).EQ.0.0)SIGMAY(I)=1.0
0078   C
0079   C      ASSUMES ERRORS = SQRT(COUNTS)
0080      666 CONTINUE
0081          GOTO 670
0082      669 WRITE(L,671)
0083      671 FORMAT(2X,"INPUT DATA: X,Y")
0084          DO 673 I=1,NPTS
0085          READ(LL,*)X(I),Y(I)
0086          SIGMAY(I)=SQRT(Y(I))
0087      673 CONTINUE
0088   C
0089          GOTO 670
0090   C
0091      680 WRITE(L,681)
0092      681 FORMAT(2X,"INPUT DATA: X,Y,SIGMAY")
0093          DO 683 I=1,NPTS
0094          READ(LL,*)X(I),Y(I),SIGMAY(I)
0095      683 CONTINUE
0096   C
0097   C
0098      670 WRITE(L,3)
0099        3 FORMAT("FIRST GUESS AT A(I) AND DELTAA(I)")
0100   C      A=FIRST GUESS TO PARAMETERS, DELTAA FIRST GUESS TO ERRO
0101        8 DO 9 I=1,NTERMS
0102          WRITE(L,4)I,I
0103        4 FORMAT("A(",I1,"),DELTAA(",I1,") ←")
0104        9 READ(L,*)A(I),DELTAA(I)
0105          FLAMDA=0.001
0106          WRITE(21,19)(I,I=1,10)
0107       19 FORMAT(4X,"CHINU",5X,5("A(",I1,")",7X)/
0108         112X,4(7X,"A(",I1,")")
0109         2,7X,"A(",I2,")")
0110       11 NFREE=NPTS-NTERMS
```

```
      IF(NFREE)13,13,20
   13 CHISQR=0.
      GOTO 170
C
C           EVALUATE WEIGHTS
C
   20 DO 30 I=1,NPTS
   21 IF(MODE)22,27,29
   22 IF(Y(I))25,27,23
   23 WEIGHT(I)=1./Y(I)
      GOTO 30
   25 WEIGHT(I)=1./(-Y(I))
      GOTO 30
   27 WEIGHT(I)=1.
      GOTO 30
   29 WEIGHT(I)=1./SIGMAY(I)**2
   30 CONTINUE
C
C           EVALUATE ALPHA AND BETA MATRICES
C
   31 DO 34 J=1,NTERMS
      BETA(J)=0.
      DO 34 K=1,J
   34 ALPHA(J,K)=0.
   41 DO 50 I=1,NPTS
      CALL FDERV(X(I),A,DELTAA,NTERMS,DERIV)
      DO 46 J=1,NTERMS
      BETA(J)=BETA(J)+WEIGHT(I)*(Y(I)-FUNCT(X(I),A))*DERIV(J)
      DO 46 K=1,J
   46 ALPHA(J,K)=ALPHA(J,K)+WEIGHT(I)*DERIV(J)*DERIV(K)
   50 CONTINUE
   51 DO 53 J=1,NTERMS
      DO 53 K=1,J
   53 ALPHA(K,J)=ALPHA(J,K)
C
C           EVALUATE CHI SQUARE AT STARTING POINT
C
   61 DO 62 I=1,NPTS
   62 YFIT(I)=FUNCT(X(I),A)
   63 CHISQ1=FCHIS(Y,WEIGHT,NPTS,NFREE,MODE,YFIT)
C
C           INVERT MODIFIED CURVATURE MATRIX TO FIND NEW PARAM
C
      WRITE(21,120)CHISQ1,(A(I),I=1,10)
  120 FORMAT(6(1X,E10.4)/14X,5(1X,E10.4)/)
   71 DO 74 J=1,NTERMS
      DO 73 K=1,NTERMS
   73 ARRAY(J,K)=DBLE(ALPHA(J,K)/SQRT(ALPHA(J,J)*ALPHA(K,K)))
   74 ARRAY(J,J)=DBLE(1.+FLAMDA)
   80 CALL MATIN(ARRAY,NTERMS,DET)
   81 DO 84 J=1,NTERMS
      B(J)=A(J)
      DO 84 K=1,NTERMS
   84 B(J)=B(J)+BETA(K)*SNGL(ARRAY(J,K))/SQRT(ALPHA(J,J)*ALPH
C
```

```
C           IF CHI SQUARE INCREASES,INCREASE FLAMDA AND TRY AG
C
   91 DO 92 I=1,NPTS
   92 YFIT(I)=FUNCT(X(I),B)
   93 CHISQR=FCHIS(Y,WEIGHT,NPTS,NFREE,MODE,YFIT)
      CHIDIF=CHISQ1-CHISQR
      IF(CHIDIF)94,101,101
   94 IF(ABS(CHIDIF)-1.E-04)101,101,95
   95 FLAMDA=10.*FLAMDA
      GOTO 71
C
C           EVALUATE PARAMETERS AND TEST FOR CONVERGENCE
C
  101 FLAMDA=FLAMDA/10.
      DO 103 J=1,NTERMS
  103 A(J)=B(J)
      IF(CHIDIF-.001*CHISQR)115,31,31
  115 WRITE(21,120)CHISQR,(A(I),I=1,10)
      DO 107 J=1,NTERMS
      SIGMAA(J)=SQRT(SNGL(ARRAY(J,J))/ALPHA(J,J))
  107 WRITE(21,130)J,A(J),SIGMAA(J)
  130 FORMAT(5X,"     A(",I1,") = ",G12.4,"  +-  ",G12.4)
      DO 131 I=1,NTERMS
      DO 132 J=I,NTERMS
      ARRAY(I,J)=ARRAY(I,J)/SQRT(ALPHA(I,I))/SQRT(ALPHA(J,J))
  132 ARRAY(J,I)=ARRAY(I,J)
  131 CONTINUE
 1131 FORMAT(///"   COVARIANCE MATRIX"/)
      DO 134 I=1,NTERMS
  133 FORMAT(6E12.4/2X,4E12.4)
  134 CONTINUE
      DO 230,I=1,NTERMS-1
      DO 231 J=I+1,NTERMS
      ARRAY(I,J)=ARRAY(I,J)/DSQRT(ARRAY(I,I)*ARRAY(J,J))
  231 ARRAY(J,I)=ARRAY(I,J)
  230 CONTINUE
      DO 232 I=1,NTERMS
  232 ARRAY(I,I)=1.0
  233 FORMAT(///"  CORRELATION MATRIX"/)
      DO 234,I=1,NTERMS
  234 CONTINUE
  135 FORMAT  (//3X,"X(I)",10X,"Y(I)",10X,"YFIT(I)",7X,"DIF")
      DO 150 I=1,NPTS
      YFIT(I)=FUNCT(X(I),A)
      DIF=YFIT(I)-Y(I)
  150 WRITE(L,160)
  160 FORMAT("TYPE 0,1 OR 2 ←")
      READ(L,*)NTEST
      IF(NTEST-1)170,1,670
  170 IH(3)=JO
      IH(4)=IH(2)
      IH(5)=IH(3)+IH(5)
      DO 667 I=1,NPTS
      IY(I)=YFIT(I)
  667 CONTINUE
```

```
      IF(IH(1).NE.99)CALL WRINT(IH,IY)
      STOP
      END

      SUBROUTINE MATIN(ARRAY,NORDER,DET)
      DOUBLE PRECISION ARRAY,AMAX,SAVE
      DIMENSION ARRAY(10,10),IK(10),JK(10)
   10 DET=1.
   11 DO 100 K=1,NORDER
C
C           FIND LARGEST ELEMENT ARRAY(I,J) IN REST OF MATRIX
C
      AMAX=0.
   21 DO 30 I=K,NORDER
      DO 30 J=K,NORDER
   23 IF(DABS(AMAX)-DABS(ARRAY(I,J)))24,24,30
   24 AMAX=ARRAY(I,J)
      IK(K)=I
      JK(K)=J
   30 CONTINUE
C
C         INTERCHANGE ROWS AND COLUMS TO PUT AMAX IN ARRAY(K,K)
C
   31 IF(AMAX)41,32,41
   32 DET=0.
      GOTO 140
   41 I=IK(K)
      IF(I-K)21,51,43
   43 DO 50 J=1,NORDER
      SAVE=ARRAY(K,J)
      ARRAY(K,J)=ARRAY(I,J)
   50 ARRAY(I,J)=-SAVE
   51 J=JK(K)
      IF(J-K)21,61,53
   53 DO 60 I=1,NORDER
      SAVE=ARRAY(I,K)
      ARRAY(I,K)=ARRAY(I,J)
   60 ARRAY(I,J)=-SAVE
C
C           ACCUMULATE ELEMENTS OF INVERSE MATRIX
C
   61 DO 70 I=1,NORDER
      IF(I-K)63,70,63
   63 ARRAY(I,K)=-ARRAY(I,K)/AMAX
   70 CONTINUE
   71 DO 80 I=1,NORDER
      DO 80 J=1,NORDER
      IF(I-K)74,80,74
   74 IF(J-K)75,80,75
   75 ARRAY(I,J)=ARRAY(I,J)+ARRAY(I,K)*ARRAY(K,J)
   80 CONTINUE
   81 DO 90 J=1,NORDER
      IF(J-K)83,90,83
```

```
0273      83 ARRAY(K,J)=ARRAY(K,J)/AMAX
0274      90 CONTINUE
0275         ARRAY(K,K)=1./AMAX
0276     100 DET=DET*AMAX
0277   C
0278   C           RESTORE ORDERING OF MATRIX
0279   C
0280     101 DO 130 L=1,NORDER
0281         K=NORDER-L+1
0282         J=IK(K)
0283         IF(J-K)111,111,105
0284     105 DO 110 I=1,NORDER
0285         SAVE=ARRAY(I,K)
0286         ARRAY(I,K)=-ARRAY(I,J)
0287     110 ARRAY(I,J)=SAVE
0288     111 I=JK(K)
0289         IF(I-K)130,130,113
0290     113 DO 120 J=1,NORDER
0291         SAVE=ARRAY(K,J)
0292         ARRAY(K,J)=-ARRAY(I,J)
0293     120 ARRAY(I,J)=SAVE
0294     130 CONTINUE
0295     140 RETURN
0296         END

0297         REAL FUNCTION FCHIS(Y,WEIGHT,NPTS,NFREE,MODE, YFIT)
0298         DIMENSION Y(150),YFIT(150),WEIGHT(150)
0299      11 CHISQ=0.
0300      12 IF(NFREE)13,13,20
0301      13 FCHIS=0.
0302         GOTO 40
0303   C
0304   C           ACCUMULATE CHI SQUARE
0305   C
0306      20 DO 30 I=1,NPTS
0307      30 CHISQ=CHISQ+WEIGHT(I)*(Y(I)-YFIT(I))**2
0308   C
0309   C           DIVIDE BY NUMBER OF DEGREES OF FREEDOM
0310   C
0311      31 FREE=NFREE
0312      32 FCHIS=CHISQ/FREE
0313      40 RETURN
0314         END

0315         REAL FUNCTION FUNCT(X,A)
0316         DIMENSION A(10)
0317         Y=(X-A(2))/A(3)
0318         Z=(X-A(5))/A(6)
0319         YY=Y*Y
0320         ZZ=Z*Z
0321         IF(YY.GT.20.0)YYY=0
0322         IF(YY.GT.20.0)GOTO 99
0323         YYY=EXP(-0.5*YY)
0324      99 IF(ZZ.GT.20)ZZZ=0
0325         IF(ZZ.GT.20.0)GOTO 999
0326         ZZZ=EXP(-0.5*ZZ)
0327     999 FUNCT=YYY+ZZZ
0328         RETURN
0329         END
```

```
      SUBROUTINE FDERV(X,A,DELA,NTERMS,DERIV)
      DIMENSION A(10),DELA(10),DERIV(10)
      Y=(X-A(2))/A(3)
      Z=(X-A(5))/A(6)
      YYY=0.0
      IF(Y*Y.GT.20)GOTO 99
      YYY=EXP(0.5*Y*Y)
   99 ZZZ=0.0
      IF(Z*Z.GT.20)GOTO 999
      ZZZ=EXP(0.5*Z*Z)
  999 DERIV(1)=YYY
      DERIV(2)=A(1)*DERIV(1)*Y/A(3)
      DERIV(3)=DERIV(2)*Y
      DERIV(4)=ZZZ
      DERIV(5)=A(4)*DERIV(1)*Z/A(6)
      DERIV(6)=DERIV(5)*Z
      RETURN
      END
```

R E F E R E N C E S.

REFERENCES

1. W. Kohler., "Fast neutron dosimetry". Rev. Atomic Energy. 9,441,(1971)
2. "WRENDA-1981". World Request List for Nuclear Data Measurements". INDC(SEC)-78/URSF,IAEA(1981)
3. C.H. Hogg et.al. "Fast neutron dosimetry at the MTR-ETR site." ASTC special technical publication NO. 341 (1963).
4. J. Konijn and A. Lauber. "Cross-section measurements of the $^{58}Ni(n,p)^{58}Co$ and $^{29}Si(n,\alpha)^{26}Mg$ reactions in the energy range 2.2MeV to 3.8MeV." Nucl. Phys. 48, 191, (1963).
5. Smith et.al. "Cross-section measurements of (n,p) reactions for ^{27}Al, $^{46,47,48}Ti$, ^{58}Ni, ^{59}Co and ^{64}Zn from near threshold to 10 MeV." Nucl. Sci. Engg. 58., 314, (1975)
6. N.A. Jalil " The measurement of neutron activation cross-sections in the energy range Of 3.5MeV to 6.0 MeV." Ph.D. thesis, University of Aston in Birmingham.,England. (1980)
7. Y. Luckic and E.E. Carroll. "Titanium (n,p) cross-section measurements." Nucl. Sci. Engg. 43., 233., (1971).
8. Ghorai et. al. " Some (n,p) cross-sections of ^{46}Ti, ^{47}Ti and ^{48}Ti." J. Nucl. Energy. 25, 319(1971)
9. J.A. Grundl. "$^{31}P(n,p)^{31}Si$ and $^{27}Al(n,\alpha)^{24}Na$ Cross-sections." Phys. Rev. 109 (2), 425, (1958)

10. Lu-Han Lin.et. al. "Excitation functions for $^{46}Ti(n,p)$ $^{48}Ti(n,p)$ reactions rel.to $^{27}Al(n,\alpha)^{24}Na$." Phys. Energy Fortis and Phys. Nucl.(China) Vol.3 , No.1, 88 (1979).

11. Gonzalez et.al. "Excitation function of the reaction $^{46}Ti(n,p)^{47}Sc$ at neutron energy between 2.0 MeV and 3.6 MeV." Phys. Rev. Vol. 126 No.1, 271, (1962).

12. F.G. Armitage."Transmitted to the National Neutron cross-section centre, Brookhaven National Laboratory., by J. Symonds(1967)." Data available from the CSISRS-file.

13. Wu et. al. " Measurement of the $^{58}Ni(n,p)^{58}Co$ cross-section with H(n,n)p as a standard." Nucl. Sci. Engg. 63, 268 (1977).

14. A. Paulsen and R. Widera."$^{58}Ni(n,p)^{58}Co$ and $^{54}Fe(n,p)^{54}Mn$ cross-section measurements for use as threshold detectors." Chemical Nuclear Data Measurements and Applications. Inst. of Civil Engg. London (1971).

15. J.K. Temperley.Nucl. Sci. Engg. 32, 195 (1968).

16. Nakai et. al. J. Phys., Soc., Jpn., 17, 1215 (1962).

17. Barry et.al. J. Nucl. Energy A/B. 16, 467 (1962).

18. J.W.Meadows and J.F. Whalen."$^{58}Ni(n,p)^{58}Co$ cross-sections and Isomer Ratio from 1.04 MeV to 2.67 MeV. Phys. Rev. 130, 2022 (1963).

19. Gonzalez et.al."$^{58}Ni(n,p)^{58}Co$ cross-sections for neutrons of energies between 2.2 MeV and 3.6 MeV." Phys. Rev. 120, 4, 1319 (1960).

20. A.B. Lillie and J.P.Conner. Rev. Sci. Instr. 22, 210(1951)

21. G.A. Sawyer. Rev. Sci. Instr. 23, 604 (1952).

22. E. Fermi. "Nuclear Physics". University of Chicago, Chicago. (1950).

23. W. Whaling. Rev. article in Handbuch der Physik Vol. XXXIV, Springer-Verlag. Berlin(1958).

24. Langmuir. Allison Butts Metallurgical Problems. (1971).

25. Liskien et.al. "Neutron angular distribution for $D(d,n)^3He$, T(p,n) andT(d,n)reactions". Nuclear data tables 11,7, 569 (1973).

26. N.Bohr. Phys. Rev. 58, 654 (1940) and 59, 27 (1941)

27. Katcoff et.al. Phys. Rev. 74, 631 (1948).

28. W.P. Jesse and J. Sadauskis. "Alpha particle ionisation in pure gases and the ave. energy to make an ion pair." Phys. Rev. 90, 1120 (1953).

29. C.E. Melton et.al. "Ionisation produced by 5MeV alpha particles in argon mixtures." Phys. Rev. 96, 643 (1954).

30. T.E. Bartner and G.S. Hurst. "Ionisation of pure gases and mixtures of gases by 5 MeV alpha particles." Phys. Rev. 93, 1236 (1954).

31. J.A. Bistline. "Some properties of BF_3 in ionisation chambers ." Rev. Sci. Instr. 19, 842 (1948).

32. W.N. English and G.C. Hanna."Grid Ionisation Chamber Measurements of electron drift velocities in gas mixtures." Can. J. Phys. 31, 768(1953).

33. P.H. White. "Alpha and Fission Counting of thin foils of fissionable materials." Nucl. Instr. Meth. 79, 1-12 (1970).

34. Rossi et.al. "Ionisation Chambers and Counters." National Nuclear Energy Ser. Div. V2 (1942).

35. M.Akhtar. "Studies to determine the uniformity of fission foils(U_3O_8)." M.Sc. thesis, Dept. of Physics, University of Aston. (1978).

36. R.W. Lamphere. "Fission Detectors." Marion and Fowler Fast Neutron Physics. Part 1 p449-506.

37. V.V. Verbinski and R.G. Giovannini. "Proportional Counter Characteristics and Applications to Reactor Neutron Spectrometry." Nucl. Instr. Meth. 114, 205 (1974).

38. P. Mulas E.L. Haines. Rev. Sci. Instr. 40, 507 (1969).

39. A.E. Grün and E. Schopper. "Argon gas scintillation Counter." Z. Natureforsch 6a, 698 (1951).

40. C. Muehlhause. "Use of a wavelength shifter in a gas scintillation detection." Phys. Rev. 91, 495 (1953).

41. Nobles et. al. "Gas Scintillation Detectors." Phys. Rev. 99, 616 (1955).

42. G.P. Boicourt and J.E. Brolley Jr. "Fast Detector for Fission Counting." Phys. Rev. Lett. 25, 1218 (1954).

43. J.A. Northrop and J.C. Gurskey. "Gaseous Scintillation Counting." Nucl. Instr. Meth. 3, 207 (1958).

44. A. Sayres. and C.S. Wu. "Gas Scintillation Counter." Rev. Sci. Instr. 28, vol10, 758 (1957).

45. L. Koch. "Gas Scintillation Counting." J. Phys. Radium 21, 169 (1960).

46. C.A.N. Conde and A.J.P.L. Policarpo. "A gas proportional Scintillation Counter." Nucl. Instr. Meth. 53, 7 (1967).

47. C.A.N. Conde. "Gas Proportional Scintillation Counter." Nucl.Instr. Meth. 149, 685 (1978).

48. C.A.N. Conde et.al. "The secondary scintillation output of Xenon in a uniform field Gas Proportinal Scintillation Counter." IEEE Trans. on Nucl. Sci. Vol. NS 24, No. 1 , 221 (1977).

49. R.L. Platzman. International J. Appl. Radn. Isotopes 10, 116 (1961).

50. G. Herzberg. "The spectra of di-atomic molecules." Van. Nostrand , New York. (1950).

51. L.Colli. Phys. Rev. 95, 892 (1954).

52. A.E. Grun. Z. Natureforsch. 9a, 55, (1954).

53. L.Koch. "Nuclear Electrònics Proc. Paris." IAEA-Vienna Vol. 1 , 151 (1958).

54. W.R. Bennett. Rev. Sci. Instr. 28, 1092 (1957).

55. O. Stern and M. Volmer.Phys. Z. 20, 183 (1919).

56. K. Schmidt. Z. Natureforsch. 11a , 1023 (1956).

57. E. Kugler. Z. Natureforsch. 12, 115 (1957).

58. R.A. Nobles. "Detection of charged particles with Gas Scintillation Detectors." Rev. Sci. Instr. 27, vol. 5 , 280 (1956).

59. J.A. Northrop and R.A. Nobles. Nucleonics, 14 vol.4 36, (1958).

60. M.A.F. Alves and A.J.P.L. Policarpo. "Effect of a wavelength shifter on the light output of Ar-N_2mixture." Nucl.Instr. Meth. 57, 321 (1967).

61. A.J.P.L. Policarpo et. al. "Argon-nitrogen proportional scintillation counter." Nucl. Instr. Meth. 55, 105 (1967).

62. J.B. Birks. "The theory and practice of scintillation counting." Pergamon Press, Oxford and London. (1964).

63. C. Eggler.and C.M. Huddleston. "Gaseous Scintillation Counting." Nucleonics , vol.14, 34 (1956).

64. M. Forte. Nuovo Cim. 3, 1443 (1956).

65. P. Avivi and G.S. Cohen. Phys. Rev. 108, 972 (1957).

66. R.D. Evans. "The Atomic Nucleus." Mc Graw Hill Brooks Co Inc. New York (1955).

67. H.A. Bethe. Rev. Mod. Phys. 22, 213 (1950).

68. W.P. Jesse and J. Sadauskis. Phys. Rev. 78, 1 (1950).

69. Cormack and Andrew. Properties and strengths of materials McMillans and Co. Ltd.

70. J.H. Neiler and P.R. Bell. Alpha , beta and gamma spectroscopy Vol. 1, (Ed. K. Siegbahn) North - Holland, Amsterdam, 245 (1968).

71. A. Bore. Ph.D. Thesis, University of Birmingham(1973.)

72. H.A. Stuart. Die Strukture des Freien Molekuls, Springer, Berlin. (1952).

73. L. Koch. and R. Lesueur. J. Phys. Radium. 19, 103 (1958).

74. W. Augustyniak et. al. Nucl. Phys. A247, 231 (1975).

75. I. Wagner. Acta Physics. Austriaca 37 vol.3, 293 (1973).

76. B.P. Bayhurst and R.J. Prestwood. J. of Inorg. Nucl. Chem. 23, 173 (1961).

77. S.M. Qaim and N.I. Molla. "Proceedings of the 9th symposium in fusion technology." p589-595 14 - 18th June, 1976.

78. Wapstra and Bos. Atomic and Nuclear Data Tables Vol. 19, (1977).

79. G. Dearnaley and A.B. Whitehead. Nucl. Instr. Meth. 12, 205 (1961).

80. Marcazzan et.al. Phys. Lett. 1, 21 (1962).

81. J. Konijn. Internal report RFA-66 Oct. , 1961.

82. A. Lauber. Internal report SSI-9 June, 1962.

83. A. Lauber and Malmskog. "Measurements of the $^{54}Fe(n,p)^{54}Mn$ reaction cross-sections in the energy range 2.3 MeV to 3.8 MeV" Nucl. Phys. 73, 234(1965).

84. R. Potenza, R. Ricamo and A. Rubbino. "(n,α) and (n,p) reactions in silicon at neutron energies upto 5.5 MeV." Nucl. Phys. 41, 298 (1963).

85. G. Dearnaley and D.C. Northrop. "Semiconductor counters for nuclear radiations". John Wiley. New York. 1966.

86. C.F. Williamson, J.P. Boujot and J. Picard. Report CEA-R-3042. July, 1966.

87. J. Konijn and P. Tollander. " Efficiency calculations for a circular detector viewing a circular radiator." Nucl.Instr. Meth. 36, 302 (1968).

88. I.R. Williams " Monte Carlo calculations of Sample to Detector Geometry." Nucl.Instr. Meth. 44, 160 (1966).

89. A.H. Jeffey. " Solid angle subtended by a circular aperture at point and spread sources." Rev. Sci. Instr. 25, vol. 4,(1954).

90. Facchini et. al. Phys. Lett. 1, vol.1, 8 (1962).

91. J.B. Hurst. " The calibration and use of long counters for the accurate measurement of neutron flux density." NPL REPORT-RS 5, (1976).

92. P.H. White. " Alpha and fission counting of thin foils of fissile material." Nucl.Instr. Meth. 79, 1-12 (1970).

93. Weast. " Handbook of Chemistry and Physics" 54th ed. 1973 - 74.

94. C.A. Rohrman. " Chart of the nuclides". compiled at Battelle-Northwest Laboratory, Richmond Washington for the U.S. At. Energy Comm. (1969).

95. A.H. Wapstra. and N.B. Gove. Nuclear Data Tables 9, 267 (1971).

96. J.Hoste. " Neutron, Photons and Charged particle reactions for activation analysis." Proc. of 1968 Int. Conf. at National Bureau of Standards; Gaithersburg, Maryland. Oct.,7-11, 1968.

97. J.J. Van Loef. Nucl.Phys. 24, 340 (1961).

98. T.S. Mudhole and N. Umakantha. Nucl. Instr. Meth.,116, 401, (1974).

99. T. Mukoyama." Fitting of Gaussian to peaks by non-iterative methods." Nucl.Instr. Meth. 105, 298(1978).

100. L. Kokta. " Determination of Peak Area." Nucl.Instr. Meth. 112, 245 (1973).

101. Dr. J. Owen "Birmingham Radiation Centre, University of Birmingham."

102. G.F. Knoll " Radiation Detection and Measurements." John Wiley and Sons, New York. p396.

103. Bresesti et.al. Nucl.Sci. Engg. 40, 331 (1970).

104. March and Morton. Phil. Mag. 3, 577 (1958).

105 J. Hopkins and G. Breit. Nucl. Data , A 9, 145 (1971).

106 C. M. Atta Vacuum Science and Engg. McGraw-Hill Book Co. (1965).

107 M.E. Ennis and R. Walton. "Targets for production of Neutrons" (J.H. Coon) ed. Marion and Fowler, Fast Neutrons Physics. Part 1.

108 G.W.C. Kaye and T.H. Laby. Tables of Physical and Chemical Constants; Longmans,Green and Co. Ltd. (1959).